Passive Control of Vortex Shedding in the Wakes of Bluff Bodies.

John Clifford Owen, MEng(Hons)

Department of Aeronautics
Imperial College of Science, Technology and Medicine
Prince Consort Road
London SW7 2AZ.

A Thesis submitted for the degree of Doctor of Philosophy in the Faculty of Engineering, University of London.

2001

Abstract

The results of an experimental investigation into the control of vortex shedding in the wakes of bluff bodies are presented. The main aim of this investigation was to gain further insight into how the wake structure of nominally 2D bodies such as circular cylinders could be modified by the introduction of some spanwise geometric disturbances. Types of models studied were those with a fixed separation point, such as square sections and thin plates and also those with moving separation points such as circular cylinders.

Experiments were conducted in both air and water over a large range of Reynolds numbers ($10^1 - 3.4 \times 10^5$) using four wind tunnels and two water tank facilities. Quantitative measurements have shown a significant drag reduction on modified bodies of up to 47% in comparison with the unmodified form. Results from particle image velocimetry (PIV) and flow visualisation have shown that even a small amount of three-dimensionality can produce large changes in the wake width and structure along the span.

It is shown that a common feature of these perturbed bluff body shapes is that they set up significant spanwise velocity components that prevent the wake from rolling up into the conventional 2D wake of von Kármán vortex shedding. This in turn leads to a steady near symmetrical wake with none of the adverse effects associated with vortex shedding.

Applications of the results of this research to practical engineering structures are also discussed. A 3D cylindrical body is developed with elliptically shaped surface protrusions that shows an absence of vortex shedding in the wake regardless of flow direction, achieving a 25% drag reduction over a conventional 2D circular cylinder. Results are also presented which indicate that these bodies may be useful in the attenuation of vortex-induced vibrations as the amplitude of oscillations is significantly reduced when sufficient spanwise three-dimensionality is present.

Acknowledgements

Whilst only one name may appear on the cover, this project would not have been possible without the work and support of numerous other people. Therefore, I would like to take the time here to express my sincerest thanks to all of them for their hard work.

Firstly I would like to thank my supervisor, Professor Peter Bearman, for his help and guidance throughout the duration of the project. I consider it a privilege to have had the chance to work with him. Other academics I would like to acknowledge for their help are Professor Albin Szewczyk (University of Notre Dame, USA), Professor Charles Dalton (University of Houston, USA), Rupad Darekar, Richard Willden, and Dr Spencer Sherwin.

My studentship was funded by the Engineering and Physical Sciences Research Council (EPSRC) and I would like to gratefully acknowledge their financial support.

Due to the experimental nature of this project a lot of technical work was required in order for it to be a success. Whilst I would like to thank all of the technical staff associated with this project equally, I feel that two of them in particular require a special mention. These are Joe Meggyesi (from the main workshop) for all the hours spent building the towing tank and numerous other things, and Alan Smith (from the woodwork shop) for all my 'It'll only take you five minutes' that ended up lasting all day! The remaining technical staff who I would like to thank for their help are John Churchward, Ian James, Roland Hutchins, Gary Senior, Russell Stracey, Bruno Collini, Russell Carter, Clive Mott, John, Wye and John O'Leary.

Also thanks to my long-suffering office mates Mike Elliott and Christine Hogan. Their help and tolerance over the duration of this research are greatly appreciated.

Finally, I would like to thank Lucy for all her help and support (and proof reading this thesis) over the duration of this research.

Publications and Patents

OWEN, J.C., BEARMAN, P.W. & SZEWCZYK, A.A. 2001 Passive control of VIV with drag reduction. *In press* Journal of Fluids & Structures, April 2001.

DALTON, C., XU, Y. & OWEN, J.C. 2001 The suppression of lift on a circular cylinder due to vortex shedding at moderate Reynolds numbers. *In press* Journal of Fluids & Structures, April 2001.

OWEN, J.C., SZEWCZYK, A.A. & BEARMAN, P.W. 2000 Suppression of Karman vortex shedding. Gallery of Fluid Motion, Physics of Fluids. Vol. 12: 1 – 13.

BEARMAN, P.W. & OWEN, J.C. 1998 Suppression of vortex shedding from bluff bodies by the introduction of wavy separation lines. ASME Fluids Engineering Division Summer Meeting, June 21-25, 1998, Washington, DC.

BEARMAN, P.W. & OWEN, J.C. 1998 Reduction of bluff-body drag and suppression of vortex shedding by the introduction of wavy separation lines. Journal of Fluids & Structures. Vol. 12: 123 – 130.

U.K. Patent filed 'Vortex shedding and Drag reduction' Patent application number 0013334.8 – 1st June 2000.

U.S. Patent (provisional) filed 'Method and apparatus for reducing drag and suppressing vortex-induced vibration' Patent application number 835910/82303, 21st November 2000.

Contents

ABSTRACT 2

ACKNOWLEDGEMENTS 3

PUBLICATIONS AND PATENTS 4

CONTENTS 5

LIST OF FIGURES 11

LIST OF SYMBOLS 22

1 REVIEW OF PAST LITERATURE. 25

1.1 BRIEF BACKGROUND TO VORTEX SHEDDING. 25

1.1.1 Introduction. 25

1.1.2 The 2D origin of vortex shedding in the wake. 26

1.2 THREE-DIMENSIONAL EFFECTS IN NOMINALLY 2D FLOWS. 27

1.2.1 Nominally 2D flows. 27

1.2.2 Oblique vortex shedding & end effects. 29

1.2.3 Vortex looping & vortex dislocations. 33

1.3 WAKE TRANSITION. 38

1.3.1 Transition to three-dimensionality. 38

1.3.2 Mode – A transition. 38

1.3.3 Mode – B transition. 42

1.3.4 Shear layer transition. 43

1.3.5 Boundary layer transition. 44

1.4 DISRUPTION OF VORTEX SHEDDING USING 3D GEOMETRY. 46

1.4.1 The effect of a linear variation in spanwise uniformity. 46

1.4.2 The effect of spanwise non-uniformity. 47

1.5 CLASSICAL METHODS FOR THE SUPPRESSION OF VORTEX SHEDDING. 50

1.5.1 Overview. 50

1.5.2 Unidirectional suppression devices. 51

1.5.3 Omnidirectional suppression devices. 56

2 INTRODUCTION TO THE PRESENT INVESTIGATION. 60

2.1 ORIGIN OF WORK. 60

2.2 AIMS OF THE PROJECT. 62

2.3 PLAN TO THE REST OF THE THESIS. 63

3 EXPERIMENTAL SET-UP AND PROCEDURE. 67

3.1 INTRODUCTION. 67

3.2 TOWING TANK EXPERIMENTS. 68

3.2.1 Introduction. 68

3.2.2 Design of the new towing tank facility. 68

3.2.3 Laser illumination system. 72

3.2.4 Flow visualisation techniques. 74

3.3 THE 3'×3' WIND TUNNEL EXPERIMENTS. 78

3.3.1 Introduction. 78

3.3.2 Pressure measurements. 78

3.3.3 Hot wire anemometry. 80

3.3.4 Experimental procedure. 81

3.3.5 Wind tunnel blockage correction. 82

3.3.6 Surface flow visualisation. 82

3.4 THE 4½'×4' WIND TUNNEL EXPERIMENTS. 83

3.4.1 Introduction. 83

3.4.2 Drag force measurements. 83

3.4.3 Experimental procedure. 85

3.4.4 Blockage correction. 86

3.5 PARTICLE IMAGE VELOCIMETRY. 86

3.5.1 Introduction. 86

3.5.2 The wind tunnel system. 87

3.5.3 PIV wind tunnel procedure. 90

3.5.4 The image interrogation system and data post processing. 91

4 THE EFFECT OF WAVY SEPARATION LINES ON RECTANGULAR SECTION BODIES. 94

4.1 INTRODUCTION. 94

4.1.1 Flow in the wake of a square section cylinder. 94

4.1.2 The effect of wavy separation lines. 98

4.2 EXPERIMENTAL ARRANGEMENT. 99

4.2.1 The use of flow visualisation for the measurement of shedding frequency. 99

4.2.2 Experimental models. 100

4.3 RESULTS – SQUARE SECTION FLOWS. 102

4.3.1 Shedding modes – the importance of end conditions. 102

4.3.2 The effect of Reynolds number. 106

4.3.3 The transition to three-dimensionality. 111

4.4 RESULTS – SQUARE SECTIONS WITH WAVY SEPARATION LINES. 114

4.4.1 The effect of increasing wave steepness. 114

4.4.2 The effect of a splitter plate on the drag of a wavy rectangular section body. 120

4.5 DISCUSSION. 123

4.5.1 Square section cylinders. 123

4.5.2 Wavy cylinders. 129

4.5.3 Experimental Errors. 133

5 FLOW IN THE WAKE OF SINUOUS CIRCULAR CYLINDERS. 135

5.1 INTRODUCTION. 135

5.1.1 Flow in the wake of a vibrating cable. 135

5.1.2 Flow in the wake of a sinuous cylinder. 135

5.1.3 Experimental models. 139

5.2 INITIAL RESULTS. 140

5.2.1 Flow visualisation. 140

5.2.2 Drag measurements. 142

5.2.3 Choice of model for detailed investigations. 144

5.3 DETAILED RESULTS. 145

5.3.1 Flow visualisation. 145

5.3.2 Drag variation and pressure distribution. 151

5.3.3 Velocity fluctuations. 155

5.3.4 Particle Image velocimetry. 162

5.4 DISCUSSION. 173

5.4.1 The three-dimensional structure of the wake. 173

5.4.2 The suppression of Kármán type vortex shedding. 175

5.4.3 Streamwise vortices. 177

5.4.4 The generation of streamwise vorticity. 178

5.4.5 Experimental errors. 182

6 THE SUPPRESSION OF VORTEX SHEDDING USING SURFACE PROTUBERANCES. 184

6.1 INTRODUCTION. 184

6.1.1 Previous devices. 184

6.1.2 The design of a vortex suppression device. 186

6.2 EXPERIMENTAL MODELS. 189

6.2.1 Model construction. 189

6.2.2 Model configurations. 190

6.3 INITIAL RESULTS. 190

6.3.1 Introduction. 190

6.3.2 Uni-directional suppression of vortex shedding. 191

6.3.3 Omni-directional suppression of vortex shedding. 194

6.4 DETAILED RESULTS. 198

6.4.1 Variation of C_D with Reynolds number. 198

6.4.2 Surface pressure distribution. 199

6.4.3 Particle image velocimetry. 203

6.5 DISCUSSION. 205

6.5.1 The effects of surface protuberances on vortex shedding. 205

6.5.2 Optimisation of surface protuberances. 209

6.5.3 Experimental errors. 210

7 VORTEX INDUCED VIBRATIONS. 211

7.1 INTRODUCTION. 211

7.1.1 Vortex induced vibrations of circular cylinders. 211

7.2 EXPERIMENTAL SET-UP. 215

7.2.1 Introduction. 215

7.2.2 Vortex induced vibrations. 215

7.3 RESULTS. 220

7.3.1 The response of a cylinder at low mass and damping. 220

7.3.2 The effect of mass damping. 222

7.3.3 The effect of two degrees of freedom. 223

7.4 DISCUSSION. 224

8 CONCLUSIONS AND RECOMMENDATIONS FOR FURTHER WORK. 226

8.1 CONCLUSIONS. 226

8.2 RECOMMENDATIONS FOR FURTHER WORK. 229

REFERENCES 231

List of figures

Figure 1.1 Schematic diagram showing the entrainment flows in the near wake, Gerrard (1966b) 28

Figure 1.2 Development of an oblique shedding mode in the wake of a circular cylinder at a Reynolds number of 95, l_{span}/D = 140. Picture (a) was taken after the cylinder had travelled a distance of 100 cylinder diameters. In picture (b) the cylinder has travelled 600 cylinder diameters and the end effects have propagated to the centre span forming a chevron shape, Williamson (1989) 28

Figure 1.3 A proposed vortex structure close to the endplate of a circular cylinder, Eisenlohr & Eckelmann (1989). 30

Figure 1.4 The promotion of parallel vortex shedding in the wake of a circular cylinder using larger diameter coaxial end cylinders, Eisenlohr & Eckelmann (1989). 30

Figure 1.5 The promotion of parallel vortex shedding in the wake of a circular cylinder at a Reynolds number of 95 using angled endplates, Williamson (1989). 32

Figure 1.6 The promotion of parallel vortex shedding in the wake of a circular cylinder using suction tubes downstream of the cylinder endplates, Miller & Williamson (1994). 32

Figure 1.7 Development of a vortex dislocation in the wake of a tapered circular cylinder, Piccirillo et al (1993). 34

Figure 1.8 Visualisation of the flow in the wake of a circular cylinder subject to a ring disturbance at centre span (Reynolds number = 100). In this figure, the symmetric vortex dislocation is clearly visible, which is far larger than the ring disturbance that caused it, Williamson (1992) 36

Figure 1.9 The 3-D structure in the wake of a segmented blunt trailing edge section, Petrusma & Gai (1994). 36

Figure 1.10 The variation of Strouhal number with Reynolds number for a circular cylinder in the 2-D to 3-D transition range, Williamson (1996a) 39

Figure 1.11 Transition modes A and B. (a) Mode A instability showing the generation of vortex loops with a spanwise wavelength of 4.01 cylinder diameters. (b) Mode B instability

showing the formation of fine scale streamwise pairs with a spanwise spacing of approximately 1.0 cylinder diameters, Williamson (1996b). 39

Figure 1.12 Smoke wire visualisation in the wake of a circular cylinder in the fully developed Mode – A regime (Reynolds number = 200), Williamson (1992). 40

Figure 1.13 Neutral stability curves for the circular cylinder wake, Reynolds number versus spanwise instability wavelength. Within the hatched area any three-dimensional instability will experience exponential growth, Barkley & Henderson (1996). 40

Figure 1.14 Transition waves in the wake of a circular cylinder, visualised by Gerrard (1978): (a), Reynolds number = 1083; (b), Reynolds number = 1968. 45

Figure 1.15 The suppression of vortex shedding from a circular cylinder using a wavy separation wire, Naumann et al (1966). 48

Figure 1.16 Measurements of drag coefficient versus wave steepness: Δ, normal plates; rectangular cross-section bodies, Bearman & Owen (1998a). 48

Figure 1.17 Inverse of formation length versus base suction coefficient for a blunt based aerofoil section, Bearman (1965). 53

Figure 1.18 Suppression of vortex shedding from a blunt based semi-ellipse model with base bleed, C_q = 0.188, Zdravkovich (1981). Picture originally unpublished work of Prof. P.W. Bearman. 53

Figure 1.19 Disruption of vortex shedding by means of a small control cylinder inserted into the wake of a circular cylinder at a Reynolds number of 3000. With the control cylinder in place (right-hand pictures) the wake width can be seen to be considerably narrower and less time dependent over a shedding cycle, Dalton et al (2001). 55

Figure 1.20 Various omni directional devices for the suppression of vortex shedding: (a), porous shrouds. (b), helical strakes. 57

Figure 1.21 The relative stability of a circular cylinder fitted with helical strakes for varying values mass-damping parameter, Scruton & Walshe (1957). 57

Figure 2.1 The various model geometries used during this investigation: (a), a square section cylinder with a wavy leading edge, Bearman & Owen (1998 a,b); (b), a sinuous circular cylinder, Owen et al (2000); (c), a circular cylinder fitted with elliptically shape surface protuberances, Owen et al (2001) 65

Figure 3.1 Details of the carriage system fitted to the towing tank: (a) View along the length of the towing tank showing the drive belts and slide rails, (b) Close-up view of the carriage wheels and rail. 69

Figure 3.2 A schematic diagram showing the layout of the towing tank when fitted with the video camera. 71

Figure 3.3 An example of a large following error in the carriage servo system due to too much velocity damping. 71

Figure 3.4 A schematic diagram of the laser illumination box. The box consists of two parallel mirrors coupled to move in the form of a parallelogram that can be operated via the control knob as shown. By adjusting the angle of the mirrors with this control knob the laser sheet can projected over a maximum distance of up to 12 metres before exiting the box. 73

Figure 3.5 The three ingredients needed to make the highly viscous sodium fluorescein solution (shown in beaker) used in flow visualisation experiments: corn syrup, methanol and sodium fluorescein solution. 77

Figure 3.6 Two of the facilities used at the Department of Aeronautics at Imperial college: (a) The 3'x 3' wind tunnel, (b) The water channel. 79

Figure 3.7 Mounting arrangements for models attached to the drag balance in the $4^1/_2$'x 4' wind tunnel: (a) Plan view of the tunnel, (b) Cross-section of the tunnel. 84

Figure 3.8 Components of the PIV system: (a) The rotating mirror system and camera, (b) The image interrogation rig, Elliott (2000). 89

Figure 4.1 The effect of Reynolds number on Strouhal number in the wake of a square section cylinder taken from Sohanker et al (1999). The solid line is expressed by St = 0.18 - 3.7/Re, Norberg (1996). 96

Figure 4.2 Flow regimes in the wake of a square section cylinder at low Reynolds numbers, Robichaux et al (1999): (a), no separation from sides; (b), separation from the upstream corners and reattachment to the sides; (c), separation from the upstream corners without reattachment to the sides. 96

Figure 4.3 Plan view visualisation of the wake of a square section cylinder at a Reynolds number of 80, $l_{span}/D = 95$. Picture (a) was taken after the cylinder had only travelled 110 base heights downstream and initially the vortices were shed parallel to the cylinder axis. In picture

(b) the cylinder has travelled a further 300 base heights downstream where the end effects have propagated to the centre span to form a chevron pattern..... 103

Figure 4.4 Variation of Strouhal number with Reynolds number for oblique vortex shedding in the wake of a square section cylinder: ♦, oblique vortex shedding – present results; Δ, non Karman instabilities – present results; , vortex shedding – Gerrard (1978); --, St = 0.18 – 3.7/Re – Norberg (1996). 105

Figure 4.5 Visualisation of imposed parallel shedding in the wake of a square section cylinder by the use of angled endplates (leading edges angled inwards by an angle of 9°), Reynolds number = 80, $l_{span}/D = 95$. 105

Figure 4.6 Cross-sectional visualisations of the wake of a square section cylinder at increasing Reynolds numbers, $l_{span}/D = 95$..... 107

Figure 4.7 The variation of Strouhal number with Reynolds number for imposed parallel shedding in the wake. 109

Figure 4.8 The probability density of mode – A wavelengths (λ_A) in the wake of a square section cylinder at a Reynolds number of 185. 109

Figure 4.9 Visualisation of the transition modes in the wake of a square section cylinder. (a) Mode – A instability causing the periodic formation of streamwise vortex loops, Reynolds number = 185. (b) Mode – B instability showing the formation of fine scale streamwise vortices, Reynolds number =240..... 113

Figure 4.10 Cross-sectional visualisations at different spanwise positions for the model with wave steepness w/L = 0.06: (a), visualisation at the peak showing the wide wake and a previously shed vortex being stretched back into the near wake; (b), visualisation at the valley showing a low intensity symmetrical wake which is observed to be similar in structure to the pre-vortex shedding wake of a square section cylinder, Reynolds number =100. 115

Figure 4.11 Plan view visualisation in the wake of a wavy square cylinder model with very low wave steepness (w/L = 0.02). This small level of wave steepness is observed to cause the early onset of mode – A at a Reynolds number of 100. Spanwise wavelength = 6h. 117

Figure 4.12 Flow visualisation picture of the wakes of the wavy square cylinder model (w/L = 0.06), showing the large-scale spanwise instabilities in the primary vortices, Reynolds number = 100. 117

Figure 4.13 Flow visualisation pictures for the model of wave steepness w/L = 0.1: (a), a cross sectional visualisation at the peak showing the wide symmetrical wake and the periodic rolling-up of vortices in the shear layers; (b), plan view of the wake showing a complete lack of conventional von Karman vortex shedding characteristics. 119

Figure 4.14 The effect of wave steepness on the drag of a wavy square section cylinder: ♦, present results, Reynolds number = 5×10^4; , Bearman & Owen (1998a), Reynolds number = 5×10^4. 121

Figure 4.15 The effect of splitter plate length (l_s) on drag: , square section cylinder; •, wavy square section cylinder (w/L = 0.10). Reynolds number = 5×10^4. 121

Figure 4.16 Comparison of results from various authors for the square section cylinder showing the variation in value of onset Reynolds number, Strouhal number & transition to three-dimensionality. Experimental results *. 124

Figure 4.17 Variation of base pressure with Reynolds number for a circular cylinder at low Reynolds numbers showing hysteresis in the value of Reynolds number for the onset of vortex shedding, Henderson (1995). 124

Figure 4.18 Flow regimes at low Reynolds numbers in the wake of a square section cylinder: o, square section parallel shedding; ---, $St = 0.219 - 0.587/\sqrt{\mathrm{Re}} - 1.205/\mathrm{Re}$; ---, $St \approx 0.905 St_{\infty}$; ---, $St = 0.1249 + \mathrm{Re}/3921$. Re_1, onset of vortex shedding in the wake; Re_2, critical Reynolds number of the separation – reattachment regime; Re_3, separation from the leading corners and the onset of mode – A. 127

Figure 4.19 Parameter space plot for wavy square section cylinders showing the effect of non-dimensional wavelength on the required wave steepness to suppress vortex shedding in the wake, Darekar & Sherwin (2001). Solid symbols represent where vortex shedding is suppressed, open symbols where vortex shedding is disrupted but not suppressed. 130

Figure 4.20 The range of unstable wavelengths in the wake of a circular cylinder versus Reynolds number, Barkley & Henderson (1996). Solid line illustrates the most unstable Mode – A wavelengths and data points are from experiments of Mansy et al (1994) & Williamson (1996a) 130

Figure 5.1 Vorticity contours showing the flow in the wake of a cable vibrating in a standing wave mode at a Reynolds number of 100, Newman & Karniadakis (1997): (a), flow in the wake downstream of an anti-node; (b), flow in the wake downstream of node. 136

Figure 5.2 Flow in the wake of a distorted cylinder at a Reynolds number of 72, Honji & Ishi (1976). Regular vortex shedding can be seen to the right of the figure where the cylinder is straight but this is replaced with large streamwise vortices where the cylinder is distorted. Cylinder wavelength λ = 12.8D and cylinder wave steepness w/λ = 0.344 where w is the peak to peak wave height of the cylinder..... 136

Figure 5.3 Flow in the wake of a sphere at a Reynolds number of 320, Leweke & Provansal (1999): (a), visualisation of the interconnecting hairpin vortex structures in the wake; (b) & (c) details of the hairpin loops at approximately 7D downstream..... 138

Figure 5.4 Schematic diagram of a typical sinuous cylinder layout illustrating the axis convention used. The origin is defined at the centre of the central peak of the model..... 138

Figure 5.5 Crossflow visualisations of the flow in the wake of sinuous cylinders of increasing wave steepness at a Reynolds number of 100. The left-hand column shows the flow in the wake of a geometric peak (where the body extends furthest upstream) whilst the right-hand column shows flow in the wake of a geometric trough..... 141

Figure 5.6 The effect of wave steepness on the drag of a sinuous cylinder at a Reynolds number of 3.3×10^4: •, measured values of C_{Dm}; , C_{Dc} corrected for the local effect of the leading edge yaw using $C_{Dc} = C_{Dm} / \int \cos\alpha \, dx$, where α is the angle of yaw..... 143

Figure 5.7 Plan view visualisation in the wake of the sinuous cylinder showing a spanwise vortex becoming increasing wavy in the wake leading to the formation of streamwise vortices. Cylinder wavelength λ = 7.5D, cylinder wave steepness w/λ = 0.167 and Reynolds number =100..... 143

Figure 5.8 Plan view visualisation of the wake of the sinuous cylinder at a Reynolds number of 100 showing pairs of interconnecting hairpin vortices shedding downstream of the troughs. Cylinder wavelength λ = 7.5D and cylinder wave steepness w/λ = 0.167..... 146

Figure 5.9 Detailed visualisations of the wake of the sinuous cylinder in the crossflow (X–Z) plane at a Reynolds number of 100: (a), flow in the wake of a peak showing the formation of a symmetrical narrow wake; (b), flow in the wake of a trough showing the heads of the hairpin vortices as large rollers in the upper and lower shear layers..... 148

Figure 5.10 Schematic diagrams showing the modes of vortex loop shedding in the wake of the sinuous cylinder: (a), symmetric shedding of loops where the loop is drawn into a vortex

from the same side of the wake; (b), anti-symmetric of vortex loops where loop is drawn into a vortex from the opposite side of the wake. 150

Figure 5.11 Computational visualisation of the flow in the wake of a wavy square section cylinder at a Reynolds number of 100 showing the anti-symmetric mode of hairpin shedding, Darekar & Sherwin (2001). Wavelength $\lambda = 5.6D$ and wave steepness $w/\lambda = 0.167$..... 152

Figure 5.12 The effect of incidence on the drag of the sinuous cylinder at a Reynolds number of 4×10^4. The solid line shows the variation with the drag coefficient based on cylinder diameter, the dotted line shows the variation in drag coefficient based on projected frontal area. 152

Figure 5.13 Spanwise variation in base pressure distribution for the sinuous cylinder at different angles of attack at a Reynolds number of 5×10^4: , 0°; ♦, 10°; •, 20°. 154

Figure 5.14 Spanwise variation in front face pressure distribution for the sinuous cylinder at different angles of attack at a Reynolds number of 5×10^4: , 0°; ♦, 10°; •, 20°. 154

Figure 5.15 Variation in velocity power spectra for a circular cylinder at various positions above the wake centre line for a Reynolds number of 5×10^4. Probe positioned 2.0D downstream of the centre span. 157

Figure 5.16 Variation in velocity power spectra for the sinuous cylinder model at various positions above the wake centre line for a Reynolds number of 5×10^4. Probe positioned 2.0D downstream of a peak at Y=0. 158

Figure 5.17 Variation in velocity power spectra for the sinuous cylinder model at various positions above the wake centre line for a Reynolds number of 5×10^4. Probe positioned 1.5D downstream of an inflection point at Y=0.25. 159

Figure 5.18 Variation in velocity power spectra for the sinuous cylinder model at various positions above the wake centre line for a Reynolds number of 5×10^4. Probe positioned 1.0D downstream of a trough at Y=0.5. 160

Figure 5.19 A schematic representation of the wake of the sinuous cylinder determined using a hot-wire probe at a Reynolds number of 5×10^4: (a), an orthographic view of the wake; (b), a side view of the wake illustrating the difference in wake profile between a peak and a trough; (c), front view of the wake. 161

Figure 5.20 Three instantaneous PIV images in the wake of a circular cylinder at a Reynolds number of 1.7×10^4. The images are taken many shedding cycles apart but are arranged so as to show the shedding of a vortex from the lower shear layer. Contours illustrate non-dimensional vorticity. 164

Figure 5.21 Three instantaneous PIV images in the wake of the sinuous cylinder downstream of a geometric peak at a Reynolds number of 1.7×10^4. The images reveal a complete lack of vortex shedding and wake unsteadiness. Contours illustrate non-dimensional vorticity. 165

Figure 5.22 Three instantaneous PIV images in the wake of the sinuous cylinder downstream of an inflection point at a Reynolds number of 1.7×10^4. The images reveal a complete suppression of vortex shedding in the wake. Contours illustrate non-dimensional vorticity.. 166

Figure 5.23 Three instantaneous PIV images in the wake of the sinuous cylinder downstream of a geometric trough at a Reynolds number of 1.7×10^4. The images show a significant increase in wake width and the random shedding from individual shear layers of vortices into the wake 167

Figure 5.24 A comparison of plan view PIV images of the centre wake for the sinuous cylinder and the circular cylinder at a Reynolds number of 1.7×10^4. The vector magnitude is represented by both its length and colour to help highlight regions of reversed flow 169

Figure 5.25 Details of the fluctuation in node position downstream of a peak: (a), node obscured in the glare region within 1D downstream of the model; (b), node clearly visible at approximately 3D downstream of the model showing the region of reversed flow towards the cylinder 171

Figure 5.26 A plan view PIV image of the sinuous cylinder taken in a plane at 0.6D above the centre wake and at a Reynolds number of 1.7×10^4. The image clearly shows the increase in freestream velocity over the leading edge of the cylinder and the large wake regions downstream of the geometric troughs. 172

Figure 5.27 A schematic diagram determined from PIV images showing the time mean streamlines in the wake of the sinuous cylinder at a Reynolds number of 1.7×10^4. 174

Figure 5.28 A schematic view from downstream showing how the shear layers are distorted under the action of the streamwise vortices in the near wake. 174

Figure 5.29 A schematic diagram determined from PIV illustrating the flow orientation at separation for the sinuous cylinder. The maximum yaw angle of the flow is found near to the inflection points and is determined to be equal to an angle of approximately 10° to the freestream flow..... 181

Figure 5.30 Velocity details at the inflection points of the separating flow for the sinuous cylinder: U_∞, freestream flow; U_{sep}, the resultant flow velocity at separation; U_n, component of velocity normal to the separation line; U_t; component of velocity tangential to the separation line..... 181

Figure 6.1 Schematic diagram of the wavy cylinder investigated by Ahmed *et al.* (1993).. 185

Figure 6.2 Schematic representation of a body where the waviness of the front and back is half a wavelength out of phase with the waviness of the sides. 185

Figure 6.3 Various geometric configurations of elliptically shaped surface protuberances: (a), protuberances fitted to the front and back of the cylinder; (b), protuberances fitted to the front, back and sides of the cylinder; (c), protuberances fitted in a spiral pattern around cylinder – angular separation 60°; (d), spiral pattern – angular separation 45°..... 188

Figure 6.4 The effect of surface steepness on C_D at various incidences for a cylinder fitted with front and rear surface protuberances, $Re = 8\times10^4$: •, 0° incidence; , 30° incidence; ×, 60° incidence; Δ, 90° incidence. 192

Figure 6.5 The effect of surface steepness on C_D at various incidences for a cylinder fitted with surface protuberances on the front, back and sides, $Re = 8\times10^4$: •, 0° incidence; , 15° incidence; ×, 30° incidence; Δ, 45° incidence..... 192

Figure 6.6 The effect of surface steepness on C_D at various incidences for a cylinder fitted with surface protuberances arranged in a spiral pattern – angular separation between adjacent protuberances = 60°, $Re = 8\times10^4$: •, 0° incidence; , 10° incidence; ×, 20° incidence; Δ, 30° incidence..... 195

Figure 6.7 The effect of surface steepness on C_D at various incidences for a cylinder fitted with surface protuberances arranged in a spiral pattern – angular separation between adjacent protuberances = 45°, $Re = 8\times10^4$: •, 0° incidence; , 7.5° incidence; ×, 15° incidence; Δ, 22.5° incidence..... 195

Figure 6.8 The effect of incidence on C_D for cylinders fitted with surface protuberances at a fixed spanwise spacing of S_P = 2D but of different relative rotations between adjacent protuberances: ×, 180° rotation between protuberances; , 90° rotation between protuberances; •, 60° rotation between protuberances; Δ, 45° rotation between protuberances. 197

Figure 6.9 The effect of Reynolds number on C_D for cylinders fitted with surface protuberances: Δ, plain cylinder; •, unidirectional suppression device; , omnidirectional suppression device 197

Figure 6.10 Schematic diagram of the layout of surface protuberances and surface pressure tapings for the omnidirectional suppression device. 200

Figure 6.11 Circumferential variation in surface pressure coefficient around the cylinder at a Reynolds Number of 10^5: Δ, plain cylinder; •, unidirectional suppression device; , omnidirectional suppression device. 200

Figure 6.12 Circumferential variation in surface pressure coefficient around the cylinder at a Reynolds Number of 2×10^5: Δ, plain cylinder; •, unidirectional suppression device; , omnidirectional suppression device. 201

Figure 6.13 Circumferential variation in surface pressure coefficient around the cylinder at a Reynolds Number of 3×10^5: Δ, plain cylinder; •, unidirectional suppression device; , omnidirectional suppression device. 201

Figure 6.14 Non-dimensional vorticity contours in the wake of the omnidirectional suppression device at various spanwise positions, Re = 2.7×10^4: (a), protuberances inline with flow; (b), protuberances at 45° to flow; (c), protuberances at 90° to flow. 204

Figure 6.15 Plan view PIV image of the centre wake of the omnidirectional suppression device at a Reynolds number of 2.7×10^4. The vector magnitude is represented by both it's length and colour to help highlight regions of reversed flow 206

Figure 7.1 Compilation of various results by Govardhan & Williamson (2000) showing the effect of combined mass damping parameter on the maximum non-dimensional amplitude of cylinder oscillation, A^*_{max} 213

Figure 7.2 The maximum transverse response amplitude for a circular cylinder as a function of reduced velocity (U^*), Govardhan & Williamson (2000): (a), Typical two branch response

for a cylinder of high mass ratio; (b), Three branch response for a cylinder of low mass ratio. 213

Figure 7.3 A schematic diagram showing the double pendulum suspension rig used to investigate vortex induced vibrations mounted above the water channel. 216

Figure 7.4 Construction details of the lightweight acrylic test cylinders used on the double pendulum suspension rig. 219

Figure 7.5 Maximum transverse response amplitude of an oscillating circular cylinder: •, Khalak & Williamson (1996), $m^* = 2.4$, $m^*\zeta = 1.3\times10^{-2}$; ◊, Khalak & Williamson (1996), $m^* = 10.0$, $m^*\zeta = 1.3\times10^{-2}$; □ present results, $m^* = 14.3$, $m^*\zeta = 3.6\times10^{-2}$ 219

Figure 7.6 Maximum transverse response amplitude of an oscillating cylinder: •, circular cylinder; Δ, unidirectional configuration of surface protuberances; □ omnidirectional configuration of surface protuberances. $m^*\zeta = 3.6\times10^{-2}$, Reynolds number = 1650 – 7500. 221

Figure 7.7 The effect of mass damping parameter ($m^*\zeta$) on the maximum transverse response amplitude of various bodies: •, circular cylinder; Δ, unidirectional configuration of surface protuberances; □ omnidirectional configuration of surface protuberances. --, three start helical strakes, $h_{st}/D = 0.08$, Wong & Cox (1978). 221

List of Symbols

b	Splitter plate length
β	Floquet mode wavelength
C_A	Added mass coefficient
C_{crit}	Critical damping
C_{sys}	System damping
C_D	Drag coefficient
C_{Dm}	Measured drag coefficient
C_{Dc}	Corrected drag coefficient
C_L	Lift coefficient
C_P	Pressure coefficient
C_{pb}	Base pressure coefficient
$-C_{pb}$	Base suction coefficient
C_q	Base bleed coefficient
D	Cylinder diameter
d_1	Cylinder diameter 1
d_2	Cylinder diameter 2
δ_s	Log decrement structural damping.
ε	Averaged absolute error
$f_{cylinder}$	Frequency of vortex shedding from cylinder
f_{ring}	Frequency of vortex shedding from ring
h	Base height

h_{st}	Strake height (helical strakes)
λ	Wavelength
l	Spanwise length
L	Wavy model wavelength
l_{span}	Model span
λ_A	Mode - A wavelength
λ_B	Mode - B wavelength
μ	Viscosity
m_{sys}	System mass
m^*	Mass ratio
m_d	Displaced mass
n	Frequency of vortex shedding
P	Probability
ρ	Density
θ	circumferential position around cylinder
Re	Reynolds number
Re_1	Reynolds number for the onset of vortex shedding
Re_2	Reynolds number for the movement of separation
Re_3	Reynolds number for the onset of Mode - A
Re_{crit}	Critical Reynolds number
R_T	Linear taper ratio
S_P	Spanwise spacing between surface protuberances
St	Strouhal number
St_{cc}	Strouhal number for circular cylinder

St_{sq}	Strouhal number for a square cylinder
T	Time period of vortex shedding
t	Time
t_{LS}	Laser sheet thickness
U^*	Reduced velocity
U_∞	Free stream velocity
w	Peak to peak wave height
w_P	Height of surface protuberance
ω	Vorticity
Y_{max}	Maximum amplitude
ζ	Damping ratio

Abbreviations

PIV	Particle image velocimetry
DPIV	Digital particle image velocimetry
VIV	Vortex induced vibrations
LIF	Laser induced fluorescence
CFD	Computational fluid dynamics
DNS	Direct numerical simulation
LES	Large eddy simulation
RMS	Root mean square

1 Review of past literature.

1.1 Brief background to vortex shedding.

1.1.1 Introduction.

Bluff body flows are of great engineering importance, as most engineering structures erected either onshore or offshore are generally far from streamlined. Countless researchers have conducted numerous investigations into bluff body flows for almost a century all keen to add to our limited understanding. This research has conventionally taken the form of experiments, but more recently with the advent of faster computers, a real contribution to our understanding of these flows is being made by Computational Fluid Dynamics (CFD).

A bluff body is characterised as a body with large regions of separated flow over its surfaces that in turn leads to a high drag. The drag coefficient for a 2D bluff body (such as a circular cylinder) is unexpectedly high because of an unsteady wake phenomenon known as 'vortex shedding'. This vortex shedding causes a low-pressure region in the wake close to the rear of the body, resulting in a high base suction and consequently high drag. If the wake can be made steady and vortex shedding suppressed, then the drag of a circular cylinder can be reduced by up to 37%, Roshko (1954). Vortex shedding has proven to be a very powerful instability in the wakes of 2D bluff bodies and has generally only been disrupted by large disturbances to the wake.

The majority of research into bluff body flows has been conducted on circular cylinders due to their engineering importance and the simplicity with which a circular cylinder experiment or computation is set up. Hence, most of the understanding of bluff body wakes is based on circular cylinders and, by comparison, there has been relatively little work that has investigated the wakes of other bluff bodies.

1.1.2 The 2D origin of vortex shedding in the wake.

At a sufficiently low Reynolds number the flow around a circular cylinder is steady and attached everywhere. As the Reynolds number is increased above about 3 the vorticity can no longer be completely diffused by the boundary layer and separation occurs. This vorticity forms two small recirculation regions immediately behind the cylinder, which grow in size as the Reynolds number is increased. At a critical value of about 49 these two recirculation regions become unsteady and roll-up to form a periodic array of discrete vortices in the wake, termed 'vortex shedding'.

Researchers have observed the existence of this periodic vortex shedding in the wakes of bluff bodies for several centuries. Strouhal first investigated this effect in 1878 and believed it to be responsible for the 'singing' of telephone wires. Strouhal showed that the frequency of vibration could depend not only on the elastic properties, but also on the aerodynamic characteristics of the wire. This led to the now widely used Strouhal number (St), a non-dimensional coefficient that links the wire diameter (D) and velocity (U_∞) to the frequency of vortex shedding (f).

$$St = \frac{fD}{U_\infty}$$

In 1911 von Kármán published his now classical work on the stability of the vortex street in the wake of a bluff body. By modelling the wake using two infinite rows of point vortices he was able to determine the relative stability of the array for various symmetric and antisymmetric arrangements. It was found that all symmetric and antisymmetric configurations were unstable except for one specific antisymmetric arrangement. It was shown that if the ratio of streamwise spacing to lateral spacing is approximately 3.5 (a value found to be in good agreement with experimental observations of the time) then the array would exhibit neutral stability. In more recent times this work has been continued by Schaefer and Eskinazi (1959). They modelled the wake using an array of vortices with a viscous core that was assumed to be growing in time and with increasing downstream distance. From this they

suggested three distinct downstream regions in the wake of the body. A vortex formation region close to the body, a stable region where interactions between vortex cores were small and an unstable region where the growing vortex cores overlapped. When comparisons with experiments were made this model was found to give quantitative agreement with the velocity distribution in the wake.

Gerrard (1966b) showed how the interaction between the two separated shear layers from a bluff body could produce the characteristic vortex shedding behaviour in the wake. Figure 1.1 shows a diagram produced by Gerrard of the various entrainment flows present in the vortex formation region. As the vortex (illustrated in the diagram) is fed by vorticity from the upper separated shear layer it grows in size until it is strong enough to draw the opposite shear layer across the wake. The vorticity from the opposite shear layer is then entrained in three possible directions. A large proportion is pulled into the forming vortex reducing its strength, whilst the remainder finds its way into the shear layer and near wake. At this point, the formation of the vortex is said to be complete and it is then cut off from the shear layer and convected downstream with the flow.

1.2 Three-dimensional effects in nominally 2D flows.

1.2.1 Nominally 2D flows.

The majority of research conducted into bluff body flows has been around the simplifying assumption that the flow is two-dimensional. The reason for this approach is that the large-scale structures of interest in the wake are essentially two-dimensional. However, in practice it has seldom been possible to produce a two-dimensional flow (except at very low Reynolds numbers) in which the spanwise velocity is zero everywhere, since turbulence by its very nature is three-dimensional. Therefore, it is necessary to make the distinction between two-dimensional flows and "nominally two-dimensional" flows. In a nominally two-dimensional flow there may be velocity fluctuations in the spanwise direction, but these fluctuations show no directional preference, and hence the time-averaged flow in the spanwise direction is

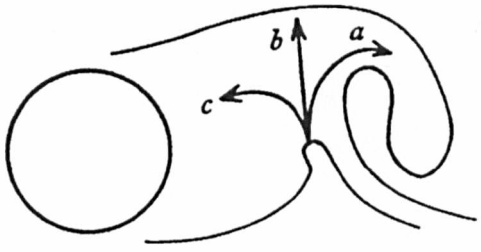


Figure 1.1 Schematic diagram showing the entrainment flows in the near wake, Gerrard (1966b)

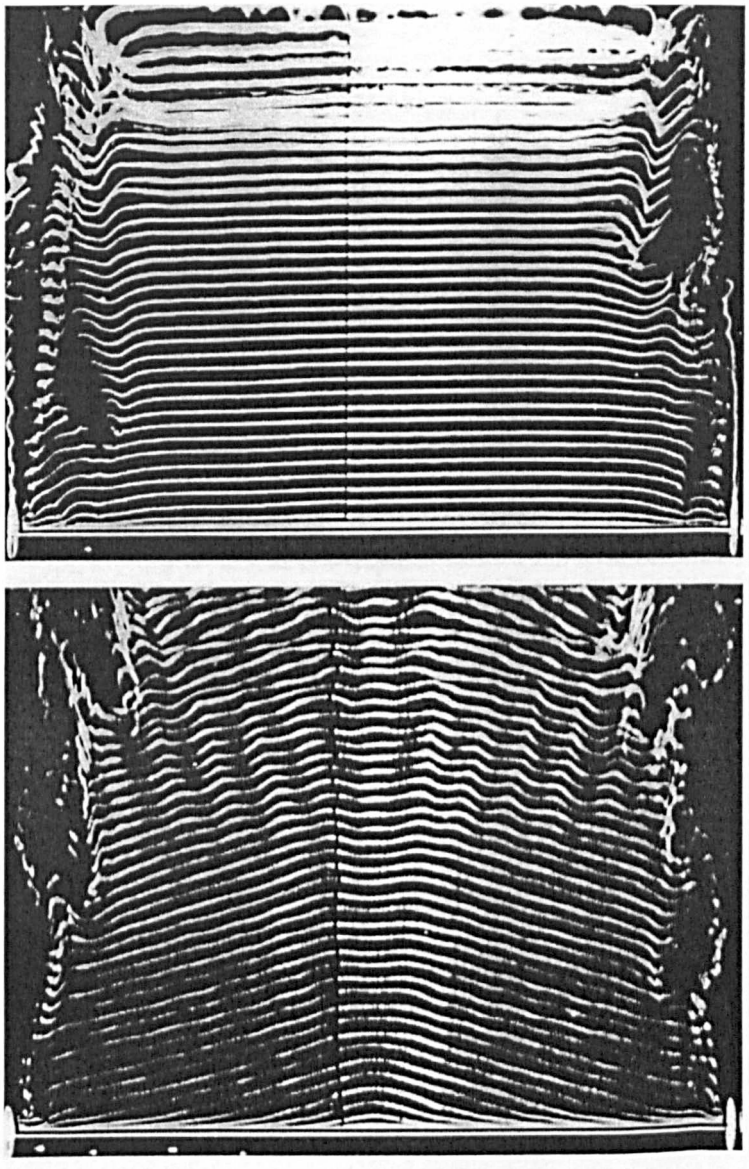


Figure 1.2 Development of an oblique shedding mode in the wake of a circular cylinder at a Reynolds number of 95, $l_{span}/D = 140$. Picture (a) was taken after the cylinder had travelled a distance of 100 cylinder diameters. In picture (b) the cylinder has travelled 600 cylinder diameters and the end effects have propagated to the centre span forming a chevron shape, Williamson (1989).

essentially zero. With this distinction clear, it is possible to consider the dynamics of the formation region under the assumption of 'nominally two-dimensional' flow.

1.2.2 Oblique vortex shedding & end effects.

It has been observed during many investigations that despite carefully controlled experimental conditions, vortices would often be shed straight and parallel to each other but at an inclined angle to the cylinder axis. This phenomenon (termed oblique shedding) was observed as early as Tritton (1959) and is surprising as it would be expected that the vortices would always be shed parallel to the cylinder axis (particularly at low Reynolds numbers) due to the predominately 2D mechanism at work in the wake.

In addition to this oblique shedding other interesting three-dimensional phenomena have also been observed in the wake. Gerrard (1978) observed curved vortices (Reynolds number ≈ 100) in the wake of a circular cylinder bowing back towards the cylinder at the endplates. Gerrard suspected that the cylinder end conditions might be the cause and in a later paper (Slaouti & Gerrard 1981) showed how manipulating the end conditions could affect the two-dimensionality of the primary vortices. It was also suggested that oblique vortex shedding could be caused by a small difference in cylinder end conditions.

Gerich & Eckelmann (1982) investigated the importance of end plates and aspect ratio on the two-dimensionality of the wake. In this paper they introduced the concept of what they called the 'affected region', a region of the wake approximately ten cylinder diameters from the endplates which was said to be directly under the influence of the end conditions. Within this affected region the vortex shedding frequency was found to be 10–15% lower than the regular Strouhal frequency found over the central portion of the cylinder. At the junction between these two frequencies they found the simultaneous existence of two shedding frequencies resulting in a beat frequency which was most pronounced at the junction between the two shedding cells. In addition, it

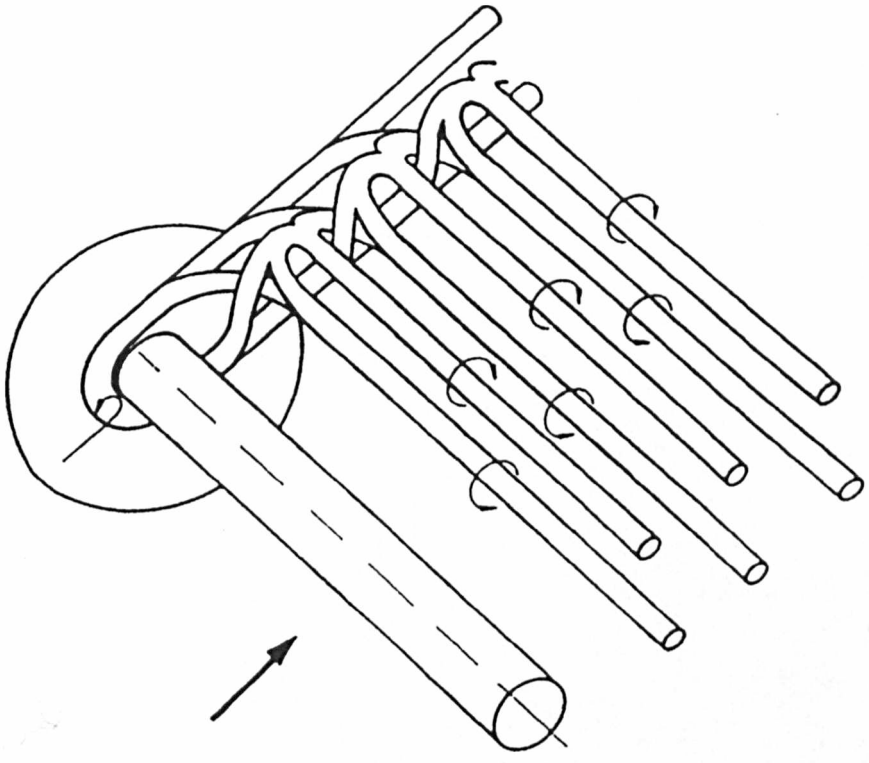


Figure 1.3 A proposed vortex structure close to the endplate of a circular cylinder, Eisenlohr & Eckelmann (1989).

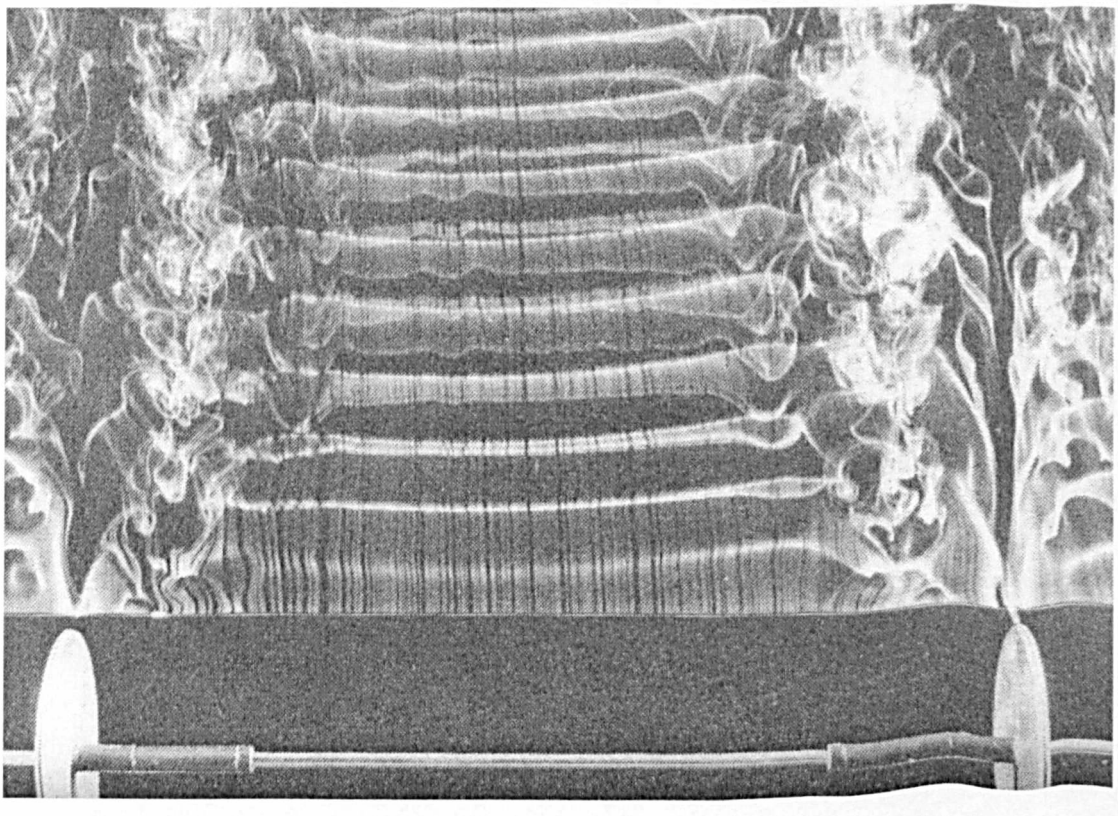


Figure 1.4 The promotion of parallel vortex shedding in the wake of a circular cylinder using larger diameter coaxial end cylinders, Eisenlohr & Eckelmann (1989).

was found that for an endplate spacing of less than 20 – 30 cylinder diameters the onset of vortex shedding in the wake could be delayed to a critical Reynolds number of 60. They concluded that the structure of the vortex shedding in the wake of the cylinder was heavily dependent on both the end conditions and the Reynolds number.

In Williamson (1989) the importance of end conditions has again been demonstrated. In a series of low Reynolds number experiments in a large towing tank, he showed that after sufficient distance had been travelled (600 cylinder diameters for a cylinder aspect ratio of 140) the end effects would propagate all the way to the centre span of the model. Initially parallel vortex shedding was observed from the cylinder, but once the end effects had fully propagated to the centre span a 'chevron-shaped' pattern was observed, figure 1.2. From this figure, it is clear just how much of the wake structure is under the direct influence of the end conditions.

Norberg (1994) has shown that parallel shedding can be achieved by using a cylinder of very high aspect ratio ($l_{span}/D > 2000$). However, in recent years parallel shedding has been achieved from cylinders in the laminar regime for lower aspect ratios via appropriate manipulation of the end conditions. If endplates are fitted, then it was suggested by Eisenlohr & Eckelmann (1989) that a horseshoe vortex structure would be generated close to the endplate that would produce a flow locally opposing the freestream flow producing a lower shedding frequency in that vicinity, figure 1.3. To overcome this they used larger coaxial cylinders as the end condition for the main cylinder. In this configuration the shedding was observed to be parallel and in phase across the whole span of the main cylinder, figure 1.4. In Williamson (1989) parallel shedding was produced by angling the cylinder endplates out (figure 1.5) whilst in Miller & Williamson (1994) it was produced using suction devices downstream of the endplates (figure 1.6). These suction devices were used to locally increase the freestream velocity at the endplates and it was found that only an increase of 1.5% in velocity could yield parallel shedding in the wake.

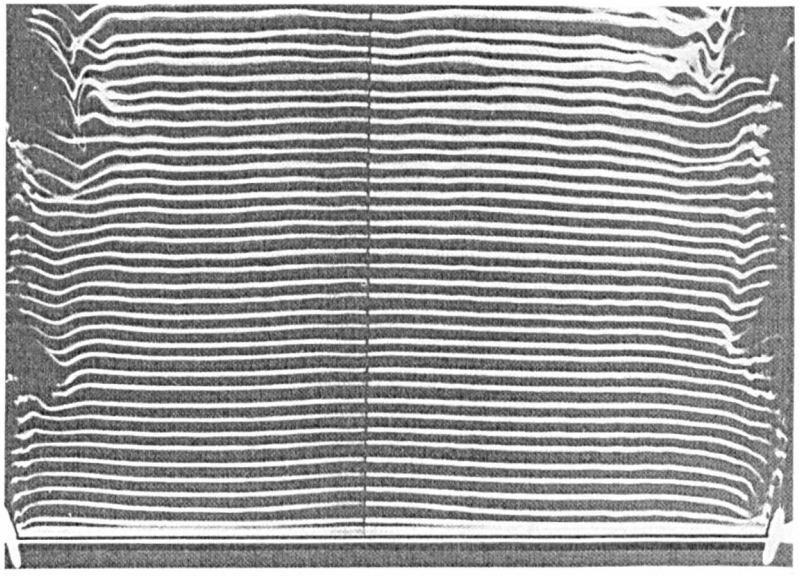


Figure 1.5 The promotion of parallel vortex shedding in the wake of a circular cylinder at a Reynolds number of 95 using angled endplates, Williamson (1989).

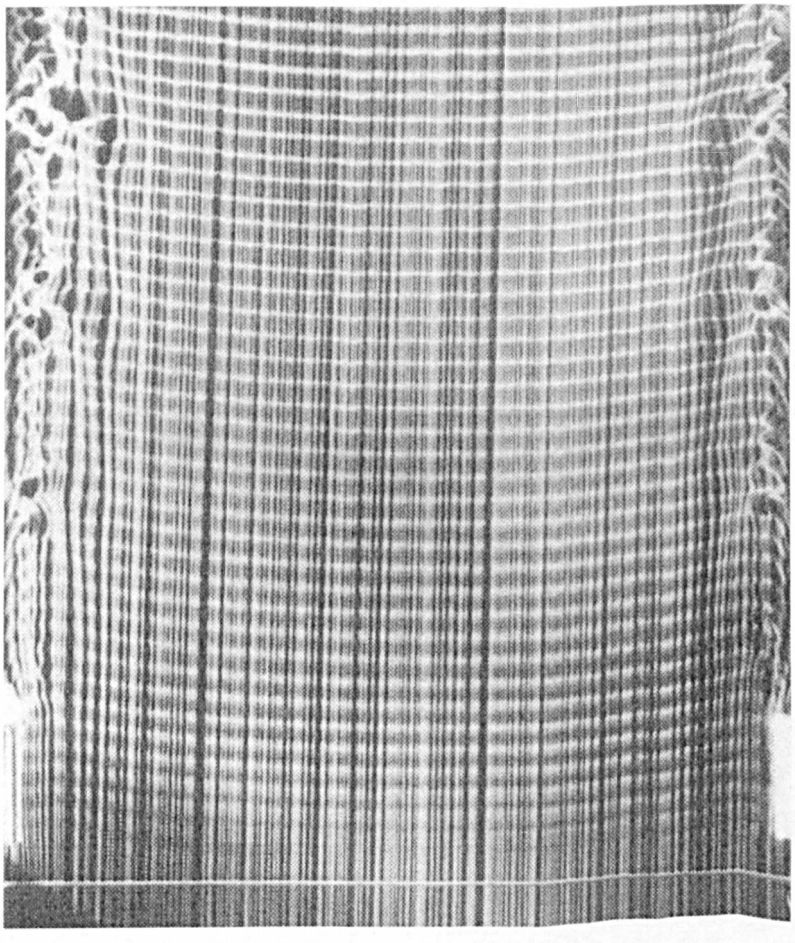


Figure 1.6 The promotion of parallel vortex shedding in the wake of a circular cylinder using suction tubes downstream of the cylinder endplates, Miller & Williamson (1994).

At higher Reynolds number the wake is generally far less coherent with the shedding only being correlated over a few cylinder diameters. Perhaps unexpectedly then, Prasad & Williamson (1997) found it possible to promote parallel or oblique vortex shedding in the subcritical regime using angled endplates in the same way as for the laminar regime. However, Szepessy & Bearman (1992) found that for a circular cylinder in the subcritical regime (Reynolds number = 10^3-10^5), a better approximation to two-dimensional flow was produced by a low aspect ratio cylinder with appropriate end conditions. At an aspect ratio of 1 they found that shedding was completely in phase across the whole span resulting in high fluctuating lift and drag forces. However, for an aspect ratio of 7 they found that the shedding was not in phase across the span and observed significant modulations in both their pressure and velocity signals. They suggested that high aspect ratio bodies were more likely to experience significant cross flows that would decorrelate vortex shedding and reduce their two-dimensionality.

1.2.3 Vortex looping & vortex dislocations.

In the presence of spanwise non-uniformities of the body or flow, the vortex shedding in the wake of a bluff body becomes increasingly disorganised which results in the formation of new vortex structures. Depending on the level of disturbance to the nominally two-dimensional wake, Gerrard (1966a) proposed two possible structures that may result. Small variations in spanwise shedding frequency were generally accommodated by the formation of a vortex split (termed 'vortex dislocation' by Williamson), whilst larger ones would be accommodated by the formation of a vortex loop.

Vortex dislocations are formed in the wake of a bluff body due to local variations in the timing of vortex shedding. In nominally two-dimensional flows these vortex dislocations are generally found to form randomly in both time and space although they can often be triggered by local variations in shedding frequency near endplates. Petrusma & Gai (1996) observed vortex dislocations in the near wake of a circular

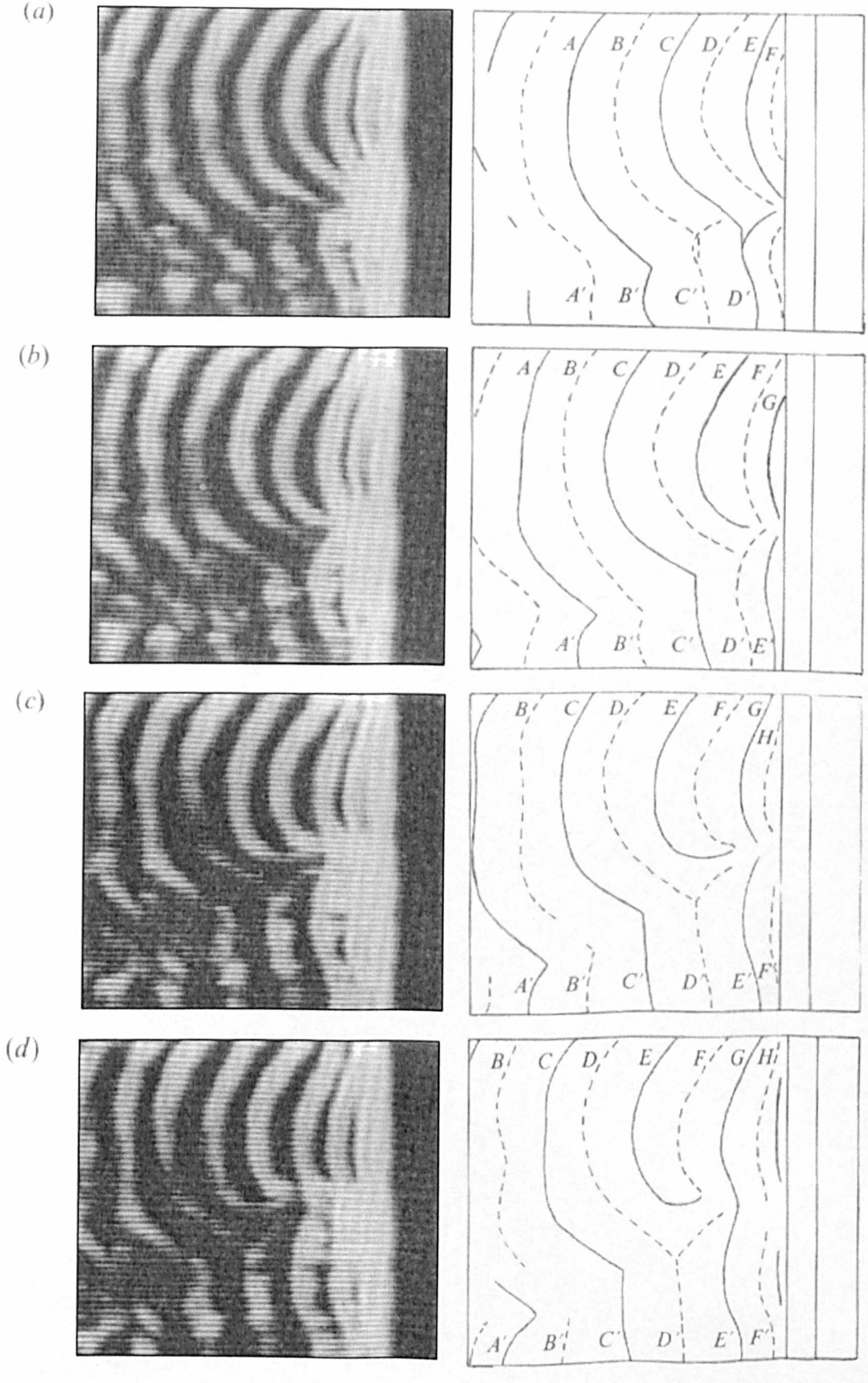


Figure 1.7 Development of a vortex dislocation in the wake of a tapered circular cylinder, Piccirillo et al (1993).

cylinder and a two-dimensional blunt trailing edge section. They found that vortex dislocations in the case of the circular cylinder generally occurred in the mid-span region, whereas for the blunt trailing edge section they occurred more towards the ends. Tombazis (1993) also observed vortex dislocations in the near wake of a blunt straight trailing edge model and found the frequency of dislocation to be independent of Reynolds number.

To gain further insight into the mechanics of vortex dislocations, many researchers have attempted to force their production using spanwise modifications to the body geometry. Piccirillo *et al.* (1993) used a tapered cylinder to investigate vortex dislocations after the earlier work of Gaster (1971) had shown the presence of cellular vortex shedding in the wake of a similarly tapered cylinder. Unlike a conventional cylinder (where the vortex dislocations appear randomly in time and space), this tapered cylinder was found to periodically generate a series of vortex dislocations between neighbouring spanwise cells, figure 1.7.

The effect of a localised modification in cylinder diameter was investigated by Williamson (1992) who conducted a series of experiments using an otherwise uniform circular cylinder but with a small ring of slightly larger diameter attached at the mid-span. This arrangement resulted in the formation of a two-sided vortex dislocation (or spot-like vortex dislocation) in the wake of the cylinder that grew in size with downstream distance, figure 1.8. Within this dislocation two distinct shedding frequencies were determined, $f_{cylinder}$ associated with the diameter of the cylinder and f_{ring} associated with the diameter of the ring. The frequency of vortex dislocations in the flow downstream of the cylinder was found to be the difference between the two shedding frequencies, or $f_{cylinder} - f_{ring}$.

In Tombazis and Bearman (1997) vortex dislocations were promoted in the wake of a blunt based semi-elliptical section by the implementation of wavy trailing edge geometry. Unlike Williamson (1992), the base height (h) of the model was held constant so it would be expected that the shedding frequency would remain constant

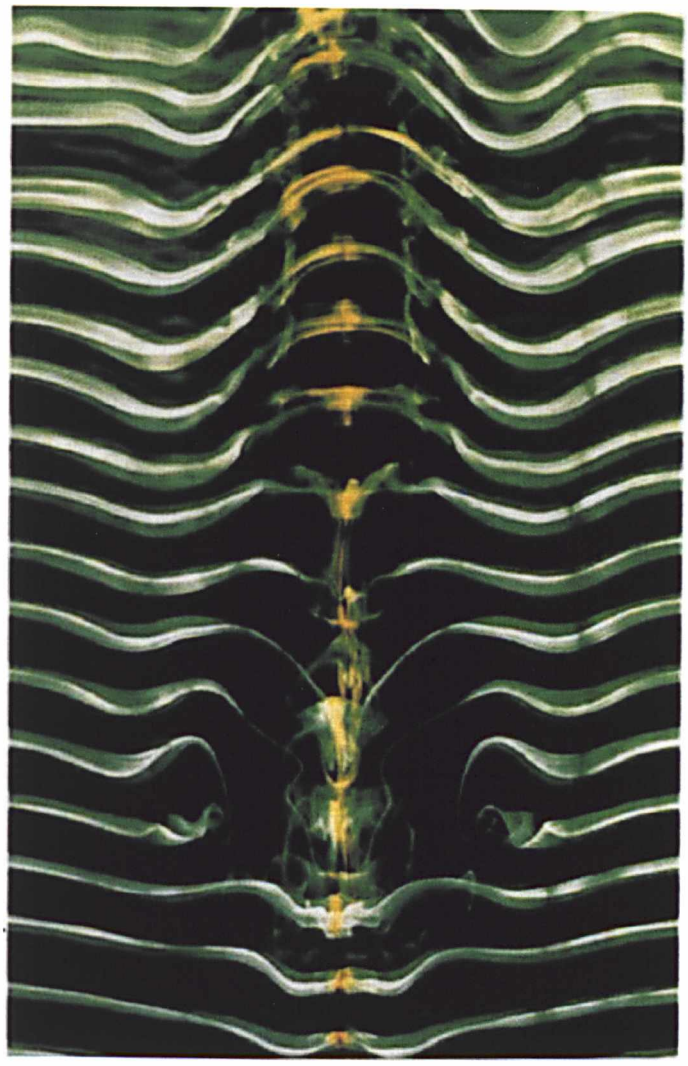


Figure 1.8 Visualisation of the flow in the wake of a circular cylinder subject to a ring disturbance at centre span (Reynolds number = 100). In this figure, the symmetric vortex dislocation is clearly visible, which is far larger than the ring disturbance that caused it, Williamson (1992).

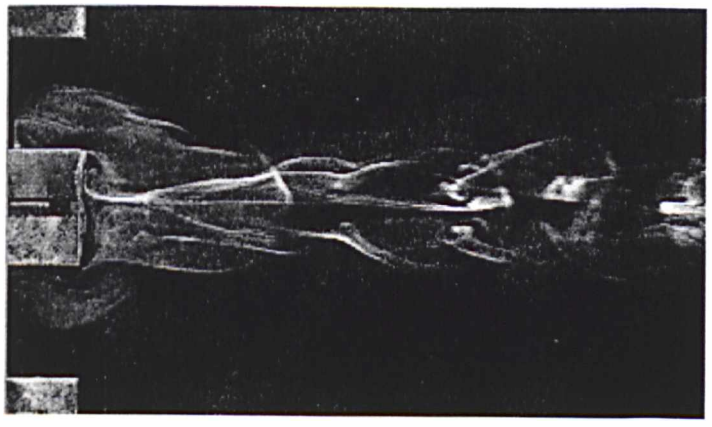


Figure 1.9 The 3-D structure in the wake of a segmented blunt trailing edge section, Petrusma & Gai (1994).

across the span. However, investigation in the wake using a hot-wire probe showed the existence of cellular shedding with two distinct shedding frequencies present in the wake. A similar dual shedding frequency effect was found in the later work of Bearman and Owen (1998a) using wavy base geometry on rectangular section bodies and normal plates.

In contrast to vortex dislocations, there has been relatively little interest in vortex looping. This is primarily because the majority of bluff body research has been centred around nominally two-dimension flows were vortex looping is not commonly observed. Vortex looping is generally only observed in situations of strong three-dimensionality such as at an endplate or free end were the vortex loops across the wake and joins with its co-rotating counterpart from the other side. However, although in general vortex loops are uncommon, one exception to this rule is mode – A transition where large scale vortex looping is readily observed in the wake (see next section).

Irregularities other than vortex loops and vortex dislocations have also been observed in the wakes of bluff bodies. Flow visualisation experiments by Rodriguez (1991) showed the presence of longitudinal vortices in the wake that were shed locally from the root of a segment on the trailing edge. Rodriguez concluded that these longitudinal vortices played an important part in base drag reduction. Petrusma & Gai (1996) also observed these longitudinal vortices when using a similar trailing edge design to that of Rodriguez. They concluded that the presence of the three-dimensional geometric disturbances leads to spanwise vorticity being partially converted into streamwise vorticity. Figure 1.9 shows a flow visualisation (Petrusma & Gai 1994) of the longitudinal vortices being shed from a segmented trailing edged section.

1.3 Wake transition.

1.3.1 Transition to three-dimensionality.

Above a critical Reynolds number (approximately 180 for circular cylinders) the nominally two-dimensional wake of a bluff body undergoes the transition to three-dimensionality. Within this transition there are two distinct regimes of instability. The first instability can be seen as a discontinuous jump in the relationship between Strouhal number and Reynolds number and is termed mode-A. This is the dominant mode of instability in the Reynolds number range 190 – 230 and results in large scale vortex looping and the production of streamwise vortex pairs, figure 1.11a. Beyond these Reynolds numbers and over the range 230 – 260, there is a gradual transfer of energy from mode-A to a second mode of instability termed mode-B. In this latter mode fine scale streamwise vortices are generated (figure 1.11b) and there is also a second discontinuity in the Strouhal number – Reynolds number relationship, figure 1.10.

1.3.2 Mode – A transition.

In mode – A transition the primary vortices deform in a wavy fashion during the shedding process that leads to the local formation of vortex loops. These vortex loops are drawn back into the forming vortex producing streamwise vortex pairs. The process of vortex loop generation is self-sustaining due to Biot-Savart induction from one loop to the next causing a whole series of loops to be formed at the same spanwise location, figure 1.11a. However, the visualisation of mode – A in figure 1.11a can be misleading. This is a picture of a transient wake with the cylinder having only travelled several diameters downstream after being impulsively started from rest. In reality the fully developed wake is highly turbulent with the vortex loops triggering the formation of spot-like vortex dislocations. A more representative illustration of the wake in the mode – A regime is given in figure 1.12.

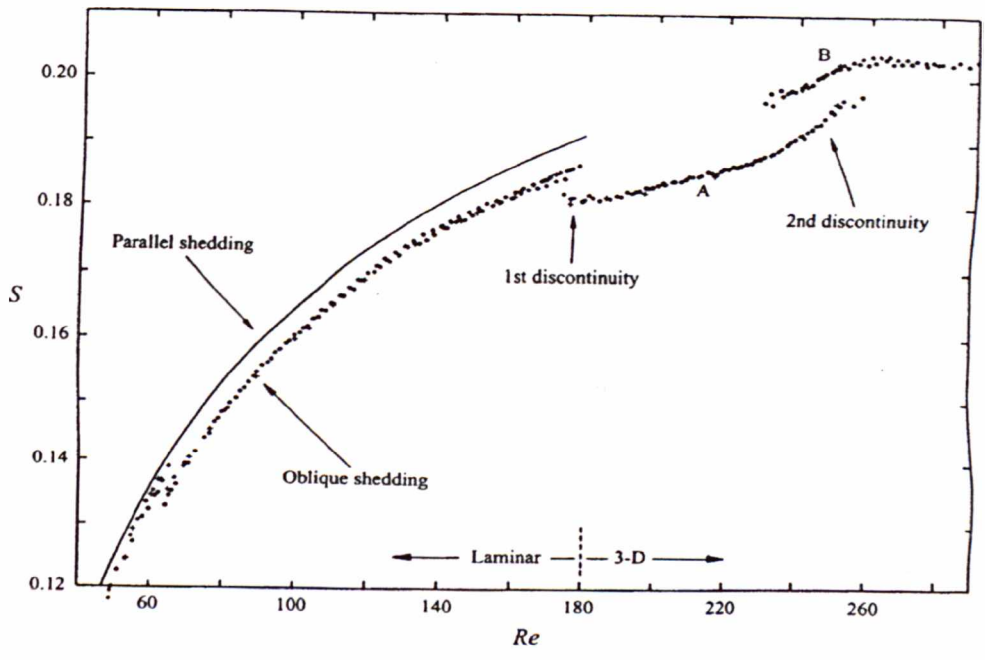


Figure 1.10 The variation of Strouhal number with Reynolds number for a circular cylinder in the 2-D to 3-D transition range, Williamson (1996a).

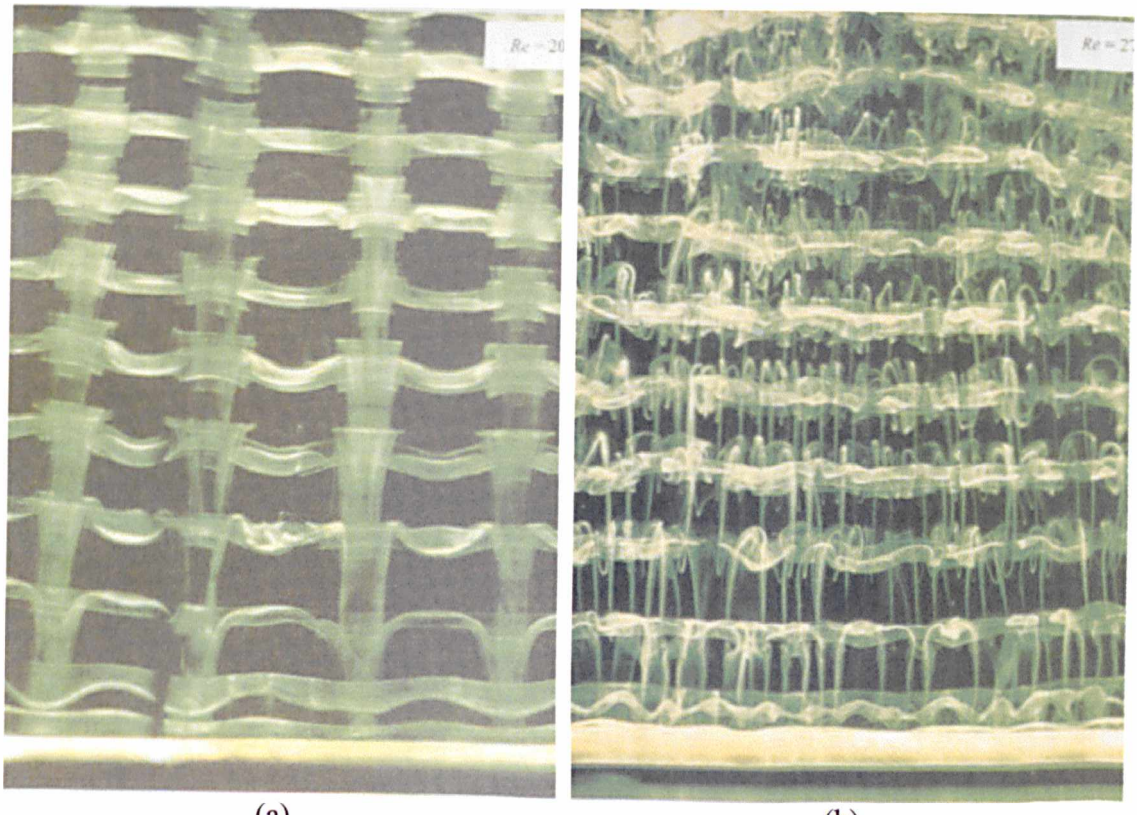


Figure 1.11 Transition modes A and B. (a) Mode A instability showing the generation of vortex loops with a spanwise wavelength of 4.01 cylinder diameters. (b) Mode B instability showing the formation of fine scale streamwise pairs with a spanwise spacing of approximately 1.0 cylinder diameters, Williamson (1996b).

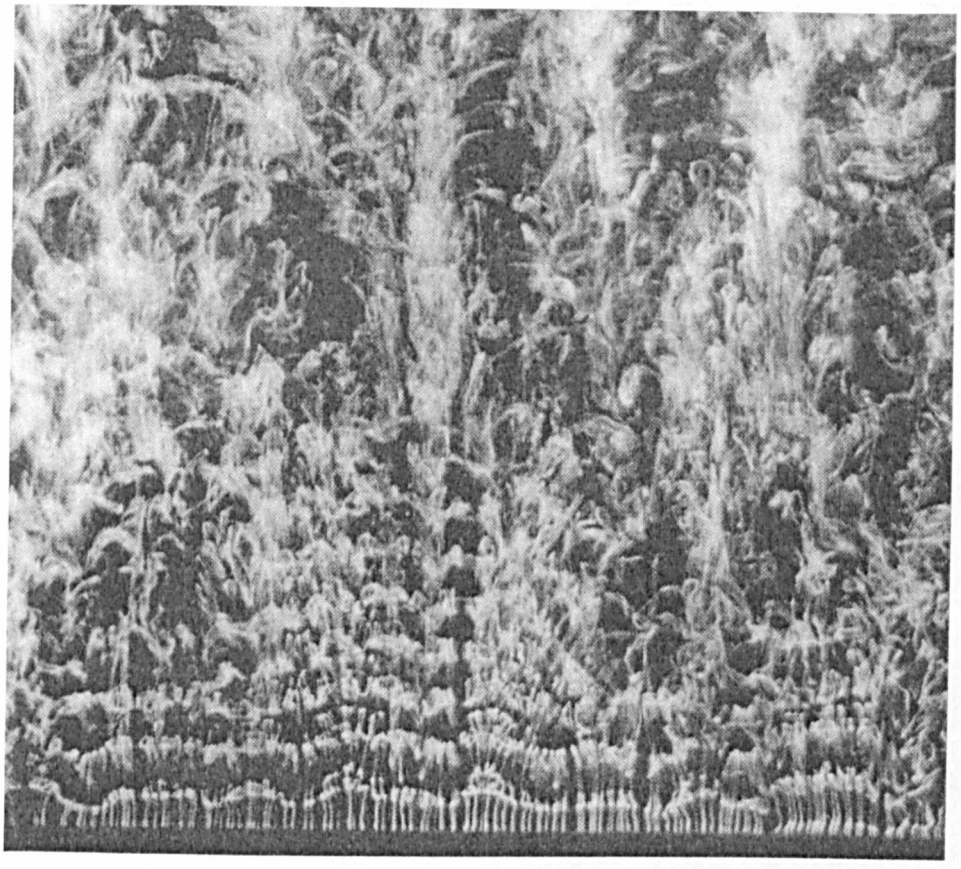


Figure 1.12 Smoke wire visualisation in the wake of a circular cylinder in the fully developed Mode – A regime (Reynolds number = 200), Williamson (1992).

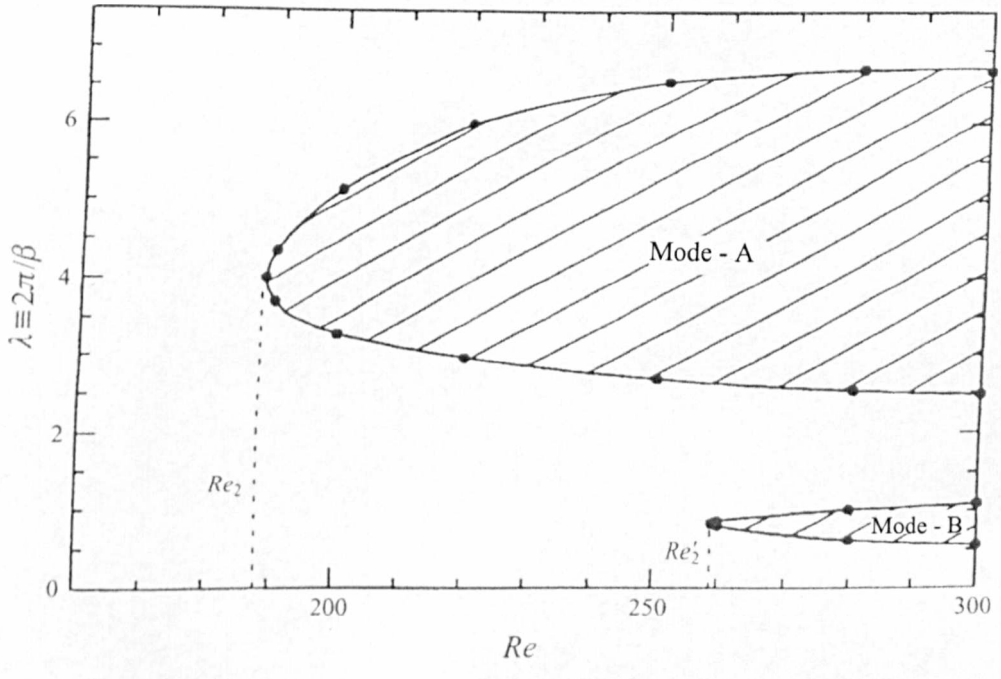


Figure 1.13 Neutral stability curves for the circular cylinder wake, Reynolds number versus spanwise instability wavelength. Within the hatched area any three-dimensional instability will experience exponential growth, Barkley & Henderson (1996).

The critical Reynolds number for the onset of mode – A has been found to vary in the range 140 – 194, depending on experimental conditions. Factors such as surface roughness, freestream turbulence intensity and end effects have all been shown to contribute to the early transition to three-dimensionality in the wake. The highest experimental value for the onset of mode – A has been recorded by Williamson (1996a). Using a towing tank and by careful manipulation of the end conditions it was found possible to delay the critical onset Reynolds number to a value of 194. In addition to this, the spanwise wavelength of vortex pairs has also been found to vary with Reynolds number, in the range of approximately 3 to 4 cylinder diameters. Williamson (1996a) determined this spanwise spacing directly from flow visualisation images of the starting flow and found it to be equal to approximately 4 cylinder diameters at a Reynolds number of 200. Williamson *et al.* (1995) suggested that the spacing would decrease as the Reynolds number increased and found that the spanwise spacing had fallen to a value of approximately 3.2 cylinder diameters at a Reynolds number of 270.

However, investigations into the transition to three-dimensionality have not just been limited to experimental methods. Barkley & Henderson (1996) performed a Floquet stability analysis employing over 10,000 degrees of freedom to determine the critical Reynolds number for the onset of mode – A. They determined that the wake would first become unstable to three-dimensional perturbations at Reynolds number of 188.5 for a spanwise wavelength of 3.96 cylinder diameters, which was found to be in good agreement with the experimental results of Williamson (1996a). However, unlike figure 1.11a (which is a transient flow), experimental observations have generally shown the local wavelength of the mode – A instability to vary considerably across the span. This variation in wavelength was also confirmed by the Floquet analysis, which showed that for Reynolds numbers of above 188.5 the wake would become unstable to three-dimensional perturbations over a broad range of spanwise wavelengths, figure 1.13.

However, one has to be careful when comparing critical onset values between experiments and computations. In experiments values can only be determined from a physical change of wake topology such as a discontinuous change in Strouhal number, spanwise waviness of the primary vortices or the local formation of vortex loops. In contrast, the Floquet analysis of Barkley & Henderson (1996) is able to determine the exact point at which the wake first becomes unstable to infinitesimally small perturbations long before they manifest themselves as physical features of the wake. Therefore, on the basis of this it would be expected that any value determined experimentally is likely to be an over prediction as the instability could be present at a slightly lower Reynolds number, just undetectable to experimental techniques. However, all experiments (however carefully performed) are subject to perturbations which if large enough have been shown to prematurely trigger mode – A. Hence, it is difficult to directly confirm or dispute some computation values due to the uncertainties in experimental conditions.

In recent times the exact mechanism of this three-dimensional instability has become the subject of much debate. Using flow visualisations and two-dimensional computations, Williamson (1996a) has proposed that mode – A is caused as the result of an elliptic instability in the primary vortex cores. However, in contrast, Brede *et al.* (1996) have suggested an alternative mechanism. Using PIV they were able to determine that the peak strength of the three-dimensional vortical structures occurred at approximately six diameters downstream and proposed that mode – A was the result of a centrifugal instability in the braid region between the primary vortices. Hence, there is still the need for further understanding before this issue can be fully resolved.

1.3.3 Mode – B transition.

In contrast to mode – A, mode – B has received relatively little interest, which is surprising as the existence of the fine scale streamwise vortices (a dominant feature of mode – B) have been reported for Reynolds numbers as high as 10^4, Mansy *et al.*

(1994). The character of mode – B is somewhat similar to that of mode – A in that there is formation of streamwise vortices. However, unlike mode – A the vortices are of much finer scale and are generated in the separating shear layers or braid region close to the cylinder body, figure 1.11b. These fine scale vortices only proceed to slightly perturb the primary vortices and the resulting wake (with the exception of the streamwise vortices) is found to be remarkably similar to the wake in the laminar regime. The spanwise spacing of these streamwise vortices is observed to be highly regular and surprisingly unaffected by spanwise waviness in the primary vortices. Williamson (1996a) reported this spanwise spacing to be approximately one cylinder diameter and that it was seemingly unaffected by Reynolds number in the Reynolds number range 260 – 300. However, unlike mode – A, experiments have shown there to be no critical Reynolds number for the onset of mode – B but instead a gradual transfer of energy between the two modes over the Reynolds number range of 230 – 260. As the Reynolds number was increased beyond this range towards 10^3 the fine scale streamwise vortices were observed to become increasingly disordered resulting in a weakening of the primary vortices and a corresponding reduction in base suction.

Barkley & Henderson (1996) using their Floquet stability analysis also detected the presence of a second mode of instability. However, in comparison to Williamson their stability analysis showed that there was a critical Reynolds number for the onset of mode – B of 259. At this Reynolds number the spanwise wavelength of this instability was determined to be approximately 0.8 cylinder diameters. They also showed that in the Reynolds number range 259 – 300 mode – B is a narrow band instability with the wavelength only varying by a maximum of 0.3 cylinder diameters, figure 1.13.

1.3.4 Shear layer transition.

Further transitions occur in the wake as the Reynolds number is increased above approximately 500. Above this Reynolds number, the separated laminar shear layers develop a convective instability known as 'transition waves' or 'Bloor-Gerrard'

vortices. Originally, Bloor (1964) noted the existence of these transition vortices during her investigation into the transition to turbulence in the wake of a circular cylinder. Using a hot wire probe in the wake the frequency of these waves was found to vary with $Re^{3/2}$. Gerrard (1978) visualised these vortices in the wake of a circular cylinder and showed that at high enough Reynolds numbers (above 1000) the shear layer would actually roll up to form discrete vortices. At certain Reynolds numbers these shear layer vortices were found to interact strongly with the primary vortices and for a time actually suppress Kármán vortex shedding, figure 1.14.

More recently, these shear layer vortices have been visualised in the wake of both flat plates and rectangular section bodies by Owen (1997). These bodies had imposed three-dimensionality in the form of wavy separation lines, which were found to suppress the regular Kármán vortex shedding in the wake. At a Reynolds number of approximately 1500 and with the dominant mode of instability removed, these shear layer instabilities were found to become far more pronounced. A similar effect was also observed in the wake of a circular cylinder by Dalton *et al.* (2000) where regular Kármán vortex shedding was disrupted by means of a small control cylinder placed in the wake, figure 1.19.

1.3.5 Boundary layer transition.

As the Reynolds number is increased beyond $2x10^5$ the base suction and drag decrease dramatically as a circular cylinder enters the critical transition regime. In this regime the laminar boundary layer separates at an angle of approximately 70° from the stagnation line (as for the subcritical regime) but reattaches forming a laminar separation bubble before separating again further downstream (approximately 140° from the stagnation line). It has been shown by Bearman (1969) that the flow can exhibit considerable asymmetry in this regime by the formation of a separation bubble on only one side of the cylinder. In this asymmetric configuration Schewe (1983) has shown that the cylinder can produce large mean lift forces of the order $C_L = 1$. As the Reynolds number is increased further this asymmetry is lost as the cylinder enters the

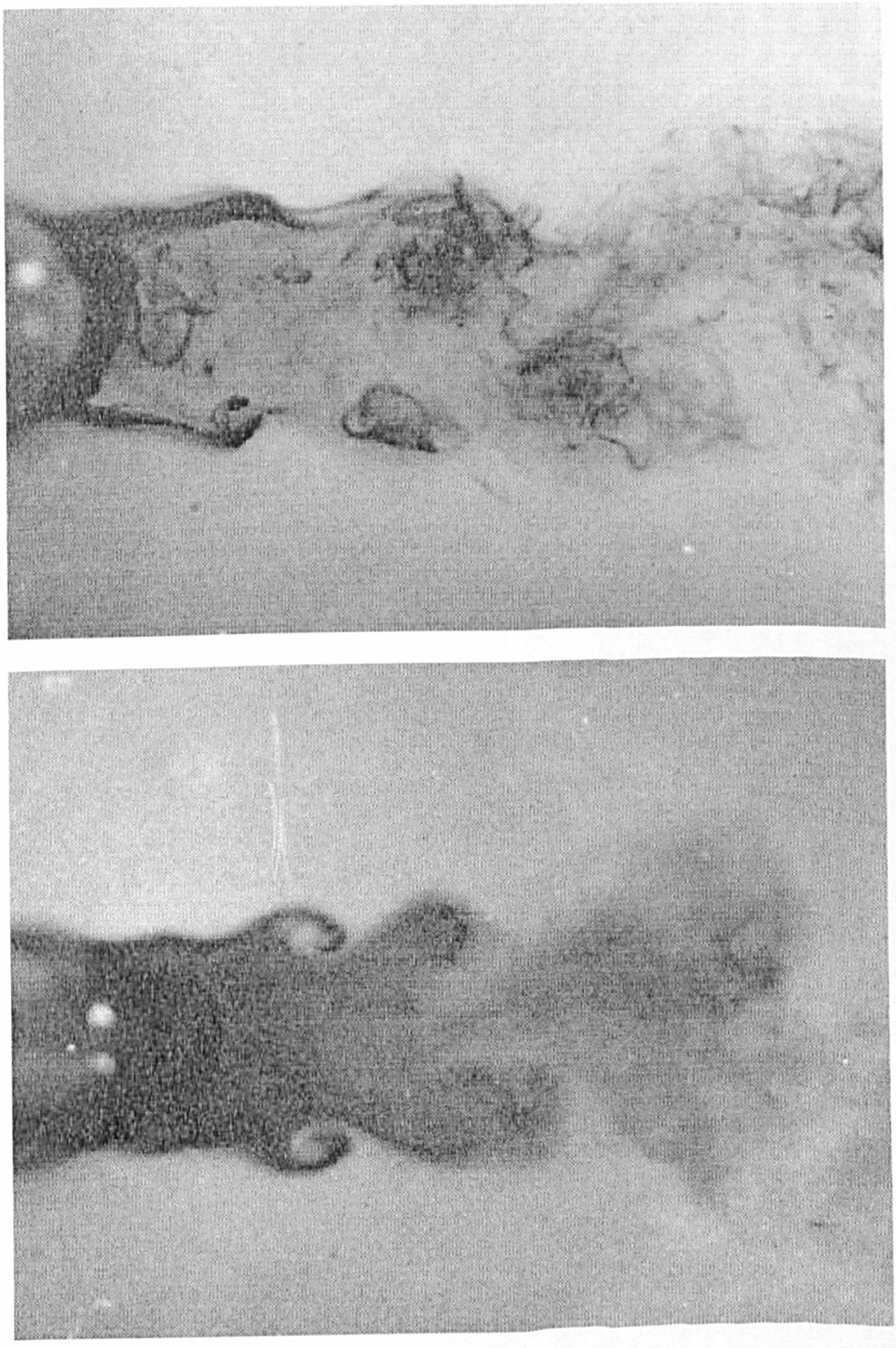


Figure 1.14 Transition waves in the wake of a circular cylinder, visualised by Gerrard (1978): (a), Reynolds number = 1083; (b), Reynolds number = 1968.

supercritical regime (at a Reynolds number of approximately 4.1×10^5 depending on experimental conditions). In the supercritical regime the wake width is a minimum, the drag on the cylinder has dropped approximately $C_D = 0.7$ (from $C_D = 1.2$ in the subcritical regime) and the Strouhal number has jumped to St = 0.4 (from S = 0.2). However, this transition regime is only observed for smooth cylinders of high aspect submerged in laminar flow.

Beyond the supercritical regime the boundary layers become turbulent on the surface of the cylinder and remain attached until an angle (from the front stagnation line) of approximately 110°. To date this regime, termed the post-critical regime is the final regime to be found in circular cylinder flows and has been observed up to Reynolds numbers as high as 10^7.

1.4 Disruption of vortex shedding using 3D geometry.

1.4.1 The effect of a linear variation in spanwise uniformity.

In the previous sections it has been shown that above a certain critical Reynolds number the flow in the wake of a two-dimensional body becomes unsteady and vortex shedding commences. At higher Reynolds numbers (above 100) vortex shedding can contribute up to 50% of the body drag and its disruption or suppression can yield substantial reductions in drag. Generally speaking, the more three-dimensional the vortex shedding, the less drag contribution the body will experience. Therefore, the promotion of three-dimensional features such as vortex dislocations and vortex loops will all serve to disrupt the regular two-dimensional vortex shedding and reduce drag.

A simple disruption to the coherence of the vortex shedding can be achieved by imposing a linear variation in shedding frequency across the span of the body. This can be accomplished in one of two ways. Firstly, the body can be subjected to a spanwise variation in freestream velocity (or linear shear flow), although this can be difficult to generate experimentally particularly at high Reynolds numbers. A second simpler method is to manufacture the body with a linear taper in the spanwise direction. Gaster (1969) conducted a study into linearly tapering circular cylinders or

what he called 'slender cones' in the laminar shedding regime. He tried two different cylinders of taper ratios R_T =18:1 & R_T =36:1. The taper ratio was defined as $R_T = l/(d_1-d_2)$, where (l) is the cylinder length and (d_1) & (d_2) are the cylinder end diameters. Unlike a conventional circular cylinder, he found that the vortex shedding in the wake of the tapered cylinders was taking place at two discrete frequencies across the whole cylinder span. He investigated this further in a later paper (Gaster 1971) using a mildly tapered cylinder (R_T = 120:1) and found that the vortex shedding was split into constant frequency 'cells'. Each spanwise cell was found to be vortex shedding at a slightly different frequency to the next with a series of vortex dislocations bridging the gap between cells. These results were later confirmed by Piccirillo *et al.* (1993) who found the spanwise cell size to be roughly constant across the span.

1.4.2 The effect of spanwise non-uniformity.

Alternatively, the spanwise coherence of the primary vortices can be disrupted by the introduction of periodic deformations in the separation line or base geometry. Naumann *et al.* (1966) showed that it was possible to suppress vortex shedding in the wake of a circular cylinder by attaching broken separation wires to the surface. It was suggested that the separation wires caused a local spanwise difference in circulation shed into the wake that affected the formation of coherent vortices. If the local variation in circulation was increased beyond a critical value by manipulating the positions of the separation wires, then vortex shedding would cease. It was also noted that both saw-tooth and wavy forms of the separation wires could also produce a similar effect, figure 1.15. However, these experiments were conducted in the supercritical regime (Reynolds number = $5x10^5$) where vortex shedding in the wake is relatively weak and it is therefore not known if they would be as successful if employed in the subcritical or postcritical regimes.

In general, the promotion of three-dimensionalities in the wakes of bluff bodies has resulted in lower forces (lift & drag). Tanner (1972) was able to produce a substantial

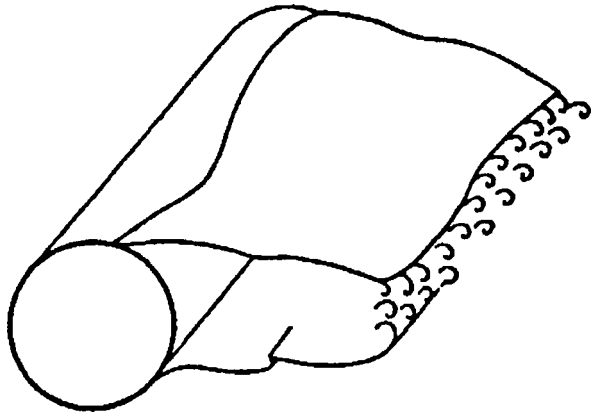


Figure 1.15 The suppression of vortex shedding from a circular cylinder using a wavy separation wire, Naumann et al (1966).

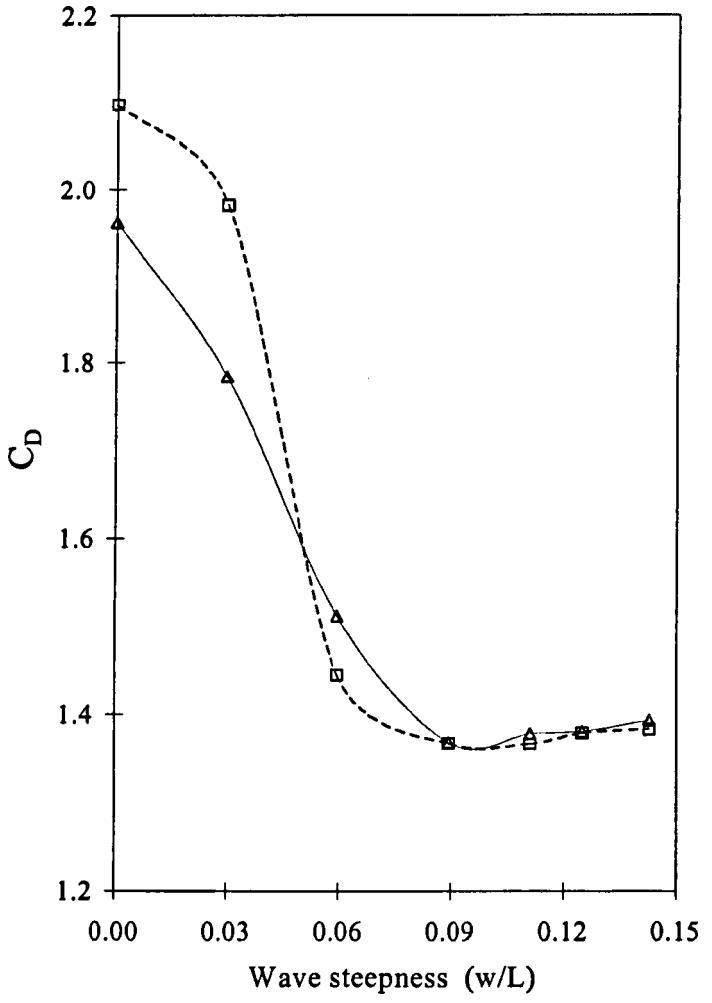


Figure 1.16 Measurements of drag coefficient versus wave steepness: Δ, normal plates; □ rectangular cross-section bodies, Bearman & Owen (1998a).

drag reduction of 64% by promoting a three-dimensional flow in the wake of a blunt based aerofoil. Three-dimensionality was introduced into the wake by breaking up the separation line using a segmented trailing edge. The effectiveness of this trailing edge was found to be governed by two parameters, namely the segment wavelength and the segment depth. Wavelengths of up to 38h (where h is the base height of the trailing edge) were tried but it was found that at these long wavelengths the drag reduction was very small and disappeared entirely at an incidence beyond 4°. However, as the wavelength was reduced to nearer 8h the drag was reduced to a minimum, with an optimum wavelength being determined as 7.6h. The drag was also found to be reduced by an increase in segment depth, although for segment depths of over 2h little additional benefit was gained.

This work was followed up by Rodriguez (1991) and Petrusma & Gai (1994, 1996) who used similar models to Tanner. Rodriguez studied the effect of thickness to chord ratio on the base drag for two sections at a higher Mach number of M = 0.7. He found that for thickness to chord ratios of 3.6% & 5.3%, the base drag was reduced by 41% & 46% respectively. Petrusma & Gai presented visualisations in which they showed a complete absence of vortex shedding in the wake of the model with the formation of a new streamwise vortex structure, figure 1.9.

The effect of different types of trailing edge geometry was investigated in Bearman & Tombazis (1993) and Tombazis & Bearman (1997), who used models with a sinusoidal disturbance to the trailing edge geometry. Using models of different geometric wave steepness (defined as peak to peak wave height divided by the wavelength), they found that an increase in wave steepness resulted in a decrease in base suction. For the most effective of these sinusoidal trailing edge models, Bearman & Tombazis estimated (from base pressure measurements) the drag reduction to be approximately 34% over the undisturbed straight form.

In Bearman & Owen (1998b) the effect of wavy separation lines was investigated further. They were interested in using wavy separation lines to reduce drag of other

common bluff body forms. By investigating models with different amounts of spanwise waviness they found it possible to suppress completely vortex shedding from normal plates and rectangular section bodies. It was found that for mild disturbances vortex shedding persisted but as the wave steepness was increased the base suction and hence the drag continued to reduce until vortex shedding from the model ceased, figure 1.16. Using a rectangular section model with just sufficient spanwise waviness to suppress vortex shedding it was found that a 35% drag reduction could be achieved over a comparable square section cylinder.

1.5 Classical methods for the suppression of vortex shedding.

1.5.1 Overview.

Due to the engineering importance of vortex induced vibrations of bluff bodies much research has been devoted to the development of an effective suppression device. These suppression devices can be essentially broken up into two groups, two-dimensional devices, which limit the interaction of the separated shear layers and three-dimensional devices, which reduce the correlation of the forming spanwise vortices. In this section we will concentrate primarily on two-dimensional suppression devices with the exception of helical strakes which will be discussed in section 1.5.3.

In addition to these two groups the suppression devices can be subdivided into two further subgroups, omnidirectional devices, which are not affected by the direction of the flow and unidirectional devices, which are only effective in one direction. Clearly an omnidirectional device would be preferable for most offshore applications as flows rarely come from a single direction although, there are instances were the flow is effectively unidirectional such as in a river or heat-exchangers where a unidirectional device could be effective. Let us first consider such unidirectional suppression devices.

1.5.2 Unidirectional suppression devices.

Splitter plates.

As discussed in section 1.1.2 vortex shedding is caused as a result of the two oppositely signed shear layers interacting with each other in the wake of the body. Therefore, if the two shear layers could be prevented from interacting then it would be expected that vortex shedding could be suppressed. One of the oldest and simplest methods of doing this is by the insertion of a splitter plate along the centreline of the wake. Roshko (1954) performed the first systematic investigation into the effects of long and short splitter plates in the wake of a circular cylinder in the subcritical range. The short splitter plate was 1.14 cylinder diameters in length and its downstream position in the wake could be varied. When attached to the trailing edge of the cylinder this splitter plate did not suppress vortex shedding. However, it did produce a reduction in base suction of approximately 35%. As the spacing between the cylinder and the plate was increased the base suction was reduced still further until at a spacing of about 2.75D where it abruptly jumped back to the isolated cylinder value. Beyond this spacing vortex shedding in the near wake would resume in a manner similar to that for no splitter plate. Roshko also tested a longer splitter plate of length 5D that showed a similar reduction in base suction to the short plate. However, unlike the short splitter plate, measurements in the wake using a hot wire probe showed no significant periodic oscillations of the flow from which he concluded that vortex shedding had been completely suppressed. These findings were confirmed in the later paper of Apelt *et al.* (1973), although it was found that the vortex shedding would resume in the wake at approximately 17D downstream of the cylinder.

Bearman (1965) studied the effects of splitter plates on semi-ellipse model (in the Reynolds number range 1.4-2.6x10^5) and was the first to identify the link between vortex formation length and base suction. It was found that the introduction of a splitter plate could prevent the interaction of the two separating shear layers until the end of the splitter plate and hence increase the vortex formation length. The base

suction was then found to vary with the inverse of formation length (figure 1.17), as any increase in formation length would result in the formed vortices being weaker and further away from the body. In agreement with Roshko, it was also shown that for a sufficiently long splitter plate (beyond 2.0h for this body) it was possible to completely suppress the vortex shedding and produce a drag reduction of approximately 50% with very little improvement in drag reduction beyond a splitter plate length of 2.5h.

Splitter plates have also been used for the suppression of vortex induced vibrations. Sallet (1980) successfully used a splitter plate to reduce the amplitude of oscillations of a cylindrical buoy subject to an ocean current. Using a splitter plate of length 3D he was able to reduce the amplitude of oscillation from 1.75D to almost zero, although a splitter plate of length 2D was found to be ineffective. In order to make the splitter plate effective from all flow directions the buoy was moored to the seabed via a series of cables that allowed it to weathercock into the impinging flow. However, a potential danger of using a splitter plate in this way is that it offers a far greater transverse area for any pressure fluctuations to act over. Therefore, if vortex shedding has not been fully suppressed or if another type of flow instability is present then more powerful oscillations could potentially result.

Base bleed.

Another way to reduce the interaction between the two separating shear layers is to provide a low flow of fluid directly between them in a method known as base bleed. This was originally done by Wood (1964) using a blunt based ellipse-section model at a Reynolds number of approximately 10^4. As the bleed rate C_q (defined as mean bleed velocity / freestream velocity) was increased, Wood found that the vortices were weaker and formed further downstream resulting in a drag reduction of the order of 65%. For bleed rates above $C_q = 0.05$ the formation length was found to increase linearly with bleed rate with the Strouhal number becoming irregular at higher rates of bleed.

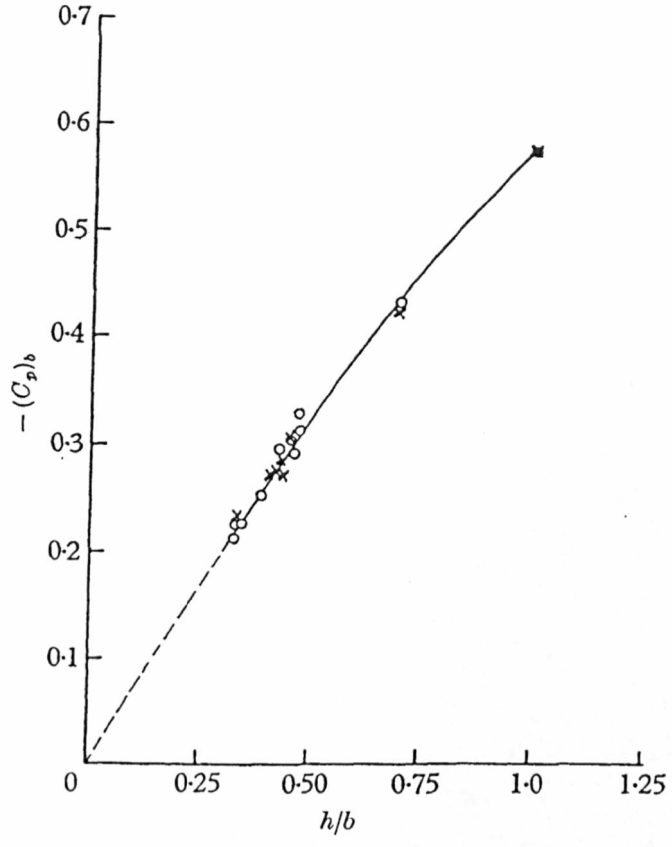


Figure 1.17 Inverse of formation length versus base suction coefficient for a blunt based aerofoil section, Bearman (1965).

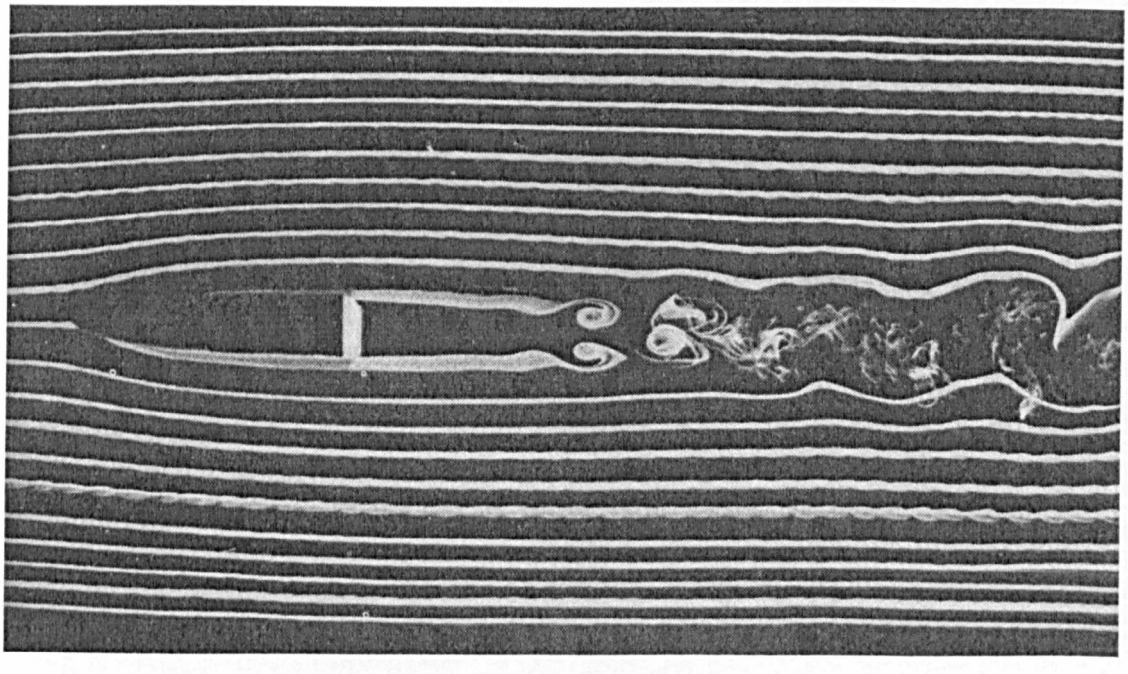


Figure 1.18 Suppression of vortex shedding from a blunt based semi-ellipse model with base bleed, $C_q = 0.188$, Zdravkovich (1981). Picture originally unpublished work of Prof. P.W. Bearman.

This phenomenon was also investigated in Bearman (1967) using a similar blunt based model to Wood. He showed that with a sufficiently large quantity of bleed (above C_q = 0.118) it was possible to suppress completely vortex shedding in the near wake, and reduce the base suction by up to 65%, figure 1.18. In direct comparison with his previous work on splitter plates (Bearman 1965), he was also able to confirm that the base pressure varied linearly with the inverse of vortex formation length, and that it was independent of the method used to control it.

Whilst the works of Wood and Bearman have demonstrated an ingenious means of flow control, they cannot be considered as a practical solution (and no claim to that effect is made) to the suppression of vortex induced vibrations due to the mechanical complexity of their design.

Shear layer control.

It has been shown previously that substantial reductions in drag and vortex shedding can be achieved if the two separated shear layers emanating from the body can be prevented from interacting. However, an alternative method to achieve this would be to interfere with the shear layers directly. Dalton *et al.* (2001) investigated this computationally in a study using large eddy simulation (LES). By positioning a small control cylinder (of diameter 0.1D) in the wake of the primary cylinder to disrupt one of the separated shear layers it was found that the interaction and roll-up of the shear layers could be affected. The effect of the control cylinder was found to be most pronounced when it was positioned just outside the shear layer of the primary cylinder. This had the effect of increasing the vortex formation length and weakening the strength of the primary vortices.

Figure 1.19 shows flow visualisation images of the wake at a Reynolds number of 3000 which demonstrate the effect of the control cylinder versus an isolated circular cylinder for a complete shedding cycle. From the figure it can be seen that the wake of

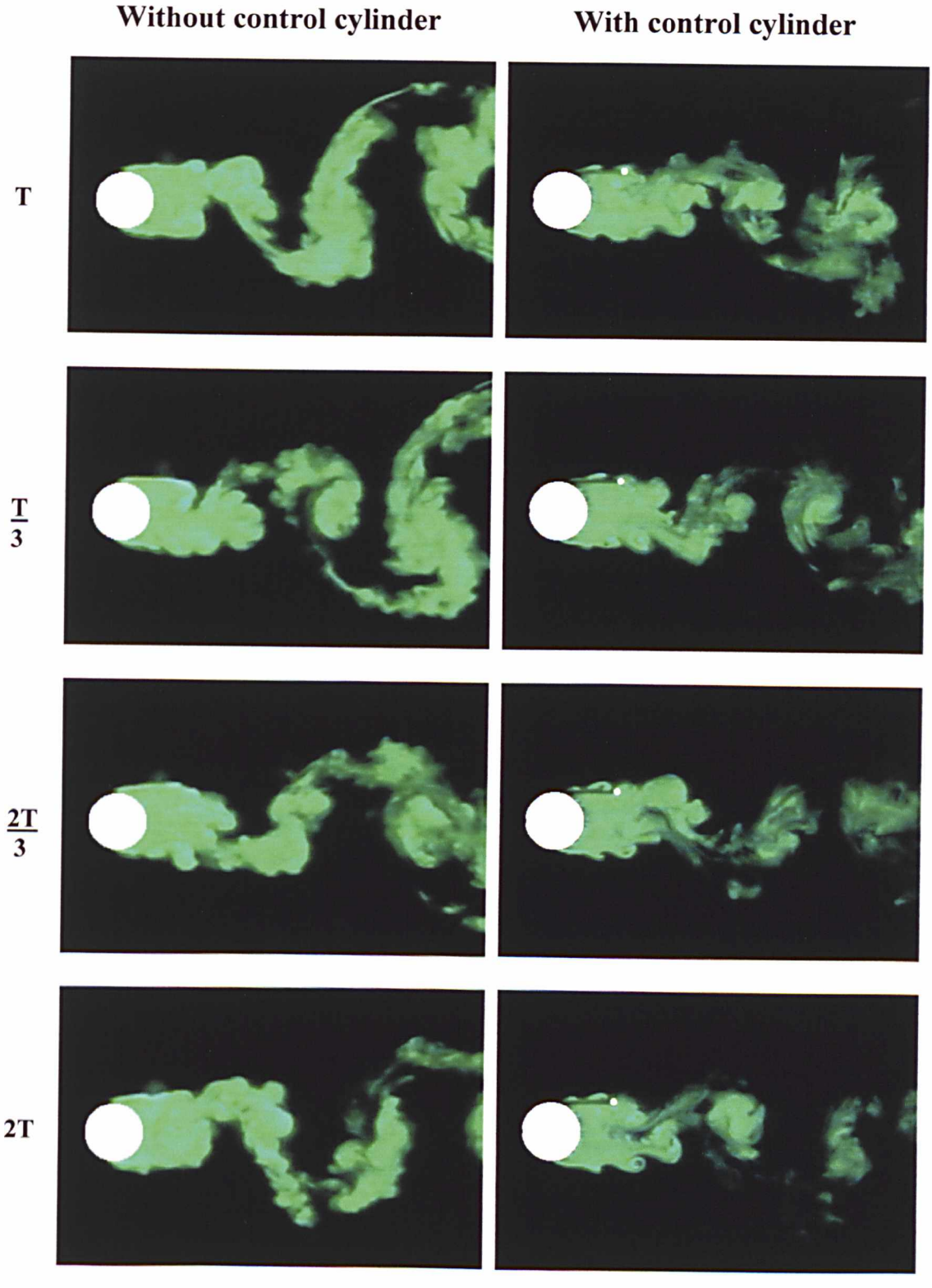


Figure 1.19 Disruption of vortex shedding by means of a small control cylinder inserted into the wake of a circular cylinder at a Reynolds number of 3000. With the control cylinder in place (right-hand pictures) the wake width can be seen to be considerably narrower and less time dependent over a shedding cycle, Dalton et al (2001).

the isolated cylinder shows the characteristic periodic vortex shedding with the wake widening as the vortices travel downstream. In contrast the wake with the control cylinder is narrower and seems far less organised with the familiar Bloor-Gerrard vortices now far more prominent in the upper shear layer. In this configuration, the LES results showed that the forces experienced by the primary cylinder were considerably reduced. The drag coefficient was found to be reduced from approximately 1.2 to 0.75 and the fluctuating lift coefficient to almost zero, although the mean value was now found to be approximately 0.1 due to the non-symmetric flow around the cylinder.

1.5.3 Omnidirectional suppression devices.

Porous shrouds.

A novel method for the suppression of vortex shedding from a circular cylinder is to enclose it in a porous shroud. Typically these shrouds are of the order of 1.25D in diameter and are generally made from perforated plate, fine mesh gauze or axial slats or rods, figure 1.20a. Primarily designed for the suppression of vortex induced vibrations shrouds have proved to be highly successful. However, their general complexity in comparison with other suppression devices (such as helical strakes) has generally prevented them from becoming widely used.

The original work on shrouds was conducted by Price (1956) who was interested in suppressing vortex induced vibrations on a cylinder in water. He tried a shroud of 37% porosity which was not only successful in suppressing vibrations (for all stiffnesses tested) but which also had the advantageous effect of reducing the drag coefficient of the cylinder from 1.2 to 0.9. Price suggested that the shroud prevented vortex shedding by breaking up the flow into a series of smaller vortices. In Zdravkovich (1971) Price's concept was developed further by encircling the primary cylinder with a series of smaller cylinders to form a shroud. It was proposed that each

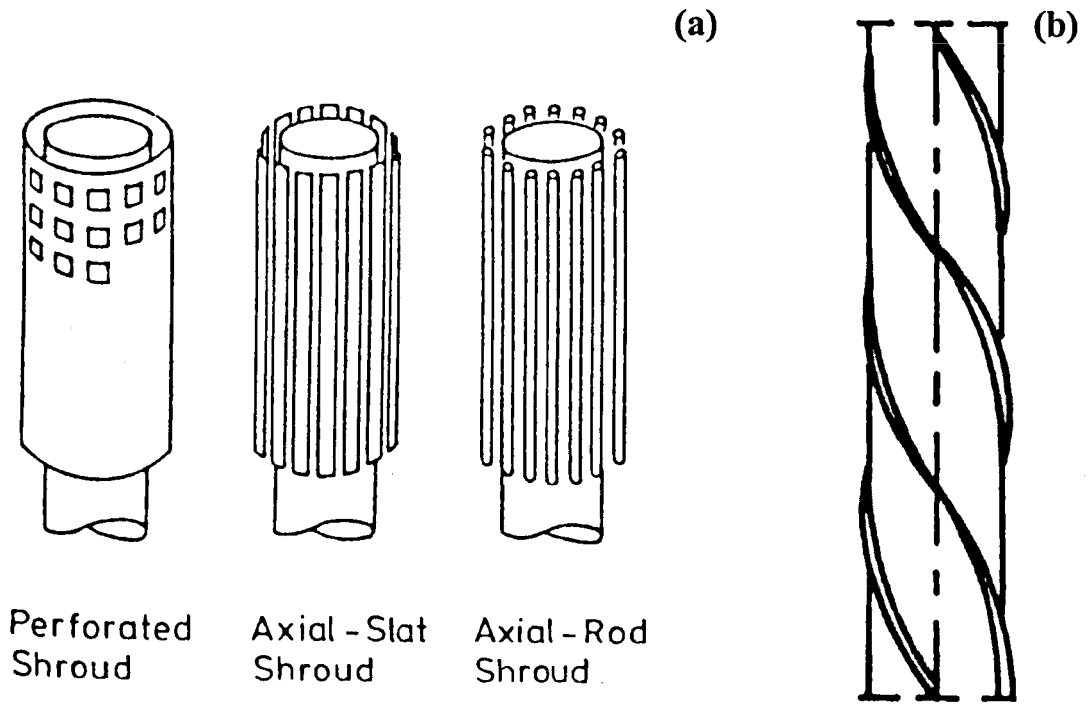


Figure 1.20 Various omni directional devices for the suppression of vortex shedding: (a), porous shrouds. (b), helical strakes.

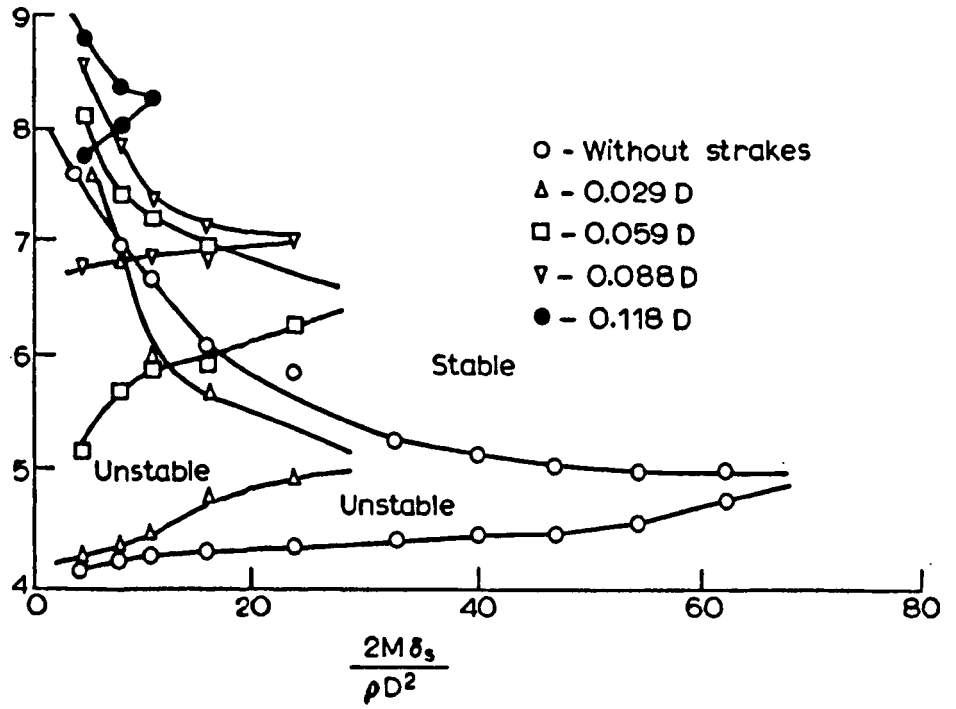


Figure 1.21 The relative stability of a circular cylinder fitted with helical strakes for varying values mass-damping parameter, Scruton & Walshe (1957).

cylinder would produce its own vortex street and this would interact strongly with the vortex street from the neighbouring cylinder in a highly irregular manner. This behaviour was later confirmed in subsequent tests of an optimised axial-rod shroud that proved it to be the most effective of all shroud designs at suppressing vortex induced vibrations.

In addition to these, numerous other types and configurations of shrouds have been tried and tested by many other researchers and it is unnecessary to consider them all in detail here. For further details and comparisons of shroud designs the reader is directed towards the excellent review paper of Zdravkovich (1981).

Helical strakes.

Perhaps the oldest and most commercially successful of all omnidirectional vortex suppression devices are helical strakes. Originally developed by Scruton & Walshe (1957) for the suppression of wind excited vibrations of cylindrical structures, they consist of three sharp edged plates wound around the cylinder surface to form helices, figure 1.20b. During their investigation the effect of different strake heights (h_{st}) in the range h_{st} = 0.029D – 0.118D was studied whilst the pitch of the helices was held constant at a value of 15D. A significant reduction in aerodynamic excitation was achieved for a strake height of only 0.029D with further improvements as the strake height was increased to the maximum value of 0.118D, figure 1.21. At this value the tests were discontinued, as the remaining area of instability was not considered large enough to be of any practical significance. Further tests to determine the optimum pitch of helical strakes were conducted by Woodgate & Maybrey (1959) who showed the optimum pitch to be 5D, which was far from that tested by Scruton & Walshe.

Despite their success helical strakes do have one major disadvantage in that they produce a substantial increase in mean drag. In the supercritical regime, where the cylinder drag would typically be reduced to a C_d = 0.5, Cowdrey & Lawes (1959) found that for a cylinder fitted with stakes (0.12D high) the drag remained almost

constant throughout this regime at a value $C_d = 1.45$. However, this has not significantly affected the success of helical strakes, as in general engineering structures tend to fail from fluctuating (due to fatigue) rather than mean forces.

2 Introduction to the present investigation.

2.1 Origin of work.

Over the past few years several research projects have been conducted in the department of Aeronautics at Imperial college which have investigated the effect of spanwise waviness on vortex shedding. Within these research projects many different types of bluff body form have been investigated. These include circular cylinders, square section cylinders, thin plates normal to the flow and blunt based aerofoil or semi-ellipse sections. To understand the progression of the research it is important to examine the origin of the work.

Initially, Szepessy & Bearman (1992) conducted an investigation into the correlation length of vortex shedding in the wakes of circular cylinders in the high subcritical regime. It had previously been shown by many other researches that above a Reynolds number of approximately 10^3 vortex shedding in the wake of circular cylinder would only be correlated over a few cylinder diameters, typically 3-4D. This short correlation length was also confirmed by Szepessy & Bearman who showed that a better approximation to nominally two-dimensional flow could be achieved by using a cylinder of very low aspect ratio, typically of the order $l_{span}/D = 1$. This was surprising because it contradicted the commonly held belief at the time that nominally two-dimensional flow was best produced by cylinders of high aspect ratio where the end effects would be minimal. Szepessy & Bearman explained their conclusion by showing that at high Reynolds numbers, large aspect ratio cylinders set-up significant spanwise crossflows that decorrelated the vortex shedding and more importantly lead to generation of vortex dislocations. At high aspect ratios vortex dislocations were found to occur both randomly in time and space but with the use of low aspect ratios these were effectively suppressed. However, the dynamics of the vortex dislocations at high Reynolds numbers was unclear.

This lack of understanding was subsequently addressed in Bearman & Tombazis (1993) and Tombazis & Bearman (1997). In these investigations the positions of vortex dislocations were fixed by machining the trailing edge of a blunt based semi-ellipse section in the form of a sinusoid along the span resulting in wavy flow separation lines. In addition to the fixation of vortex dislocation positions, the introduction of wavy separation lines was also found to reduce drag. It was found that the level of this drag reduction was controlled by the waviness or wave steepness of the trailing edge design, where wave steepness was defined as the ratio of peak to peak wave height (w) to the wavelength (L) or w/L. Increasing wave steepness resulted in increasing drag reductions of up to a maximum (w/L = 0.143) drag reduction of the order of 35% where vortex shedding in the wake was found to be weakened but not suppressed. This result suggested the possibility that wavy separation lines may also be effective at reducing the drag of other bluff body forms.

In Bearman & Owen (1998 a,b) the separation lines of square section cylinders and thin plates normal to the flow were forced to be wavy by making the front face of the body sinusoidal. In similarity with the previous work of Bearman & Tombazis, drag reductions of over 30% where achieved as the wave steepness was increased. However, in contrast to this previous work, only relatively mild levels of wave steepness were needed and it was found that vortex shedding in the wake was suppressed completely beyond a wave steepness of $w/L > 0.06$.

Despite these investigations, our understanding of how spanwise waviness affects vortex shedding is still very limited. Therefore, this project will attempt to address this gap in our knowledge through a detail study of the flow in the wakes of such bodies.

2.2 Aims of the project.

The central focus of this work will be the understanding and effectiveness of spanwise waviness and three-dimensional geometries at 'engineering' Reynolds numbers, although flow visualisation at low Reynolds numbers (where the vortices are laminar) will also be used to gain further insight into the fundamental dynamics of the wake. Throughout, emphasis will be placed on gaining a physical understanding and explanations for how the fluid dynamics are modified by the presence of spanwise waviness and how it ultimately disrupts and suppresses vortex shedding in the wake. Attempts will be made to uncover the key requirements needed if the wake is to be stabilised and the potential for applying the concepts to other bluff body forms will be investigated.

From a practical perspective, attempts will be made to develop a first generation of vortex suppression devices that incorporate the fundamental components for shedding suppression gained from the investigation of spanwise waviness. In addition, importance will be placed on the minimising of drag and the simplification of geometric form. Finally the application of such devices for the suppression of vortex induced vibrations will be considered.

Having set out the aims of this project it would also be appropriate at this stage to consider the areas that lie beyond the scope of this project. This project will not consider the effects of small-scale turbulence but will concentrate primarily on the dynamics of the large-scale structures in the wake. Also investigations of the dynamics of these large-scale structures will be limited to a region of the order of 10 cylinder diameters downstream of the model commonly ~~refereed~~ referred to as the near wake. Determination of the optimum wavelength or body geometry for the suppression of vortex shedding, suppression of vortex induced vibrations (VIV) and the minimisation of drag are also beyond the scope of the project.

At low Reynolds numbers the wakes of bluff bodies produce many exciting and unique features (such as mode – A and mode – B transitions, section 1.3.2) which are worth investigating purely for ~~there~~ their own sake. However, whilst these are currently the subject of much discussion in the research community they are generally of little importance at higher Reynolds numbers where the wake is highly turbulent and the correlation length of vortex shedding is typically only a few cylinder diameters. Therefore, although these effects will be observed at low Reynolds numbers, they will not be considered in great detail and no attempts will be made to explain the mechanisms behind such fundamental wake instabilities.

2.3 Plan to the rest of the thesis.

The subsequent chapters of the thesis will be laid out as follows:

- **Experimental set-up and procedure.**

This chapter will describe the various experimental techniques and procedures used during this investigation. These will include drag and pressure measurement, hot wire anemometry, particle image velocimetry (PIV) in air and the measurement of vortex induced vibrations (VIV) in water. In addition, the design, development and commissioning of a 3 meter long glass towing tank for low Reynolds numbers flow visualisation experiments will also be described.

- **The effect of wavy separation lines on rectangular section bodies.**

Following on from the original works of Bearman & Owen (1998 a,b), flow in the wavy rectangular sectioned bodies (where the separation line is forced to be sinusoidal, figure 2.1a) will be investigated further. Detailed flow visualisations using the new towing tank at low Reynolds number will show the emergence of streamwise or longitudinal vortices in the wakes of these bodies and the complete suppression of Kármán type vortex shedding. In addition, a detailed investigation is performed into the flow in the wake of a regular square section cylinder where the wake is found to

exhibit many of the features found in the wakes of circular cylinders at low Reynolds numbers.

- **Flow in the wake of sinuous circular cylinders.**

In extension of the work from the previous chapter the flow in the wake of sinuous circular cylinders (where the axis of the cylinder is forced to be sinusoidal, figure 2.1b) will be investigated. Results will be presented that show that the wake of a sinuous cylinder is almost identical to that a wavy rectangular section body and that the suppression of vortex shedding in the wake of a sinuous cylinder is accompanied by drag reductions of up to 47%. A detailed analysis of the resulting three-dimensional structure in the wake will be presented, from which, the key features of the flow will be determined that lead to the suppression of vortex shedding. Finally a mechanism is proposed that links the orientation of the flow at separation to the potential for wake stabilisation.

- **The suppression of vortex shedding using surface protuberances.**

Using the ideas for the suppression of vortex shedding presented in the previous chapter a new series of three-dimensional bodies that suppress vortex shedding will be presented. This chapter will determine the potential for the development of a practical device for the suppression of vortex shedding using the ideas of flow orientation at separation discussed in the previous chapter. It will be shown that vortex shedding can be suppressed by the installation of elliptically shaped surface protuberances along the leading edge resulting in a 33% reduction in cylinder drag. Furthermore, an omnidirectional suppression device will be demonstrated that produces a 25% drag reduction (based on cylinder diameter) when the previously mentioned elliptically shaped surface protuberances are installed in a spiral pattern along the cylinder, figure 2.1c.

- **Vortex induced vibrations.**

In this chapter the potential for suppressing vortex induced vibrations using a cylinder fitted with the surface protuberances is investigated. The results show that at very

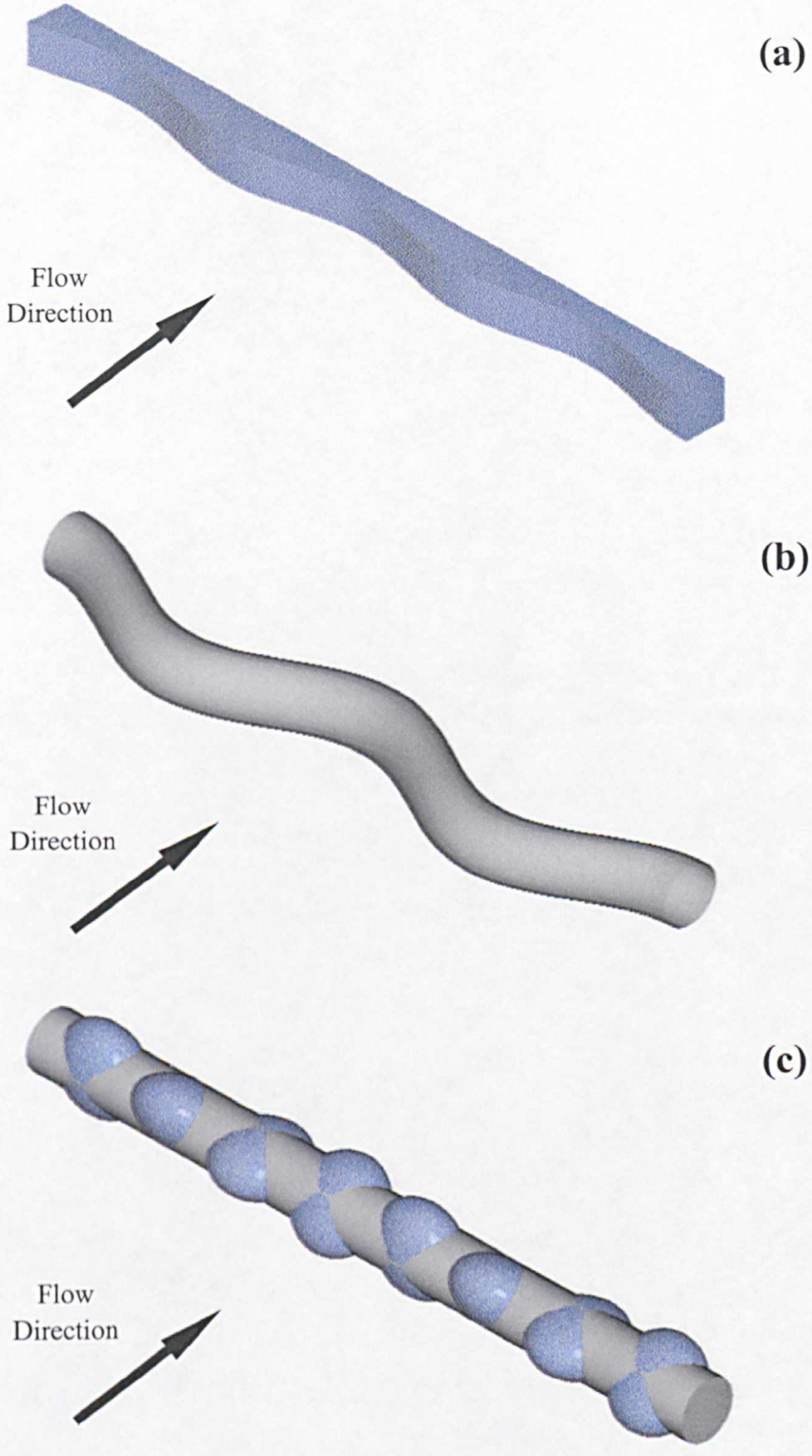


Figure 2.1 The various model geometries used during this investigation: (a), a square section cylinder with a wavy leading edge, Bearman & Owen (1998 a,b); (b), a sinuous circular cylinder, Owen et al (2000); (c), a circular cylinder fitted with elliptically shape surface protuberances, Owen et al (2001).

low values of combined mass and damping, the surface protuberances are ineffective at significantly reducing the amplitude of cylinder vibrations. However, it is shown that the amount of mass damping needed to suppress vibration is significantly reduced when surface protuberances are fitted. Overall it is shown that for the suppression of vortex induced vibrations, surface protuberances are of similar effectiveness to helical strakes of height 0.08D.

- **Conclusions and further work.**

Finally the potential for further research suggested by this investigation will be highlighted and discussed before closing conclusions are drawn.

3 Experimental Set-up and Procedure.

3.1 Introduction.

During the course of this investigation experiments have been conducted using a large number of test models and over a wide range of Reynolds numbers (approximately 10^1-10^5). In this chapter the general experimental techniques and procedures that were used during these experiments will be described. However, it should be noted that the experimental techniques documented here do not refer to any particular experiment but instead are intended to give the reader an overview of many of the individual experiments that will be described in later chapters.

In the early stages of this investigation, a large number of flow visualisation experiments were performed and great deal of time and effort was put into developing a successful flow visualisation technique. As part of this research program, a new larger towing tank was designed and developed that allows models to be towed up to five times the distance of the original facility. Once commissioned, and in conjunction with the new visualisation techniques, this facility was capable of producing very high quality flow visualisation images that would give a detailed insight into the nature of the flow, Owen *et al.* (2000).

Later in the investigation many experiments were performed in one of two wind tunnels for the quantitative measurement of drag and pressure. To compliment these, experiments were also performed which investigated the nature of the flow in the wake using hot-wire anemometry and particle image velocimetry (PIV). Finally vortex-induced vibration experiments were conducted to measure the response of an elastically mounted cylinder exposed to a steady current in a water channel.

3.2 Towing tank experiments.

3.2.1 Introduction.

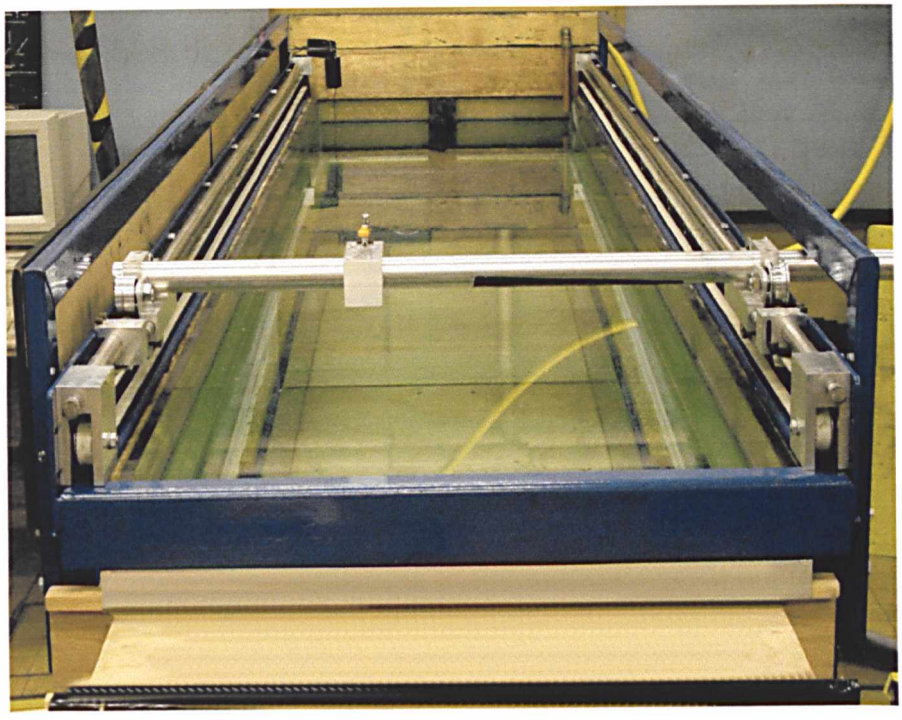
It was found during previous investigations that flow visualisation could be a very useful tool in the understanding of bluff body wakes as many of the important features present in the wake at lower Reynolds numbers often persisted to higher ones. In this way many of the initial investigations into bluff body models involved flow visualisation and were performed in the Reynolds number range 50-500 where the flow could be easily observed and recorded.

Initial low Reynolds number flow visualisation experiments were performed in an existing small Perspex towing tank. This original towing tank had cross-sectional dimensions of $600 \times 600mm$ and a computer-controlled carriage, which could traverse a model over a distance of approximately $650mm$ downstream. However, due to the constraints of the facility it was only possible to traverse the models (of base height $15mm$) approximately 50 base heights downstream and it was felt during early experiments that this downstream distance was too short to be sure that the flow had fully developed. Therefore, it was decided that a larger tow-tank should be commissioned.

3.2.2 Design of the new towing tank facility.

Experience with previous facilities had shown that problems could occur when glass windows were fitted into metal tanks due to corrosion of the metal and differential thermal expansion between the metal and the glass. This would often lead to leaking cracked windows and also severe contamination of the water due to metal corrosion. In an attempt to avoid any of these problems and also for ease of manufacture, the new towing tank was designed and built around an all-glass aquarium (of dimensions, 3m long by 0.8m wide by 0.6m deep). The aquarium formed a self-contained unit and was constructed from large pieces of plate glass ($10mm$ thick on the sides and $25mm$ thick for the base) that were glued together along their edges using Silicon sealant to

(a)



(b)

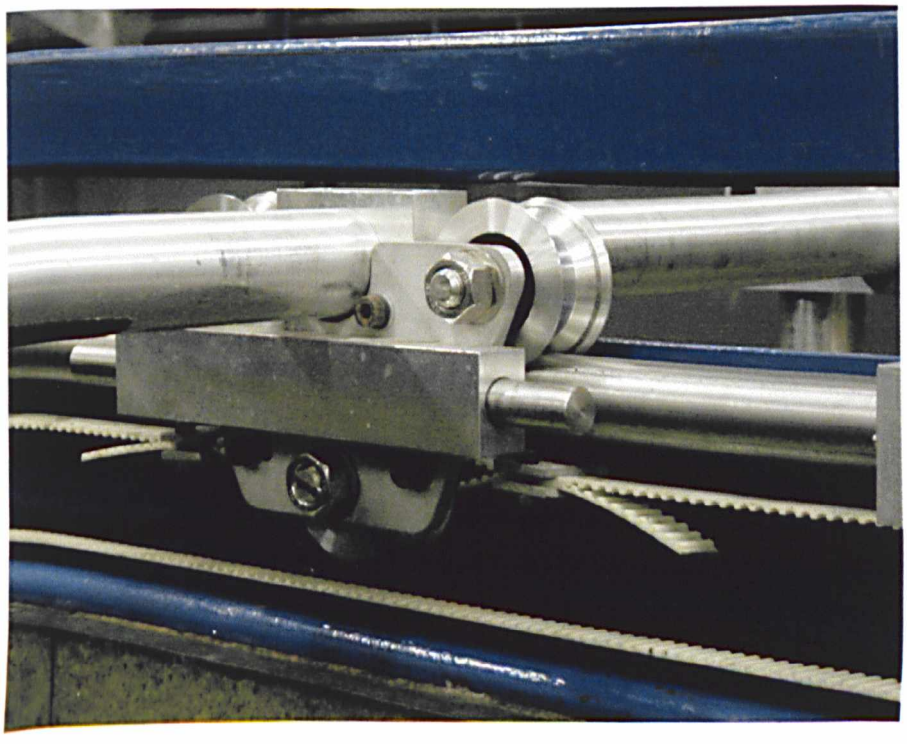


Figure 3.1 Details of the carriage system fitted to the towing tank: (a) View along the length of the towing tank showing the drive belts and slide rails, (b) Close-up view of the carriage wheels and rail.

form a water tight joint. The whole aquarium was then supported on a bed of cork around the edges of its base and housed in a large purpose built box-section steel framework, figure 3.3. In this way the flow could be viewed easily from all sides and all of the conventional problems associated with leaking glass-frame interfaces and metal corrosion were avoided.

In order to ensure a smooth motion of the test models through the tank, a considerable amount of time and effort was put into the development of a vibration free linear motion system for the carriage. This consisted of a pair of stainless steel rails that were attached to the framework along the length of the tank on which the carriage wheels would run, figure 3.1. For filming purposes, it was possible to fit the carriage with a large arm that could be used to support a camera alongside or underneath the tank so that it could be traversed with the model, figure 3.2.

The carriage motion was powered using a 48Volt DC servomotor installed in a housing at one end of the tank. This drove the carriage via a pair of large toothed drive belts installed either side of the tank and connected to the carriage at either end, figure 3.1. The motor was driven by a closed-loop servo amplifier that was configured for both velocity and displacement feedback and that was linear to within 0.01%. Whilst displacement feedback was controlled via a potentiometer driven from the carriage, the level of velocity feedback could be adjusted by the user depending on the type of motion required. In general, for low Reynolds number constant velocity experiments, it would be necessary to increase the velocity feedback until a smooth motion of constant speed was achieved. However, for high Reynolds number experiments or where the carriage was required to produce high accelerations, the velocity feedback would be reduced to minimise any following error (where the carriage motion fails to track the input signal). Figure 3.3 demonstrates a large following error when the carriage motion fails to closely track the input signal due to excessively high velocity damping. The servo amplifier could then be controlled using a signal generator or the output from a computer based D-A convert in order for the carriage to perform a pre-programmed motion.

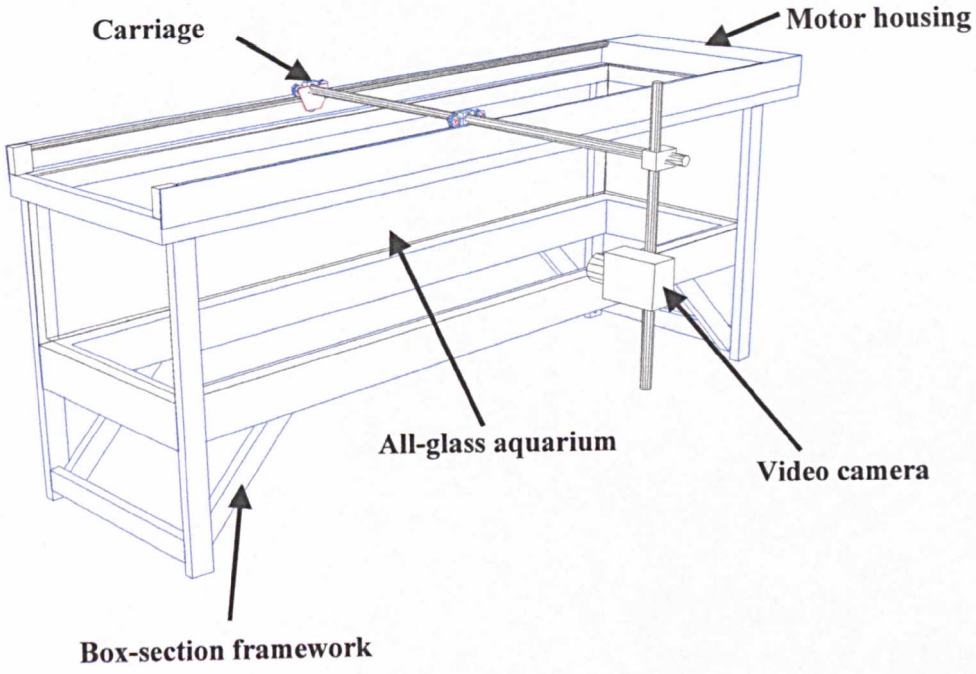


Figure 3.2 A schematic diagram showing the layout of the towing tank when fitted with the video camera.

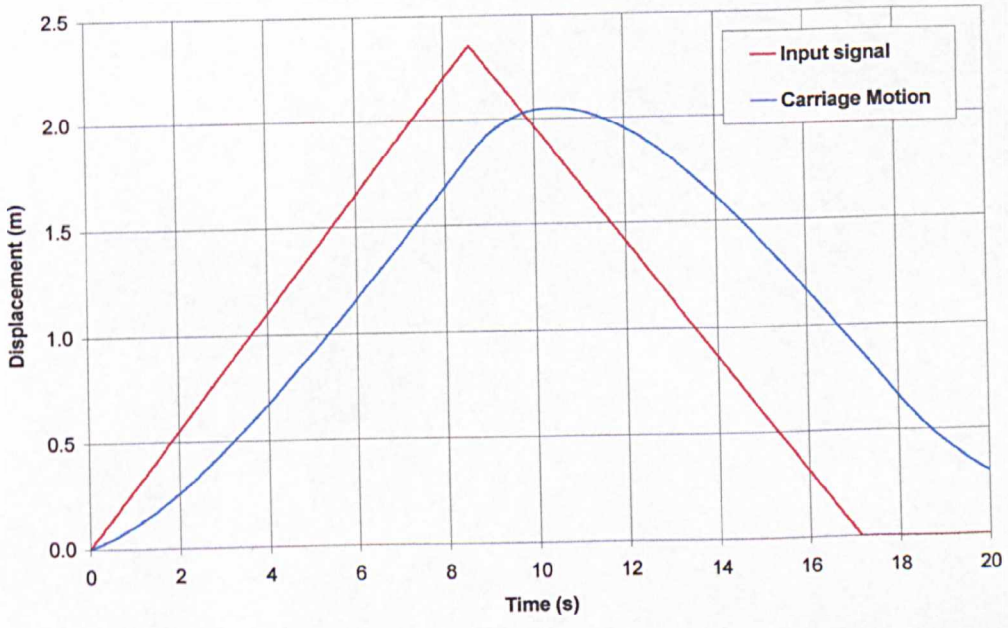


Figure 3.3 An example of a large following error in the carriage servo system due to too much velocity damping.

3.2.3 Laser illumination system.

In conjunction with the design and manufacture of the new towing tank, an improved laser illumination system was also being developed. The original system as used in previous investigations (Owen 1997) consisted of a simple laser sheet that was produced using a single cylindrical optic placed in the beam of a 4-watt, class IV argon-ion laser. The width of this sheet could then be adjusted by changing the focal length of the optic and by varying the distance between the optic and the towing tank. However, due to the limited space available in the laboratory, it was not possible to position the optic very far from the towing tank and so an optic of short focal length needed to be used. In this configuration the sheet produced was highly tapered and this resulted in large variations of laser intensity over the length of the towing tank. In addition to this problem, the system was inconvenient to use and lacked versatility and hence a new laser illumination system was developed.

The first problem the new illumination system would have to overcome was the production of a parallel or near parallel (or mildly tapering) sided sheet of laser light. After a general investigation into the problem, it became apparent that the production of a parallel sided laser sheet would have required a considerable financial investment as large cylindrical optics (the width of the laser sheet) or large parabolic mirrors would have been needed. Therefore, a slowly tapering laser sheet created by a cylindrical optic of long focal length was chosen as the preferred option for the final system.

The new laser optics system essentially consisted of three main components, an illumination device (for which the original Argon-ion laser was retained), a large enclosed optics box for the production of the laser sheet and a heavy-duty framework to support the optics box and the laser. This supporting framework was then securely bolted to the table of an old milling platform that allowed the table and hence the laser sheet a full three axes of movement, figure 3.4.

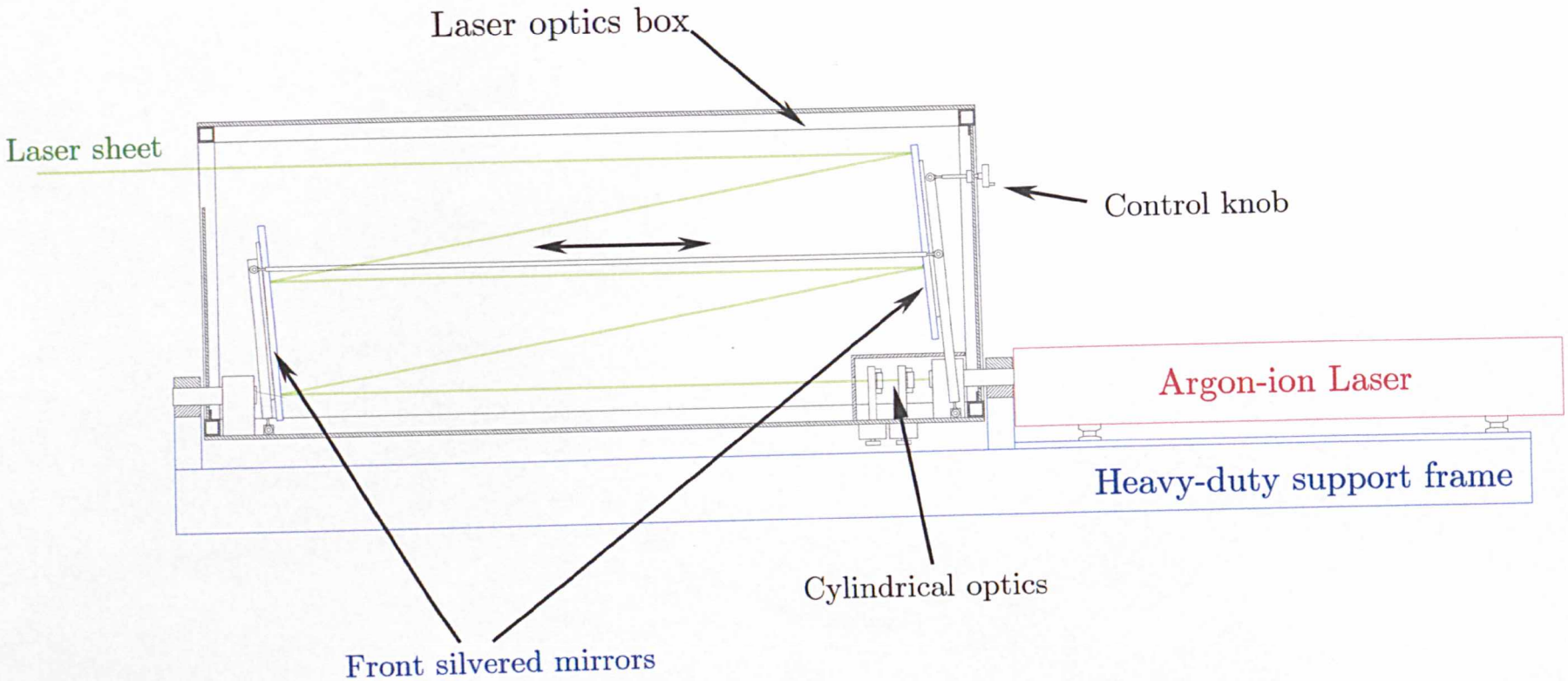


Figure 3.4 A schematic diagram of the laser illumination box. The box consists of two parallel mirrors coupled to move in the form of a parallelogram that can be operated via the control knob as shown. By adjusting the angle of the mirrors with this control knob the laser sheet can be projected over a maximum distance of up to 12 metres before exiting the box.

The main features of the laser optics box were a pair of high quality front silvered mirrors (93% reflectivity) installed parallel to each other at either end of the box that would essentially reflect the sheet over a large distance before it left the box (figure 3.4). The mirrors were pivoted to the bottom of the box and maintained parallel to each other via a long connecting rod attached between the two mirrors to form a parallelogram. The angle of these two mirrors relative to the laser sheet could then be adjusted via a simple control knob on the outside of the box that in effect controlled the distance the sheet would have to travel before leaving the box. As before, the laser sheet was produced using a single cylindrical optic but, by using the parallel mirrors, it was now possible to fan the sheet out much more gradually with an optic of longer focal length. The box also incorporated the provision for another cylindrical lens to be installed that could be used to thicken up the beam for experiments that required bulk illumination of the flow. Finally the whole optics box could be rotated in the supporting framework about the laser axis in order to produce laser sheets in different orientations.

3.2.4 Flow visualisation techniques.

During the course of this investigation, three different flow visualisation techniques were tried for the visualisation of flow in the towing tank. These were the lead precipitate method, methyl blue dye washed from the model surface and laser induced fluorescence (LIF). By far the most successful technique of these was laser induced fluorescence and most of the subsequent results presented were produced using this technique. However, the other techniques should not be considered redundant as they both had advantages to offer.

All of these techniques are ideally suited to the visualisation of the initial vorticity field as the precipitate or dye is released on the surface of the model where the vorticity is generated. This results in high concentrations of dye or precipitate being entrained in the shed vortices, which makes them clearly visible. However, one has to be careful when interpreting images of the wake far downstream of the model, where

vorticity diffusion or cancellation may leave the dye or precipitate in areas of low vorticity.

In early tests, flow in the wake of the models was visualised using the electrolytic precipitation method as described by Taneda *et al.* (1979). The technique was ideally suited to the visualisation of starting flows as the model could be left in the tank almost indefinitely before the start of a run. Therefore, after the model had been installed in the tank it could then be left until the water had completely settled before the run was commenced.

The method used electrolysis to precipitate a thick white cloud of tin oxide from a piece of tin foil submerged in the tank. This piece of tin foil would be smoothly attached to the leading edge of the model and connected to the positive pole of a power supply. To complete the circuit, a brass cathode was connected to the negative pole and this was then installed in the far end of the tank. The precipitation of tin oxide would then commence once a voltage of approximately 50-60V had been applied by the power supply. Finally, the flow was illuminated using a sheet of laser light from the laser illumination system as described in the previous section.

Dye visualisations using methyl-blue were used when the wake widths produced by certain models were too large to be effectively illuminated by the laser system. This technique was relatively simple to use as methyl-blue dye would be painted on to the surface of the model and then washed off as the model was traversed through the flow. The resulting dye traces would then be observed by back-lighting the flow against a white background. In practice this technique was rarely needed and only used for some of the visualisations performed on square section flows (section 4).

As mentioned earlier the most successful flow visualisation technique proved to be laser induced fluorescence. In essence this technique is not that dissimilar to the previous one in that dye would be painted onto the surface and as before washed off as the model was towed through the tank. The dye washed from the model would

then fluoresce brightly when illuminated using an Argon-ion laser which made it ideal for any kind of photography or filming.

Due to the high solubility of the dye, problems were encountered in early experiments whereby the fluorescein dye would be washed off the model very quickly leading to an uneven distribution of dye along the run with the dye typically running out before half way. In order to solve this problem a slow release technique was developed for the dye. Many mixtures where tried in an attempt to reduce the rate of fluorescein release until the end solution, of mixing the dye with 'Corn syrup' was finally reached. On advice from Mohamed Gad-el-Hak (from the University of Notre Dame, Indiana USA) the sodium fluorescein solution was mixed with methanol and corn syrup to produce a thick viscous mixture that could then be pasted onto test models. Initially this mixture was of similar consistency to the corn syrup and although the dye would now be released far more evenly over a run, the mixture was not neutrally buoyant and would tend to roll off the model in a thick viscous sheet. However, over the course of several weeks, the mixture was observed to thicken up considerably to the point where it needed to be heated in order to apply it to the models. In this new form the mixture produced highly successful results with none of the previous problems of a heavy viscous dye falling from the model. The proportions for the mixture used were 25% sodium fluorescein solution, 25% methanol and 50% corn syrup, figure 3.5.

Finally, the flow could then be filmed for the duration of a complete run using a standard video camera or photographed using a Sony DSC-F505 digital camera. The digital camera had a resolution of 1600×1200 pixels and could hold up to 140 high-resolution images on a single 64Mb memory stick. In addition, still pictures could also be captured from the videotape using a Pinnacle systems DC-10 jpeg motion video capture card fitted into a 450MHz Pentium III PC. The capture card could also record the whole videotaped run on to the PC in the form of a movie (Windows Avi) whereby a whole series of time evolution images could then be stored. Although images produced by the video camera were of lower resolution than the digital



Figure 3.5 The three ingredients needed to make the highly viscous sodium fluorescein solution (shown in beaker) used in flow visualisation experiments: corn syrup, methanol and sodium fluorescein solution.

pictures, using the video camera it was possible to take 500 still pictures in a little over 20 seconds compared to the digital camera, which could only have taken five.

3.3 The 3'×3' wind tunnel experiments.

3.3.1 Introduction.

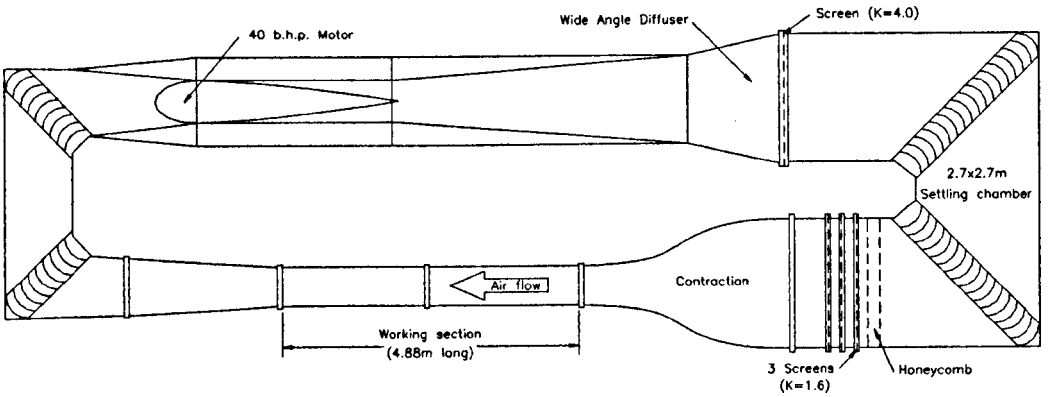
Quantitative measurements of pressure and fluctuating velocities were made in the 3'×3' wind tunnel of the Department of Aeronautics at Imperial College (figure 3.6a). The tunnel is of the closed-return type with a maximum velocity of 45m/s and working section of 0.92m by 0.92m and 4.9m long. Preceding the working section is a 9:1 contraction and large 2.7m by 2.7m settling chamber consisting of a honeycomb and three fine wire mesh screens. This arrangement results in a high quality of airflow in the working section which is uniform to within 0.5% and has a turbulence intensity of less than 0.05%.

The main benefit of using this wind tunnel, apart from the high quality of airflow, is that it was fitted with a 3-axis computer controlled traverse which could be used to traverse a hot-wire or pitot probe throughout the wake of the model. In using this traverse it was possible to quickly investigate many spatial positions. The traverse was actuated by the open-loop control of three stepper motors. During their operation it was possible for these stepper motors to occasionally loose steps and hence compromise their positional integrity. In order to ensure positional reliability the traverse would be periodically be driven on to one of its limits in order to recalibrate itself.

3.3.2 Pressure measurements.

Many different experiments involving pressure measurement were conducted during this investigation and these were generally performed by the conventional means of surface tappings connected to multitube manometers. However, in some later

(a)



(b)

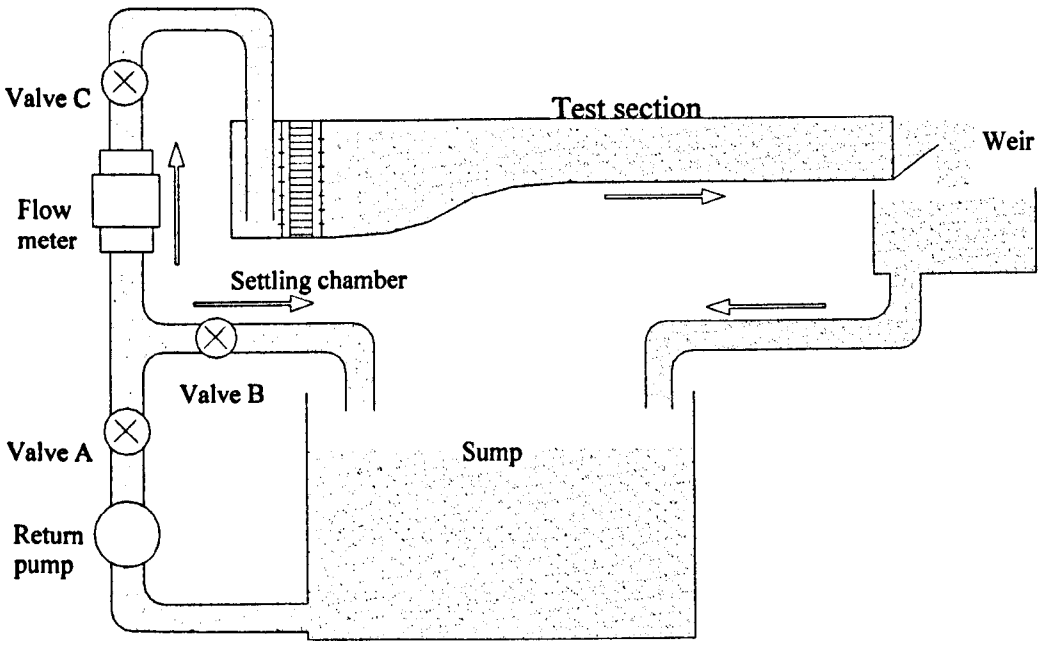


Figure 3.6 Two of the facilities used at the Department of Aeronautics at Imperial college: (a) The 3'x 3' wind tunnel, (b) The water channel.

experiments pressures were measured using an ultra-sensitive Honeywell pressure transducer connected to surface pressure tappings via a 48-way scanivalve. The signal from the pressure transducer was recorded with, and the scanivalve controlled by, a DAS08-AOH PC capture card fitted to a Pentium 166 PC. When stepping the scanivalve to a new tapping, the pressures would be allowed to settle for a second before being sampled for three seconds at a frequency of 1000Hz. Due to the large length of pressure tubing between the transducer and the tapping and also the dynamic limitations of the transducer, it was not possible to record pressure fluctuations accurately above a frequency of 200Hz. However, this did not present a problem as the main frequency of interest (the vortex shedding frequency) was rarely above 60Hz.

In addition to surface pressure tappings, pitot-static probes were also used in the wakes of some of the models to investigate the wake momentum deficit. The probes were moved down through the wake using the traverse and the pressure difference measured using one of the Honeywell pressure transducers. In addition to this another Honeywell pressure transducer was also used to evaluate the tunnel speed by measuring the pressure drop across the wind tunnel contraction. To ensure accuracy, all pressure transducers were regularly calibrated against a Betz manometer and found to be extremely consistent.

3.3.3 Hot wire anemometry.

Only single hot-wire probes were used in this investigation and were set to operate at a constant temperature of 250°C. The probes themselves were made by Dantec and were of the gold plated type whilst the anemometer used was the WOMBAT constant-temperature hot-wire anemometer system (I.C. Aero TN 81-102). As the wires were of high aspect ratio the cooling velocity was taken to be the component normal to the wire, and any cooling effect of the axial component was taken to be negligible (Richards 1977). The wires were not calibrated to record absolute velocities

as only the frequencies and relative intensities of the fluctuating velocity components were required during these experiments.

The fluctuating velocity signal from the anemometer was first amplified using a precision instrument amplifier and then low pass filtered at a frequency of 200Hz. The signal was then recorded by one of the differential inputs of an eight channel DAS – 1400 A-D PC capture card installed in a Pentium 90 PC computer. The signal was sampled for 30 seconds at a frequency of 1000Hz and then displayed by a data acquisition program where the signal could be saved for later analysis and post processing.

3.3.4 Experimental procedure.

- Installation of the appropriate model in the wind tunnel.

- Movement of the traverse to the appropriate position to align the hot-wire probe and set to a datum for subsequent traverse movements.

- Measurement of the atmospheric pressure and tunnel temperature.

- Start wind tunnel and ensure the tunnel speed has fully stabilised before recording the freestream velocity and taking any measurements.

- Move traverse to first hot-wire position.

- Sample signal.

- Record value of R.M.S velocity fluctuations or velocity power spectra depending on type of experiment.

- Movement of traverse to next hot-wire position.

The general tunnel running procedure used for the measurement of mean pitot pressures was similar to that for the hot-wire measurements and it would be unnecessary to include a further detailed procedure here.

3.3.5 Wind tunnel blockage correction.

For all models mounted in the 3'×3' wind tunnel the solid blockage was less than 3%. However, a blockage correction (Maskell 1963) was applied to all base pressures. Essentially this paper uses various time steady momentum considerations and measured body drag to calculate a correction for the effective increase in freestream velocity due to the presence of the model and its wake. Thus it was only possible to apply the correction factor after the base drag had been measured. The maximum correction needed for the models was in the range of 2 to 3%.

3.3.6 Surface flow visualisation.

In an attempt to investigate the nature of the flow over the surfaces of the models a surface flow visualisation was tried. ~~Three~~ Two techniques were tried. Initially a mixture of talcum powder and white spirit was used for wind tunnel surface visualisations although, this was not found to be very successful as the mixtures did not tend to flow very well on the surface of the model. Therefore, a second technique was tried that used a mixture consisting of sodium fluorescein and smoke oil. This method proved to be highly successful and was adopted as the chosen technique in all subsequent wind tunnel based surface flow visualisations.

3.4 The 4½'×4' wind tunnel experiments.

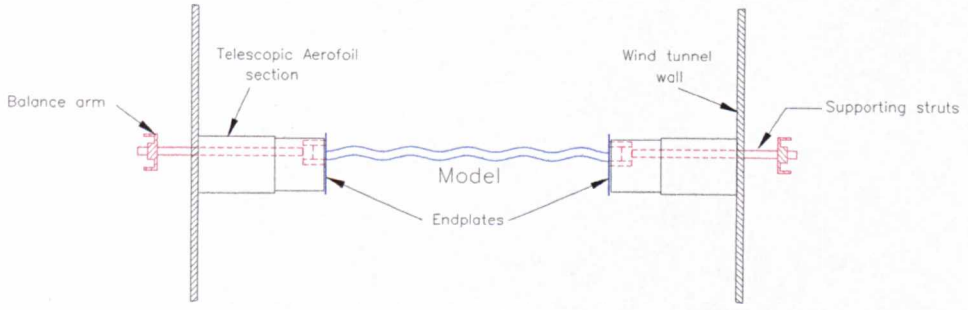
3.4.1 Introduction.

For the purpose of drag measurement and primarily PIV (Particle Image Velocimetry, see section 3.5), experiments were also conducted in the 4½'×4' wind tunnel of the Department of Aeronautics at Imperial College. The wind tunnel is of the closed-return type and is similar in design to the 3'×3' but has a moderately higher turbulence intensity of 0.5% due to fewer screens fitted in the settling chamber and a smaller contraction ratio of 5:1. Situated above the test section is a three-degree of freedom weigh-beam balance that can be used to measure directly the mean lift force, drag force and pitching moment of a model attached to it. The balance is highly accurate (to within a resolution of ± 0.05N in the drag direction) and evaluates the force exerted by moving weights along a weigh-beam to resolve the out of balance moment.

3.4.2 Drag force measurements.

As explained previously, the mean drag force was measured directly by means of a weigh beam balance mounted above the test section. The balance could be fitted with two large arms that hung down outside the tunnel to which the experimental models were attached via struts that passed through holes in the test section walls. In order to minimise the drag acting on the supporting struts, they were shrouded inside telescopic aerofoil sections that attached to the test section walls, figure 3.7a. In all instances models were fitted with endplates and these contribute approximately 3% to the total drag of the model. It was expected that the drag force exerted on the endplates would have been largely unaffected by the presence of the model to which it was attached. Consequently, as the contribution to the total drag from the endplates was relatively small the model drag was taken to be equal to the total drag minus the contribution from the endplates.

(a)



(b)

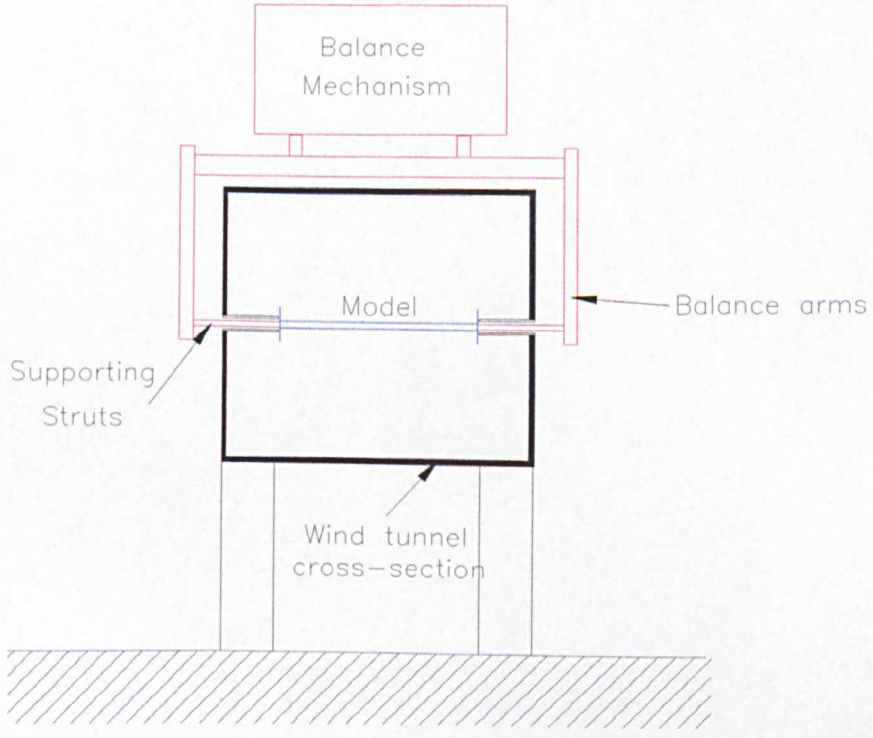


Figure 3.7 Mounting arrangements for models attached to the drag balance in the $4^1/_2$'x 4' wind tunnel: (a) Plan view of the tunnel, (b) Cross-section of the tunnel.

In all instances the drag coefficients calculated were based on the model span, model base height (or cylinder diameter D) and by using the free-stream velocity which was calculated using the pressure difference measured across the wind tunnel contraction.

3.4.3 Experimental procedure.

The experiments conducted in the 4½'×4' wind tunnel essentially involved using the balance to measure the drag force on the models directly. This led to a series of short experiments with the majority of the testing time being used to set-up the models in the wind tunnel. Once the model was properly set up in the tunnel an experiment consisted of a few simple steps:

- Measurement of the atmospheric pressure and tunnel temperature.
- Zero the force balance.
- Start wind tunnel and adjust to correct speed.
- Record the force necessary to balance the wind tunnel balance.
- Increase the tunnel speed to the next speed and record the new balance force.
- The previous step was repeated until all force measurements had been recorded.
- Stop the wind tunnel and check for any zero error in the balance.

Although only the drag force was of interest it was also important to balance the lift force and pitching moment due to a slight coupling between forces measured on the balance.

3.4.4 Blockage correction.

As described for the 3'×3' wind tunnel experiments a blockage correction was applied (Maskell 1963) to the dynamic pressure and used to correct the measured drag coefficients. The tunnel solid blockage for these experiment ranged from between 1.5 and 6% and this resulted in a maximum correction to the drag coefficient of 9%.

3.5 Particle image velocimetry.

3.5.1 Introduction.

In some later experiments a wind tunnel based PIV system (situated in the 4½'×4' wind tunnel, see section 3.4) was used to investigate the flow in the wake of various models at higher Reynolds numbers (approximately 2×10^4). The major benefit of using this system was that it allowed data to be collected instantaneously and unobtrusively in a single plane of interest rather than an obtrusive point measurement technique such as hot wire anemometry.

The PIV system used was built 'in house' by the department several years ago and had recently under gone an extensive refurbishment (see Elliott 2000). As a consequence of this refurbishment, both the quality and the accuracy of the final data was increased and the time taken to process a finished picture considerably reduced by the introduction of a new interrogation system.

To produce finished PIV data, images of the flow would be photographed in the wind tunnel using a conventional large format camera after which the film would be developed and the resulting images 'interrogated' using a specially designed rig in order to enable the velocity field to be evaluated. In this configuration the system was capable of producing high quality, high resolution images that generally contained in excess of 5000 vectors. Therefore, for the purpose of discussion, the PIV system can be essentially be regarded as consisting of two parts, a wind tunnel based system

(see section 3.5.2) and a laboratory based image interrogation system (see section 3.5.4).

3.5.2 The wind tunnel system.

The wind tunnel system basically consisted of three main components. A seeding system used to inject smoke particles into the flow, a high-powered pulsed laser for illuminating the particles in the flow and finally a large format photographic camera to record the resulting images. In addition to these, a Pentium 60 PC computer was used to control the timing of events and the firing of the camera and the laser.

In order to produce a successful negative the flow needed to be evenly seeded with tracer-particles that would follow the path of the fluid motion. This was done by injecting non-persistent smoke particles from an array of perforated vertical tubes situated in the wind tunnel contraction immediately downstream of the final turbulence screen. The smoke particles (approximately $10\mu m$ in diameter) were produced using a Concept Comet smoke generator and were blown out of the tubes using air fed from a centrifugal turbine. The density of the smoke particles could then be controlled by adjusting the output from the smoke generator and by varying the speed of the centrifugal turbine. The resulting air-smoke mix reduced many of problems associated with smoke condensing prematurely in the injection tubes and produced very even distribution of seeding particles in the test section flow.

The smoke particles were illuminated in the wind tunnel using a laser sheet produced by a class IV 1GW Ruby HLS4 pulsed laser. The laser was set to output two equal pulses of duration $20ns$ at a known time interval apart (typically of $15\mu s$ separation). The laser sheet was projected using a cylindrical lens placed in the path of the beam and its thickness could be varied by adjusting the position of a collimating lens placed in front of the laser. As there was generally some component of velocity through the plane of the laser sheet, it was important that the beam had sufficient thickness in order to ensure that a high proportion of the particles captured in the sheet for the first pulse remained in time for the second (generally termed 'particle pairs'). The

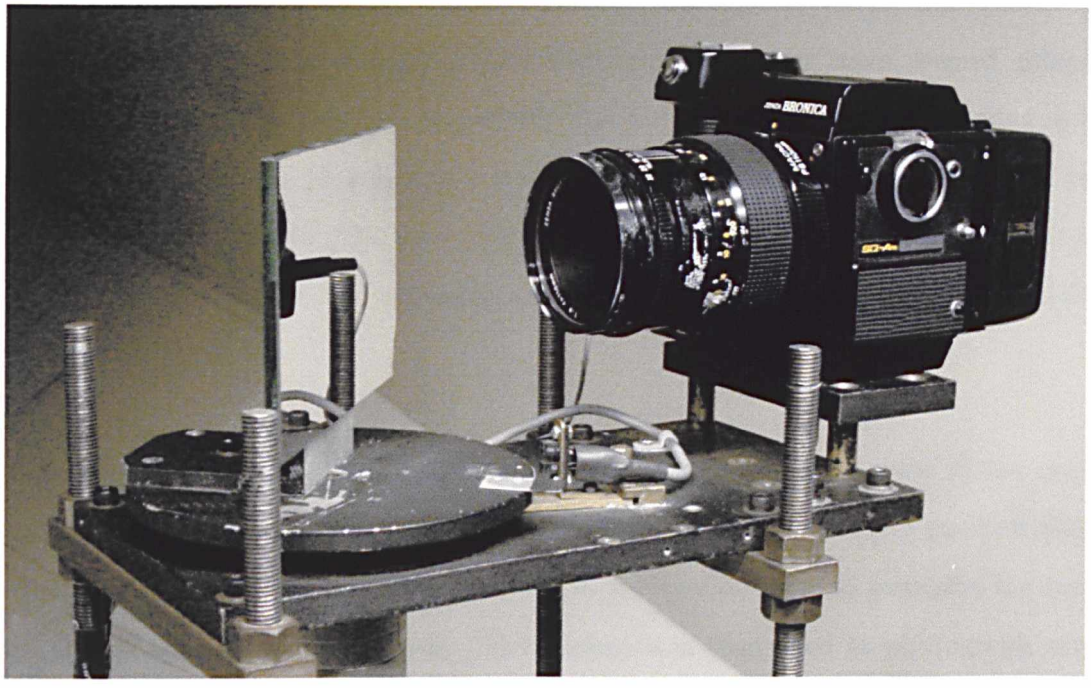
required sheet thickness (t_{LS}) was calculated in this instance using the following formula:

$$t_{LS} = \frac{U_N \Delta t(P+1)}{(1-P)}$$

Where U_N in the component of velocity normal to the laser sheet, Δt is the laser pulse separation and P the probability of finding particle pairs. In the present investigation the laser sheet thickness was determined by ensuring a higher than 90% probability of particle pairs or $P = 0.9$.

The images of particles in the flow were captured on photographic film (Kodak TP 120) using a Bronica SQ-AM large format camera that was aligned normal to the plane of the laser sheet. Due to the short separation between laser pulses, the camera would record the particle images from each laser pulse on the same photographic negative. Therefore, any group of particles would appear twice on the same picture allowing the velocity components to be calculated using a 2D auto-correlation technique. Whilst this technique would have been able to evaluate the magnitude of a given velocity component, it would not have been able to determine the direction of it as a 180^0 direction ambiguity existed. This ambiguity comes about due to the fact that for a given particle pair captured on the negative there is no way of determining which way the particle has moved. To resolve this ambiguity the camera was set-up to view the flow field via a rotating mirror placed directly in front of the lens (see figure 3.8a). This rotating mirror has the effect of adding an artificial shift velocity to all of the particles present in the flow field. If this shift velocity then is made to be higher than the largest velocity components present in the flow field then the directional ambiguity would be resolved because all the resulting velocities must lie in the direction of this shift. The true velocities can then be calculated during the interrogation process by simply subtracting the mirror shift velocity.

(a)



(b)

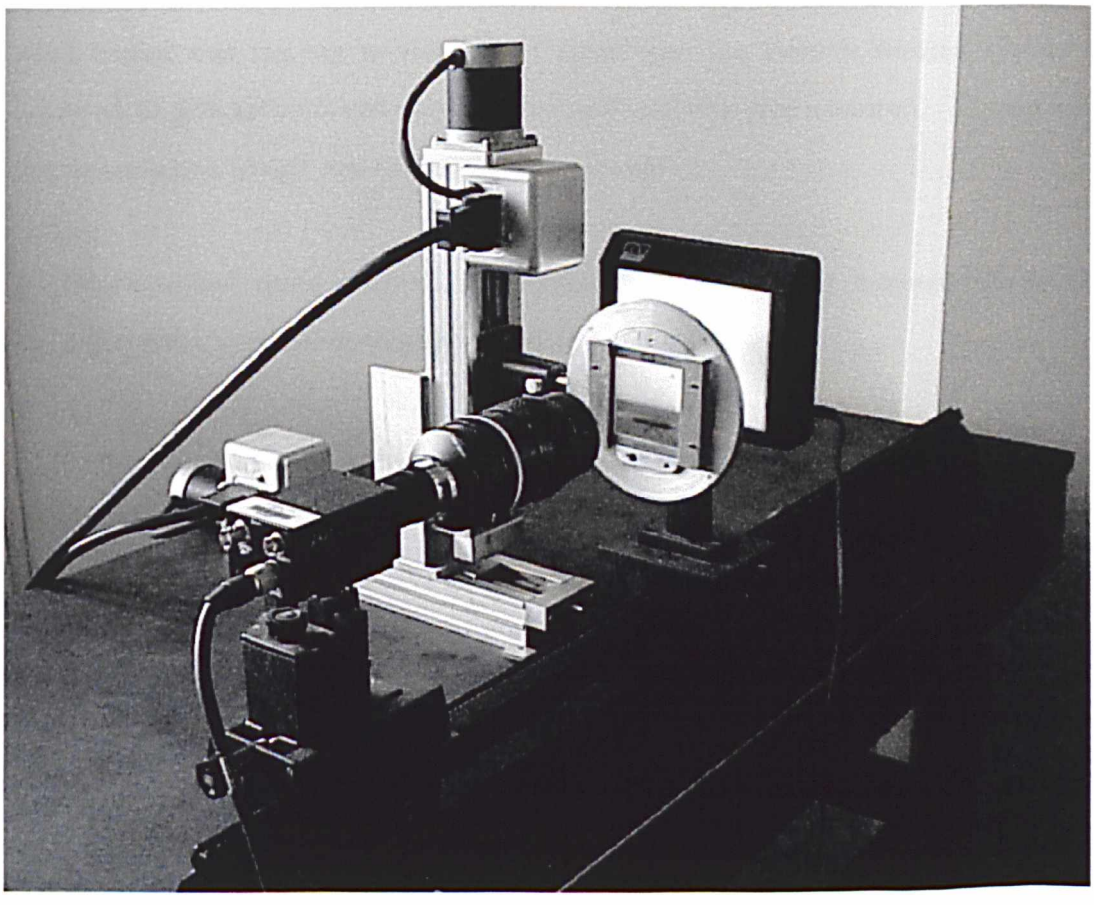


Figure 3.8 Components of the PIV system: (a) The rotating mirror system and camera, (b) The image interrogation rig, Elliott (2000).

3.5.3 PIV wind tunnel procedure.

Whilst the production of high quality PIV negatives may have seemed relatively simple, in reality the process required the fine adjustment of many conflicting system parameters with the journey to a completely trouble-free experiment often being anything but successful. However, once the system was correctly tuned to give good results the procedure of acquiring pictures was generally quick and relatively straightforward.

The first stage of any experiment was the setting-up and calibration of the system. Firstly, the control computer required information about the camera's position relative to the laser sheet and the desired image shift velocity in order to prescribe the correct rotational velocity for the mirror. The camera was then used to photograph several calibration grids placed in the plane of the laser sheet that were needed to determine the spatial geometry when calibrating the image interrogation system. Finally the wind tunnel was run up to the correct speed and the particle seeding system was adjusted to give an even distribution of smoke over the area required. The procedure for capturing an image was then simply as follows:

- Check tunnel speed using Betz manometer (connected to measure the pressure difference across the contraction) and adjust if necessary.

- Switch seeding smoke on, start laser charging and prepare the computer to perform the firing sequence.

  The computer would now set all the on board timers and move the rotating mirror to its start position.

- When the laser was fully charged (this would take approximately 60 seconds) the fire sequence would then be initiated using the computer.

The computer would now spin the mirror up to the correct speed for the required image shift. Once the mirror had attained the correct speed the camera would be triggered and moments later when the mirror arrived at the correct position the laser would be fired producing two 20ns pulses. After this the mirror would spin down and the computer would display the energy levels of the two laser pulses.

- The smoke would then be switched off and the values of the two laser energies noted down.

- This procedure would then be repeated a further eleven times until the film in the camera had been finished.

- The wind tunnel was then stopped and the film developed to produce an image of high contrast using Kodak Polymax developer for $3\frac{1}{2}$ minutes @ 30^0C.

3.5.4 The image interrogation system and data post processing.

The interrogation system was used to extract the flow field data from the images captured in the wind tunnel. It consisted of a miniature X-Y traverse for traversing the negative in front of a variable intensity light box and a high-resolution CCD camera that was fitted with a microscope lens for capturing the image on to a PC. A photograph of the system can be seen in figure 3.8b.

Once an image had been captured it was broken up into a series of 16 small 'interrogation cells' for analysis. In essence the computer would calculate a velocity vector from the first interrogation cell by performing a 2D auto-correlation on the greyscale pixel values present in the cell. From the auto-correlation the second highest peak was used to determine the average particle spacing from which the velocity could then be calculated by dividing by the time interval between laser pulses. However, it is important to ignore the highest peak in the auto-correlation as this is always produced at the origin where there is no particle separation and where

the images are perfectly correlated with themselves. Finally, the artificial shift velocity added by the rotating mirror was subtracted and the resultant velocity vector displayed on the screen and recorded to file. The calculation was performed for the remaining 15 interrogation cells before the negative was traversed to the next position on a predetermined grid and a new image acquired. This process was repeated until the whole of the area of interest on the negative had been interrogated and the data saved to file. The images could then be post-processed.

It was necessary to post-process the data as not all of the velocities calculated by the interrogation system were the result of true particle motions. This would lead to so called 'rogue vectors' in the data. These rogue vectors were caused by areas of the flow where it was not possible to determine particle pairs. Examples of where this was likely to occur were areas of very low seeding (no particles), areas with very high seeding (no gaps between particles) and areas of laser glare caused by the laser sheet striking the model (particles not distinguishable from background).

Post-processing was performed on a PC using a separate piece of software that was written and developed by Elliott (2000). In principle it was then a simple task of using this software to remove the rogue vectors individually or by using a series of filter routines performed by the program. If desired, missing vectors could then be replaced by looking for the next highest peak in the auto-correlation or by using an interpolation routine that calculated the value of this vector based on neighbouring cells.

The post-processor also allowed vector plots of the same area to be averaged with each other. If pictures were to be averaged, it was important that they could be accurately superimposed about a known datum. The edge of the picture could not be used for this datum as the position of the model would tend to move fractionally on the negative due to it being viewed through the rotating mirror system. Therefore, to overcome this problem two fine wires were placed in the laser sheet to act as a datum off which the images could be accurately aligned.

A full description of the system accuracy and calculation of potential errors in the interrogation system can be found in Elliott (2000). However, errors associated with the technique are in general very small (less than 1% of freestream) and can be corrected for via post-processing of the interrogated data.

4 The effect of wavy separation lines on rectangular section bodies.

4.1 Introduction.

4.1.1 Flow in the wake of a square section cylinder.

In contrast to circular cylinders, the flow in the wake of a square section cylinder has received relatively little experimental attention. This lack of interest is particularly apparent at low Reynolds numbers where the majority of investigations have been undertaken using CFD with very little experimental data available for accurate comparisons. For both the experimental and computational data there is a large scatter in results with much uncertainty as to the types of flow regimes and exact values of drag and shedding frequencies at these low Reynolds numbers.

The work of previous authors has shown the wake of a square section cylinder to be steady at very low Reynolds numbers. However, as the Reynolds number is increased the wake becomes unsteady in a similar manner to that found in the wake of a circular cylinder and vortex shedding commences. The exact Reynolds number for this onset of vortex shedding has been reported in many investigations and is found to vary widely depending on computational or experimental conditions. In Gerrard (1978) the critical Reynolds number for the onset of vortex shedding was determined to be 36 via a series of flow visualisation experiments performed at low blockage in a towing tank. In a later investigation, Norberg (1996) determined the value for the onset of vortex shedding to be 47 ± 2 in a series of almost zero blockage experiments. However, the majority of values for this onset have been determined computationally using C.F.D. In Kelkar & Patankar (1992) the onset value was determined as 53 although this investigation was performed at a relatively high domain blockage of 14.2%. However, a similar value was also found by Sohankar *et al.* (1998) who placed the critical onset for vortex shedding at a Reynolds number of 52, based on computations performed at a blockage of 5%. They suggested that the large variation

in the values of the onset Reynolds number observed in previous investigations was due to the effects of blockage. Conventionally it would be expected that increasing blockage would increase the local velocity in the region near the model and hence result in a local increase in Reynolds number. Therefore, increasing blockage would be expected to reduce the onset Reynolds number. However, it was conjectured by Sohankar *et al.* (1998), that increasing blockage would actually delay the onset of vortex shedding due to higher local accelerations of the flow providing a stabilising effect on the wake.

In circular cylinder flows the Strouhal number is found to increase in the laminar regime with increasing Reynolds number and a similar trend is found for the vortex shedding in the wake of a square cylinder. Using experimental results, Norberg (1996) defined this variation between Strouhal number (St) and Reynolds number (Re) as,

$$St = 0.18 - \frac{3.7}{\mathrm{Re}}$$

which gives a vortex shedding frequency of 0.143 at a Reynolds number of 100. However, this equation is not found to be a perfect fit to the data at a Reynolds number of 100 and a closer value of Strouhal number at this Reynolds number would be St = 0.146. However, comparisons with data from other investigations show a significant variation in the value of Strouhal number found at this Reynolds number. In figure 4.1 the variation of Strouhal number with Reynolds number (from Sohankar *et al.* 1999) is plotted where the data of Norberg (1996) can be seen in comparison with the data from various other investigations. It is apparent from the figure that there is a large scatter in the results particularly in computational data at a Reynolds number of 100 where the Strouhal number is found to vary from approximately St = 0.12 to St = 0.16. There have been few experimental investigations from which comparisons can be drawn, although Okajima (1982) did perform a series of experiments in water from which he was able to deduce that the Strouhal frequency was 0.14 for a Reynolds number of 100.

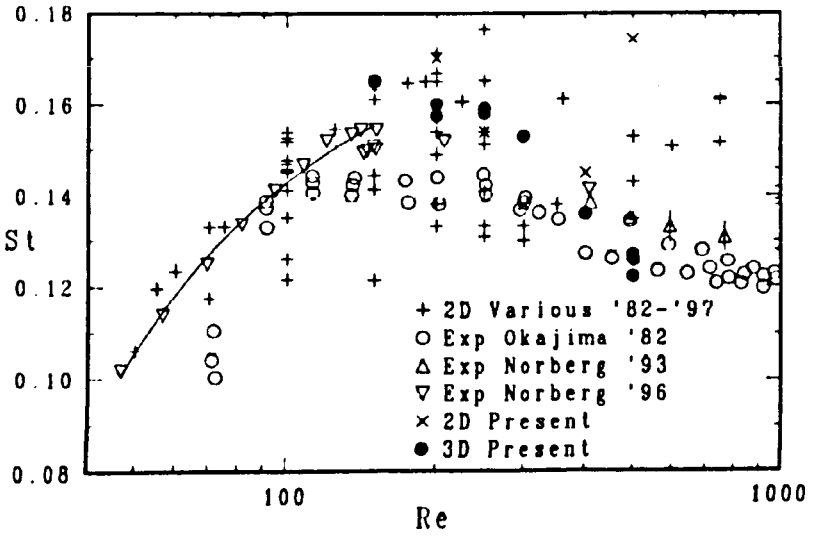


Figure 4.1 The effect of Reynolds number on Strouhal number in the wake of a square section cylinder taken from Sohanker et al (1999). The solid line is expressed by St = 0.18 - 3.7/Re, Norberg (1996).

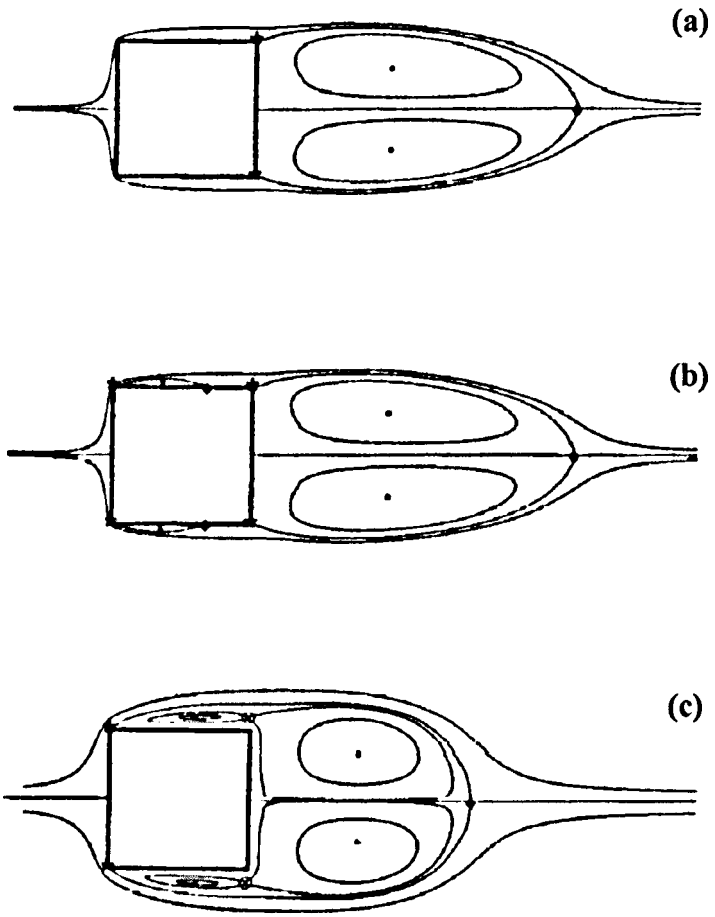


Figure 4.2 Flow regimes in the wake of a square section cylinder at low Reynolds numbers, Robichaux et al (1999): (a), no separation from sides; (b), separation from the upstream corners and reattachment to the sides; (c), separation from the upstream corners without reattachment to the sides.

Throughout the onset regime and up to a Reynolds number of approximately 120 Robichaux *et al.* (1999) reported that the flow remains attached around the upstream corners and only separates to form a Kármán street in the wake from the downstream corners. However, as the Reynolds number is increased above this value, it was found that the flow began to separate from the upstream corners but would then reattach to the upper and lower surfaces a short distance downstream forming a pair of separation bubbles, figure 4.2. This was also confirmed by Sohankar *et al.* (1995) who computed that the flow would remain attached to the front corners until a Reynolds number of about 125 had been exceeded. In Robichaux *et al.* (1999) the separation bubbles were found to grow in size as the Reynolds number was increased until beyond a value of approximately 150 where reattachment no longer occurred on the side faces. A similar result was found experimentally by Okajima (1982) who observed the flow to separate from the upstream corners for Reynolds number in excess of 150.

In Norberg (1996) vortex shedding in the wake of the square cylinder was found to become broad-banded as the Reynolds number was increased beyond 150. It was suggested that beyond this Reynolds number the wake underwent the transition to three-dimensionality, with the Strouhal frequency becoming increasingly difficult to determine as the Reynolds number was increased. The cylinder used in these experiments had an aspect ratio of 200 and was fitted with coaxial end cylinders of three times the diameter to promote parallel shedding in the wake. However, coaxial cylinders tend to produce rather unsteady end flows and it has been demonstrated for a circular cylinder (section 1.3.2) that experimental conditions and in particular end conditions are of prime importance if an early transition to three-dimensionality is to be avoided. Hence, it is possible that the transition could have been triggered at a lower Reynolds number in these experiments due to the cylinder end conditions.

Robichaux *et al.* (1999) performed a Floquet stability analysis in the wake of a square section to determine the dominant modes of three-dimensional instability. Unlike Norberg (1996), at a Reynolds number of 150 they found that the wake was completely stable to three-dimensional perturbations over all spanwise wavelengths.

However, as the Reynolds number was increased to 175 the wake was found to become unstable over a range of spanwise wavelengths with the highest growth rate found at a wavelength of 5.07h. Investigation of the wake at this Reynolds number revealed that the cylinder had entered the mode – A regime, with the production of streamwise vortex pairs. They did not extend their test to determine the exact value for this transition but instead concluded that the critical Reynolds number for the onset of mode – A was 162 ± 12.

At higher Reynolds numbers other modes of instability were detected. At a Reynolds number of 205 a second short-wave instability was determined with wavelength of 1.16h that corresponded to the mode – B transition found previously in circular cylinder flows. However, as the Reynolds number was increased to 225 a third instability of intermediate wavelength was also discovered. Termed 'mode – S', this instability was found to have a spanwise wavelength of 2.8h and is believed to be a mode exclusive to the wakes of square section cylinders.

4.1.2 The effect of wavy separation lines.

Bearman & Tombazis (1993) & Tombazis & Bearman (1997) studied the effect of a wavy separation line on a semi-ellipse section. In order to categorise the deformation of the 2D separation line or waviness, they introduced the parameter of wave steepness defined as peak to peak wave height (w) divided by wavelength (L) or w/L. They found that significant reductions in base suction of up to 35% could be achieved with increasingly wavy separation lines leading to drag reductions of a similar magnitude. However, despite these large reductions in drag, vortex shedding was still found to persist in the wakes of these bodies, although the introduction of waviness did produce a significantly three-dimensional wake. Investigations in the wake using a hot wire probe showed the emergence of two shedding frequencies that were found to vary in strength periodically across the span. Bearman & Owen (1998a) found a similar type of dual shedding frequency behaviour in the wakes of thin plates and rectangular section bodies. However, these dual-shedding frequencies were only

present at small levels of wave steepness of approximately w/L = 0.03. At a value of wave steepness slightly above this, the base suction was found to drop dramatically with a reduction of approximately 50% for a wave steepness of w/L = 0.06. This value of base suction was found to be in good agreement with the value determined by Jaroch & Fernholz (1989) for a normal plate fitted with a splitter plate and led to an overall reduction in drag of approximately 30%.

More recently a computational study has been under taken by Darekar & Sherwin (2001) to investigate the wake of wavy square section cylinders at low Reynolds numbers. Using a 3D spectral element solver, they investigated the effect of wave steepness and wavelength on a body of constant square cross-section but with an axis deformed into the shape of a sinusoid. They identified several different flow regimes depending on wavelength and found that vortex shedding could be suppressed with the introduction of sufficient waviness into the base geometry. It was found that the wake was particular receptive to spanwise forcing at a wavelength of 5.6h where minimal wave steepness was needed to suppress vortex shedding. In addition to the suppression of vortex shedding it was also found that a drag reduction of up to 16% could be achieved in comparison with a 2D cylinder.

4.2 Experimental arrangement.

4.2.1 The use of flow visualisation for the measurement of shedding frequency.

Measurement of the vortex shedding frequency in the wake of a square section cylinder at low Reynolds numbers presents us with several interesting experimental challenges. Primarily, low Reynolds number experiments in air need to be conducted at small scale with cylinder diameters for circular cylinder experiments typically of the order of less than $1mm$. Whilst circular cylinders of these orders are readily available in the form of fine wire, square section cylinders are neither readily available nor easily manufactured at this scale. Hence, experiments must be performed at a larger physical scale with a low Reynolds number being achieved through a low freestream velocity. However, at low velocities it can be difficult to ensure good flow uniformity

with the freestream velocity becoming increasingly difficult to measure as the velocity is reduced. Therefore, experiments in a towing tank become the most viable option where the velocity can be accurately prescribed and where the flow uniformity can be carefully controlled. Conventionally, the frequency of vortex shedding is determined from velocity fluctuations measured in the wake using a hot-wire probe situated some distance downstream. Hot-wire probes can be optimised to measure wake fluctuations for use in water as demonstrated by Okajima (1982), although he found it difficult to accurately determine the vortex shedding frequency due to what he called 'a lack of information' at these low Reynolds numbers. Hence, in the present investigation the frequency of vortex shedding was determined directly from flow visualisation performed in the wake of the model where it could be easily confirmed if the wake had become fully established before frequency measurements were made.

The flow in the wake of the cylinder was filmed over the duration of an entire run using a conventional VHS video camera after which the tape was analysed and the number of vortices shed over a specific time period was used to calculate the vortex shedding frequency. For imposed parallel shedding (where the frequency was found to be constant across the majority of the span), the vortex shedding frequency was determined from cross-flow visualisations of the model taken at centre span. However, for oblique shedding, the frequency measured at the centre span of the cylinder was found to vary as the chevron-shedding pattern became established in the early part of the run. Therefore, to avoid this problem, the wake was visualised in plan view for oblique shedding measurements to ensure that the chevron pattern had fully developed before any frequency data was collected.

4.2.2 Experimental models.

A great deal of time and effort was put into the manufacture of a highly accurate square section cylinder for use in the low Reynolds number towing tank experiments. The square section cylinder model was made from a piece of brass bar that was machined to the approximate dimensions before being fine surface ground (but not

polished as this would have rounded-off the corners) on all four sides to ensure an accurate surface and sharp corners. The base height of the model was kept to the minimum which could be accurately manufactured so as to increase the aspect ratio and the towing speed for a given Reynolds number. The final models were manufactured with a base height of 4.75mm (accurate to within 0.01mm), an aspect ratio of 95 and with no measurable twist along their length.

For the purpose of frequency measurements in the wake, a very thin coating of sodium fluorescein solution was smeared on to the front face of the model and allowed to dry. The fluorescein was then washed off into the wake over the duration of a run and illuminated using an argon laser as described in section 3.2.4. This arrangement proved adequate for determining the shedding frequency in the wake but was not able to produce detailed visualisations near the end of a run as the concentration of the fluorescein shed into the wake reduced. Therefore, for specific flow visualisation experiments a second square section cylinder model was manufactured with a fine slit (0.5mm wide by 2mm deep) machined a long the front stagnation line to act as a reservoir for the fluorescein. The presence of this slit was found to make no detectable difference to the flow although the previous cylinder model without the slit was used in subsequent frequency experiments for consistency. The fluorescein used in these visualisation experiments was mixed with corn syrup as described in section 3.2.4 and when melted into this small slit would produce a very even distribution of dye in the wake over the entire run.

For experiments with imposed three-dimensionality a series of six rectangular section models (similar to those tested in Owen 1997) were constructed from black Nylon 6 (a thermo-plastic) with increasingly wavy separation lines. These wavy separation lines were produced by machining the front face of the model in the form of a sinusoid using a three-axis computer controlled milling machine. The wave steepness (defined as w/L by Bearman and Owen 1998a) of this sinusoid was varied in the range $w/L = 0$ to $w/L = 0.1$ by manufacturing each model with a varying wave height for a constant wavelength of 6h. The resulting models had a base height of 15mm, an

aspect ratio of 30 and were used for both drag measurements (in a wind tunnel) and for flow visualisation experiments in water using the methyl-blue dye technique as described in section 3.2.4

For constancy with the previous convention established by Tombazis (1993), the geometric maxima and minima of the model where defined as peaks and valleys. A peak was defined as the geometric position where the model stretches furthest downstream or where the body's streamwise thickness is a minimum. A valley was then simply defined as the opposite position or where the body's cross-section is square.

4.3 Results – Square section flows.

4.3.1 Shedding modes – the importance of end conditions.

For circular cylinders, end effects have been shown to be of prime importance if parallel shedding is to be promoted in the wake, section 1.2.2. Hence, a series of experiments were performed at Reynolds number of 80, in order to investigate the importance of end effects on square section cylinders. For these experiments the end conditions could be manipulated by angling the endplates relative to the cylinder axis in a similar way to Williamson (1989) for circular cylinders.

Initial visualisations were performed with the endplates attached perpendicular to the cylinder axis and the wake observed in plan view. It was found that initially the vortices would be shed straight and parallel to the cylinder axis over the majority of the cylinder span with only small cells of oblique shedding observed close to the cylinder end plates, figure 4.3a. However, as the model was traversed further downstream and in a manner similar to Williamson (1989), these oblique end cells were observed to propagate towards the centre span of the model. Eventually, and after the model had travelled approximately 300 base heights downstream, these oblique cells reached the centre span of the model forming the now familiar chevron pattern, figure 4.3b. In subsequent experiments this chevron pattern was always

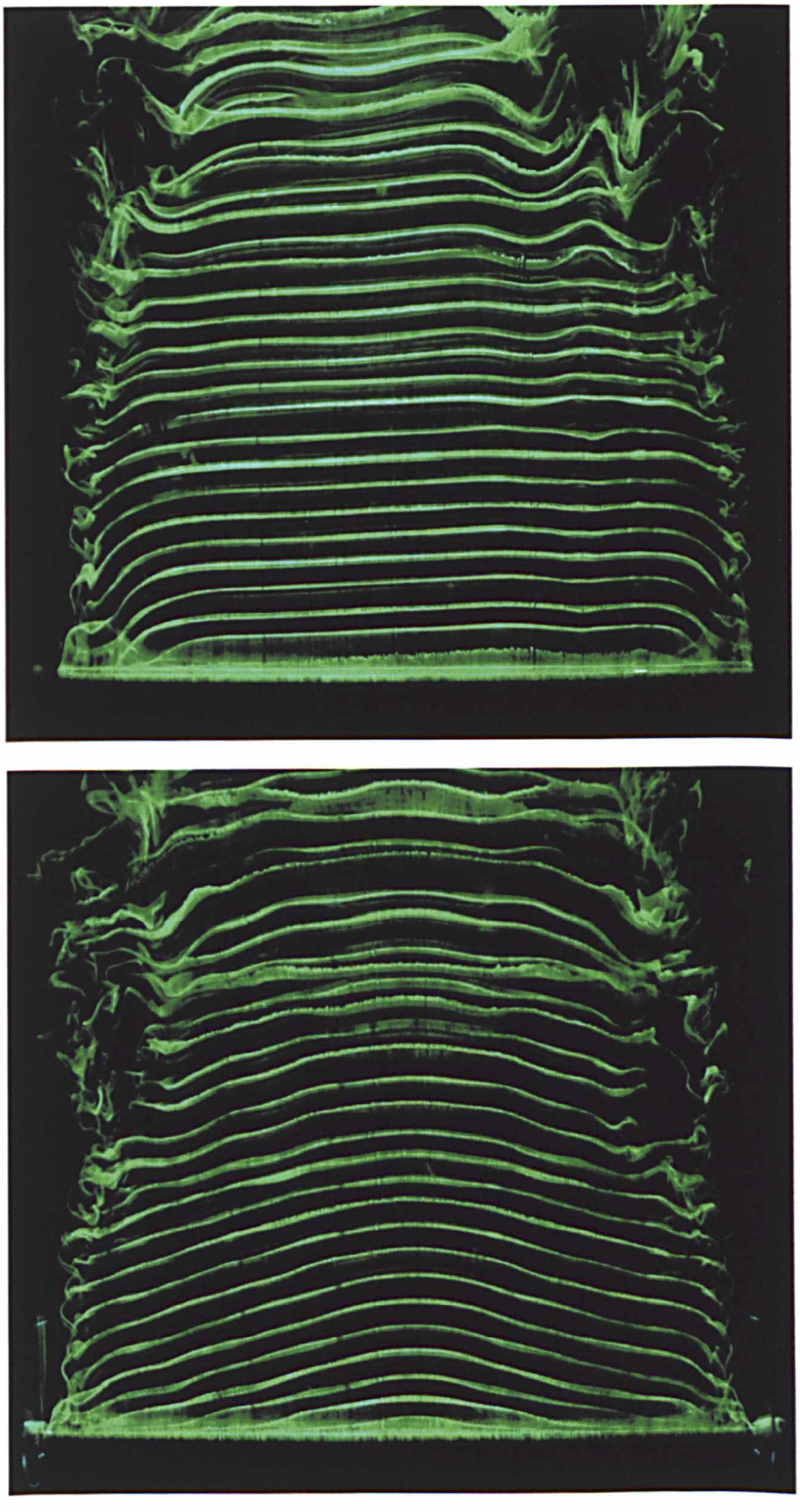


Figure 4.3 Plan view visualisation of the wake of a square section cylinder at a Reynolds number of 80, $l_{span}/D = 95$. Picture (a) was taken after the cylinder had only travelled 110 base heights downstream and initially the vortices were shed parallel to the cylinder axis. In picture (b) the cylinder has travelled a further 300 base heights downstream where the end effects have propagated to the centre span to form a chevron pattern.

observed to develop in the wake and continued to be shed in this configuration to the end of the run, approximately 300 base heights further downstream.

At this Reynolds number the angle of the oblique vortices was found to be approximately 15° relative to the model axis, which was found to be in good agreement with the values previously determined for circular cylinders by Williamson (1989). This angle was found to be both constant and stable up to a Reynolds number of approximately 150 and down to a Reynolds number of approximately 60. Below this value the chevron was initially observed to develop as normal but would then become unstable with the oblique angle increasing and decreasing as the run continued. This made accurate measurements of the Strouhal frequency in this regime difficult as the frequency was continually changing as the chevron pattern varied in shape. A similar effect was observed by Williamson (1989) in the wakes of circular cylinders and this was found to be responsible for the discontinuity in the relationship between Strouhal number and Reynolds number. A similar discontinuity can also be seen in the present data as an increase in scatter of the Strouhal frequency below a Reynolds number of about 60, figure 4.4.

In an attempt to promote parallel shedding in the wake of the square section cylinder the leading edges of the endplates were angled inwards. For circular cylinders it was reported by Williamson (1989) that angling the endplates inwards had little effect on the angle of oblique shedding until after an endplate angle of 12°, relative to the direction of motion, had been exceeded. Beyond this angle the vortices were observed to shed parallel to the cylinder with an increase in angle up to 20° having no additional effect on shedding angle. However, unlike Williamson, in the present investigation it was immediately apparent that any increase in the endplate angle beyond 0° resulted in an immediate reduction in the angle of oblique vortex shedding. As the angle of the endplates was increased further the angle of oblique shedding was reduced, until where parallel shedding was achieved at an endplate angle of 9°, figure 4.5. Beyond this angle of 9°, it was found that the angle of the vortices continued to be reduced with a slightly reverse chevron being produced by an endplate angle of 18°.

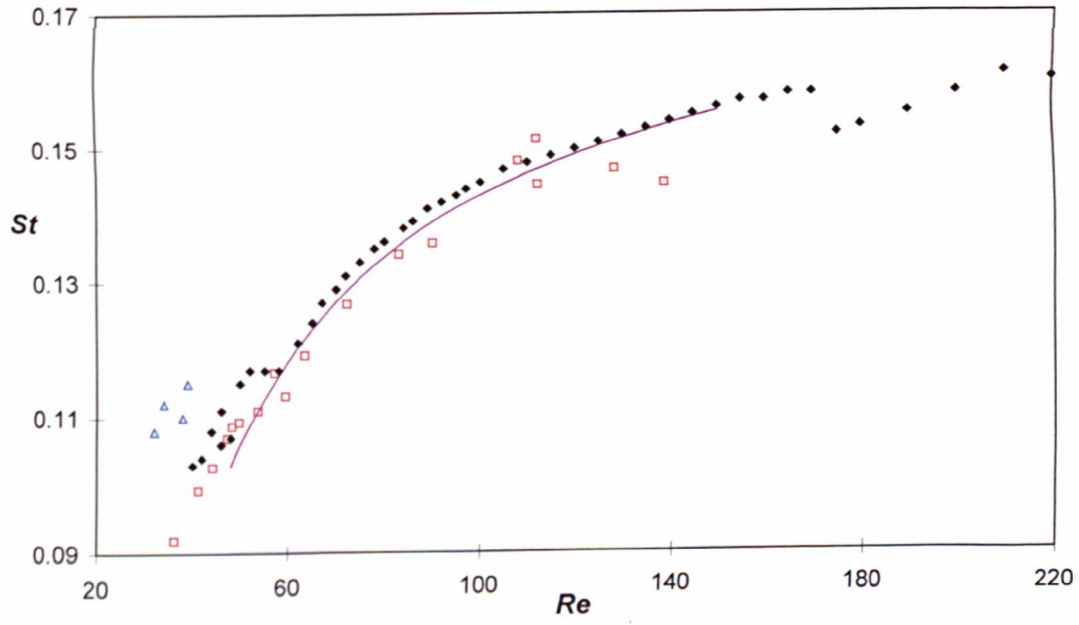


Figure 4.4 Variation of Strouhal number with Reynolds number for oblique vortex shedding in the wake of a square section cylinder: ♦, oblique vortex shedding – present results; Δ, non Karman instabilities – present results; □, vortex shedding – Gerrard (1978); --, St = 0.18 – 3.7/Re – Norberg (1996).

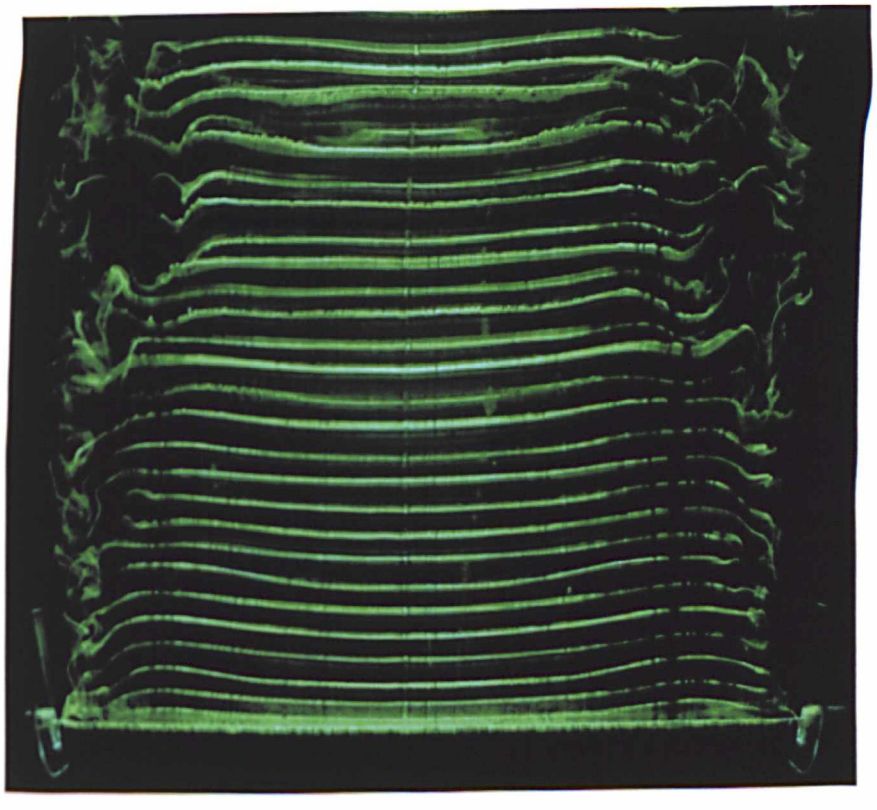


Figure 4.5 Visualisation of imposed parallel shedding in the wake of a square section cylinder by the use of angled endplates (leading edges angled inwards by an angle of 9°), Reynolds number = 80, $l_{span}/D = 95$.

Despite the difference in sectional geometry, these results suggest that at low Reynolds numbers the wake of a square section cylinder is in fact surprisingly similar to that of a circular cylinder with very similar modes of vortex shedding being observed.

4.3.2 The effect of Reynolds number.

At a sufficiently low Reynolds number the flow in the wake of a square section cylinder is found to be steady. Initial observations of the wake at a Reynolds number of 20 showed a thin, perfectly straight stream of dye trailed along the centre line of the wake with two small recirculation cells forming in the near base region, figure 4.6a. These two recirculation cells were then found to grow in size as the Reynolds number was increased with the wake remaining in this steady configuration until a Reynolds number of approximately 30. Beyond this value, the far wake begins to undergo a mild oscillation that is intensified and moves further upstream as the Reynolds number is increased. This instability is most energetic at a Reynolds number of about 39, just before the onset of vortex shedding and develops at approximately 10 base heights downstream of the cylinder, figure 4.6b. However, this wake oscillation is not vortex shedding but is a convective instability associated with the merging of the two oppositely signed shear layers downstream in the wake.

In the present investigation, the onset of vortex shedding was found to occur at a Reynolds number of approximately 40 ± 1 for oblique shedding and at a slightly higher Reynolds number of approximately 41 ± 1 for parallel shedding. However, the exact Reynolds number for the onset of vortex shedding in the wake can be difficult to determine experimentally due to the sometimes random appearance of Kármán structures in the wake. Therefore, if accurate comparisons are to be made with results of previous investigations, it is important to state exactly when the wake will be considered as 'vortex shedding'. In the present investigation the wake was only defined as vortex shedding when this vortex shedding was found to be self-sustaining

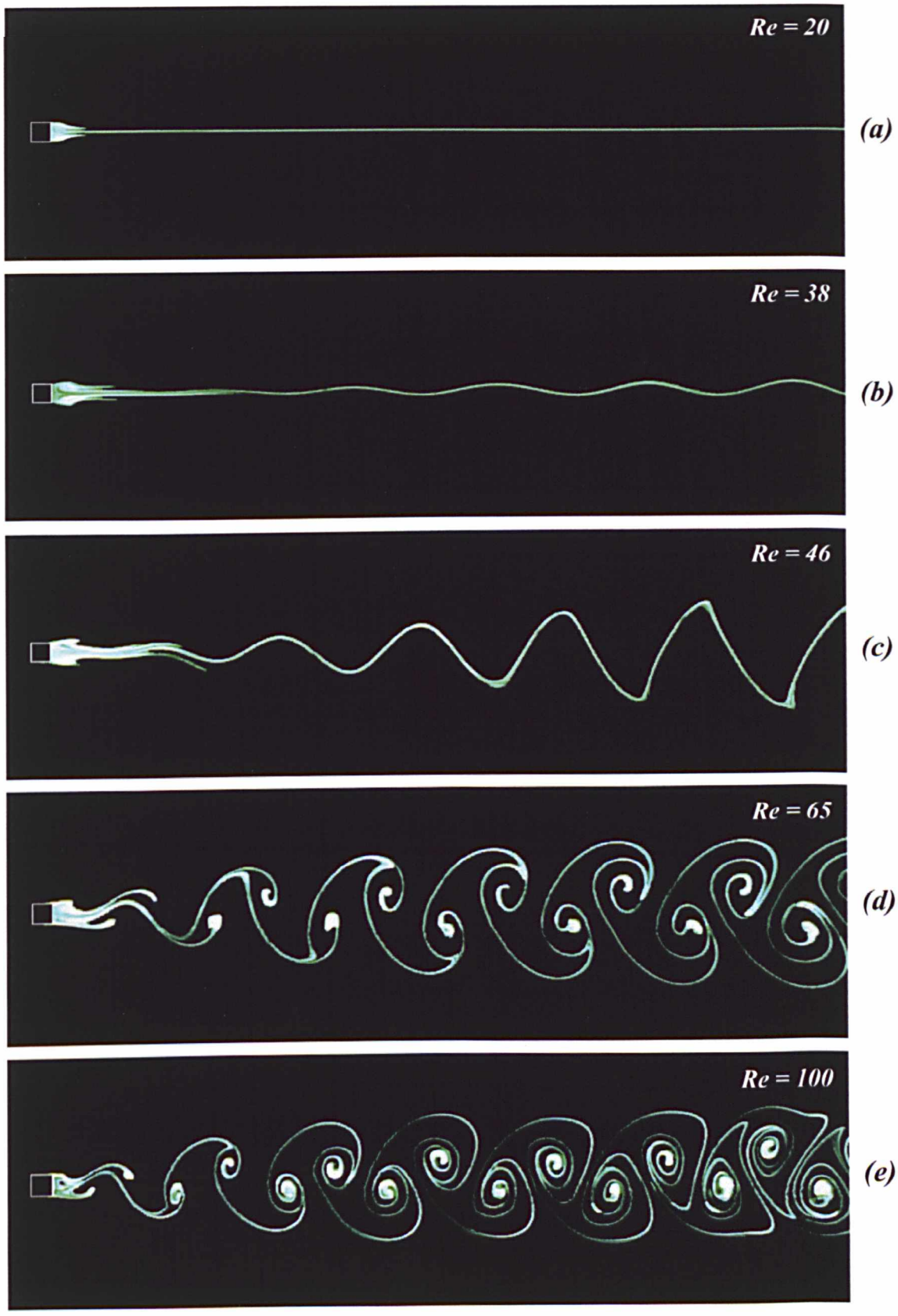


Figure 4.6 Cross-sectional visualisations of the wake of a square section cylinder at increasing Reynolds numbers, $l_{span}/D = 95$.

over an entire run. However, at Reynolds numbers close to the onset it was often difficult to determine whether the wake was vortex shedding or whether the wake was just becoming wavy downstream due to the previously described convective instability. Hence, the frequency of oscillation of the wake was used to resolve this ambiguity. It was found that if the Strouhal numbers of the wake were plotted against Reynolds number, then a discontinuous jump in Strouhal number could be observed at the onset of vortex shedding, figure 4.4. From the figure this onset point can be easily seen at a Reynolds number of approximately 40 where the frequency of oscillation abruptly drops to a lower value as vortex shedding commences. It was also found that the onset Reynolds number was particularly sensitive to small perturbations in the flow with an early onset of vortex shedding resulting unless careful experimental conditions were observed. Hence, it is possible that the earlier onset of vortex shedding observed in the data of Gerrard (1978) at a Reynolds number of 36 was caused as a result of larger perturbations than during the present experiments, figure 4.7.

As the Reynolds number is increased beyond the onset value the primary vortices grow in strength with increasing Reynolds number and the near base formation region is observed to shrink in size, figures 4.6c-4.6e. At a Reynolds number of 100 the Strouhal number is found to be 0.145 for oblique shedding and 0.148 for parallel shedding. These values are in good agreement with Norberg (1996) who found the Strouhal number to be approximately 0.145 using a square section fitted with larger diameter coaxial end cylinders to promote parallel shedding in the wake, although parallel shedding was not confirmed.

As the Reynolds number was increased above 115 the flow was observed to separate from the front corners and then reattach to the upper and lower surfaces a short distance downstream forming two small separation bubbles. However, it was difficult to determine accurately from flow visualisation the exact Reynolds number at which the flow first separates from the leading edge corners due to the small scale of the model. A further increase in Reynolds number caused the separation bubbles to grow

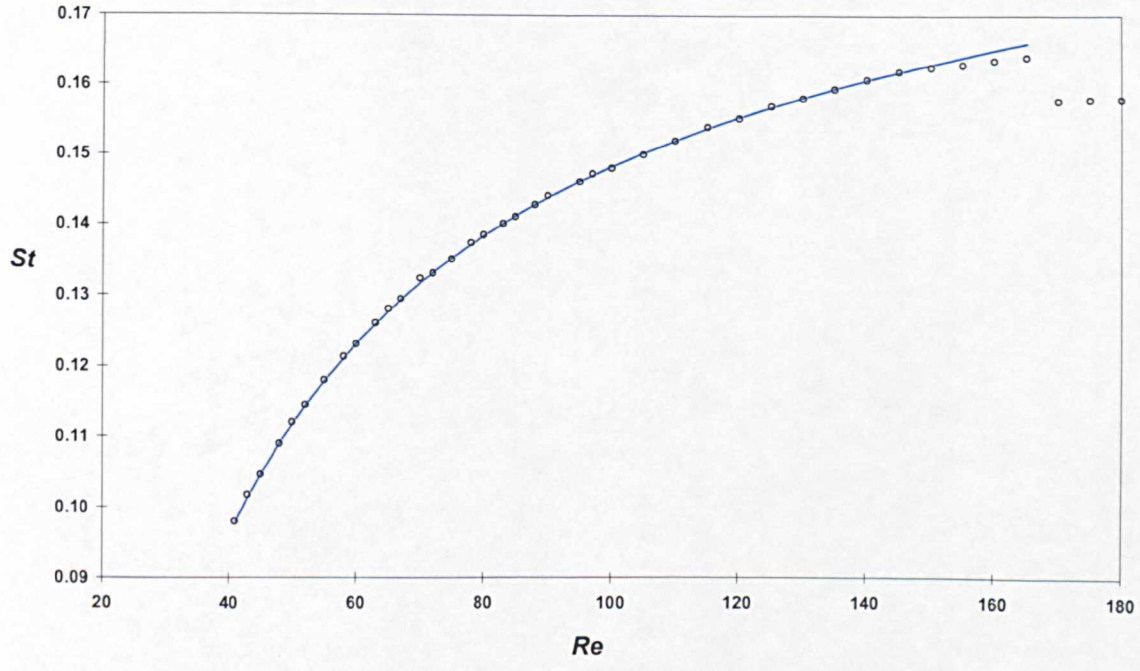


Figure 4.7 The variation of Strouhal number with Reynolds number for imposed parallel shedding in the wake.

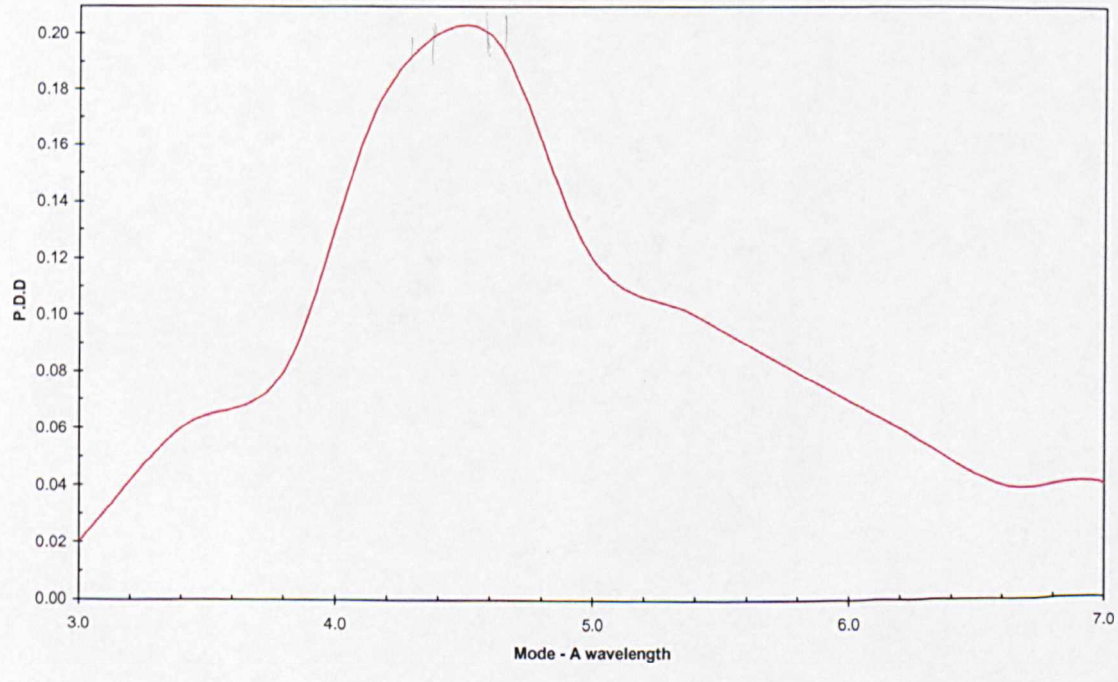


Figure 4.8 **The** probability density of mode – A wavelengths (1_A) in the wake of a square section cylinder at a Reynolds number of 185.

in size. These bubbles were observed to fluctuate in length over the duration of a shedding cycle. At a Reynolds number of about 150 the flow would detach from the upper surface of the cylinder during part of the shedding cycle and separate from the upstream corner. This reattachment to the upper and lower surfaces became less as the Reynolds number increased until in the Reynolds number range of about 160 – 170 where the flow was observed to no longer reattach.

In past investigations it has been popular to define a mathematical relationship between Strouhal number (St) and Reynolds number (Re) in the laminar shedding regime. This has been expressed for circular cylinders as:

$$St = 1.6\times10^{-4}\,\mathrm{Re} + 0.18 - \frac{3.32}{\mathrm{Re}}$$

However, with recent advances in our understanding of circular cylinder flows and with increasing accuracy in both experimental and computational techniques, this formula has proved inadequate as data from various studies now typically agrees to within 1%. This inadequacy was addressed by Williamson & Brown (1998) who proposed a new expression that represented the variation between Strouhal number and Reynolds number with a series in $1/\sqrt{\mathrm{Re}}$. This new expression was found to give a significantly better fit to the data for a circular cylinder and has therefore been used in the present investigation to represent the data for imposed parallel shedding in the wake of a square cylinder. This relationship is determined for the square section as:

$$St = 0.219 - \frac{0.587}{\sqrt{\mathrm{Re}}} - \frac{1.205}{\mathrm{Re}}$$

where the coefficients have been determined using a least squares fit to the data over the Reynolds number range 45 – 165, figure 4.7. Using this expression the absolute error (ε) averaged over all values is found to be $\varepsilon = 0.0003$.

4.3.3 The transition to three-dimensionality.

In similarity with circular cylinders and other bluff sectioned bodies, the wake of the square section cylinder is found to undergo a transition to three-dimensionality with increasing Reynolds number. Within this transition regime both mode – A and mode – B type instabilities have been observed with the wake becoming increasingly disordered with downstream distance. It was also suggested by Robichaux *et al.* (1999) that for Reynolds numbers above 230 the wake would also become unstable at a third intermediate wavelength, although the appearance of this third mode of instability (termed mode – S) was not observed during the present investigation.

From visualisations of the wake in plan view it could be observed that the primary vortices would become increasingly wavy as the Reynolds number was increased above 155. By a Reynolds number of approximately 160 the classical mode – A wake could be observed over part of the cylinder span with the local formation of vortex loops and streamwise vortex pairs. However, in this shedding regime it was possible to determine two different Strouhal frequencies simultaneously in the wake, one associated with the laminar shedding and one associated with the mode – A shedding. The laminar mode of vortex shedding was observed in the wake up to a Reynolds number of approximately 170 after which only the lower Strouhal frequency associated with mode – A shedding could be detected, figure 4.7. For circular cylinders the onset of mode – A is typically determined as the Reynolds number when vortex loops appear in the wake and there is a discontinuous drop in Strouhal frequency. However, the present results suggest that these two events are not coincidental, as there can be a local formation of vortex loops but without an overall drop in shedding frequency. Therefore, in order to avoid confusion the Reynolds number for the onset of mode – A (Re_A) is defined in the present investigation as the point at which laminar shedding (nominally two-dimensional) can no longer be detected in the wake and there is a discontinuous drop in Strouhal number. From the current results this value is found to be in the Reynolds number range 165 – 170 or approximately $Re_A = 167 \pm 2$. Above this Reynolds number, frequency measurements in the wake became increasingly difficult due to the apparent chaotic nature of the flow. Therefore, the values of

Strouhal frequency plotted in figure 4.7 are subject to greater inaccuracy above a Reynolds number of about 170 and hence should only be treated as a guide. A plan view visualisation of the wake in the mode – A regime at a Reynolds number of 185 is included in figure 4.9a.

The mode – A wavelength was determined via direct measurement of the flow visualisation images in a similar manner to Williamson (1996a). However, it had been observed during previous visualisations that the mode – A instability occurred over a broadband of wavelengths and could only be easily measured during the early stages of a run before the formation of vortex dislocations. Therefore to further investigate this range of mode – A wavelengths, the spanwise spacing of over 200 individual vortex loops was measured digitally from 25 separate flow visualisation pictures taken near the start of a run. From these results the mean wavelength of the mode – A instability in the wake of a square section cylinder was determined to be approximately 4.9 base heights. However, when the probability of finding a wavelength within a particular spanwise interval was plotted, the most dominant spacing was found to be in the interval 4.4 – 4.6, figure 4.8. Based upon these results, the mode – A wavelength for a Reynolds number of 185 is determined as $\lambda_A = (4.5 \pm 0.1)h$.

In accordance with circular cylinder flows, no critical Reynolds number was determined for the onset of mode – B but instead a gradual transfer of energy between the two modes was observed as the Reynolds number was increased above a value of about 200. Beyond this value the mode – A vortex shedding was observed to become less intense until at a Reynolds number of approximately 230 where the wake was observed to be in a purely mode – B shedding regime with the appearance of fine scale streamwise vortices in the wake. A plan view visualisation of the wake in the mode – B regime at a Reynolds number of 240 is included in figure 4.9b. The mode – B wavelength was determined directly from flow visualisation images at a Reynolds number of 240 in a similar manner to that used for mode – A. However, the mode – B instability was found to be far more narrow-banded with wavelengths only being

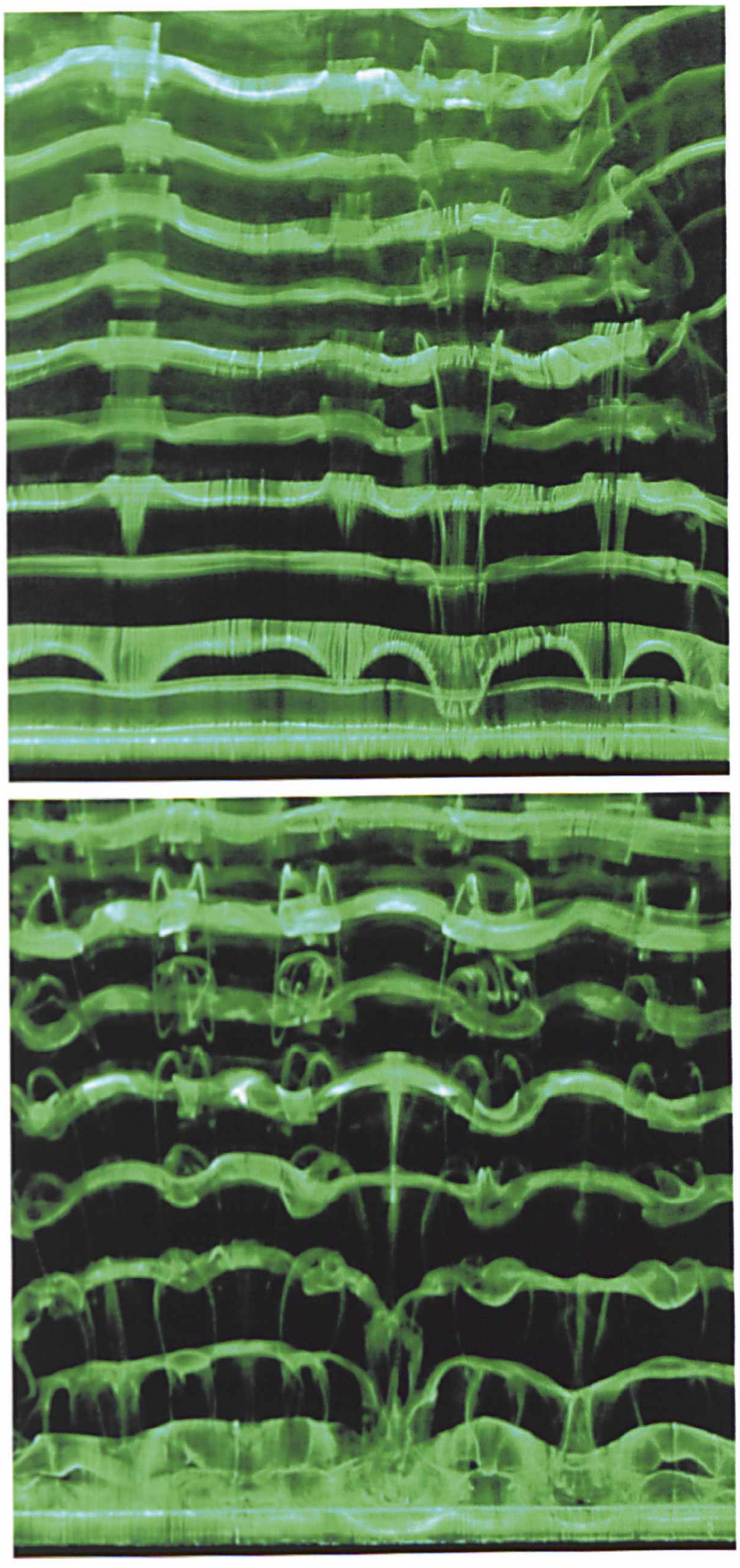


Figure 4.9 Visualisation of the transition modes in the wake of a square section cylinder. (a) Mode – A instability causing the periodic formation of streamwise vortex loops, Reynolds number = 185. (b) Mode – B instability showing the formation of fine scale streamwise vortices, Reynolds number =240.

recorded in the small range of 1.1h – 1.3h. Therefore, due to this small variation in wavelengths it is possible to state the mean wavelength for the mode – B instability with far more certainty as $\lambda_B = (1.18 \pm 0.02)h$.

4.4 Results – Square sections with wavy separation lines.

4.4.1 The effect of increasing wave steepness.

In a continuation of the previous work of Owen (1997) a new series of small wavy square section cylinder models were made to visualise the flow in the wake at low Reynolds numbers. It had been found in the previous investigation that the flow was largely unaffected by changes in Reynolds number and it was anticipated that the features of the wake visualizations at these low Reynolds numbers would persist to higher ones.

Initially flow visualisations were carried out at low Reynolds numbers using the original shorter tow tank. These visualisations were performed using the electrolytic precipitation method described in section 3.2.4 and images were photographed using a digital camera. The pictures presented have been inverted from the originals and can essentially be considered as negatives of the flow. Visualisations in the wake of the wavy models revealed two distinctly different wake structures. Downstream of a peak it was found that a wide wake is formed, with the shear-layers rolling up to produce discrete vortices as they are convected downstream, figure 4.10a. However, downstream of a valley the wake was found to be significantly narrower with two counter-rotating vortices close to the base of the body between the two shear-layers, figure 4.10b. From these results it was possible to confirm that the widths of the wakes downstream of a peak and a valley were distinctly different as originally suggested by Owen (1997).

Once the new tow tank had been commissioned it was possible to conduct a much more detailed study of the wake of the wavy models. The flow in the wakes of the models was visualised using the methyl-blue dye technique (as described in section

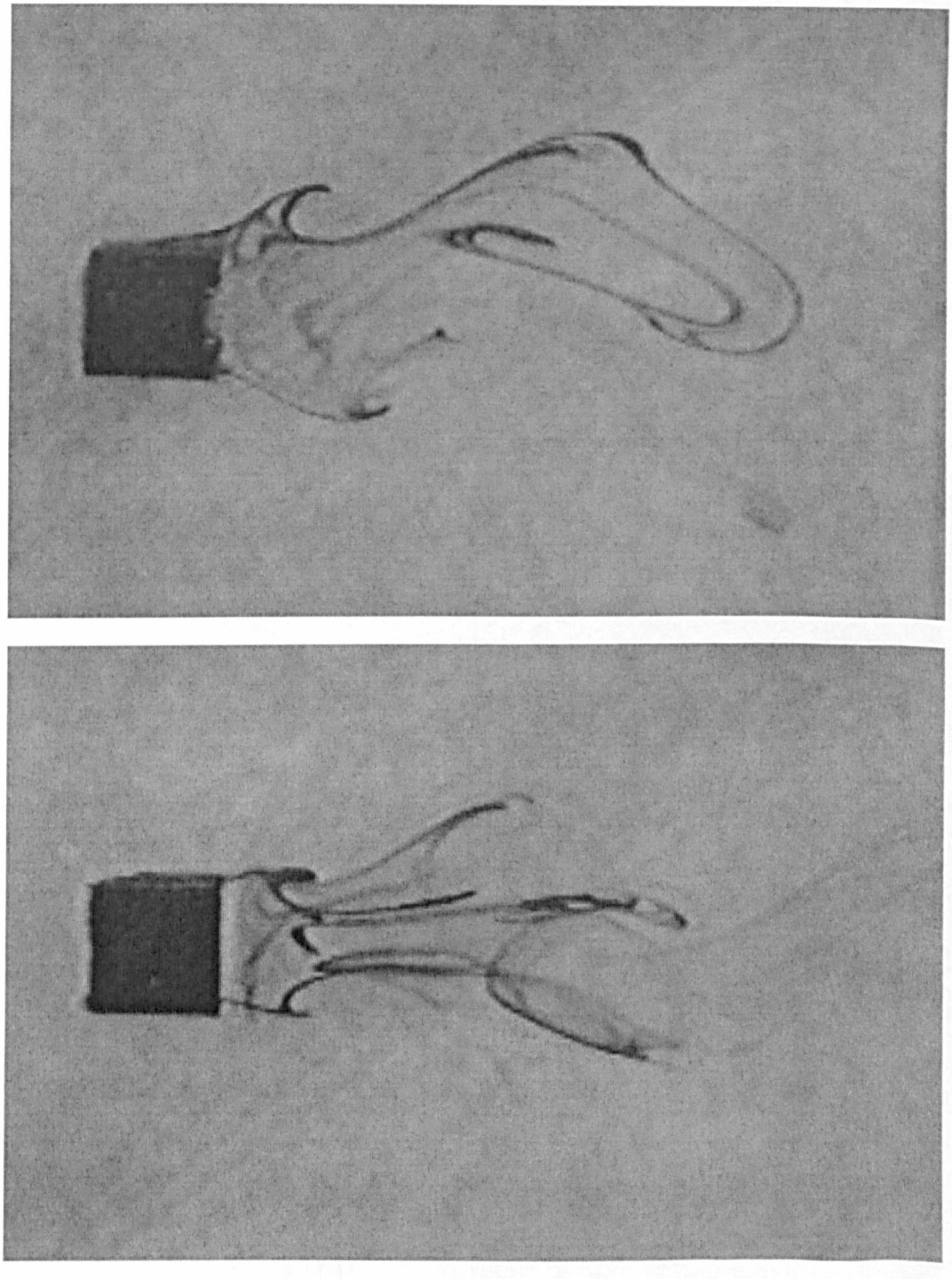


Figure 4.10 Cross-sectional visualisations at different spanwise positions for the model with wave steepness w/L = 0.06: (a), visualisation at the peak showing the wide wake and a previously shed vortex being stretched back into the near wake; (b), visualisation at the valley showing a low intensity symmetrical wake which is observed to be similar in structure to the pre-vortex shedding wake of a square section cylinder, Reynolds number =100.

3.2.4) where a dense blue dye is smeared over the front face of the model and then washed off over the duration of a run. For plan view observations, only one of the shear layers was visualised with dye and this was then back-lit using a powerful light source. All visualisations were conducted at a Reynolds number of 100.

When the wake is subject to a disturbance by means of a wavy separation line, its structure becomes far more three-dimensional. In figure 4.11, the leading edge of the square section model is subject to a wavy separation line of wave steepness 0.02. At this low level of wave steepness cross flow visualisations of the wake confirm that Kármán vortex shedding is still the dominant mechanism present in the wake with the vortices being shed approximately parallel to the cylinder. However, it is also apparent from the figure that the vortices in the wake of the wavy cylinder are subject to a three-dimensional spanwise instability that causes the generation of vortex loops in the near wake. This visualisation shows immediate similarities with the wake of the square section cylinder observed in figure 4.9a at a Reynolds number of 185, wherein the cylinder is in the mode – A regime, although it should be noted when making comparisons that both sides of the wake are visualised in figure 4.9a. Hence, it would appear that the presence of low levels of spanwise waviness leads to the formation of a wake similar to that of mode – A.

However, for values of wave steepness in excess of approximately 0.04 Kármán Vortex shedding is no longer seen with vortices forming in individual free shear layers. The picture presented in figure 4.12 is of a model with $w/L = 0.06$ and is a single frame captured from a video produced of the wake. From this video it was observed that the vortices form in the shear layers and are convected downstream with the flow. At approximately four base heights downstream of the trailing edge, the vortex is rapidly distorted into a regular spanwise pattern of hairpin vortices. This leads to the formation of streamwise vortex pairs downstream of the peaks, figure 4.12. As the vortex travels downstream, the spanwise vorticity is rotated and stretched into streamwise vorticity before the vortex eventually breaks up forming a chaotic pattern of vortex filaments in the far wake. This cycle of vortex formation and destruction

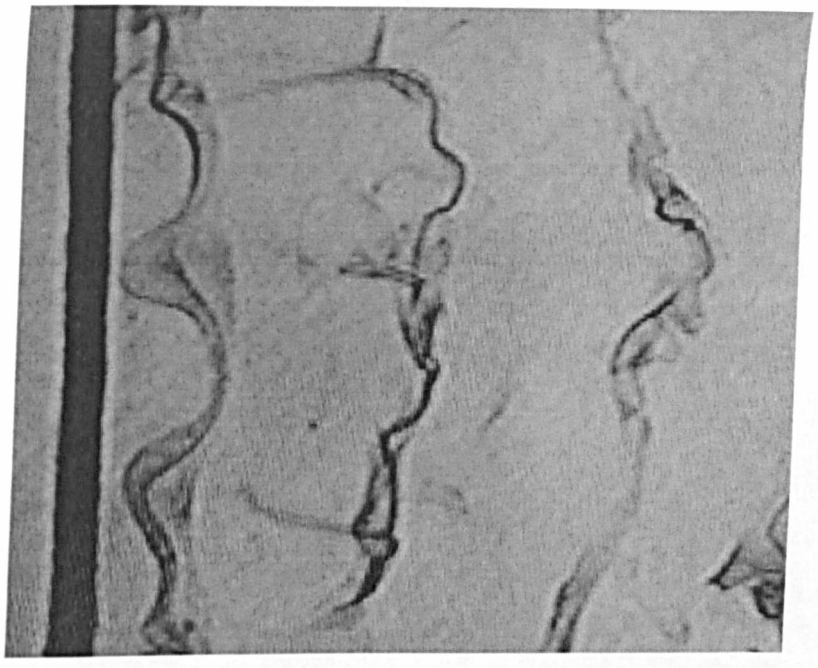


Figure 4.11 Plan view visualisation in the wake of a wavy square cylinder model with very low wave steepness (w/L = 0.02). This small level of wave steepness is observed to cause the early onset of mode – A at a Reynolds number of 100. Spanwise wavelength = 6h.



Figure 4.12 Flow visualisation picture of the wakes of the wavy square cylinder model (w/L = 0.06), showing the large-scale spanwise instabilities in the primary vortices, Reynolds number = 100.

repeats periodically in the wake of the body. However, this wake structure should not be mistaken for the mode – A wake as at this value of wave steepness true Kármán vortex shedding has ceased.

Further insight into the wake structure can be gained from a comparison of cross-flow visualisations taken downstream of the geometric peaks and valleys. Figure 4.10a. shows such a visualisation taken downstream of the geometric peak. From the figure, it can be observed that the wake at this spanwise position is significantly wider than for conventional vortex shedding and there is little evidence of the classic von Kármán Vortex Street (figure 4.1a). The vortices evident in the wake would appear to be shear layer vortices similar in type to the vortices found in the wake when a splitter plate is fitted and where the shear layers are free to roll-up independently without interaction. However, at approximately four base heights downstream these vortices become caught up in the upstream flow along the centre wake and are consequently stretched back into the near wake and the next forming vortex. For this intermediate level of wave steepness, this cycle of vortex convection and stretching is found to be a dominant mechanism in the wake downstream of a geometric peak.

Downstream of a geometric valley the wake is found to be narrow and shares many similarities with the pre-vortex shedding wake observed in the wake of the square section cylinder, figure 4.6a. In this spanwise location two small symmetric vortices are periodically shed into the wake which are observed to slowly dissipate as they are convected downstream, figure 4.10b.

If the wave steepness is increased to w/L = 0.10, the flow in the wake becomes organised into a more regular three-dimensional structure. If the wake is visualised in cross-flow downstream of a geometric peak a symmetrical wake structure is observed, figure 4.13a. However, unlike for the intermediate levels of wave steepness, the vortices are no longer stretched back into the near wake at four base heights downstream due to the increased width of the wake. This results in a reversal in direction, in which the vortices deform along the span with vortex loops now being

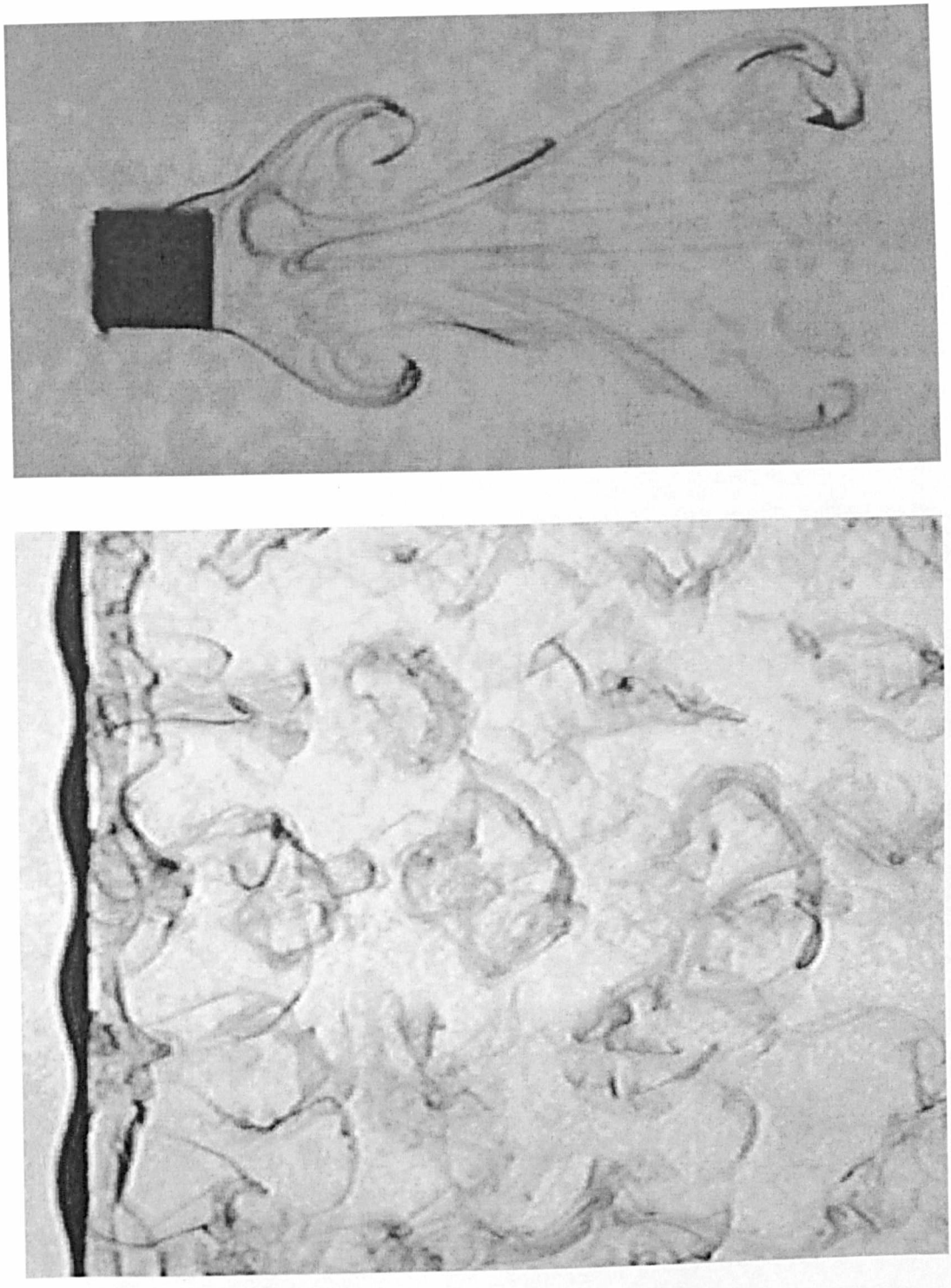


Figure 4.13 Flow visualisation pictures for the model of wave steepness w/L = 0.1: (a), a cross sectional visualisation at the peak showing the wide symmetrical wake and the periodic rolling-up of vortices in the shear layers; (b), plan view of the wake showing a complete lack of conventional von Karman vortex shedding characteristics.

generated downstream of the peaks. This reorganisation of the wake is visualised in the plan in figure 4.13b. Another striking feature of the wake at this high level of wave steepness is the low intensity of dye in the regions downstream of the valleys. As explained previously, the dye was evenly released from the front face of the body and hence gives a good indication of the motion of vorticity generated on the surface of the model. From this it would appear that at this level of wave steepness a large portion of spanwise vorticity is being diverted away from the regions downstream of the valleys and into the regions downstream of the peaks. Therefore it is not surprising that regular Kármán vortex shedding is suppressed, as the spanwise vorticity would appear to be discharged into the wake through small cells downstream of the peaks, thus preventing the correlation of large-scale spanwise vortices.

4.4.2 The effect of a splitter plate on the drag of a wavy rectangular section body.

Computations by Darekar & Sherwin (private communication 1999) had highlighted the existence of vortical structures in the near wake that crossed the centre wake, which they believed to be important in the formation of a steady wake. It was uncertain whether these structures would be important at higher Reynolds number but it was thought that if they were, then they could probably be disrupted by the introduction of a splitter plate into the near base region. Hence would the flow over a wavy body remain unchanged when the wake was divided along its centre?

Initially the drag measurements of the wavy models were made (as described in section 3.4.2) in a wind tunnel at a Reynolds number of 50,000 and the variation of drag with wave steepness plotted in figure 4.14. It was found that despite the small differences in wavelength and Reynolds number, the models showed an almost identical variation of drag with wave steepness to the models of Bearman & Owen (1998a). Based on this comparison it would appear that at high Reynolds numbers the wavelength of the geometric disturbance is not as sensitive as found at lower Reynolds numbers by Darekar & Sherwin (2001).

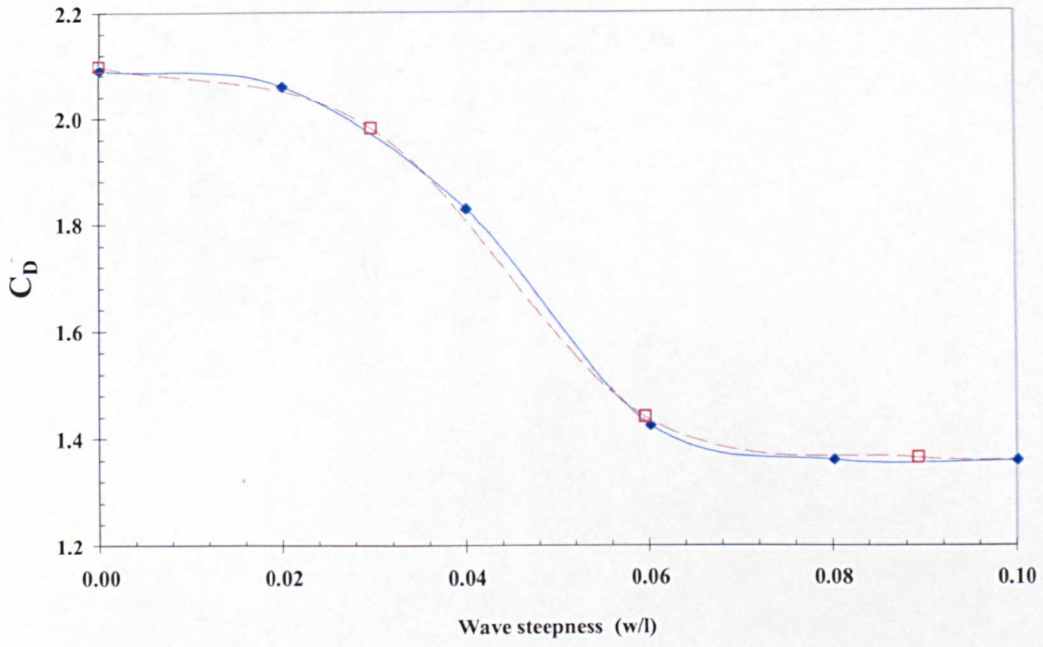


Figure 4.14 The effect of wave steepness on the drag of a wavy square section cylinder: ♦, present results, Reynolds number = 5×10^4; , Bearman & Owen (1998a), Reynolds number = 5×10^4.

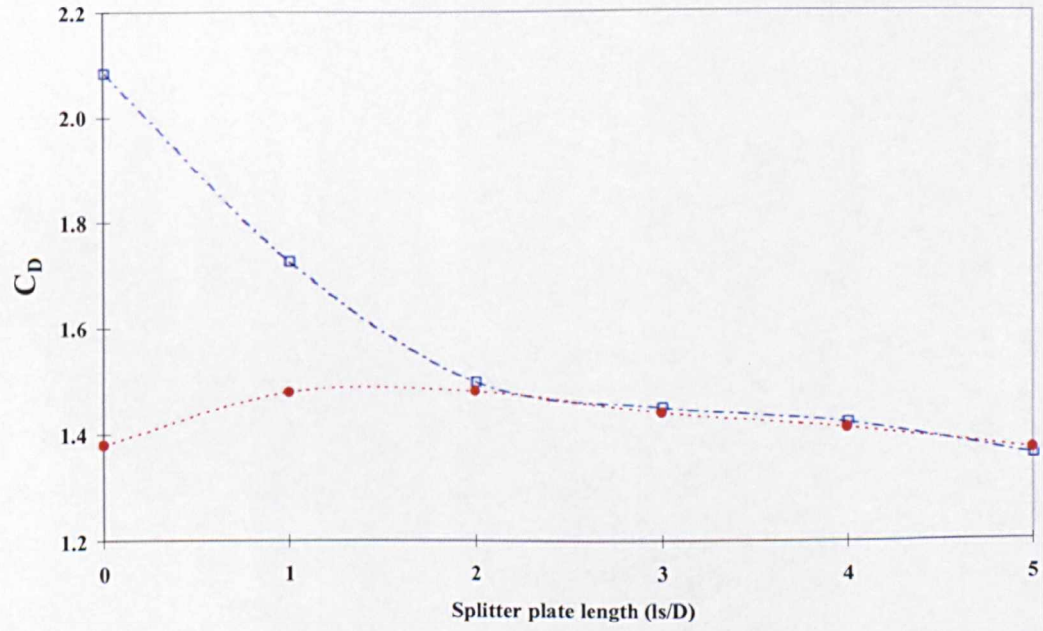


Figure 4.15 The effect of splitter plate length (l_s) on drag: , square section cylinder; •, wavy square section cylinder (w/L = 0.10). Reynolds number = 5×10^4.

The drag characteristics of two of the models fitted with splitter plates of varying lengths were then investigated. Initially, the drag variation of a square section cylinder fitted with splitter plates ranging in length from 1h – 5h was investigated. With no splitter plate fitted, the drag of the body was found to be approximately C_D = 2.1. However, the introduction of a splitter plate of only 1h in length was found to cause a substantial reduction in drag with the drag falling to a value of less than C_D = 1.7, figure 4.15. An increase in the length of the splitter plate to 2h caused a further drop in drag to a value of less than C_D = 1.5 with the drag levelling off to a value of approximately C_D = 1.4 as the splitter plate was increased in length up to a value of 5h. This led to an overall drag reduction for the square section of approximately 33% which was found to be in good agreement with a similar reduction determined by Arie & Rouse (1956) for a normal flat plate fitted with a long splitter plate.

Splitter plates were then fitted to the wavy model with wave steepness w/L = 0.10. This model was chosen for further investigation because as it can be seen from the flow visualisations in the previous section, this model was observed to have the most symmetric wake. Therefore, it was expected that this model exhibited the least communication between the opposite shear layers and would hence be the least disrupted by the presence of a splitter plate. The effect of the splitter plate on this wavy model is plotted in figure 4.15. With no splitter plate fitted the drag is found to be less than C_D = 1.4. However, the introduction of a splitter plate only 1h in length actually causes an increase in drag to C_D = 1.5. For an increase in splitter plate length to 2h, no additional increase in drag is found, although the drag is now found to be at a similar value to that for the square section cylinder fitted with a splitter plate. Beyond this value it would appear that the splitter plate in the wake becomes the dominant effect with the drag reducing back to its original value of below C_D = 1.4 at the same rate as for a square sectioned cylinder, figure 4.15.

4.5 Discussion.

4.5.1 Square section cylinders.

In circular cylinder flows, the critical onset Reynolds number for vortex shedding has been the subject of both experimental and computational investigations and as a result has been determined to be approximately $Re_{crit} = 47$. However, there is far more uncertainty about this value for square section flows with the critical Reynolds number found to vary in the range of $Re_{crit} = 36$ to $Re_{crit} = 53$, figure 4.16. From the table in figure 16 it can be seen that the lowest value for the onset of vortex shedding of $Re_{crit} = 36$ was determined experimentally by Gerrard (1978). However, despite attempts, it was not possible during the present investigation to observe vortex shedding at this Reynolds number and it is thought that this low value was probably caused as a result of oblique shedding and low aspect ratio. Norberg (1996) also performed an experimental investigation into the wake of a square section cylinder and found the critical onset to be considerably higher at a value of $Re_{crit} = 47 \pm 2$. The aspect ratio in this case was 200, although few other details of experiments are available and it would be difficult to determine any reason for the difference in onset value in comparison with the present results.

In 2D simulations, computations are unaffected by aspect ratio or oblique shedding and this tends to lead to a higher value of onset. Sohankar *et al.* (1998) predicted the onset Reynolds number for vortex shedding to be 52 using the linearized Stuart-Landau equation. Their method involved calculating the instantaneous growth rate of the instability and plotting it against Reynolds number at values close to the critical onset for vortex shedding. The critical Reynolds number could be then determined by simply extrapolating this trend back to a point at which the instantaneous growth rate was found to be zero. This value was then confirmed by simulations in which the cylinder was impulsively started from rest at a Reynolds number of 50. Initially vortex shedding was detected in the wake due to the starting process but this was found to decay in time whereas simulations at a Reynolds number of 55 showed the development of the classical vortex shedding wake. Therefore, it is possible that the

Author	Onset of Vortex shedding	Strouhal number at Re =100	Onset of Mode - A
Gerrard (1978) *	36	0.142	...
Present results *	41 ± 1	0.148	167 ± 2
Darekar (2001)	43 ± 1	0.146	160 ± 5
Norberg (1996) *	47 ± 2	0.145	150
Sohankar et al (1998)	52	0.146	150 - 200
Kelkar & Patankar (1992)	53	0.13	...
Robichaux et al (1999)	...	0.154	162 ± 12

Figure 4.16 Comparison of results from various authors for the square section cylinder showing the variation in value of onset Reynolds number, Strouhal number & transition to three-dimensionality. Experimental results *.

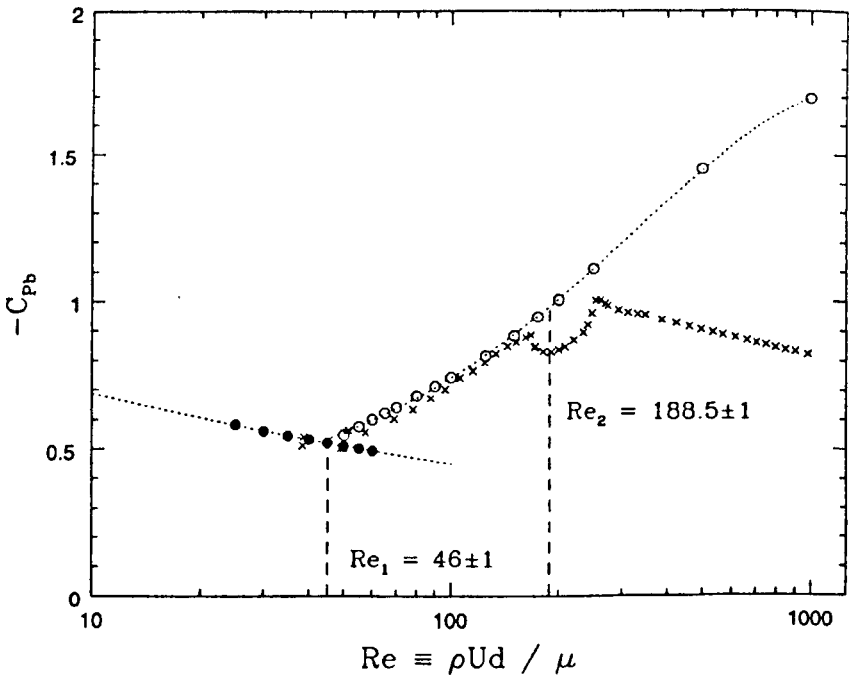


Figure 4.17 Variation of base pressure with Reynolds number for a circular cylinder at low Reynolds numbers showing hysteresis in the value of Reynolds number for the onset of vortex shedding, Henderson (1995).

critical Reynolds number is in fact higher than determined in the present investigation and that small perturbations in the experimental system could have been responsible for this lower value of $Re_{crit} = 41$.

However, Henderson (1995) showed for circular cylinders that the onset of vortex shedding is not a fixed value but is subject to hysteresis depending on whether the Reynolds number is being increased or reduced. It was found that if the Reynolds number was gradually increased the critical onset of vortex shedding could be delayed until a value of almost 60 followed by a sharp transition into the vortex shedding mode. However, if the Reynolds number was then gradually reduced from this value, vortex shedding could be observed down to a Reynolds number of 46 ± 1, figure 4.17. Therefore, it is possible that the value determined by Sohankar *et al.* (1998) is in fact higher than what would be conventionally regarded as the onset of vortex shedding due to a similar hysteresis in the value of onset for a square section cylinder.

The presence of this hysteresis in square section flows was investigated in the present investigation by over speeding the cylinder run by approximately 10% at the start of a run (for approximately 150h). However, it was found that this procedure only had a limited effect on the onset value, reducing it to only $Re_{crit} = 40$, which is within the range of experimental uncertainty stated for the original value of 41 ± 1. A similar level of hysteresis in the value for the critical onset of vortex shedding was also observed by Darekar (2001) using 2D DNS computations. When the simulation was started from a vortex shedding state and the Reynolds number gradually reduced until the wake became stable, the critical Reynolds number was found to be $Re_{crit} = 43$. However, in contrast to Henderson (1995) it was found that the onset of vortex shedding in the wake of a square section cylinder could only be delayed to a value of $Re_{crit} = 44$ if the simulation was started from a steady state. Therefore, although hysteresis in the onset Reynolds number for vortex shedding has been shown, it would appear too small to account for the differences in previous experimental and computational values.

As explained in section 4.3.2, the square cylinder essentially exhibits three flow regimes at low Reynolds number, figure 4.18. Initially the flow is attached around the front corners and separates from the trailing edge. In this regime (Reynolds number = 41 – 115) the rate of increase in the Strouhal number with Reynolds number is found to be approximately equal to that of a circular cylinder. It is found that within this regime the value of Strouhal number for a square section is approximately 10% lower than the corresponding value for a circular cylinder at the same Reynolds number. Hence, it is possible to approximate the Strouhal number for a square section cylinder (St_{sq}) as:

$$St_{sq} \approx 0.905 St_{cc}$$

where St_{cc} is the Strouhal number for a circular cylinder at the same Reynolds number. Alternatively by multiplying the variation of Strouhal number with Reynolds number for a circular cylinder (from Williamson & Brown 1998) by a factor of approximately 0.89, the variation of Strouhal number with Reynolds number for a square section cylinder can be expressed as:

$$St_{sq} \approx 0.258 - \frac{1.258}{\sqrt{\mathrm{Re}}} + \frac{1.635}{\mathrm{Re}}$$

This variation of Strouhal number versus Reynolds number is plotted in comparison with the parallel shedding data for the square in figure 4.18. From the figure it can be seen that the above expression gives a good fit to the data up to a Reynolds number of approximately 110 above which, the two curves diverge as the cylinder enters the next flow regime.

In the second regime, the flow separates from the leading edge above a Reynolds number of about 115 but then reattaches a short distance downstream forming two separation bubbles. From figure 4.18 it is apparent that the Strouhal number is no

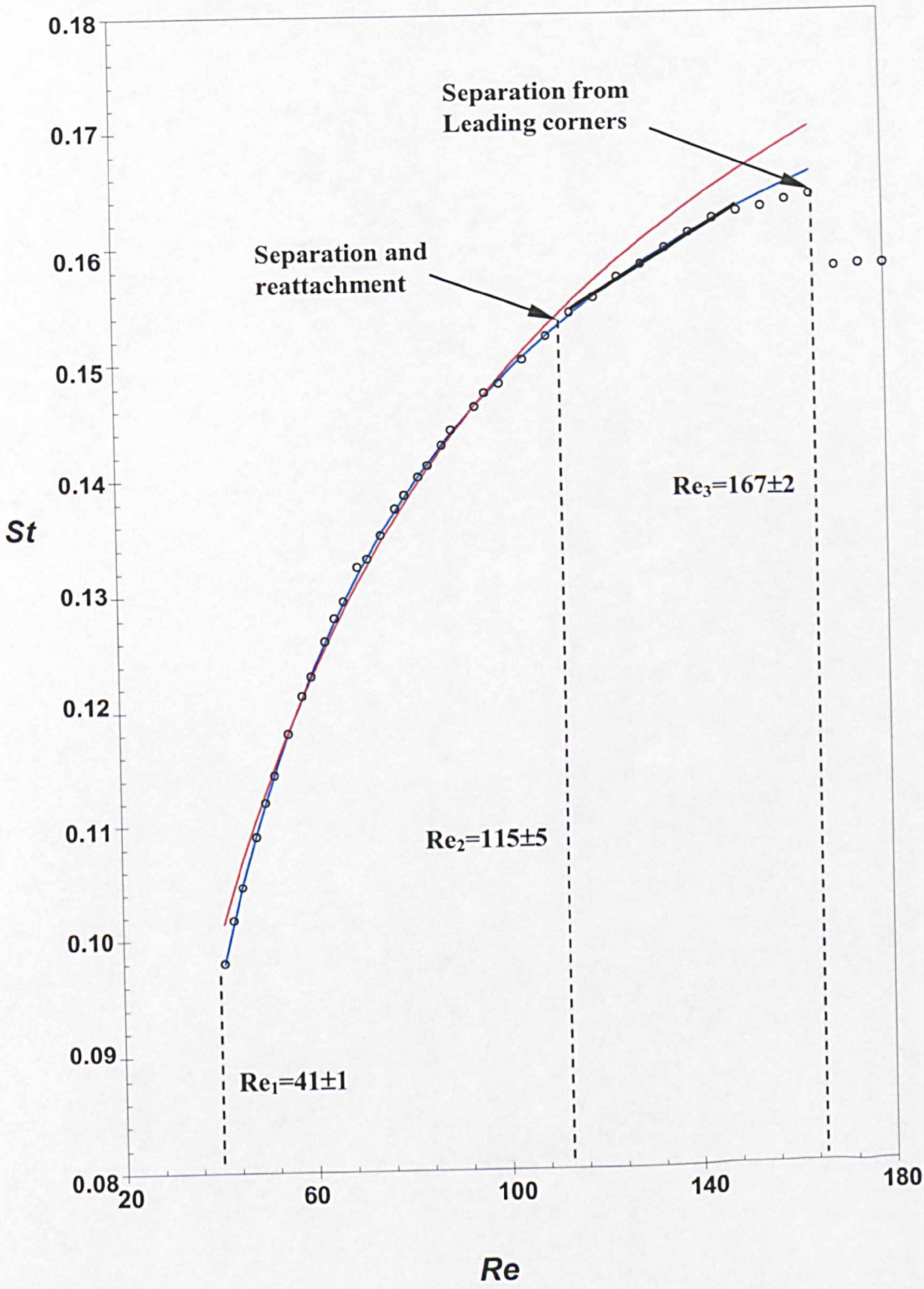


Figure 4.18 Flow regimes at low Reynolds numbers in the wake of a square section cylinder: o, square section parallel shedding; ---, $St = 0.219 - 0.587/\sqrt{\mathrm{Re}} - 1.205/\mathrm{Re}$; ---, $St \approx 0.905 St_{ee}$; ---, $St = 0.1249 + \mathrm{Re}/3921$. Re_1, onset of vortex shedding in the wake; Re_2, critical Reynolds number of the separation – reattachment regime; Re_3, separation from the leading corners and the onset of mode – A.

longer increasing with Reynolds number at the same rate as for a circular cylinder due to the continually changing flow characteristics caused by the growing separation bubbles. This results in an almost linear variation of Strouhal number with Reynolds number throughout this regime, with the two separation bubbles continuing to grow in size with increasing Reynolds number. This linear variation can be expressed for this regime as,

$$St = 0.1249 + {}^{\mathrm{Re}}/_{3921}$$

In the final regime the flow separates from the upstream corners of the square but only reattaches to the sides periodically during the shedding cycle. As the Reynolds number is increased the separation into the wake is predominately from the upstream corners until above a Reynolds number of approximately 165 where the flow fails to reattach. It would be expected that this change in separation point would lead to a discontinuous change in the value of Strouhal number and this can be seen from figure 4.18 as a corresponding drop in the shedding frequency. However, it is unclear whether this drop in shedding frequency is as a result of the movement of the separation point, the transition to three-dimensionality or a combination of both.

The transition to three-dimensionality in the wake of a circular cylinder has been considered in great detail, although recently the transition in the wakes of other bluff bodies has also been considered. Hourigan & Thompson (2000) showed that the transition to three-dimensionality by the onset of mode – A occurs at a Reynolds number of approximately 270 in the wake of a semi-ellipse body. At a higher Reynolds number the existence of a mode – B wake was also observed. For a thin normal plate Bearman (1997) has suggested that this transition to three-dimensionality may occur at a Reynolds number as low as 60, although no detailed investigation has been performed to confirm this. In the present investigation the transition to three-dimensionality for a square section is found to occur at a Reynolds number of 167 ± 2 which is approximately confirmed by the value of Robichaux *et al.* (1999) of 162 ± 12. However, this value of transition is almost coincidental with the

observed movement of the separation point from the downstream corners to the upstream corners (figure 4.18) and it is possible that this movement affects the transition Reynolds number. With the flow reattaching to the sides of the square and separating from the downstream corners the wake is similar in character to that of the circular cylinder and semi-ellipse section of Hourigan & Thompson (2000). In this configuration it would be expected that the separation velocity would be lower and that the transition Reynolds number would be higher. However, when the flow separates from the upstream corners as in the case of a normal plate, it would be expected that the separation velocity would be higher and hence the transition Reynolds number lower. Therefore, this movement in separation point may effectively cause the flow to switch to the wake of a normal plate leading to the immediate onset of mode – A. In the absence of detailed data on the transition in the wake of a normal plate, this explanation remains purely hypothetical.

4.5.2 Wavy cylinders.

At low Reynolds numbers and at low levels of wave steepness (less than 0.03), the wake is observed to show similar characteristics to the wake of a square section cylinder in the mode – A regime, figure 4.11. It is observed that the dominant structures in the wakes of these mildly wavy bodies are Kármán vortices but these are found to deform locally downstream of the peaks forming vortex loops. These vortex loops are then stretched into streamwise vortex pairs in a similar fashion to the mode – A regime. This behaviour was also observed by Darekar & Sherwin (2001) who suggested that at low Reynolds number this mild spanwise waviness triggered the early onset of mode – A in the wake. By investigating the effect of spanwise wavelength for a constant wave steepness, they found that vortex shedding could be suppressed in the wake with a minimum amount of wave steepness at a spanwise wavelength close to that of the mode – A, of approximately 5.6h, figure 4.19. Although, the mode – A wavelength for a square section cylinder has been determined in the present investigation as approximately $4.5h \pm 0.1$ and by Robichaux *et al.* (1999) as 5.07h. However, despite this difference in wavelength it is still possible that

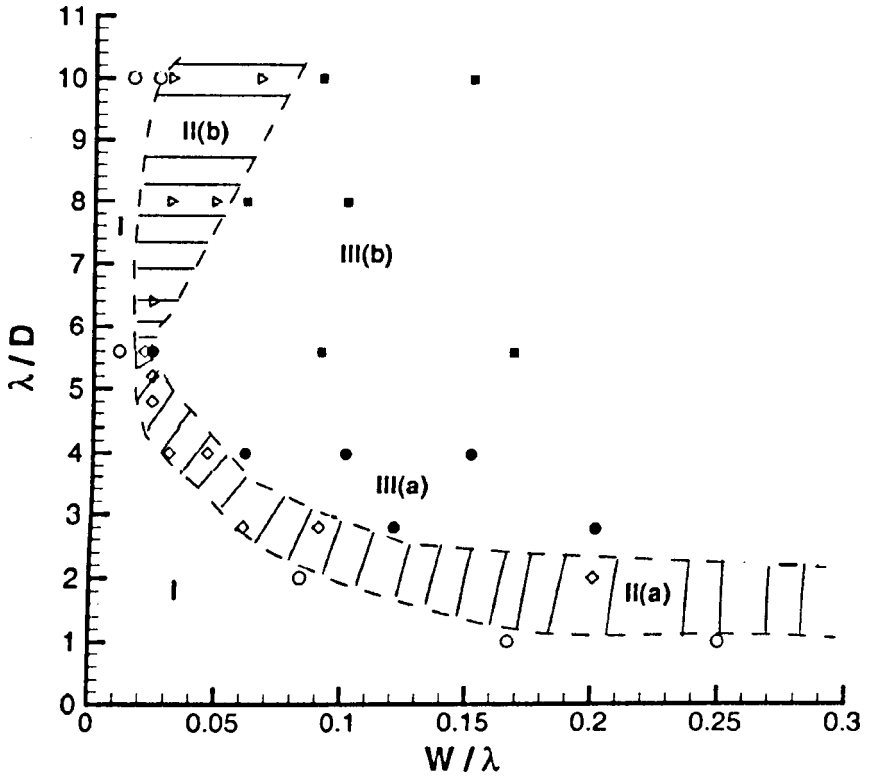


Figure 4.19 Parameter space plot for wavy square section cylinders showing the effect of non-dimensional wavelength on the required wave steepness to suppress vortex shedding in the wake, Darekar & Sherwin (2001). Solid symbols represent where vortex shedding is suppressed, open symbols where vortex shedding is disrupted but not suppressed.

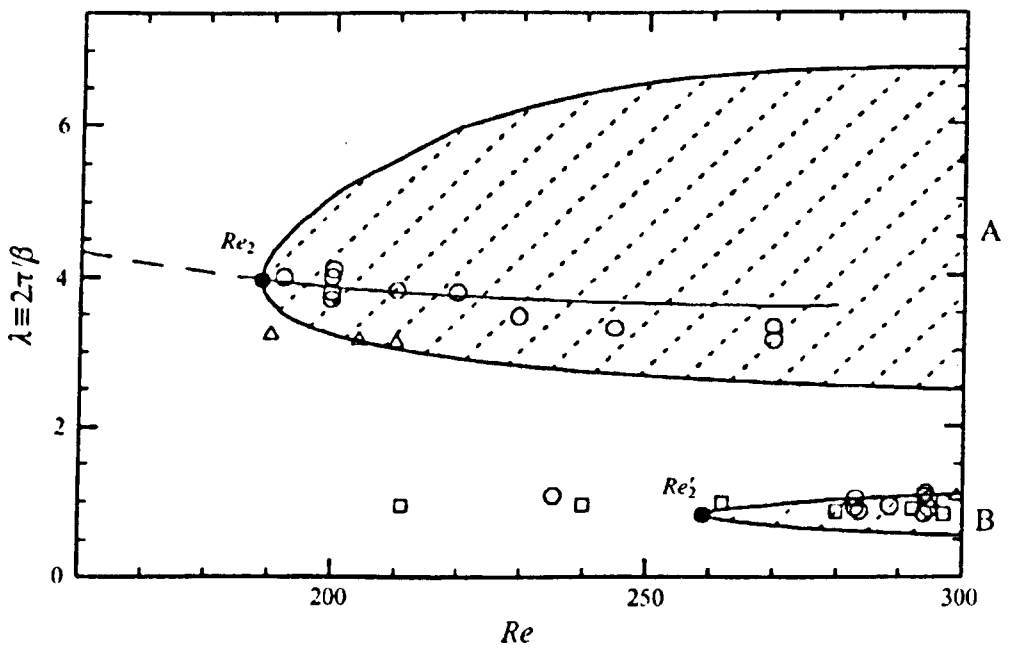


Figure 4.20 The range of unstable wavelengths in the wake of a circular cylinder versus Reynolds number, Barkley & Henderson (1996). Solid line illustrates the most unstable Mode – A wavelengths and data points are from experiments of Mansy et al (1994) & Williamson (1996a)

the wavy body may be responsible for an early triggering of mode – A transition, as the wavelength of mode – A may be nearer to 5.6h at Reynolds number of 100. For circular cylinders, Barkley & Henderson (1996) have demonstrated that the mode – A wavelength increases with reducing Reynolds number, figure 4.20. Therefore, it is likely (given all the similarities between circular cylinder and square cylinder wakes) that the mode – A wavelength for a square section cylinder will also increase towards the value of 5.6h with reducing Reynolds number. Also, as discussed in the previous section, at a Reynolds number of 100 the wake topology is significantly different to that at the natural onset of mode – A (Reynolds number = 167) with the flow reattaching to the sides before separating from the downstream corners. It is therefore possible in this different flow regime that an alternative wavelength may be dominant.

A further similarity with mode – A is demonstrated in figure 4.20. In the figure the stability plot for circular cylinders from Barkley & Henderson (1996) can be compared with the parameter space plot from Darekar & Sherwin (2001) for wavy square section cylinders, figure 4.19. On the horizontal axes are Reynolds number and wave steepness (w/L), which in both instances can be regarded as intensity of three-dimensional perturbations. On the vertical axes are the wavelength of the instability, which in the case of the wavy body is a forced wavelength. The two plots show many similarities and it can be seen that the regular two-dimensional Kármán vortex shedding becomes unstable over a broader band of wavelengths as the intensity of three-dimensional perturbations is increased. A further similarity in the two plots is that for a given intensity of perturbation both wakes are more receptive to higher rather than lower wavelengths. However, it should be noted that the two sets of data are for bodies of different cross-section and it should not be expected that the wavelengths between the two plots should agree. This figure simply shows the possible link between Reynolds number and wave steepness as a source of three-dimensional perturbations at these low Reynolds numbers and it would be interesting to compare data from similar bodies to see whether the wavelengths agree.

At higher Reynolds numbers, these low levels of wave steepness are not found to be particularly successful at reducing drag or suppressing vortex shedding, with a value of w/L = 0.06 needing to be exceeded before vortex shedding is suppressed. Also, at these higher Reynolds numbers the flow seems almost unaffected by small changes in wavelength or Reynolds number, as a comparison between the present data and the data of Bearman & Owen (1998) shows almost perfect agreement, figure 4.14. However, whilst the importance of wavelength at higher Reynolds number is yet to be determined, it is expected that there will still be an optimum wavelength for the suppression of vortex shedding with minimal wave steepness. This is because as the wavelength tends to zero the waviness will effectively become surface roughness, whereas if the wavelength tends to infinity there will effectively be a large areas of two-dimensional flow (such as downstream of the peaks and valleys) where vortex shedding can be expected to occur.

Whilst much insight into the near wake dynamics has been gained at low Reynolds number through the use of flow visualisations and simulations (Darekar & Sherwin 2001), there still remains a large gap in our knowledge at higher Reynolds numbers. For example, the effect of introducing a small splitter plate into the essentially symmetric wake of a wavy body ~~should~~ increase in drag ~~are~~ is particularly unexpected. In this instance it is unclear how the splitter plate disrupts the low-drag three-dimensional wake to cause a small increase in drag, although it can be concluded that any communication between the opposite sides of the wake only plays a small part in the overall disruption of vortex shedding. Whilst there still remained a vast amount of work that could be conducted on wavy square section flows, attention was now diverted to the study of wavy circular cylinders with a constant circular cross-section but with a sinusoidal axis. It was found that these bodies produced almost identical characteristics to the wavy square section bodies and ultimately led to an explanation as to why wavy square section cylinders and other wavy bodies were so effective in the suppression of vortex shedding. This research highlighted the importance of the leading edge geometry in addition to separation line as the fundamental components

in the disruption and suppression of vortex shedding. Further details can be found in chapter 5.

4.5.3 Experimental Errors.

Throughout the study of wavy squares section cylinders attempts were made to keep experimental inaccuracies to a minimum. However, all experimental measurements are subject to some amount of error and the magnitude of this error on the present results needs to be quantified.

Errors in Reynolds number can be attributed to four sources, inaccuracies in carriage speed and model base height, and variations in water density and viscosity. Errors in carriage speed are found to be extremely small due to the highly accurate towing tank facility used in these experiments and a conservative estimate of the inaccuracy in carriage speed would be $\pm 0.125\%$. Errors in model dimensions were also found to be extremely small. As described previously, models were fine-surface ground to a size 4.75mm and this was found to be constant to within ± 0.01mm across the span, resulting in an error in base height of less than 0.25%. Variations in water viscosity come about due to variations in water temperature and this was compensated for by measuring the water temperature prior to a run using a digital thermometer that was accurate to ± 0.1°C. However, this limited accuracy in the water temperature results in an error in water viscosity of approximately 0.3%. Variations in water density were harder to quantify and were not corrected for prior to a run. The sodium fluorescein used for flow visualisation is essentially a soluble salt and has the effect of increasing the water density, although several subsequent measurements have shown this to have little effect on the density in the concentrations used. The water in the towing tank was also regularly changed which introduced the possibility of long-term variation in the density of the tap water although no variation could be detected between random samples and hence the density was always assumed constant. Although it was not possible to accurately determine this variation in density, a conservative estimate of

the error would be about $\pm 0.25\%$. This results in an overall error of calculated Reynolds number less than 1%.

The inaccuracy in Strouhal number was mainly as a result of the limited number of cycles available for frequency measurements to be made from. Typically measurements would be made over 100 cycles for parallel shedding and 50 cycles for oblique shedding and could be determined from the video to within ± 0.025 shedding cycles. This results in an overall error in Strouhal number of 0.5% for parallel shedding and 1% for oblique shedding, where the timing device used to measure the period of shedding is assumed to be free from any significant error. Subsequent experiments have shown that in general parallel shedding data is repeatable to within 0.25% whilst oblique shedding data is only repeatable to within about 1.5%.

Errors in wind tunnel measurements of drag where typically of the order of 0.5% between repeats with the balance accurate to within 0.1% in drag. Further details of the accuracy and set-up of the wind tunnel experiments can be found in section 3.4.

5 Flow in the wake of sinuous circular cylinders.

5.1 Introduction.

5.1.1 Flow in the wake of a vibrating cable.

During the research into wavy square cylinders (Bearman & Owen 1998a) it was discovered that Professor Albin Szewczyk (from the University of Notre Dame, USA) was undertaking a similar type of investigation into the flow in the wake of wavy circular section cylinder. This research had been stimulated as a result of the then recent publication of Newman & Karniadakis (1997) into the flow around a freely vibrating cable. In this work it was shown that a circular cross-section cable vibrating transverse to the flow in the form of a standing wave would show two distinctly different wake structures between the spanwise positions of a node and anti-node. At an anti-node the wake structure was found to be similar to that of Kármán type vortex shedding with large scale spanwise vortices being periodically shed into the wake from alternate sides of the cylinder, figure 5.1a. However, at a node Kármán type vortex shedding was suppressed in the wake and replaced by a new structure consisting of symmetric pairs of small-scale vortices shed at frequency approximately twice that of the frequency of vibration, figure 5.1b. This structure at the node was of particular interest because it was symmetric and hence exerted no alternating side force on the cable at that spanwise location. Therefore, to study this phenomenon further, Szewczyk constructed several cylinder models that were deformed into the shape of a sinusoid in order to investigate the nature of the flow in the wake under the simplifying assumption of quasi-steady flow.

5.1.2 Flow in the wake of a sinuous cylinder.

Initial investigations were performed with the sinuous cylinders orientated similar to Newman & Karniadakis with the plane of the sinusoid normal to the freestream flow, although in this orientation Kármán type vortex shedding was found to be largely unaffected, Szewczyk (1998). However, when the cylinders were orientated inline with

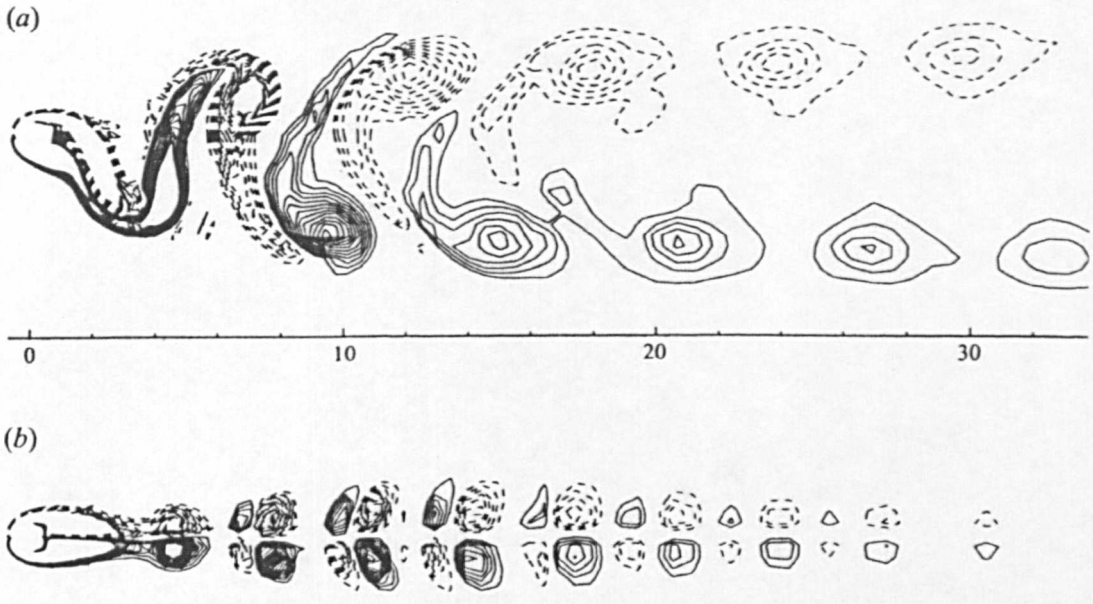


Figure 5.1 Vorticity contours showing the flow in the wake of a cable vibrating in a standing wave mode at a Reynolds number of 100, Newman & Karniadakis (1997): (a), flow in the wake downstream of an anti-node; (b), flow in the wake downstream of node.

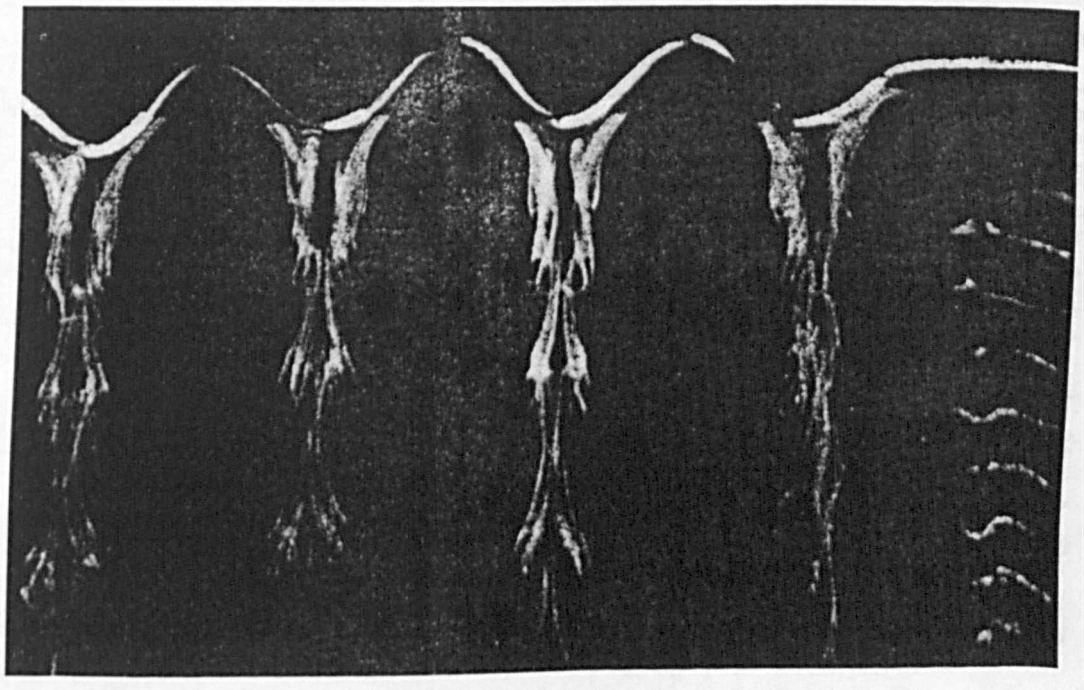


Figure 5.2 Flow in the wake of a distorted cylinder at a Reynolds number of 72, Honji & Ishi (1976). Regular vortex shedding can be seen to the right of the figure where the cylinder is straight but this is replaced with large streamwise vortices where the cylinder is distorted. Cylinder wavelength $\lambda = 12.8D$ and cylinder wave steepness $w/\lambda = 0.344$ where w is the peak to peak wave height of the cylinder.

the freestream flow (flow was in the plane of the sinusoid) the wake structure was found to be dramatically altered. Flow visualisation in a water tunnel at a Reynolds number of approximately 10^3 showed that conventional Karman type vortex shedding was suppressed and revealed large differences in wake widths across the span. A narrow wake was observed where the body extends furthest upstream (geometric peak) whilst a wide wake was observed downstream of a geometric trough. Whilst the wide and narrow wakes showed similarities with the wake of the vibrating cable of Newman & Karniadakis, it was evident that a different type of wake structure was present, Szewczyk (1998). The cylinder used during these visualisations had a wavelength of 6D and a wave steepness of $w/\lambda = 0.167$, where w is defined as the peak to peak wave height and λ is defined as the wavelength of the sinuous cylinders.

However, the first work on sinuous or deformed cylinders was performed at low Reynolds numbers by Honji & Ishi (1976). Using the lead precipitation method of flow visualisation and a cylindrical model deformed into the shape of a sinusoid (λ = 12.8D and $w/\lambda = 0.344$) they found a significant departure from the regular vortex shedding in the wake. Figure 5.2 shows a plan view of the wake visualised at a Reynolds number of 72. From the figure it can clearly be seen that vortex shedding is completely suppressed downstream of the sinuous portions of the model and that a new structure of interconnecting vortex loops has been developed. It can also be seen that the vortex loops are found to be in phase with each other between neighbouring cells. However, as the Reynolds number was increased to a value 121, Kármán vortex shedding in the wake downstream of the peaks was observed. On the basis of this result and the results of an investigation in the wake of a kinked wire it was concluded by Honji & Ishi that there seemed to be no possibility for the effective suppression of vortex shedding in the wake of a cylinder by simply distorting the body.

Interconnecting vortex loops have also been observed in the wakes of other bluff bodies. In Leweke & Provansal (1999) the wake of a sphere was visualised at low Reynolds numbers. They found that above a Reynolds number of 320 the wake lost

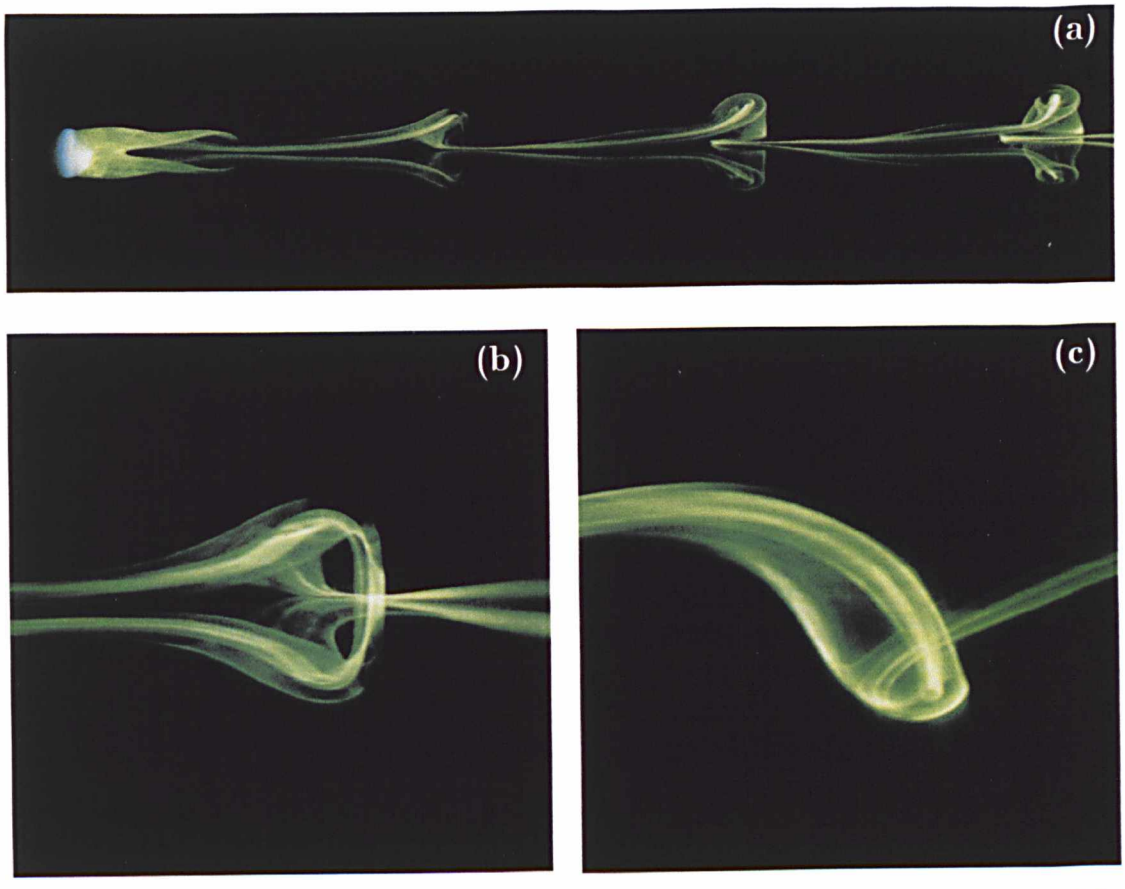


Figure 5.3 Flow in the wake of a sphere at a Reynolds number of 320, Leweke & Provansal (1999): (a), visualisation of the interconnecting hairpin vortex structures in the wake; (b) & (c) details of the hairpin loops at approximately 7D downstream.

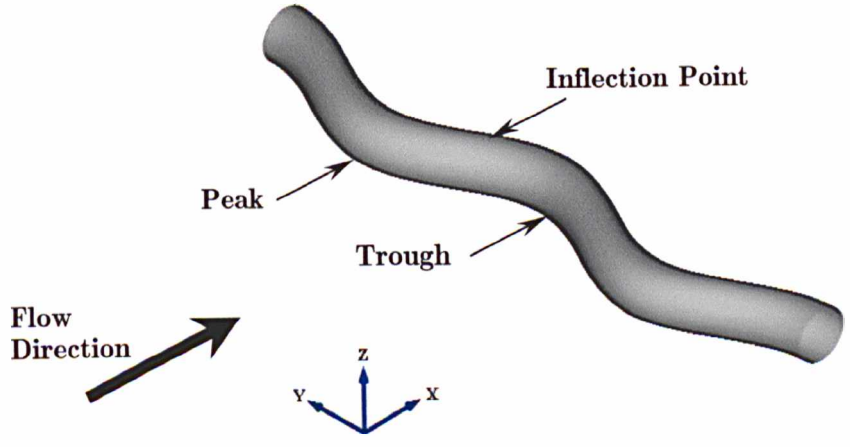


Figure 5.4 Schematic diagram of a typical sinuous cylinder layout illustrating the axis convention used. The origin is defined at the centre of the central peak of the model.

its axial symmetry and a new time dependent wake structure was developed where the sphere would alternately shed vortex loops into the wake, figure 5.3.

5.1.3 Experimental models.

The sinuous cylinder models used during this investigation were designed and manufactured under the guidance of Professor Albin Szewczyk from the University of Notre Dame, USA. All of the models were constructed from a high-density thermoset plastic (thermoset epoxy 206) that was cast using a mould. In addition, for the smaller diameter models a high tensile steel rod was also cast into the model to improve it's strength and stiffness.

Originally two models were constructed for the purpose of flow visualisation in a water tunnel using the lead precipitation method (section 3.2.4). These models had diameters of $25.4mm$ and $12.7mm$ and wave steepnesses of $w/\lambda = 0.167$ and $w/\lambda = 0.333$ respectively. However, from previous experience with wavy square cylinders it was suspected that these values of wave steepness would be considerably in excess of the minimum values needed to suppress Kármán type vortex shedding. Therefore, it was decided that a series of small models ($D = 12.7mm$) with low values of wave steepness should be constructed. This new series of models had wave steepnesses of $w/\lambda = 0.042$, 0.083, 0.167 & 0.333 and had a span of five wavelengths and a wavelength of 7.5D.

After initial flow visualisation experiments using the series of small models it was decided that a large model should be constructed for use in wind tunnel experiments at higher Reynolds numbers. This model had a diameter of $25.4mm$, a wave steepness of $w/\lambda = 0.167$, a wavelength of 6D and was fitted with 77 pressure tappings that were cast into the cylinder surface. Figure 5.4 shows the layout of a typical sinuous cylinder model and also the axis convention used within this part of the investigation.

5.2 Initial results.

5.2.1 Flow visualisation.

Flow visualisation was performed at a Reynolds number of 100 in a towing tank using the laser induced fluorescence technique, as described in section 3.2.4. The benefit of performing flow visualisation at low Reynolds numbers is that the vortical structures are still laminar making the resulting vortices easily visible in the wake. Although, this Reynolds number was considerably lower than that at which drag measurements were to be made it was expected that many of the predominant large-scale features of the wake would still be evident at higher Reynolds numbers.

For an initial comparison, the wakes of the sinuous cylinder models were visualised in crossflow at various spanwise positions and illuminated using a laser sheet. In the wake of a plain circular cylinder the familiar Kármán vortex shedding was observed which was found to be parallel over the central portion of the span, figure 5.5. However, in agreement with previous observations of Szewczyk (1998), the wakes of the sinuous cylinder models were found to vary in both width and character in a periodic fashion across the span. The relative difference in wake structures across the span is illustrated in figure 5.5. Downstream of a geometric peak (the most upstream portion of the model) a 'narrow wake' was observed where the wake was found to be narrowest and approximately symmetrical, figure 5.5. In contrast, a 'wide wake' was formed downstream of a geometric trough where large-scale vortical structures were observed being shed into the wake. At low levels of wave steepness ($0.00<w/\lambda<0.05$) these structures appeared to be shed periodically from alternate sides of the wake in a fashion similar to Kármán type vortex shedding, figure 5.5. However, as the wave steepness was increased the shedding became far less periodic and increasingly disorganised with a significant increase in the mean wake width, figure 5.5. For higher levels of wave steepness ($w/\lambda > 0.15$) the wake became organised into a new three-dimensional structure with Kármán type instabilities being replaced by the symmetric shedding of large vortical structures in to the wake, figure 5.5.

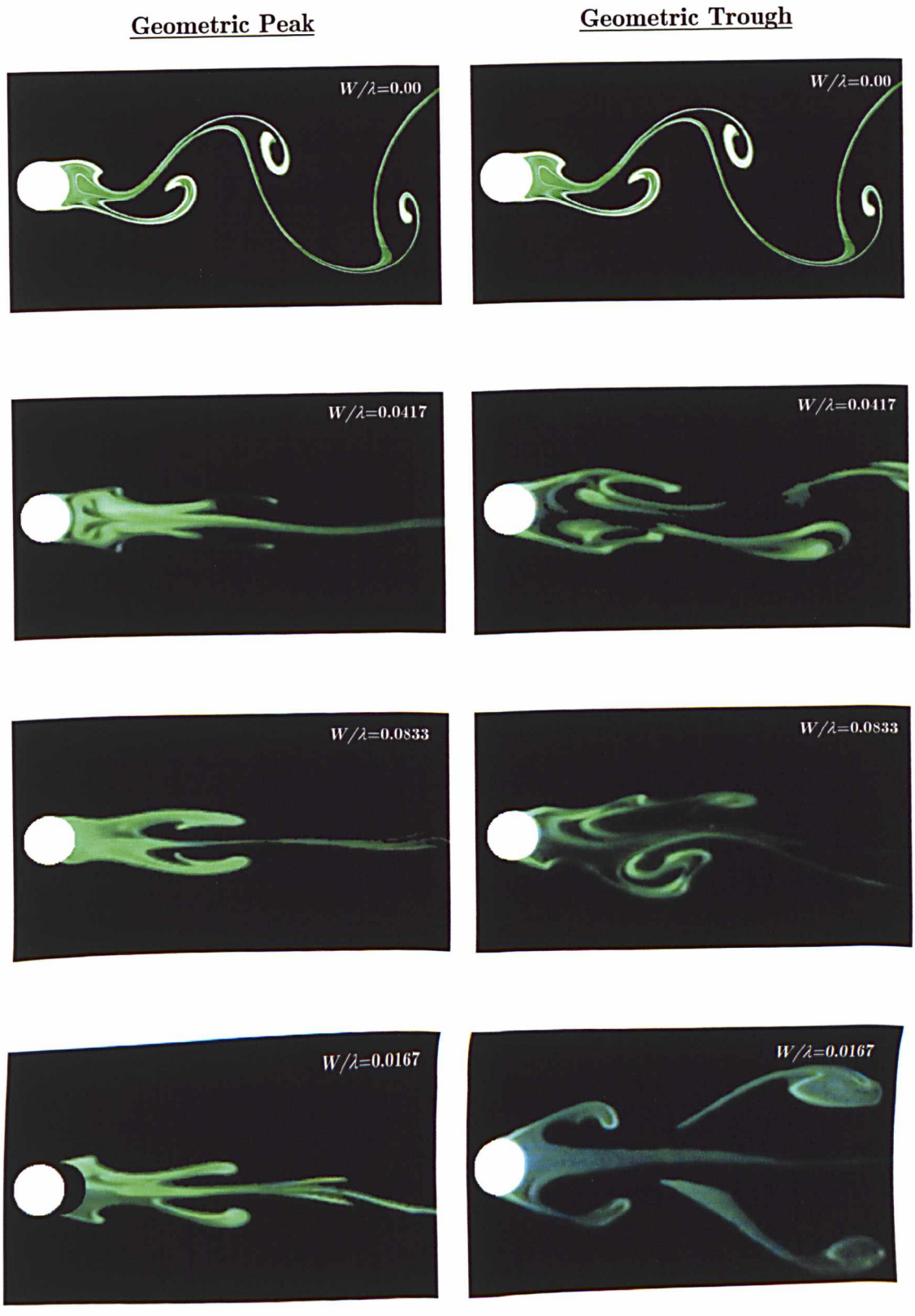


Figure 5.5 Crossflow visualisations of the flow in the wake of sinuous cylinders of increasing wave steepness at a Reynolds number of 100. The left-hand column shows the flow in the wake of a geometric peak (where the body extends furthest upstream) whilst the right-hand column shows flow in the wake of a geometric trough.

5.2.2 Drag measurements.

In the previous works of Bearman and Owen (1998a) and Tombazis and Bearman (1997) it was found that the introduction of spanwise waviness produced significant reductions in drag. Therefore, as an initial comparison between the various cylinder models, the drag was measured. Firstly the drag coefficient of a plain cylinder was determined at a Reynolds number of 3.3×10^4 and found to be approximately $C_D=1.2$. This value was found to be in good agreement with the value determined by other researchers and showed little variation with small changes in Reynolds number around this value. However, the introduction of a small amount of waviness into the cylinder axis resulted in an immediate drop in the value of C_D. Figure 5.6 shows the effect on increasing wave steepness on C_D for the sinuous cylinders at a Reynolds number of 3.3×10^4. It is clear from the figure that the results show a similar trend to the work of Bearman and Owen (1998a) and Tombazis and Bearman (1997) with increasing wave steepness resulting in a dramatic drop in cylinder drag. For the sinuous cylinder models with wave steepnesses of 0.042, 0.083, 0.167, 0.333 the drag reduction were found to be 21%, 30%, 39%, 47% respectively.

Roshko (1954) showed that a similar percentage drag reduction could be achieved if vortex shedding was suppressed in the wake of a circular cylinder by using a long splitter plate in the wake. Therefore, at these Reynolds numbers the drag reductions achieved by the sinuous cylinders are consistent with vortex shedding being suppressed if a value of wave steepness of $w/\lambda = 0.15$ is exceeded. However, from figure 5.6 it can be seen that further reductions in C_D can be achieved if the wave steepness is increased beyond this level and up to a value of $w/\lambda = 0.333$. At these high levels of wave steepness the leading edge of the cylinder becomes increasingly yawed to the freestream flow in the regions near the inflection points. This results in an additional reduction in C_D which can be approximately corrected for if the local drag coefficient is evaluated using the component of freestream velocity normal to the leading edge. If the resulting sectional drag coefficient is then integrated across a complete cylinder wavelength then the overall drag coefficient (C_{Dc}) without the effects of leading edge yaw can be calculated. This can be expressed mathematically as

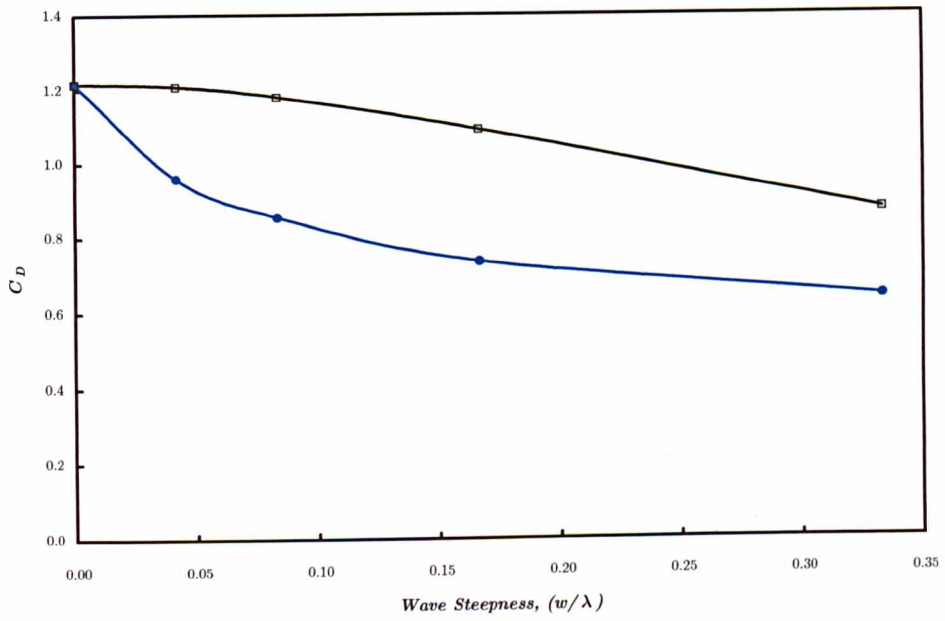


Figure 5.6 The effect of wave steepness on the drag of a sinuous cylinder at a Reynolds number of 3.3×10^4: •, measured values; □, values calculated to include the local effect of the leading edge yaw using $C_{Dc} = C_{Dm}\int\cos^2\alpha dx$, where α is the angle of yaw.

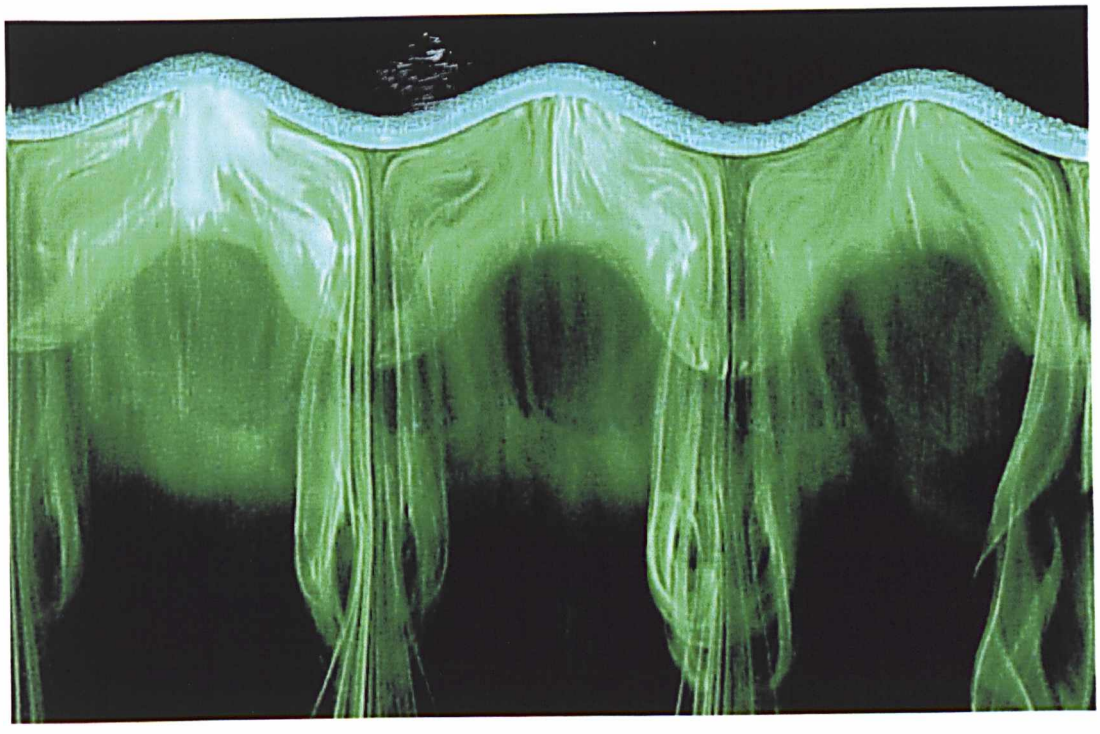


Figure 5.7 Plan view visualisation in the wake of the sinuous cylinder showing a spanwise vortex becoming increasing wavy in the wake leading to the formation of streamwise vortices. Cylinder wavelength λ = 7.5D, cylinder wave steepness w/λ = 0.167 and Reynolds number =100.

$$C_{Dc} = C_{Dm} \int_0^{\lambda} \cos^2 \alpha dx$$

where C_{Dm} is the experimentally measured drag coefficient for a circular cylinder, λ is the cylinder wavelength and α is the angle between the component of velocity normal to the local leading edge and the freestream flow. The effect of the locally yawed leading edge of the sinuous cylinders can be seen in figure 5.6 where the calculated value of C_{DC} shows a maximum drag reduction of only 28% in comparison with the measured reduction of 47%. Therefore, these results clearly demonstrate that the effects of cylinder yaw alone are insufficient to account for the substantial reductions observed in C_D and are consistent with vortex shedding being suppressed.

5.2.3 Choice of model for detailed investigations.

The suppression of Kármán vortex shedding and its replacement by the emergence of a new highly three-dimensional wake structure is of particular interest. It was shown in the previous chapter that a similar suppression of vortex shedding could be achieved in the wake of a square cylinder although little was understood about the resulting wake. Hence, it would appear that the fundamental instability responsible for Kármán type vortex shedding ~~that~~ can be effectively suppressed by the use of three-dimensional geometry. Therefore, in order to gain further insight into the wake dynamics, it was decided that the investigation into sinuous cylinders should focus primarily on one particular model.

The one chosen for further investigation was the model with a wave steepness of $w/\lambda = 0.167$. It was chosen because it had the lowest value of wave steepness for which the required wake characteristics could be attained. At low Reynolds numbers it showed an organised three-dimensional wake structure whilst at high Reynolds numbers wind tunnel measurements indicated a considerable drag reduction consistent with the complete suppression of Kármán type vortex shedding.

5.3 Detailed results.

5.3.1 Flow visualisation.

It was shown in the previous section from cross flow visualisations of the wake that the sinuous circular cylinder models exhibited a significant variation in wake structure between different spanwise positions. However, it is unclear from simple crossflow visualisations how the vortical structures link-up across the span. Therefore, in order to gain further insight into the full three-dimensional nature of the flow, the wake was visualised in plan view.

Figure 5.8 shows a plan view of the wake at a Reynolds number of 100. A striking feature of the wake is the complete absence of Kármán type vortex shedding and the emergence of streamwise vortex loops. From the figure it can be seen that these vortices are observed downstream of the troughs with little vortex activity downstream of the peaks. These structures would appear to be the same vortex loops visualised by Honji & Ishi (1976) in the wake of a similarly deformed cylinder (figure 5.2), although the wavy cylinder used in their study had a considerably larger wave steepness ($w/\lambda = 0.344$) and wavelength ($\lambda = 12.8$). In addition the vortex loops also show many similarities to the vortices generated in the wake of a sphere at similar Reynolds numbers, figure 5.3.

The vortex loops were observed to be formed in the wake by the deformation of an initially straight spanwise vortex. This vortex appeared to vary in both size and strength periodically across the span with a comparatively large vortex observed in the wake downstream of the troughs and comparatively small vortex being observed downstream of a peak, figure 5.5. As the vortex began to form it was shed downstream at the troughs whilst remain almost captive in the near wake downstream of the peaks. This effect can be seen from figure 5.7 where the vortex in the near wake can be observed becoming increasingly wavy as it is convected away from the body at the troughs. As the vortex is convected away it continues to rollup downstream of the troughs and is eventually stretch into a series of streamwise vortex

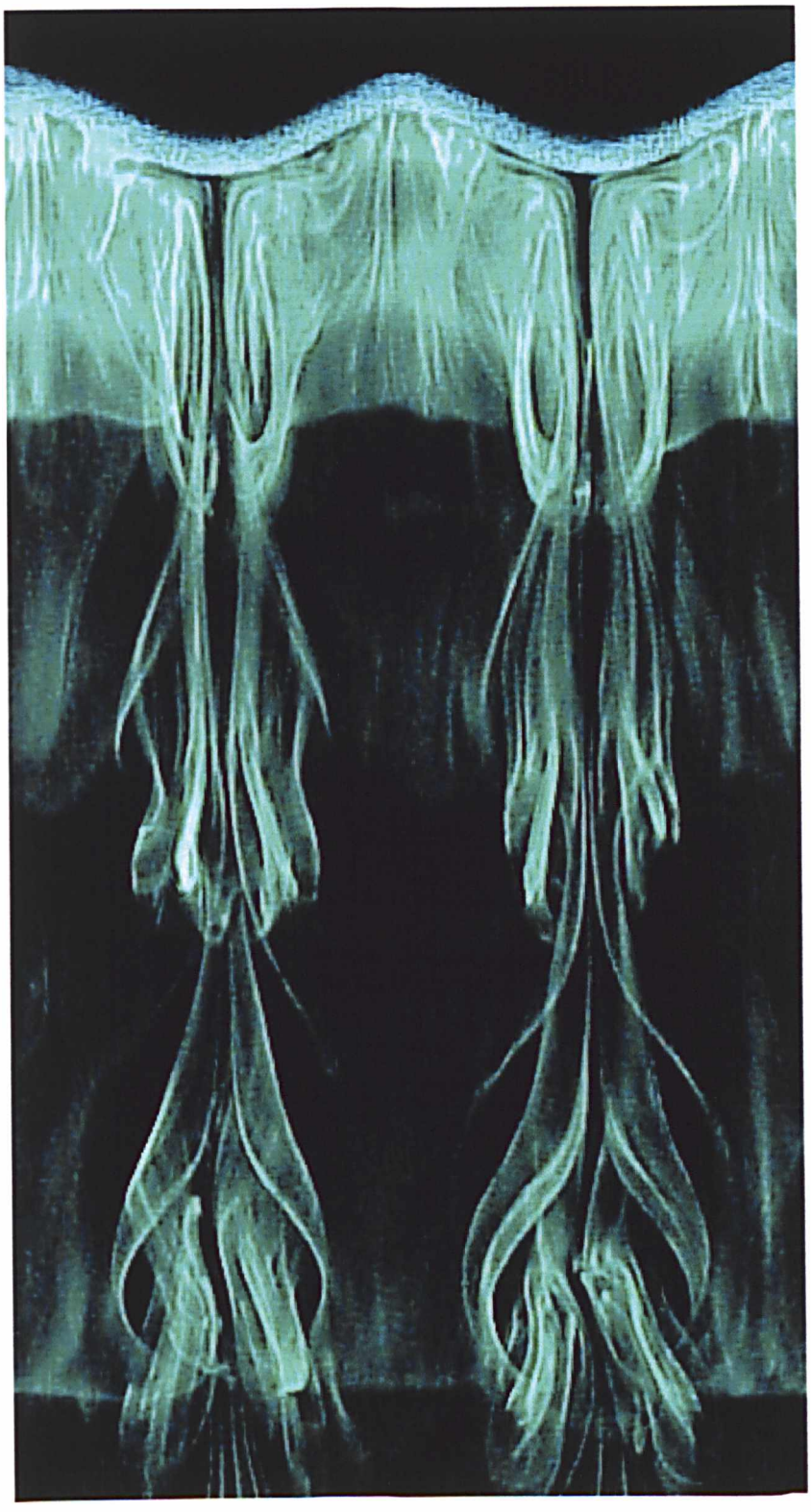


Figure 5.8 Plan view visualisation of the wake of the sinuous cylinder at a Reynolds number of 100 showing pairs of interconnecting hairpin vortices shedding downstream of the troughs. Cylinder wavelength $\lambda = 7.5D$ and cylinder wave steepness $w/\lambda = 0.167$.

loops. The legs of these vortex loops are then stretched back upstream in the near wake under the action of, and into, the next forming vortex causing the formation of elongated vortex loops as seen in figure 5.8.

Unlike the flow in the wake of a circular cylinder, the flow in the wake of the sinuous cylinder showed little dependence on end conditions with the vortex loops always observed to be in phase across the span. The only noticeable effect of end conditions was to cause a local disturbance to the flow in the regions of the endplates, although this affected region rarely extended beyond 3 cylinder diameters.

Detailed visualisations of the wake in crossflow at a peak and a trough are shown in figure 5.9. It can be seen from the figure that downstream of the peak the wake shows similarities to the wake of the wavy square sectioned cylinder at a similar spanwise position, figure 4.10a. At this Reynolds number (100) the flow downstream of the peaks is characteristic of the pre-vortex shedding wake (Reynolds number < 46) with the flow recirculating in two cells close to the cylinder. However, similar to the observations in Honji & Ishi (1976), Kármán type vortex shedding was observed in these regions downstream of the peaks as the Reynolds number was increased towards the slightly higher value of 250.

Downstream of a trough, large pairs of vortical structures can be observed in the wake, figure 5.9b. From the figure it can be seen that at this Reynolds number and spanwise position that Kármán type vortex shedding is not observed. However, unlike the wake downstream of a peak, at this spanwise position Kármán type vortex shedding did not resume as the Reynolds number was increased. The vortical structures visualised in figure 5.9b are the heads of the vortex loops and these are observed to drive a large component of upstream flow along the centre wake between the two separated shear layers. In this instance the vortex loops are generated in a symmetric fashion from either side of the wake. However, this is only one of two dominant shedding modes observed in the wake of the model.

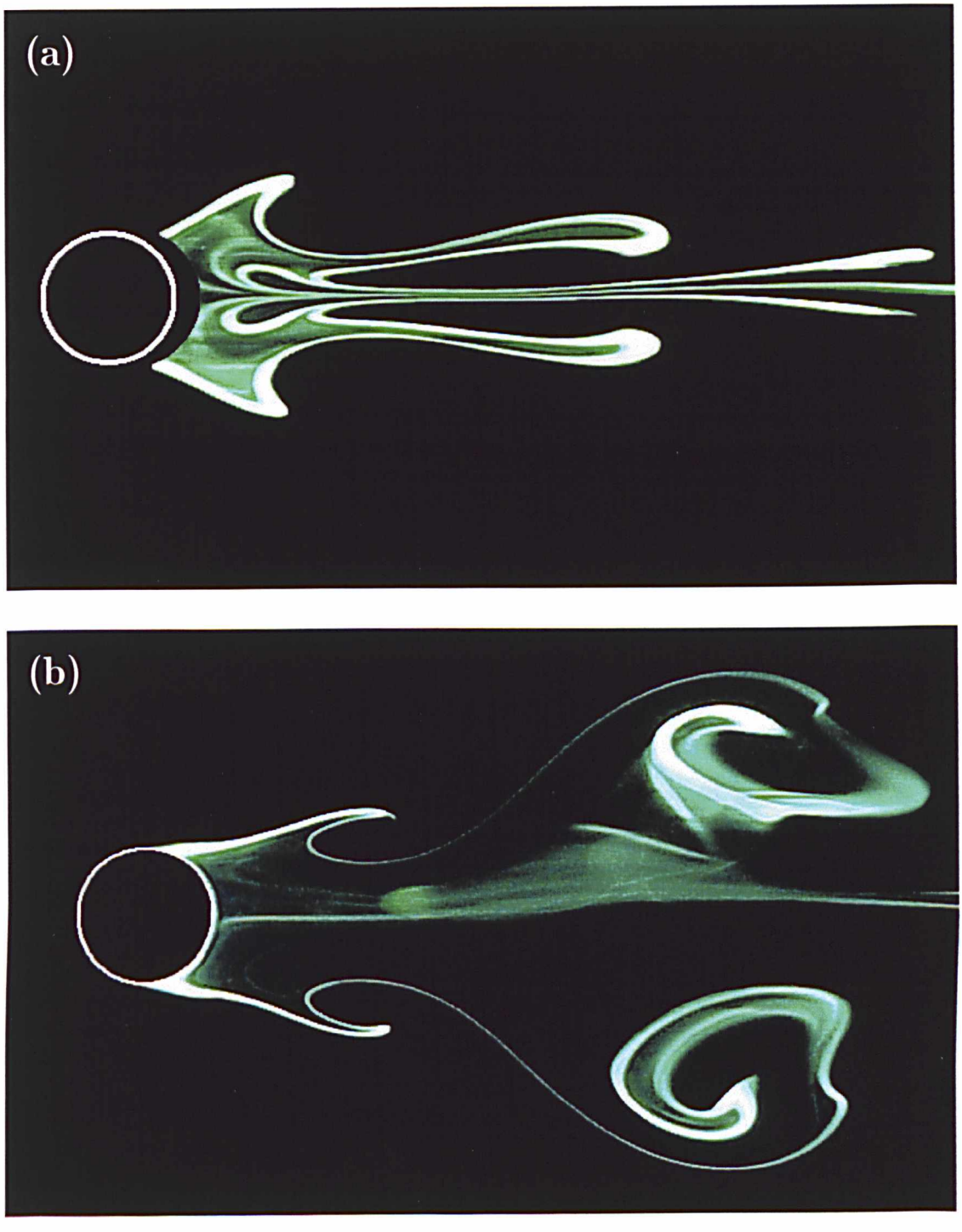


Figure 5.9 Detailed visualisations of the wake of the sinuous cylinder in the crossflow (X–Z) plane at a Reynolds number of 100: (a), flow in the wake of a peak showing the formation of a symmetrical narrow wake; (b), flow in the wake of a trough showing the heads of the hairpin vortices as large rollers in the upper and lower shear layers.

As explained previously, vortex loops were formed as a result of vortex loops being stretched under the action of the next forming vortex. In the case of symmetric shedding of vortex loops, vortex loops would be drawn into the next forming vortex from the same side of the wake, figure 5.10a. However, an anti-symmetric arrangement of vortex loops was also observed where vortex loops crossed the wake and were drawn into a vortex of opposite sign and from the opposite side of the wake, figure 5.10b. Generally the flow would exhibit the same mode across all of the spanwise periods, although a variation in modes across the span was observed near the start of several runs. For the sinuous cylinder both modes appeared to be stable and once established would continue for the entire duration of a run, approximately 200 diameters downstream. However, the symmetric mode was far less stable than the anti-symmetric mode and was particularly sensitive to perturbations of flow. In general this mode was only observed in the wake of the model when care was taken to avoid perturbations at the start of a run. In addition, it was also important to ensure that the model was accurately aligned at zero incidence as small variations in the angle of incidence ($\pm 1°$) would cause an asymmetry in the strength of the vortices leading to the formation of the anti-symmetric mode. Therefore, it is possible that the symmetric mode may have been marginally unstable and would have reverted to the anti-symmetric mode if the model had been traversed over a greater downstream distance.

In their CFD study, Darekar & Sherwin (2001) observed similar modes of shedding of vortex loops in the wake of a wavy square section cylinder of equal wave steepness ($w/\lambda = 0.167$) and similar wavelength ($\lambda = 5.6$). It was found that the mode of shedding was influenced by initial conditions. When the waviness was impulsively added to the fully developed Kármán vortex shedding wake of a square section cylinder, the anti-symmetric loop shedding mode was always found to develop. Simulations of the wake for a further 220 diameters downstream revealed that the wake remained unchanged and stable in this anti-symmetric loop shedding mode. However, if the wavy cylinder was impulsively started from rest, the wake would initially develop into the symmetric mode of loop shedding. The wake would continue

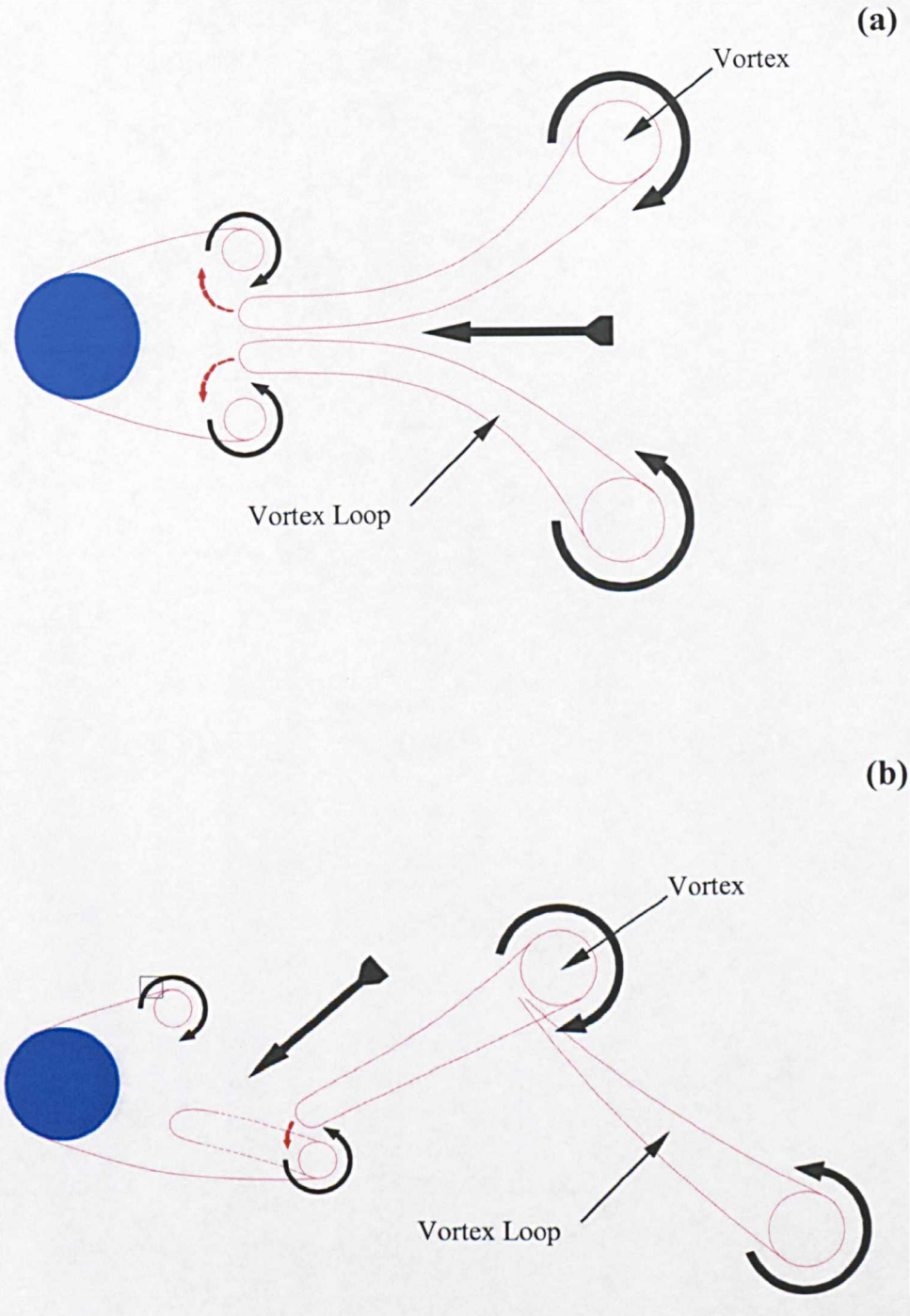


Figure 5.10 Schematic diagrams showing the modes of vortex loop shedding in the wake of the sinuous cylinder: (a), symmetric shedding of loops where the loop is drawn into a vortex from the same side of the wake; (b), anti-symmetric of vortex loops where loop is drawn into a vortex from the opposite side of the wake.

in this mode until approximately 60 diameters downstream, where upon the wake became unstable and reverted to the anti-symmetric mode of shedding. The wake subsequently remained stable in this mode until the end of the run, figure 5.11.

Measurements of the lift and drag forces between the two modes revealed that the shedding mode had virtually no effect on the drag and only caused a very small fluctuating lift force for the anti-symmetric mode. This fluctuating lift force was approximately two orders of magnitude less that the fluctuating lift force measured for Kármán vortex shedding. From these results it was concluded that the final mode of loop shedding in the wake was unaffected by initial conditions, although they did influence the time taken for the wake to reach the stable anti-symmetric mode. Therefore, when the simulation was started from the vortex shedding state it is likely that the anti-symmetric mode was triggered early due to the perturbations of the initial vortex shedding.

5.3.2 Drag variation and pressure distribution.

To carry out wind tunnel measurements of drag and surface pressure a large sinuous cylinder model was constructed. The model incorporated 77 surface pressure tapings and was of identical wave steepness ($w/\lambda = 0.167$) to the model used for flow visualisation. However, this model had a wavelength of 6D, which was slightly shorter than the wavelength of the previous model (7.5D) that was used during the low Reynolds number flow visualisation experiments. Therefore, the reader should be cautious when making direct comparisons between the results from high and low Reynolds numbers due to this slight difference in geometric wavelength.

One effect of this decrease in wavelength can be seen from figure 5.12 where the drag of the sinuous cylinder with wavelength 6D (at zero incidence) is found to be $C_D = 0.68$ opposed to $C_D = 0.74$ for the cylinder of wavelength 7.5D, figure 5.6. This small change in wavelength represents an additional 5% reduction in drag over a plain circular cylinder and clearly illustrates the potential for further optimisation of the

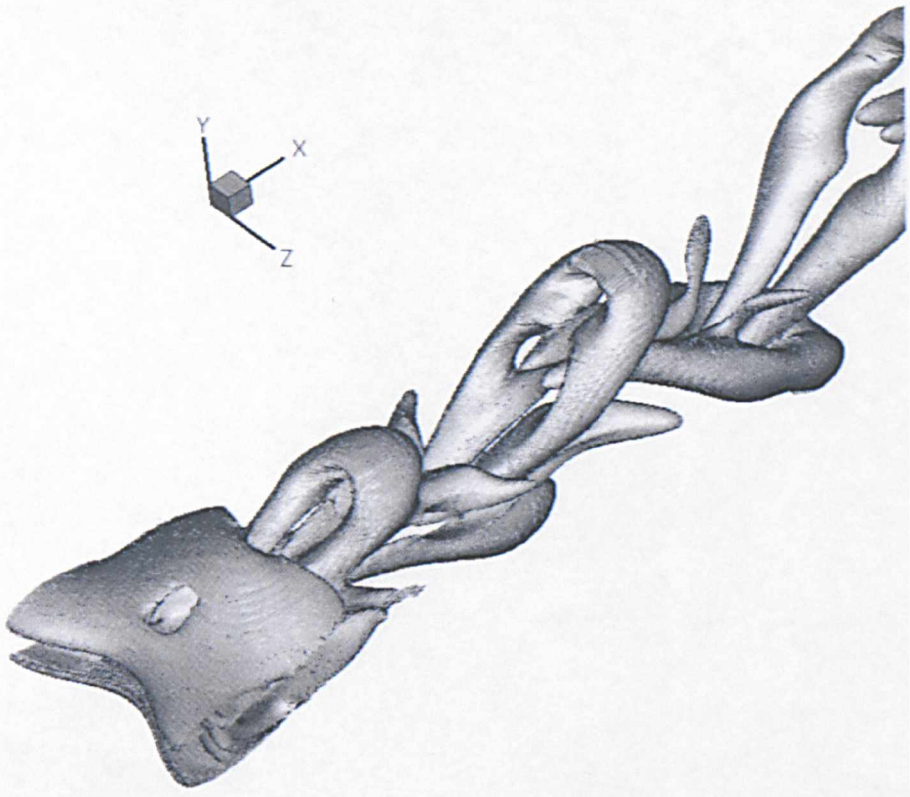


Figure 5.11 Computational visualisation of the flow in the wake of a wavy square section cylinder at a Reynolds number of 100 showing the anti-symmetric mode of hairpin shedding, Darekar & Sherwin (2001). Wavelength $\lambda = 5.6D$ and wave steepness $w/\lambda = 0.167$.

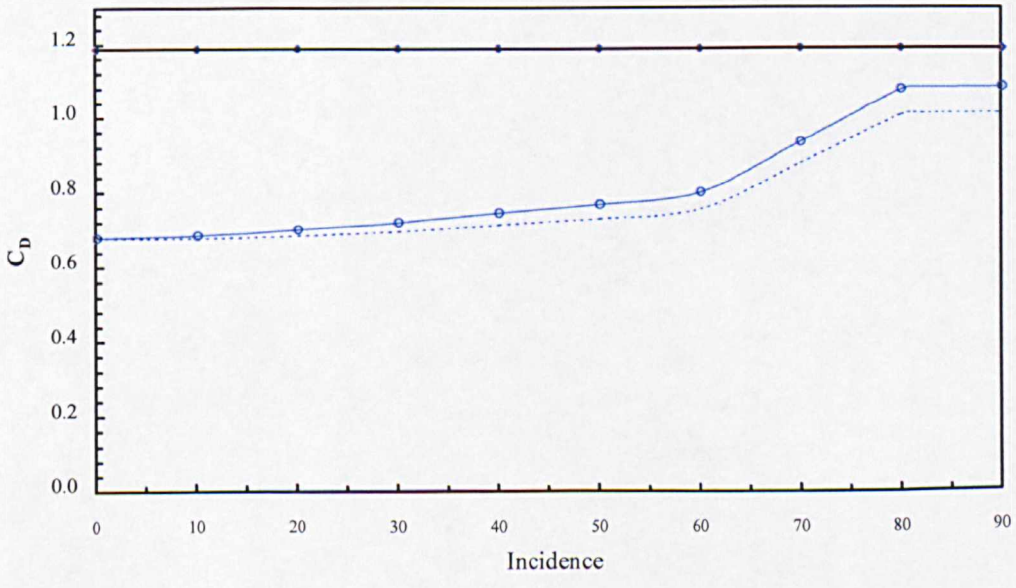


Figure 5.12 The effect of incidence on the drag of the sinuous cylinder at a Reynolds number of 4×10^4. The solid line shows the variation with the drag coefficient based on cylinder diameter, the dotted line shows the variation in drag coefficient based on projected frontal area.

sinuous cylinder configuration. In addition the figure also illustrates the lack of incidence sensitivity up to an incidence of approximately 60°. In the incidence range of 0° – 60° the drag is found to increase gradually from $C_D = 0.68$ to $C_D = 0.80$ although this increase is partly due to the increase in frontal area as the incidence is increased. Therefore, if the drag coefficient is evaluated based on the projected frontal area, then the drag is only found to increase to a value of $C_D = 0.75$ at an incidence of 60°, figure 5.12. Beyond an incidence of approximately 60° the drag rises sharply suggesting a return to vortex shedding in the wake as the incidence is increased towards 90°. However, even at an incidence of 90° the drag is still found to be less than for the plain circular cylinder ($C_D \approx 1.1$) despite an increase in frontal area of approximately 6.5%.

Further insight into this substantial drag reduction was gained by the investigation of the surface pressure distribution at a slightly higher Reynolds number of 5×10^4. Figure 5.13 illustrates the effect of incidence on the base pressure distribution in the wake of the sinuous cylinder. It can be seen from the figure that the base pressure is found to vary periodically across the span of the sinuous cylinder where an increase in base pressure can be seen in the region of the troughs ($Y = 0.5$). At the troughs the base pressure is found to be $C_{PB} = -0.52$ and is found to gradually decrease towards the inflection points to a value of $C_{PB} = -0.65$. It is then found to remain approximately constant at this value towards the peaks. The figure also shows that there is very little variation in the level or distribution of base pressure with increasing angle of attack. In addition this spanwise variation in base pressure is also accompanied by a variation in spanwise separation point. From circumferential pressure measurements and surface flow visualisation the separation point is found to be approximately constant at an angle 80° from the peaks to the inflection points and then gradually move forward to an angle of approximately 65° in the region close to the troughs.

Figure 5.14 shows the pressure distribution along the leading edge of the model. From the figure it can be seen that the pressure coefficient (C_P) reaches 1 at the both the

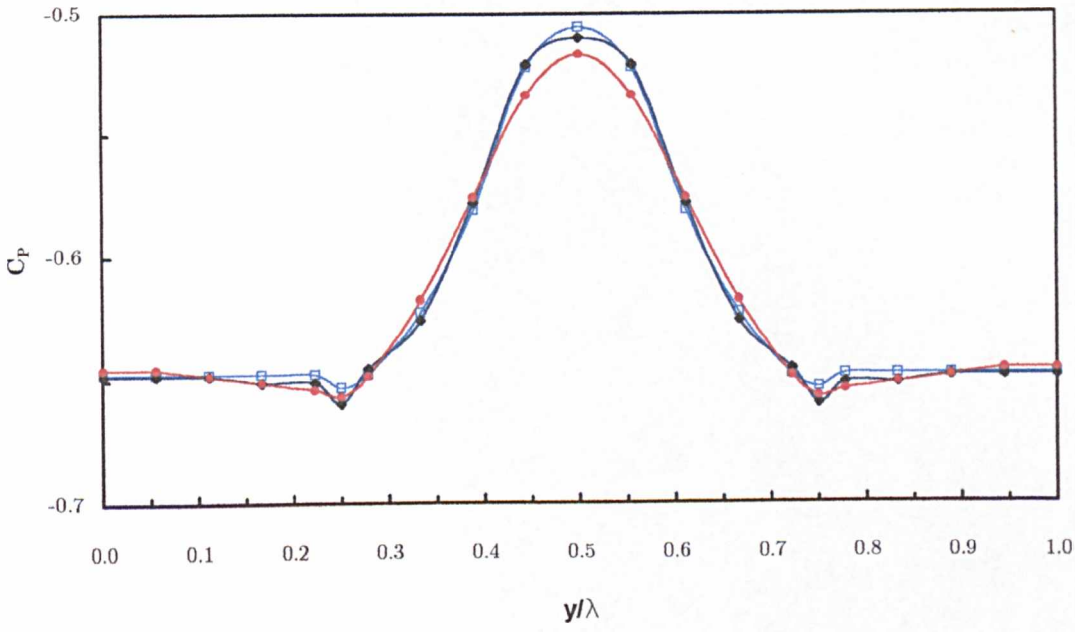


Figure 5.13 Spanwise variation in base pressure distribution for the sinuous cylinder at different angles of attack at a Reynolds number of 5×10^4: □, 0°; ♦, 10°; •, 20°.

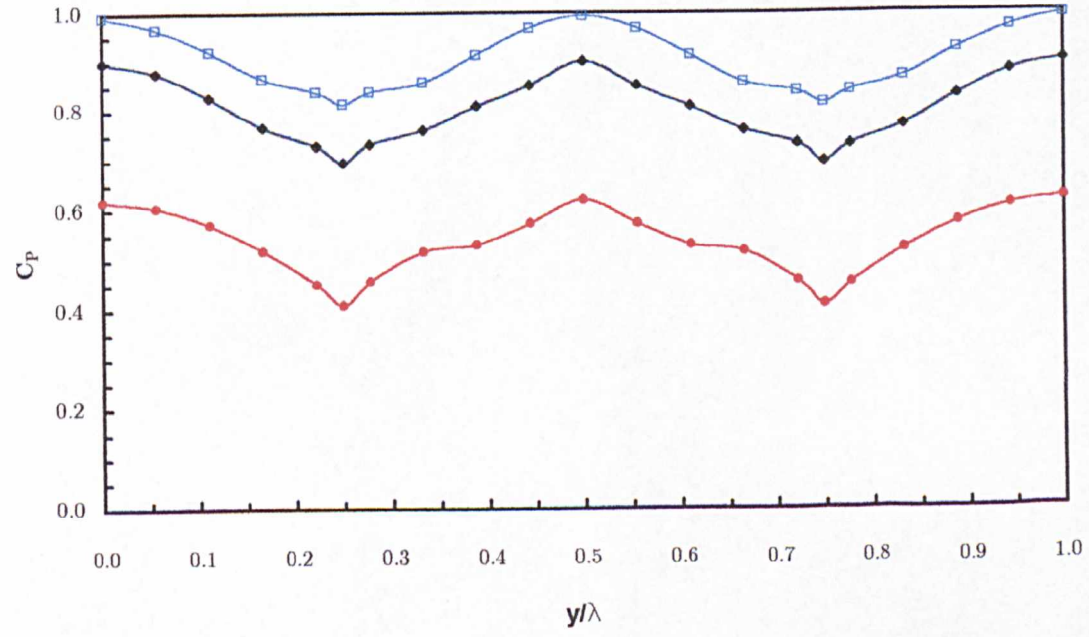


Figure 5.14 Spanwise variation in front face pressure distribution for the sinuous cylinder at different angles of attack at a Reynolds number of 5×10^4: □, 0°; ♦, 10°; •, 20°.

peak and the trough indicating the presence of stagnation points. However, the flow is not fully stagnated along the rest of the leading edge as the pressure is found to vary reaching a minimum of $C_P = 0.85$ at the inflection points. Using Bernoulli's equation it can be determined that a velocity component of approximately 40% of freestream would be required at the edge of the attached flow boundary layer to produce a pressure drop of this magnitude. By assuming steady flow and by arguments of symmetry about the centre plane of the model it can be concluded that this velocity component must lie in the centre plane of the model or along the leading edge. This spanwise flow was subsequently confirmed by surface flow visualisation and found to be from the peaks to the troughs. With increasing incidence this local drop in pressure at the inflection points continued to be evident up until angles of approximately 60°, where the model showed a sharp rise in drag. It is possible that this leading edge crossflow plays an important part in the disruption of vortex shedding.

5.3.3 Velocity fluctuations.

To investigate the nature of the vortex loops at higher Reynolds numbers, the velocity fluctuations in the wake were investigated using a hot-wire probe. At low Reynolds number the loop structures had been observed to be almost periodic and shed at a frequency of approximately half that of the Kármán vortex shedding frequency. Furthermore the vortex loops would always be in phase across the span and only shed from the body downstream of the troughs. Therefore, experiments were performed to investigate the frequencies present in the wake downstream of various spanwise positions to see if the shedding of the loops could be detected or if Kármán vortex shedding had recommenced.

For comparison purposes the wake of a simple 2D circular cylinder was briefly investigated. The probe was situated at a distance of two cylinder diameters downstream from the centre of the cylinder and the velocity fluctuations recorded at various heights above the centre plane of the wake, figure 5.15. At a distance of

0.75D above the centre plane the spectrum shows a strong single peak at a Strouhal frequency of 0.19, which is consistent with the frequency of Kármán type vortex shedding at this Reynolds number. However, as the probe is traversed down through the wake the strength of the vortex shedding peak is reduced until it is no longer detectable when the probe is on the wake centre line. At this position the dominant peak in the spectrum is found to be at a frequency of 0.38 or twice the vortex shedding frequency due to the contribution of velocity fluctuations from both sides of the wake.

Investigations in the wake of the sinuous cylinder revealed a very different type of behaviour. Figure 5.16 shows spectra in the wake of the sinuous cylinder at a distance of two diameters downstream of the peak. Just outside the wake at this downstream position the spectra shows a complete absence of wake fluctuations at the vortex shedding frequency for a circular cylinder of approximately 0.19. As the probe is traversed down into the wake no evidence of vortex shedding is detected although there is an increase in energy of fluctuations at low values of reduced frequency, approximately 0.03 – 0.07. A similar trend can also be seen in figures 5.17 and 5.18 which are measured downstream of an inflection point and a trough respectively. However, it is apparent that the low frequency wake fluctuations are a maximum downstream of the peak and reduce in strength as the probe is traversed towards the wake downstream of a trough. In these regions downstream of the troughs there appears to be no evidence of discrete frequencies that could be attributed to the periodic shedding vortex loops as observed at lower Reynolds numbers. Therefore, it would appear that at this Reynolds number the main unsteadiness in the wake is found downstream of the peak although this unsteadiness is considerably less than that associated with vortex shedding.

In order to gain further insight into the three-dimensionality of the wake a detailed time averaged wake shape was produced by traversing a hot wire probe in the wake. By comparing variations in turbulence intensity the boundary between the wake (highly turbulent) and the freestream flow (approximately laminar) could be

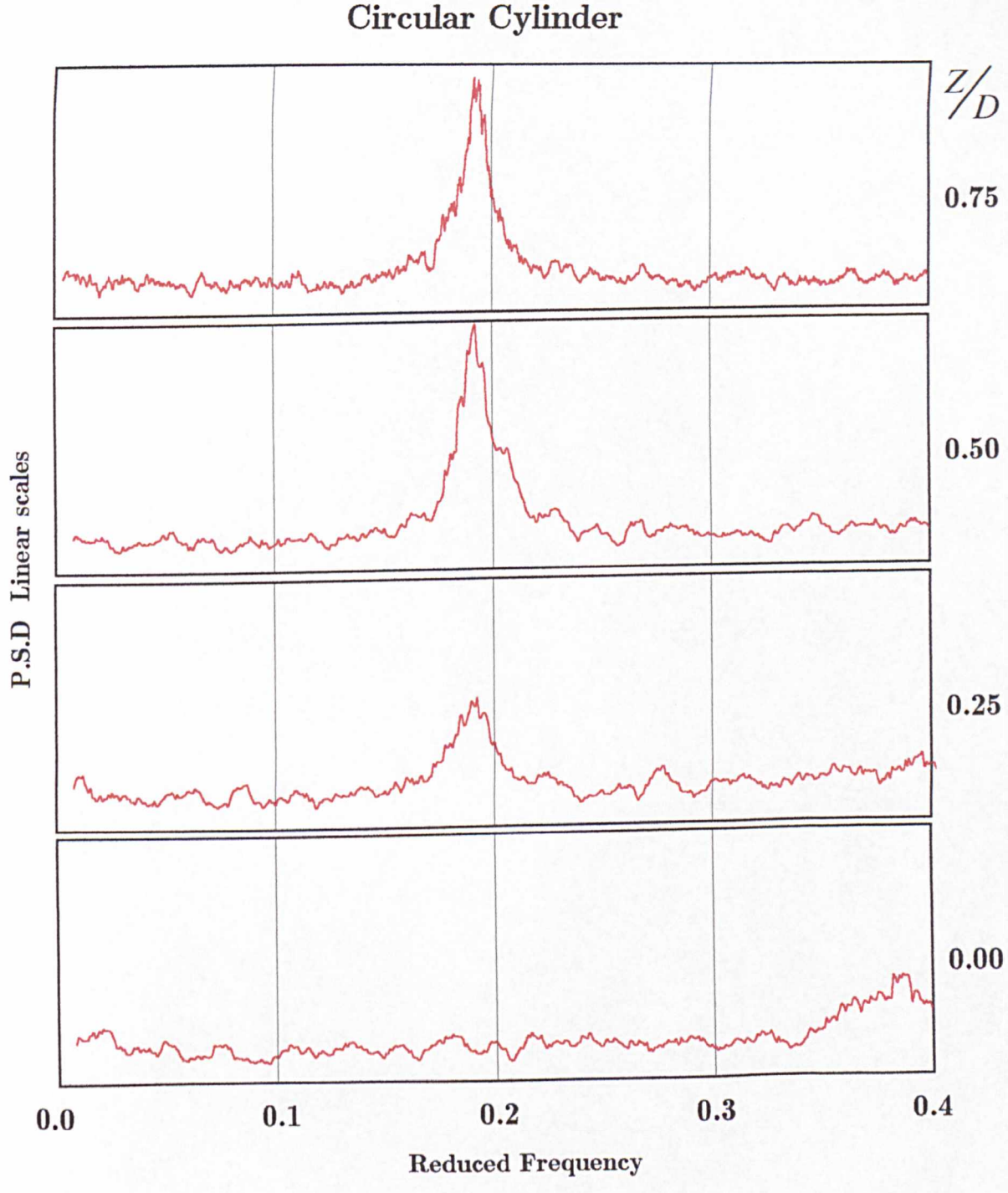


Figure 5.15 Variation in velocity power spectra for a circular cylinder at various positions above the wake centre line for a Reynolds number of 5×10^4. Probe positioned 2.0D downstream of the centre span.

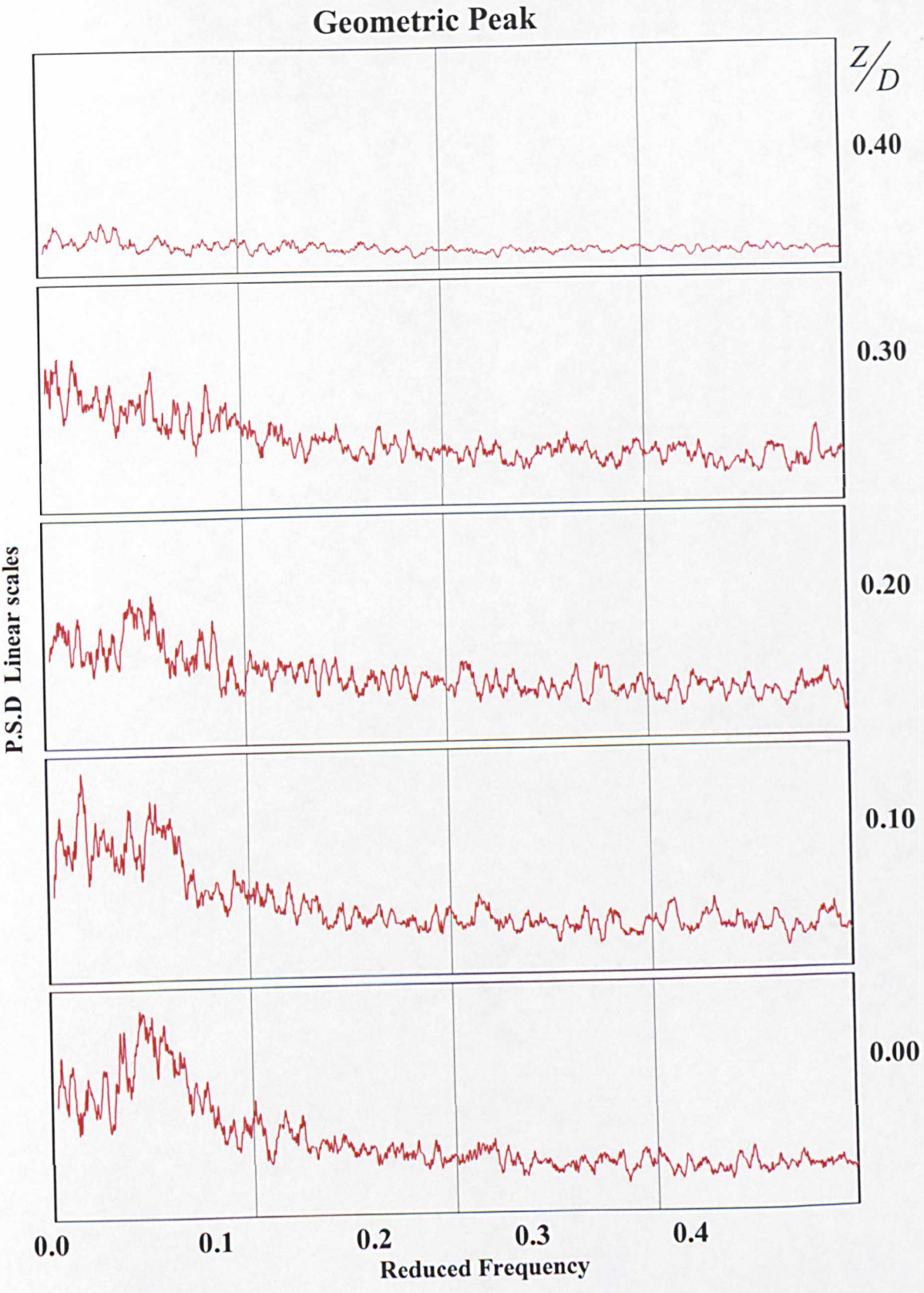


Figure 5.16 Variation in velocity power spectra for the sinuous cylinder model at various positions above the wake centre line for a Reynolds number of 5×10^4. Probe positioned 2.0D downstream of a peak at Y=0.

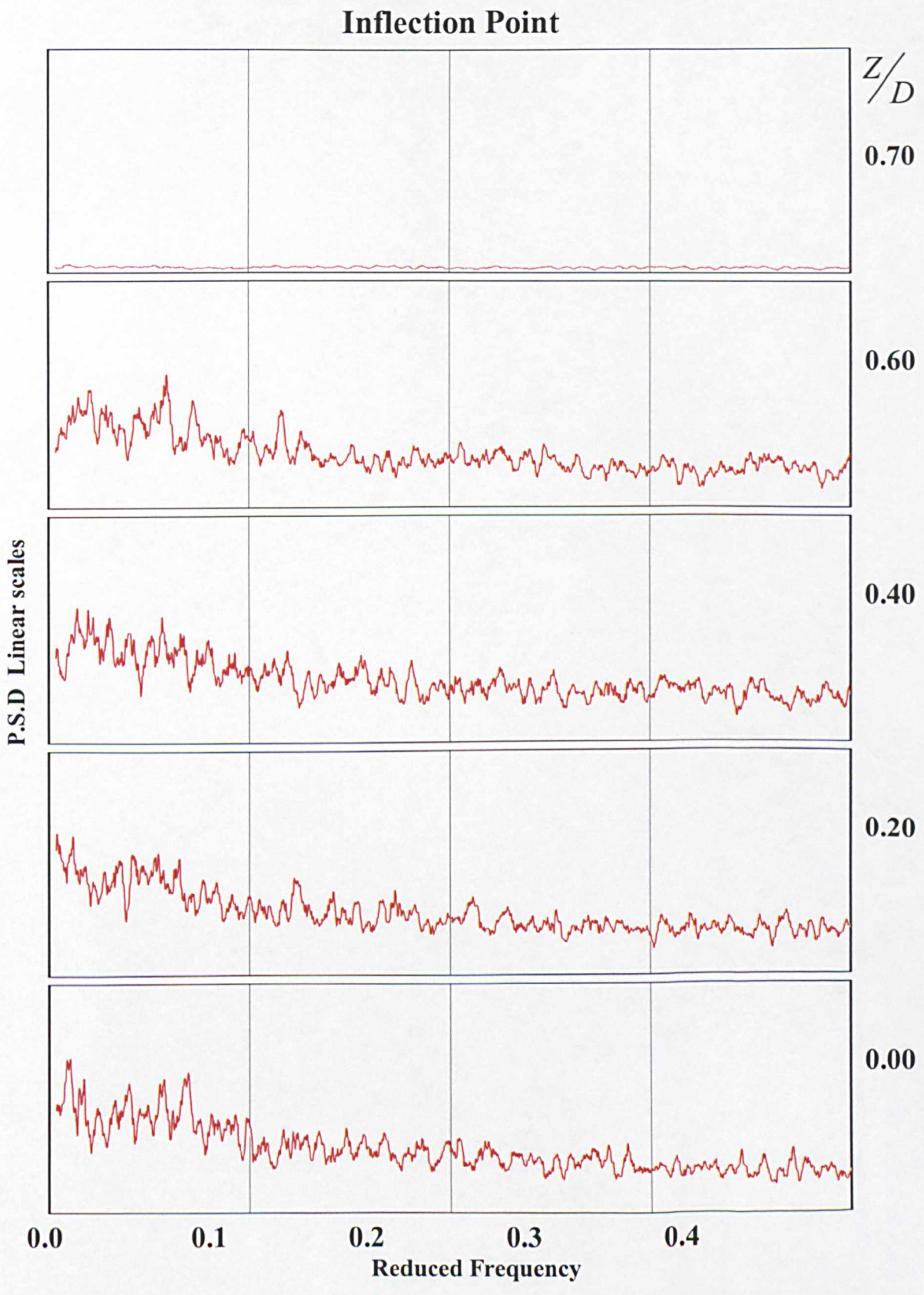


Figure 5.17 Variation in velocity power spectra for the sinuous cylinder model at various positions above the wake centre line for a Reynolds number of 5×10^4. Probe positioned 1.5D downstream of an inflection point at Y=0.25.

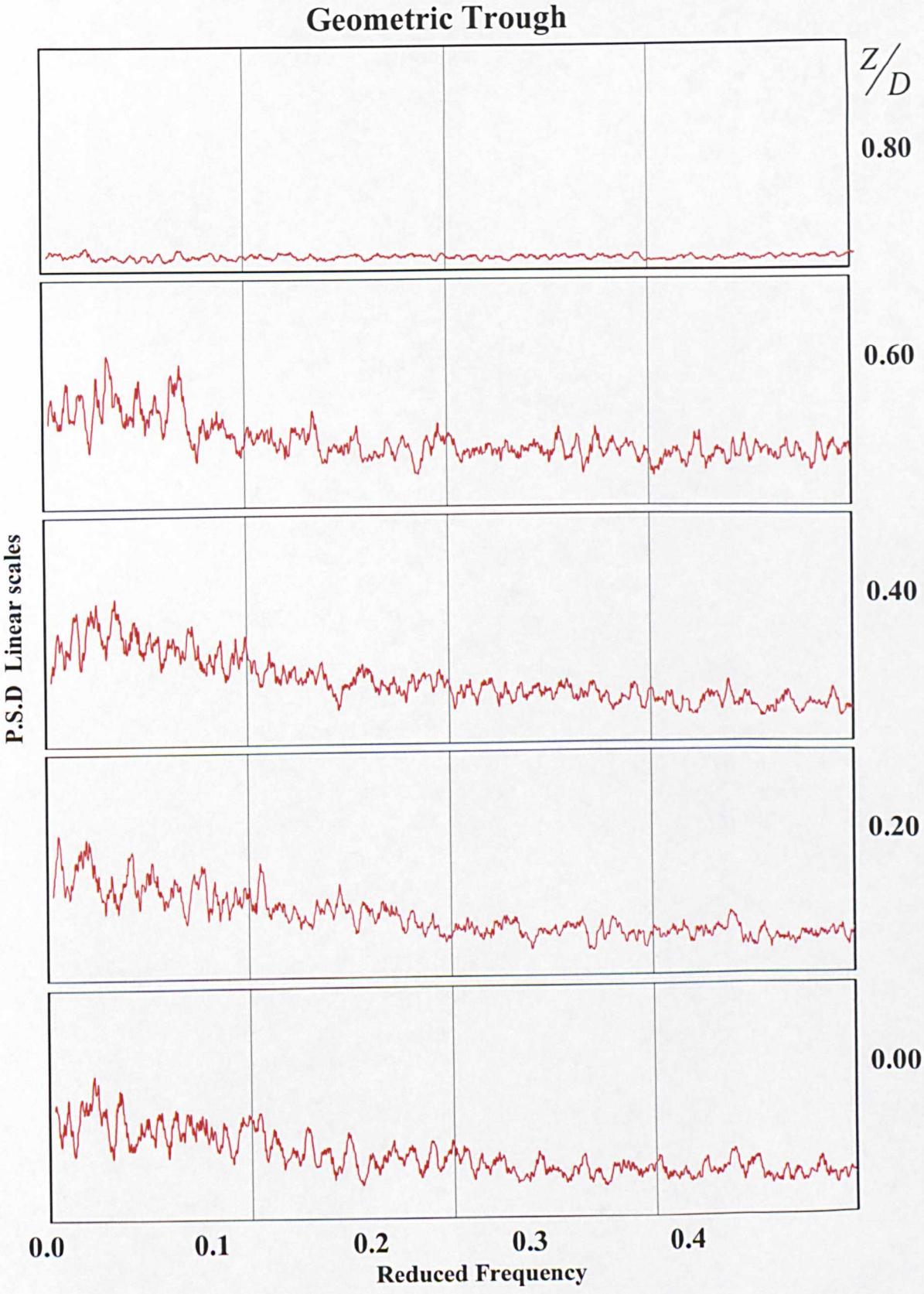


Figure 5.18 Variation in velocity power spectra for the sinuous cylinder model at various positions above the wake centre line for a Reynolds number of 5×10^4. Probe positioned 1.0D downstream of a trough at Y=0.5.

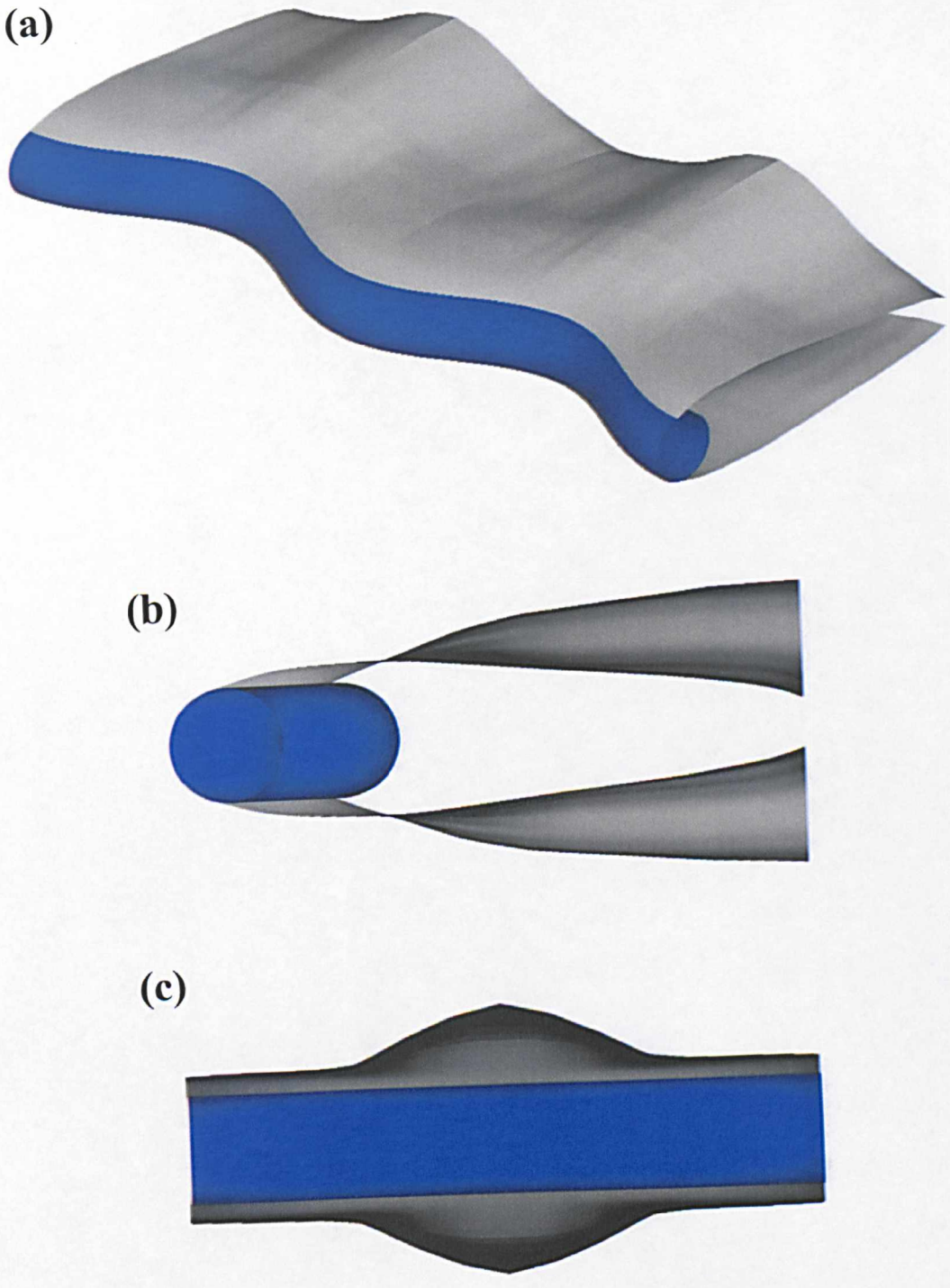


Figure 5.19 A schematic representation of the wake of the sinuous cylinder determined using a hot-wire probe at a Reynolds number of 5×10^4: (a), an orthographic view of the wake; (b), a side view of the wake illustrating the difference in wake profile between a peak and a trough; (c), front view of the wake.

established. Figure 5.19 shows the wake shape determined using this technique. It can be seen that the variation in wake width across the span is similar to the variation found at low Reynolds numbers. Downstream of a peak the wake is narrow and reducing in size with downstream distance whilst downstream of a trough the wake is significantly wider and growing in size with downstream distance. At a distance downstream of 3D this variation in wake width is found to be from 1D downstream of a peak to approximately 2.2D downstream of a trough. Hence, it is not surprising that vortex shedding is suppressed in such a three-dimensional wake as it is the result of a fundamentally a two-dimensional instability mechanism.

5.3.4 Particle Image velocimetry.

Whilst hot wire measurements in the wake of the sinuous cylinder showed an absence of vortex shedding they revealed very little about the wake structure that replaced it. Therefore, to visualise the flow and make quantitative measurements, the wake was investigated using Particle Image velocimetry (PIV) at a slightly lower Reynolds number of 1.7×10^4. A full description of the PIV system used in this investigation and its operation can be found in section 3.5.

For comparison purposes, the flow in the wake of a circular cylinder was initially investigated in a plane perpendicular to the axis of the cylinder. The results of this investigation are shown in figure 5.20 where the flow in the wake at the mid-span of the cylinder is illustrated at three time instances. In each of the plots the flow is shown using both velocity vectors (in the plane of the laser sheet) and the associated vorticity contours. For velocity vectors, the direction of the vector indicates the direction of flow whilst the length of the vector indicates the magnitude of the velocity. Whereas for vorticity contours, the contour lines link regions of equal (within a specified interval) vorticity and the colours of the lines represent the level of the vorticity. From the three plots it can be seen how the shear layers interact to produce the Kármán vortex shedding in the wake. In the first plot a vortex is forming in the near wake as it is fed with positive vorticity from the lower shear layer. In the

second plot the vortex starts to be shed into the wake as the upper shear layer is drawn into the near wake. Finally in the third plot the vortex is completely shed as the upper shear layer begins to roll up into the next forming vortex. This cycle is repeated and results in the periodic shedding of alternately signed vortices into the wake that can clearly be seen from the three plots as the large local concentrations of vorticity downstream of the cylinder. However, it should be emphasised that whilst the three plots demonstrate the time evolution of the flow, they are instantaneous images of the flow taken hundreds of shedding cycles apart. The influence of these vortices on the flow in the wake can also be seen from the velocity vectors where the flow is found to oscillate in direction across the wake in a sinusoidal fashion as it travels downstream. This wake oscillation is found to be strongest in the near wake of the cylinder or vortex formation region where the local flow direction is found to be almost perpendicular to the freestream direction. However, this wake oscillation is found to reduce as the vortices weaken and travel downstream.

The flow in the wake of the sinuous cylinder was then investigated in a similar crossflow orientation at three parallel planes downstream of a peak, a trough and an inflection point. In figure 5.21 three plots of the flow in the wake downstream of a peak are illustrated. A striking feature of these plots in comparison with the flow in the wake of the circular cylinder is the complete absence of Kármán vortex shedding or any large vortical structures in the wake. The wake downstream of this spanwise location is found to vary very little over time and the three plots which are chosen represent the differences in the wake at three randomly chosen time instances. At each time interval the two separating shear layers show no signs of interaction in the near wake close to the cylinder although there may be a mild interaction at approximately 4D downstream as the wake closes up and the shear layers merge. The result of this lack of interaction can clearly be seen from the velocity vectors in the plots where the flow is found to be almost completely steady and symmetrical about the centre line. Hence, at this spanwise location the wake is found to be very similar in character at this high Reynolds number to the wake visualised at a Reynolds number of 100.

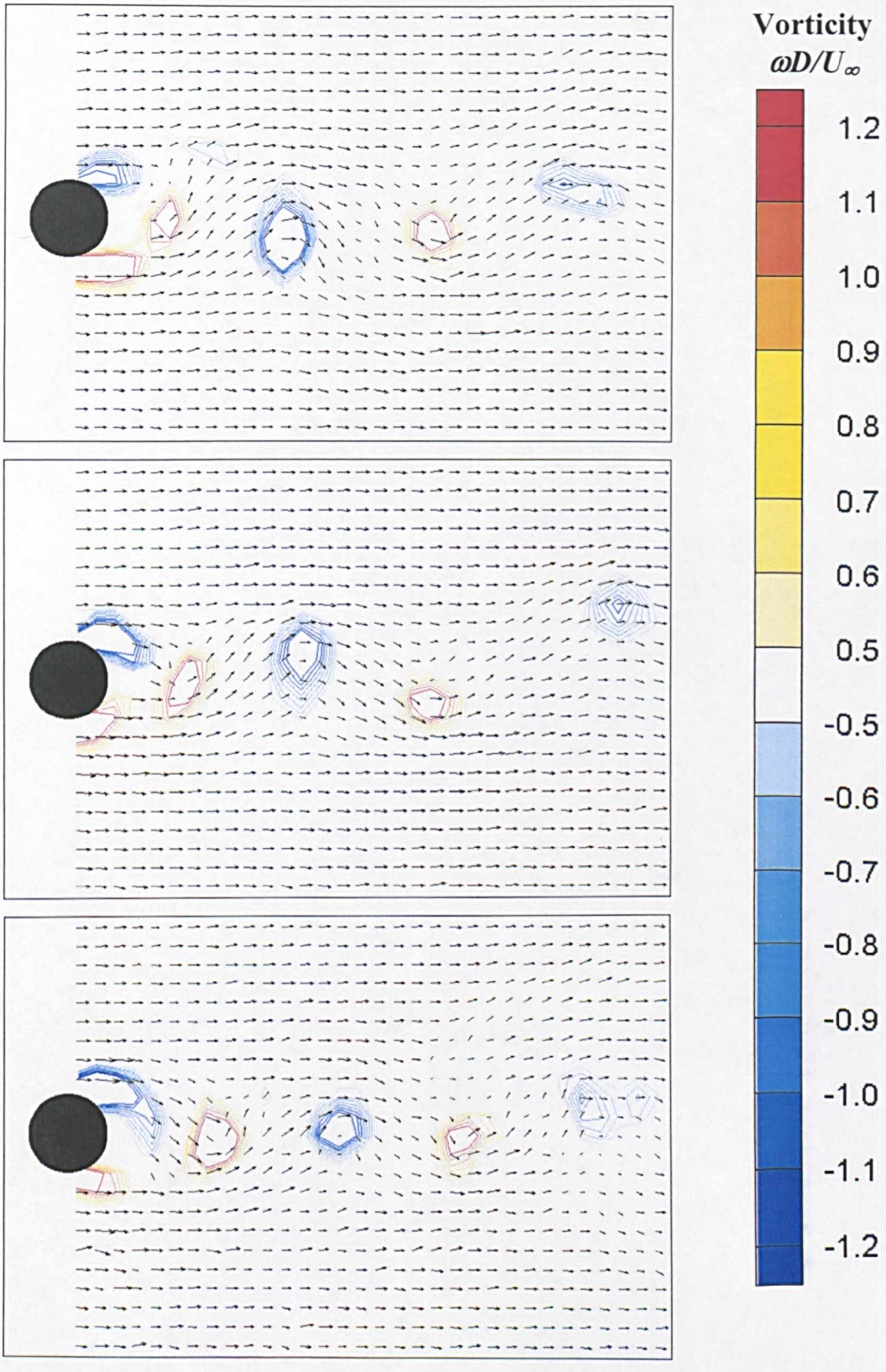


Figure 5.20 Three instantaneous PIV images in the wake of a circular cylinder at a Reynolds number of 1.7×10^4. The images are taken many shedding cycles apart but are arranged so as to show the shedding of a vortex from the lower shear layer. Contours illustrate non-dimensional vorticity.

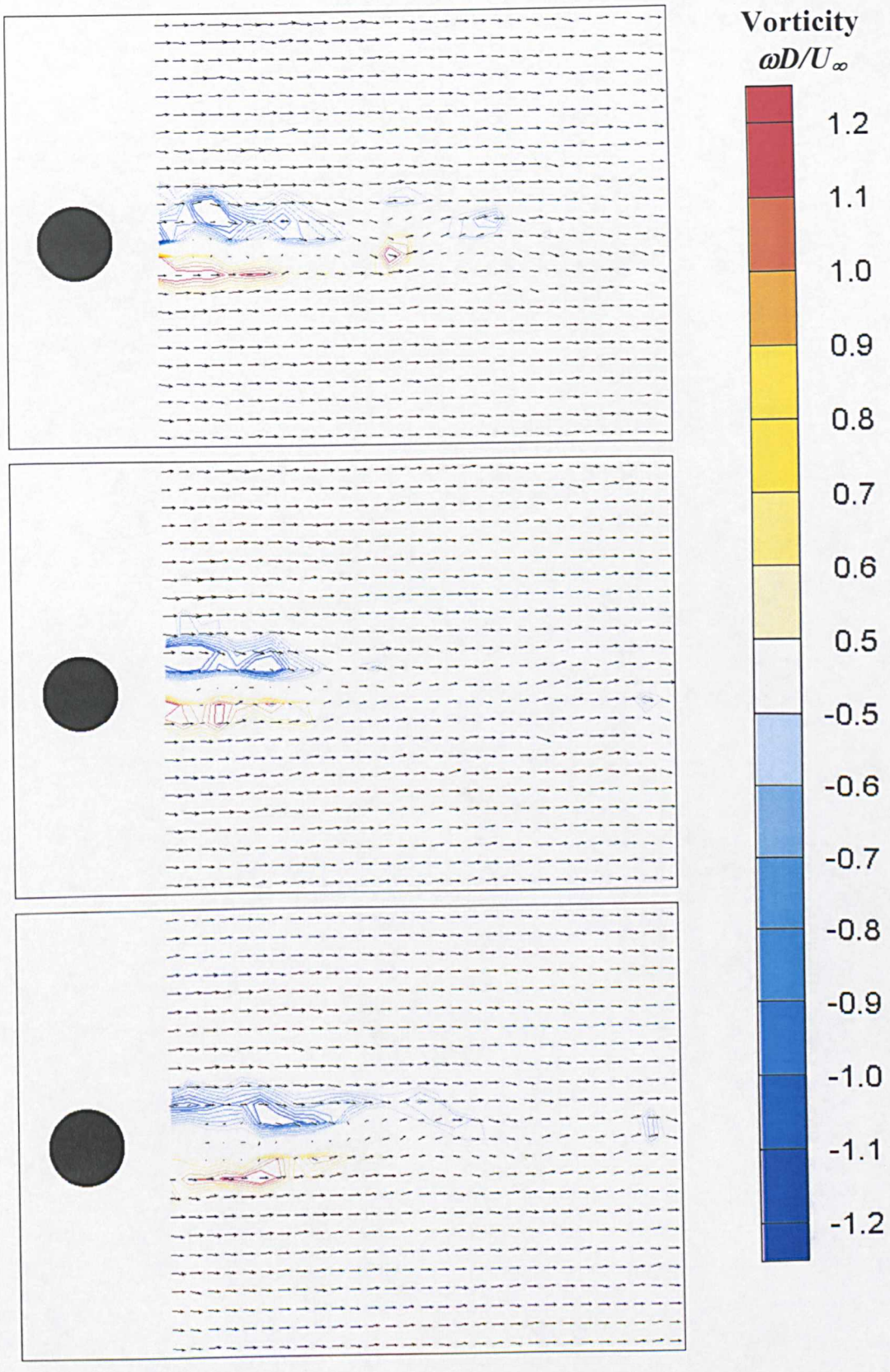


Figure 5.21 Three instantaneous PIV images in the wake of the sinuous cylinder downstream of a geometric peak at a Reynolds number of 1.7×10^4. The images reveal a complete lack of vortex shedding and wake unsteadiness. Contours illustrate non-dimensional vorticity.

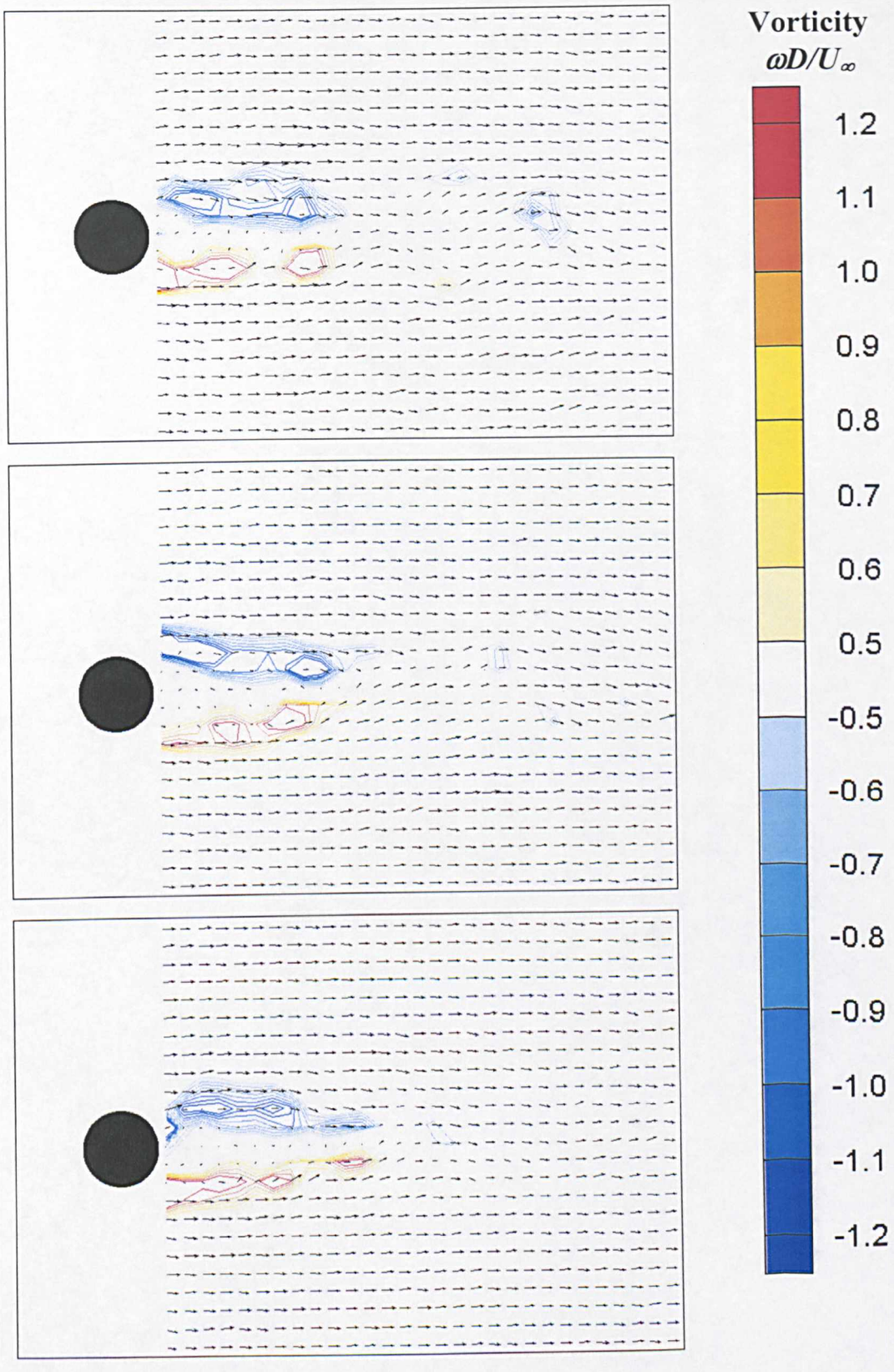


Figure 5.22 Three instantaneous PIV images in the wake of the sinuous cylinder downstream of an inflection point at a Reynolds number of 1.7×10^4. The images reveal a complete suppression of vortex shedding in the wake. Contours illustrate non-dimensional vorticity.

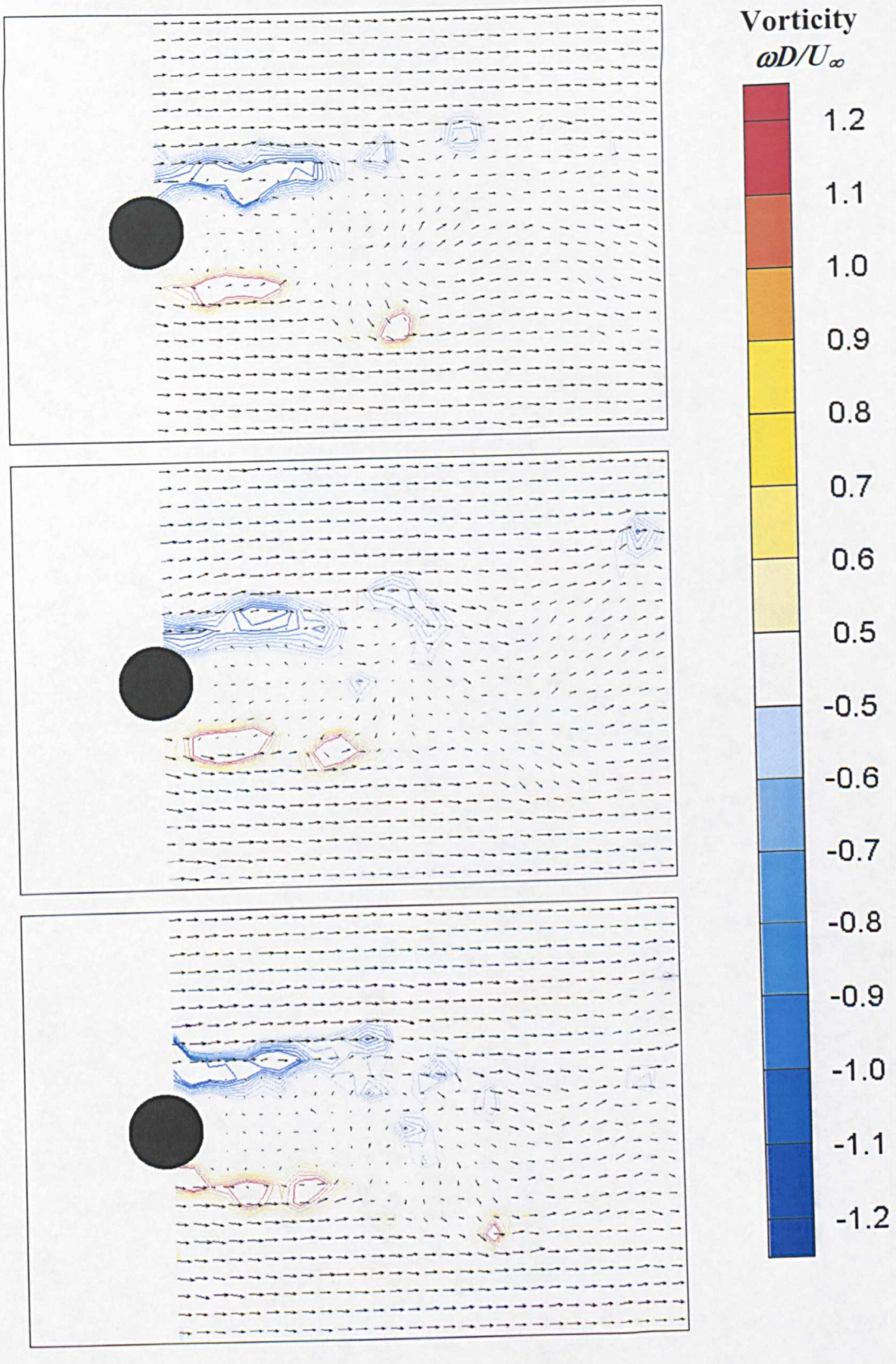


Figure 5.23 Three instantaneous PIV images in the wake of the sinuous cylinder downstream of a geometric trough at a Reynolds number of 1.7×10^4. The images show a significant increase in wake width and the random shedding from individual shear layers of vortices into the wake.

An almost identical type of wake is found downstream of an inflection point and is illustrated in figure 5.21. At this spanwise location the shear layers also show no signs of interaction within the near wake region although the overall width of the wake is found to be slightly larger than downstream of a peak. However, the wake is found to be significantly different downstream of a trough, figure 5.22. One of the most striking features of the wake at this spanwise location is that as suggested by hot-wire measurements and flow visualisation at lower Reynolds numbers, the wake downstream of a trough is substantially wider. In further confirmation of the hot-wire measurements the PIV results also illustrate that the width of the wake increases with downstream distance. The shear layers do not interact in the wake but rollup independently to form smaller shear layer vortices. The shedding of the vortices into the wake appears to be somewhat random, with no discrete frequency (as confirmed by hot wire measurements, figure 5.18) or dominant shedding mode, i.e. symmetric or anti symmetric shedding. However, unlike the wake downstream of the peak or inflection point the shedding of these shear layer vortices results in the wake downstream of the trough being mildly unsteady beyond approximately 4D downstream. At a distance of approximately 2-3D downstream of the cylinder flow can be observed emanating in all directions from an apparent source in the wake resulting in a region of reversed flow along the centre wake of the cylinder. Hence, the source is being fed with fluid flow from out of the plane. To investigate this further the wake was investigated in plan view.

In figure 5.24a the flow in the centre plane of the sinuous cylinder is shown in plan view, whilst in figure 5.24b flow in the wake of a conventional cylinder is shown for comparison. In the figures the flow is illustrated using velocity vectors. However, in this instance the colour is also used to signify the magnitude and direction of the vector upstream or downstream. Initial investigations in the wake of the sinuous cylinder found very little difference in the overall wake structure between pictures taken at different time instances. Therefore, for the purpose of improved clarity, the

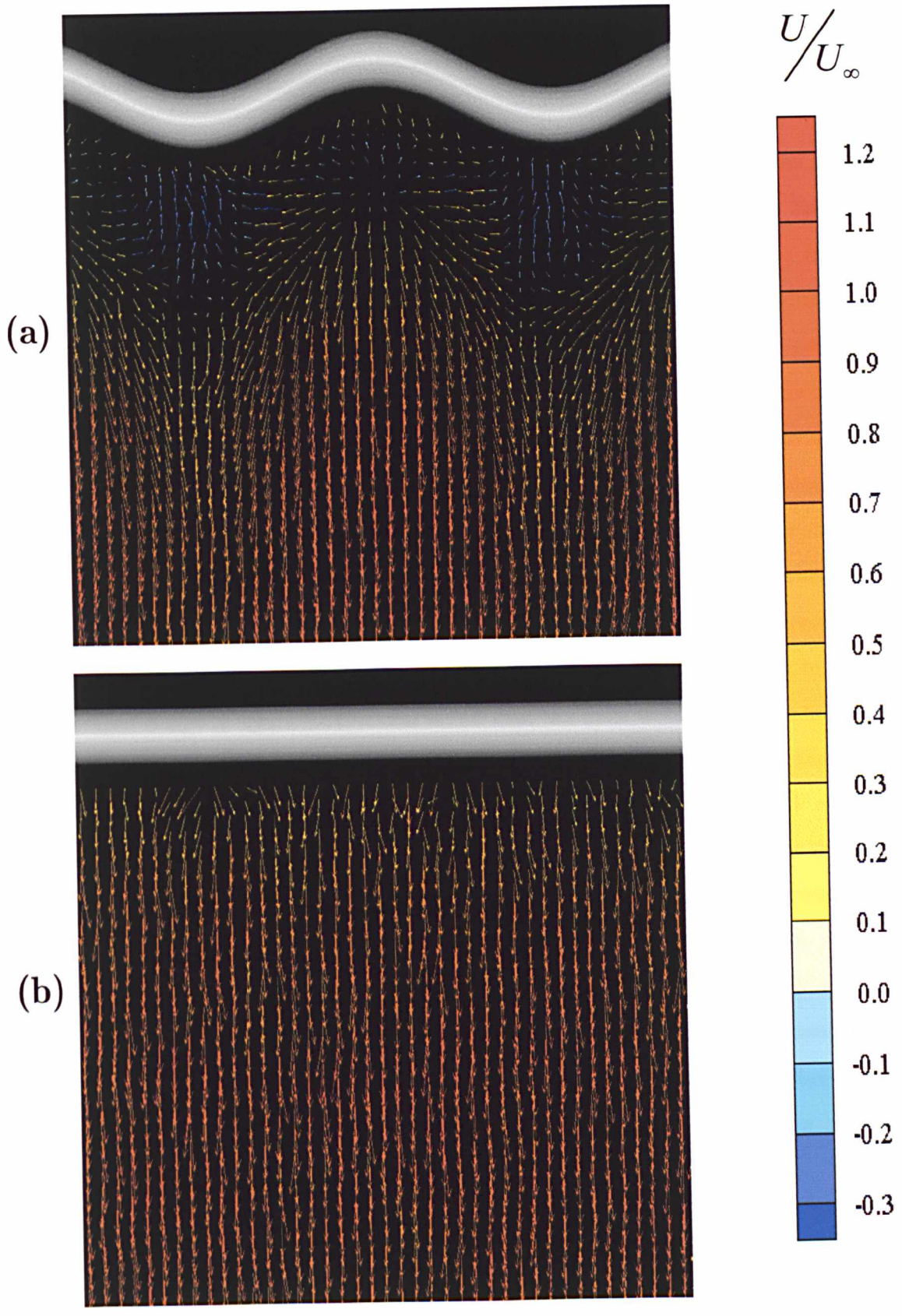


Figure 5.24 A comparison of plan view PIV images of the centre wake for the sinuous cylinder and the circular cylinder at a Reynolds number of 1.7×10^4. The vector magnitude is represented by both its length and colour to help highlight regions of reversed flow.

two plots presented in figure 5.24 are produced from an average of 10 PIV images taken at random time instances.

Comparison of the two plots in figure 5.24 reveals some dramatic differences in the wake structure between the two bodies. In the wake of the circular cylinder the flow appears almost two-dimensional whilst in the wake of the sinuous cylinder a regular three-dimensional structure is formed. Observations at approximately 3D downstream of the trough show the presence of a node in the flow confirming the previous hypothesis that flow enters this spanwise location from outside of the crossflow plane, figure 5.23. A further node can also be observed from figure 5.24a at approximately 2D downstream of a peak in the form of a source where flow can be seen entering the centre plane. The presence of this node can also be confirmed by re-examination of this location in the crossflow plane, figure 5.21. However, the position of this node downstream of the cylinder was found to vary between images taken at different time instances. By careful examination of individual PIV images that were used to build the averaged image in figure 5.24, it was found that the node would fluctuate between approximately 3D downstream and less than 1D downstream. At less than 1D downstream it was not possible to confirm the existence of a node as the PIV system was unable to determine any velocity components due to laser glare from the trailing edge of the model. However, the presence of a node can be inferred by the presence of downstream flow in this region close to the base of the model, figure 5.25a. At 3D downstream the node is out of the glare region and clearly visible to the PIV system as shown in figure 5.25b. This fluctuation in node position can also be confirmed from the frequency spectra in figure 5.16. The spectra were measured at a distance 2D downstream of the peak where the oscillations in node position can be seen on the centre wake as low frequency velocity fluctuations.

Further insight into the time mean structure of the wake can be gained from figure 5.26 that is an average of 10 instantaneous pictures. In the figure the flow is shown in a plane parallel to the centre plane but at a distance of 0.6D above it. In this configuration it is also possible to observe the flow approaching the cylinder although

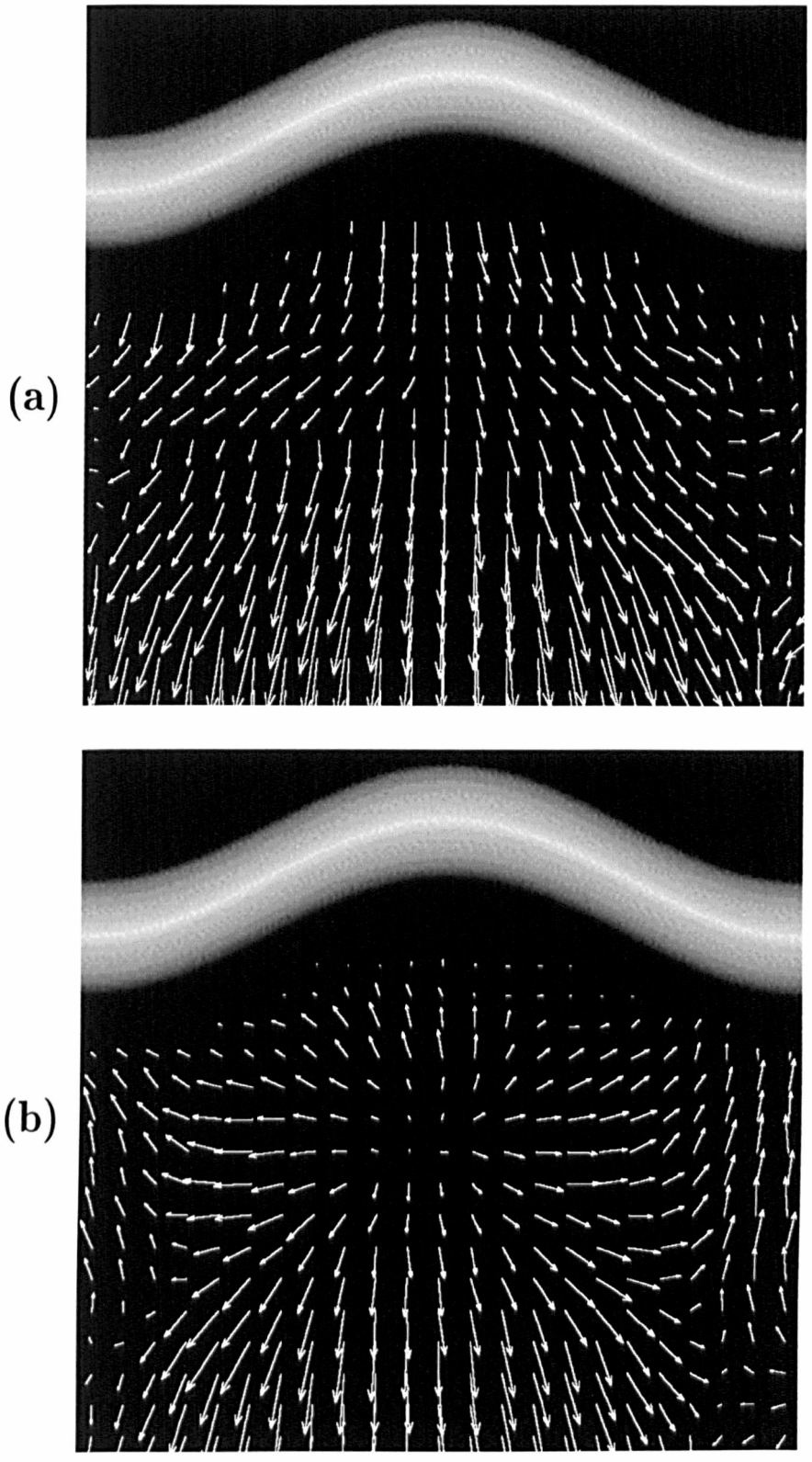


Figure 5.25 Details of the fluctuation in node position downstream of a peak: (a), node obscured in the glare region within 1D downstream of the model; (b), node clearly visible at approximately 3D downstream of the model showing the region of reversed flow towards the cylinder.

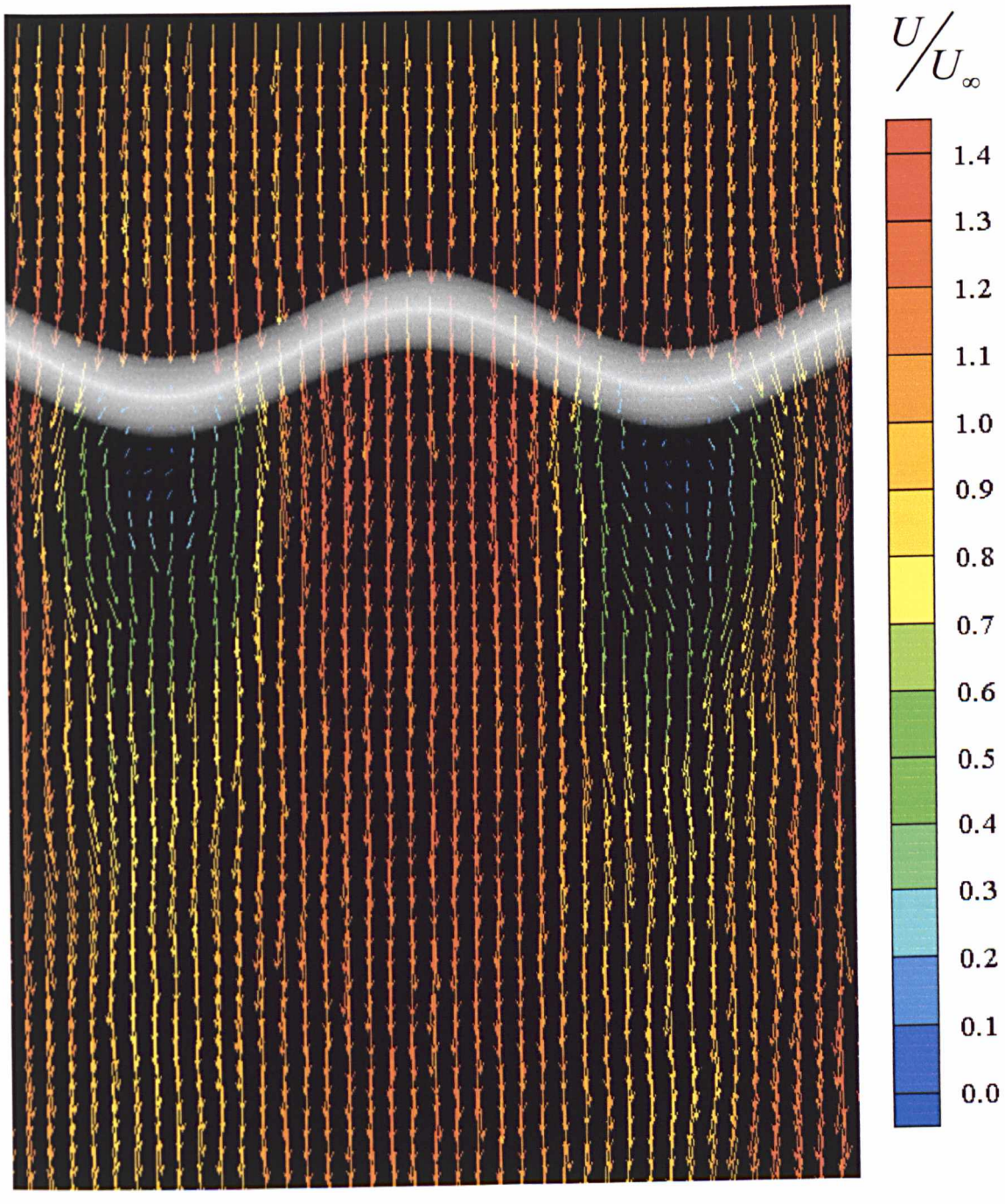


Figure 5.26 A plan view PIV image of the sinuous cylinder taken in a plane at 0.6D above the centre wake and at a Reynolds number of 1.7×10^4. The image clearly shows the increase in freestream velocity over the leading edge of the cylinder and the large wake regions downstream of the geometric troughs.

due to problems with laser glare from the cylinder surface the PIV system was unable to determine velocities in close proximity to the model. However, it should be noted that the velocity vectors in the figure only represent components of velocity in the plane of the laser sheet. From the figure it is apparent that whilst the flow downstream of peaks and inflection points within this plane returns to the freestream conditions relatively rapidly, the flow downstream of the troughs still shows a significant velocity deficit at over 10D downstream of the model. However, the effect of the sinuous geometry is also apparent upstream of the cylinder. From the figure the component of freestream velocity in the plane can be seen to locally yaw in a direction perpendicular to the leading edge as it flows over the cylinder in the regions of the inflection points. Hence, in addition to the separation line being forced to be approximately sinuous by the cylinder geometry, the sinuous geometry of the cylinder also leads to both streamwise and spanwise components of velocity at separation.

5.4 Discussion.

5.4.1 The three-dimensional structure of the wake.

At both high and low Reynolds numbers the preceding results confirm the existence of an organised three-dimensional structure in the wake and a complete absence of Kármán type vortex shedding for a wavelength $\lambda = 6D$ and wave steepness of $w/\lambda = 0.167$. However, if the mechanism for the suppression of Kármán type vortex shedding is to be understood, then it is important to examine this new wake structure in more detail. In figure 5.27 the experimental results for the sinuous cylinder at high Reynolds numbers are summarised in the form of a schematic diagram. By careful consideration of both PIV and base pressure results, it is possible to determine the critical points in the wake and establish the bulk flow between them. For clarity the flows in horizontal (parallel to the X-Y plane) planes are represented in blue whilst the flows in vertical planes (parallel to the X-Z plane) are represented in black.

Immediately apparent from the figure are the substantial differences in wake structure between the peaks and troughs and the flows between them. At a peak the wake

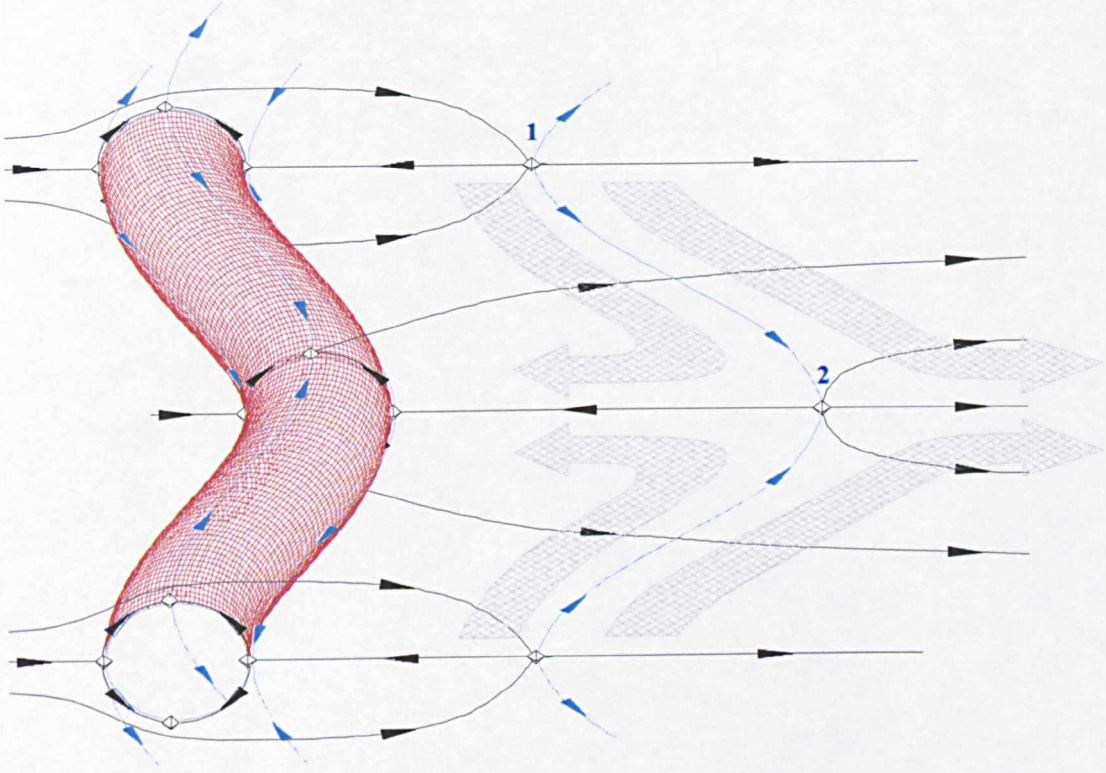


Figure 5.27 A schematic diagram determined from PIV images showing the time mean streamlines in the wake of the sinuous cylinder at a Reynolds number of 1.7×10^4.

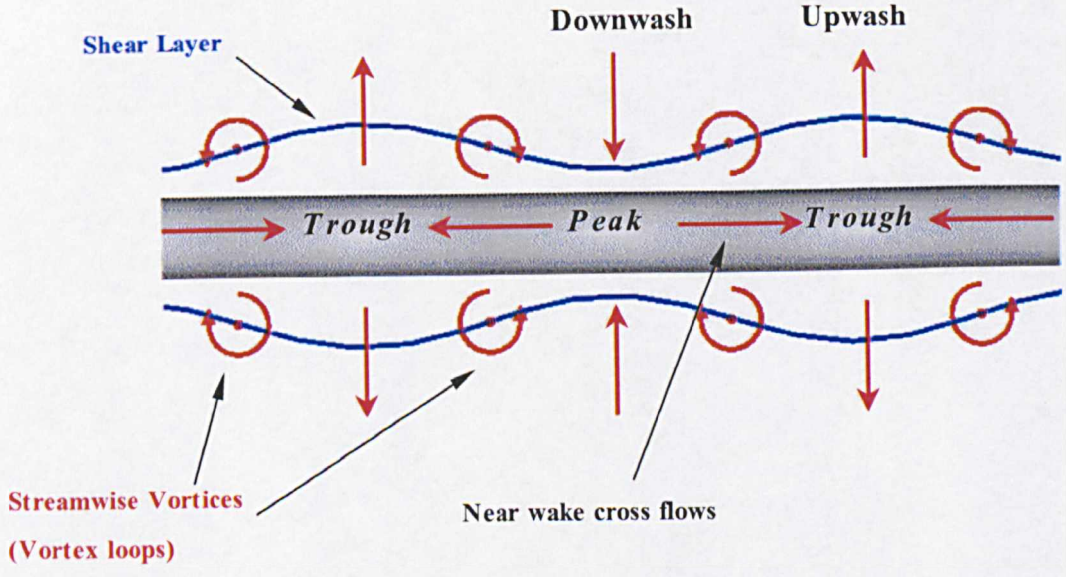


Figure 5.28 A schematic view from downstream showing how the shear layers are distorted under the action of the streamwise vortices in the near wake.

closes downstream of the cylinder at node 1 to form a node in space which was shown to oscillate in streamwise direction in figure 5.25. This wake closure subsequently results in flow entering the wake at this spanwise position being channelled across the base region and into the wakes of the troughs. In contrast to the peaks, the wake downstream of the troughs is widening with downstream distance and a second node is observed in space (node 2) as an apparent source in the vertical plane, figure 5.23. The supply of fluid for this apparent source is provided by the flow that is channelled across the near wake from node 1. The figure also illustrates the flow on the surface of the cylinder inferred from the surface pressure distribution. Importantly it shows that the predominant flow on the front face of the cylinder is from the peaks to the troughs, whilst the flow across the rear face of the cylinder is in the reverse direction from the troughs to the peaks.

A similar transport of fluid out of the wake downstream of the peaks and into the wakes of the troughs is also apparent at low Reynolds numbers in figures 5.7 & 5.8. In the figures the fluorescein dye used for flow visualisation is released evenly along the leading edge of the cylinder but is channelled into the wake downstream of the troughs. This effect is particularly evident in figure 5.7 where the shape of the near wake can clearly be seen with a much higher intensity of dye observed downstream of the troughs. In comparison with the flows in the wake at higher Reynolds number, this near wake shape shows many similar to the schematic representation of the wake in figure 5.27. Hence, an important feature of the wake at both high and low Reynolds numbers would appear to be the spanwise transport of fluid from the wakes of the peaks to the wakes of the troughs.

5.4.2 The suppression of Kármán type vortex shedding.

Gerrard (1966b) showed that interaction between the shear layers was a fundamental component of Kármán vortex shedding and that if the shear layers could be prevented from interacting then vortex shedding could be suppressed. Bearman (1967) showed that one way to prevent this interaction was to bleed fluid between the two separating

shear layers. By doing this it was found that the wake of a semi-ellipse section could be stabilised and Kármán vortex shedding suppressed if sufficient quantity of fluid was bled into the wake. In the present investigation a similar type of base flow can be observed in the wake of the sinuous cylinder downstream of the troughs where fluid from the wakes of the peaks travels across the wake and is injected between the two separating shear layers, figure 5.27. This injected fluid is then entrained between the two shear layers and prevents them from interacting as the flow is convected downstream. The resulting free shear layers are then observed from PIV and flow visualisation to rollup independently to form a series of discrete vortices at both high (figure 5.23) and low (figure 5.9b) Reynolds numbers. Therefore, it is likely that entrainment of fluid between the shear layers is the mechanism by which vortex shedding is suppressed in the wake downstream of the troughs.

PIV investigations in the wake downstream of the peak (figure 5.21) and inflection point (figure 5.22) show a very similar wake structure. This similarity is also confirmed by the resulting base pressure distribution (figure 5.13) where the base pressure is found to be approximately constant from the peak to the inflection point. Therefore, it would it would appear that the wake structure and flow conditions are approximately constant between a peak and an inflection point resulting in a spanwise cell of uniform flow over approximately half a geometric wavelength or approximately 3D. Investigations of the wake in this cell at high Reynolds numbers show the wake to be steady (apart from a low frequency in-line wake fluctuation downstream of the peak) with a complete absence of vortex shedding. At low Reynolds numbers where the flow is laminar, vortex shedding has been observed downstream of the peaks and inflection points both by Honji & Ishi (1976) at Re = 121 and in the present investigation at Re = 250. However, both of these observations where made for cylinders of longer wavelengths, λ = 12.8D for Honji & Ishi (1976) and λ = 7.5D in the present investigation at low Reynolds number. Therefore, at higher Reynolds numbers where the shear layers are turbulent and with a cylinder of shorter wavelength (6D) it is possible that the wake cannot become sufficiently correlated to establish vortex shedding in the wake. Hence further research is needed before the

mechanism for the suppression of vortex shedding over these regions of the cylinder span can be fully explained although it is suspected that the optimum wavelength for the sinuous cylinder is likely to be less than 6D.

5.4.3 Streamwise vortices.

In the previous sections it was proposed how the wake of a sinuous cylinder which varied in width periodically across the span could remain stable and prevent vortex shedding. In addition, a fundamental component of this suppression involved the transport of fluid in the near wake from the peaks to the troughs, although the mechanism for the generation of this wake structure is so far unclear. However, up to this point in the analysis the presence of streamwise vorticity and its effects have yet to be considered.

It has been shown in may previous studies that a common feature of three-dimensional bluff body wakes where vortex shedding is suppressed is the emergence of streamwise vortices. For example, Petrusma & Gai (1994, 1996) visualised streamwise vortices in the wake of a segmented trailing edge aerofoil that suppressed vortex shedding in the wake, figure 1.9. They suggested that the presence of streamwise vortices was as a result of spanwise vorticity being partially 'converted' into streamwise vorticity. A similar effect can be seen in the present investigation for the sinuous cylinders at low Reynolds numbers where forming spanwise vortices are rapidly stretched into streamwise vortices downstream of the troughs, figures 5.7 & 5.8. By considering the rotational sense of these streamwise vortex loops, the induced velocity field can be evaluated in a vertical plane at several diameters downstream of the sinuous cylinder, figure 5.28. From the figure it is quickly apparent that the presence of the streamwise vortices accounts for the variation in wake width across the span. Downstream of a peak the streamwise vortices generate a downwash forcing a narrow wake whilst downstream of a trough the streamwise vortices produce an upwash forcing the formation of a wide wake. In addition, the streamwise vortices also account for the transport of fluid from the wakes of the peaks to the wakes of the

troughs by inducing a velocity component across the centre of the wake from the peaks to the troughs. By considering the velocities that the vortices induce on themselves it can be determined that the vortices will move apart across the wake and move together downstream of the peak which is found to be consistent with observations of the vortex loops as they move downstream.

Whilst the above analysis and figure 5.28 are based on the observation of vortex loops at low Reynolds numbers there results are also consistent with observations at higher Reynolds numbers. The resulting wide and narrow wakes and near wake crossflows imply the existence of streamwise vorticity although it was not possible to confirm the existence of discrete streamwise vortices in the wake due to experimental inadequacies. Therefore, it can be concluded that the generation of streamwise vorticity in the configuration illustrated in figure 5.28 is fundamental to the generation of a three-dimensional wake structure (figure 5.27) and consequently the suppression of vortex shedding.

5.4.4 The generation of streamwise vorticity.

In the previous section streamwise vortices have been shown as the fundamental component in the suppression of vortex shedding. Therefore, the generation of streamwise vorticity is of great importance if vortex shedding is to be avoided.

Wu *et al.* (1994) investigated the flow in the wake of a circular cylinder where streamwise vortices were superimposed on the regular Kármán shedding. The streamwise vortices were generated using an array of small delta wings (span $\approx$ 0.25D) that were positioned several diameters upstream of the cylinder. However, these were found to have very little effect on the regular Kármán shedding in the wake. Therefore, whilst the intention of the study was not to suppress vortex shedding it demonstrates the principle that the superposition of relatively small or weak vortices on the wake of a circular cylinder has little or no effect on the vortex shedding in the wake.

However, an important effect that has so far remained unaddressed is the rollup of the shear layers. Unlike the investigation of Wu *et al.* (1994), the streamwise vortices in the wake of the sinuous cylinder are not simply superimposed on the wake but are contained within the shear layers. This results in the three-dimensional rollup of the shear layers with the shear layers rolling in both the spanwise and streamwise directions. With a small component of streamwise vorticity the wake continues to shed vortices in an approximately two-dimensional fashion. However, as the amount of streamwise vorticity in the shear layers is increased regular Kármán type vortex shedding begins to breakdown. Initially it would be expected the cells of different shedding frequency would emerge resulting in vortex dislocations as was shown by Tombazis & Bearman (1997) for the wake of a semi-ellipse section. But as the level of streamwise vorticity is increased still further the three-dimensional rollup of the shear layers would cause a spanwise transport of flow in the near wake from the peaks to the troughs eventually leading to the organised wake structure illustrated in figure 5.27. Therefore, it can be concluded that the generation of three-dimensional shear layers is fundamental in the generation of a three-dimensional wake structure and the suppression of vortex shedding.

If the shear layer contains components of both streamwise and spanwise vorticity then this implies that at the point of separation there must be components of both streamwise and spanwise velocity. Therefore, the flow must be yawed to the freestream flow direction at separation in order to generate the required three-dimensional shear layers in the wake. In addition, just as there is a level of wave steepness that needs to be exceeded before vortex shedding is suppressed so it follows that there must be a local yaw angle of the flow at separation that needs to be exceeded before shedding is to be suppressed. Hence wave steepness ultimately controls the local yaw angle of the flow at separation and consequently the component of streamwise vorticity shed into the shear layers.

For the sinuous cylinder of wave steepness of $w/\lambda = 0.167$, the maximum local yaw angle at separation can be found using the PIV image in figure 5.25. From the figure the maximum yaw angle of the flow is found close to the geometric inflection points where the local flow is yawed to an angle of approximately 10° to the freestream, figure 5.29. From this local yaw angle, the streamwise component of vorticity (at this spanwise location) is found to be approximately 18% of the spanwise. Therefore, as the sinuous cylinder suppresses vortex shedding in the wake completely it can be concluded that the generation of a streamwise component of vorticity of approximately 18% of spanwise is sufficient to prevent the correlation of Kármán type vortex shedding in the wake.

From the leading edge pressure distribution (figure 5.14) and surface flow visualisation, a component of velocity of approximately 40% of freestream was found across the front face of the model from peak to trough, section 5.3.2. This flow along the front face was discovered during early investigations and was initially believed to be beneficial in the disruption and suppression of vortex shedding. However, by considering the velocity components normal and tangential to the separation line it can be seen that this flow is in fact detrimental to the cylinder's ability to suppress shedding, figure 5.30. In the figure the separation velocity (U_{sep}) at a geometric inflection point is resolved into its components normal to (U_n) the separation line and along (U_t) the separation line. By considering the velocities it can be seen that the effect of the flow from the peak to the trough along the separation line is to reduce the local yaw angle of the flow at separation and hence the component of streamwise vorticity shed into the wake. Alternatively, this reduction in the strength of streamwise vorticity can also be explained by considering the sign of the vorticity generated by this crossflow along the separation line. It is found that this vorticity is of the opposite sign to the favourable streamwise vorticity in the wake (generated by the yawed flow at separation) and hence reduces its strength. Therefore it is expected that the sinuous cylinders would be more effective at suppressing vortex shedding and reducing drag if this leading edge crossflow could be reduced.

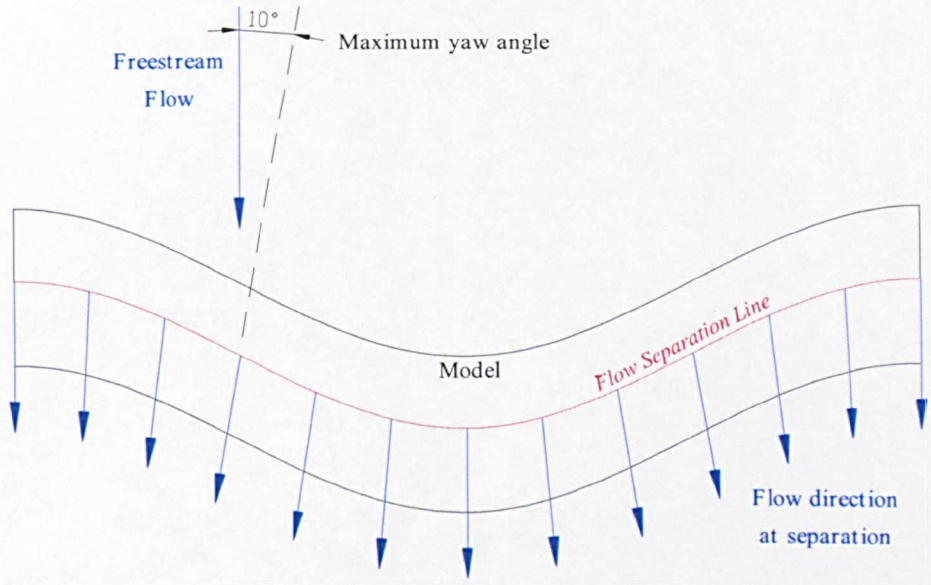


Figure 5.29 A schematic diagram determined from PIV illustrating the flow orientation at separation for the sinuous cylinder. The maximum yaw angle of the flow is found near to the inflection points and is determined to be equal to an angle of approximately 10° to the freestream flow.

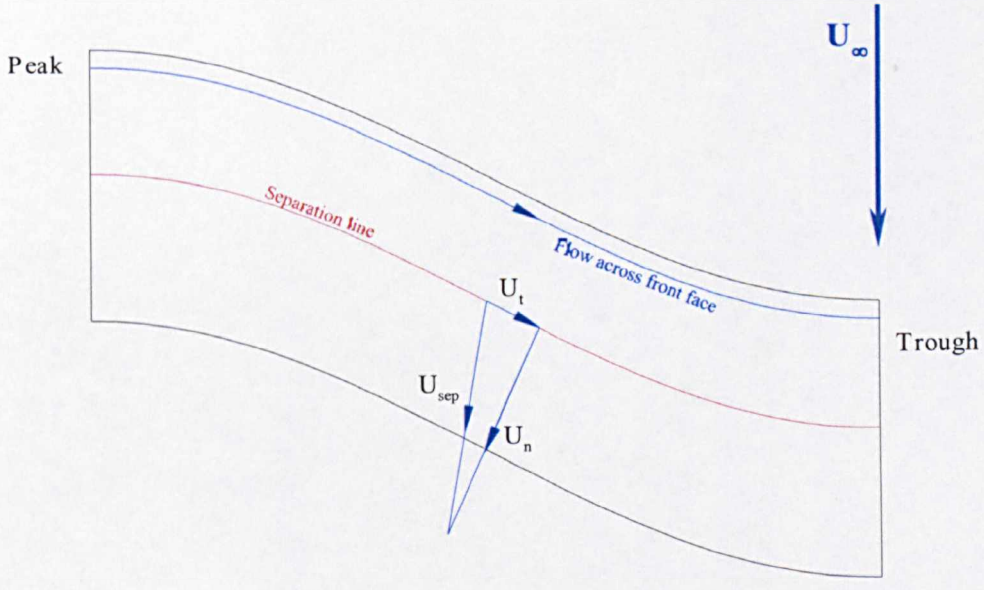


Figure 5.30 Velocity details at the inflection points of the separating flow for the sinuous cylinder: U_∞, freestream flow; U_{sep}, the resultant flow velocity at separation; U_n, component of velocity normal to the separation line; U_t; component of velocity tangential to the separation line.

The concept of local yaw angle of the flow at separation is also useful because it removes the geometric dependence of the model in our understanding of the suppression of vortex shedding. In previous studies (Naumann *et al.* (1966), Tombazis & Bearman (1997), Bearman and Owen (1998a)) the geometry of the flow separation line has been highlighted as an important parameter in the suppression of vortex shedding although equally the geometry of the leading edge has also been considered important (Darekar & Sherwin 2001). However, from a geometric perspective, a model only needs to be designed that can set-up the desired variation in flow separation angle across the span. In designing such a model both separation line and attachment line will be important but the underlying requirement is for a geometry that can yaw the flow at separation leading to the production of three-dimensional shear layers. The design and development of new body geometries that use the concept of local yaw angle at separation and practical applications of sinuous cylinders will be discussed in chapter 6.

In summary it has been shown that the wake of a sinuous circular cylinder shows many similarities to the wake of a wavy square section cylinder. Vortex shedding is suppressed above a critical wave steepness and substantial drag reductions are achieved as a new three-dimensional wake structure is produced. The ratio of streamwise to spanwise vorticity is suggested to be the parameter that governs the suppression of vortex shedding and this ratio is expressed through the concept of local yaw angle of the flow at separation.

5.4.5 Experimental errors.

Errors in wind tunnel measurements of drag where typically of the order of 0.5% between repeats with the balance accurate to within 0.1% in drag. Further details of the accuracy and set-up of the wind tunnel experiments can be found in section 3.4.

Errors in the PIV data are in general very small (less than 1% of freestream) and can be corrected for via post-processing of the interrogated data. A full description of the

system accuracy and calculation of potential errors in the interrogation system can be found in Elliott (2000).

6 The suppression of vortex shedding using surface protuberances.

6.1 Introduction.

It was shown in the previous chapter that vortex shedding could be suppressed in the wake of a cylindrical body by the introduction of sufficient spanwise three-dimensionality. The resulting wake was observed to vary in both size and character along the span although fundamentally the wake was approximately symmetrical about the centre plane at all spanwise positions. From an engineering perspective the resulting wake from the sinuous cylinder used in these experiments is far more desirable as it suppresses the unsteady transverse forces associated with vortex shedding that act on the cylinder. However, a possible problem with the sinuous cylinder is that it is found to be directionally sensitive (figure 5.12) which makes it impractical in the majority of applications were the flow direction is unknown. Therefore, the motivation behind the work in this chapter was to determine the possibility for producing a body that could generate the favourable wake of the sinuous cylinder from all approaching flow directions.

6.1.1 Previous devices.

Before any new geometric configuration can be considered, it is important to examine previous attempts at the suppression of vortex shedding using spanwise three-dimensionality. Within this field of research many ideas have been proposed and tested although some have proved more successful than others. An example of one such successful device would be the helical stake as has been previously considered in section 1.5. However, the majority of other three-dimensional geometries have proved unsuccessful in their attempts to suppress vortex shedding. An example of such a geometry would be the wavy cylinder of Ahmed *et al.* (1993), illustrated in figure 6.1. This cylinder consists of a circular cross-section body that varies in diameter periodically along the span. In Ahmed *et al.* (1993), the two spanwise extremities

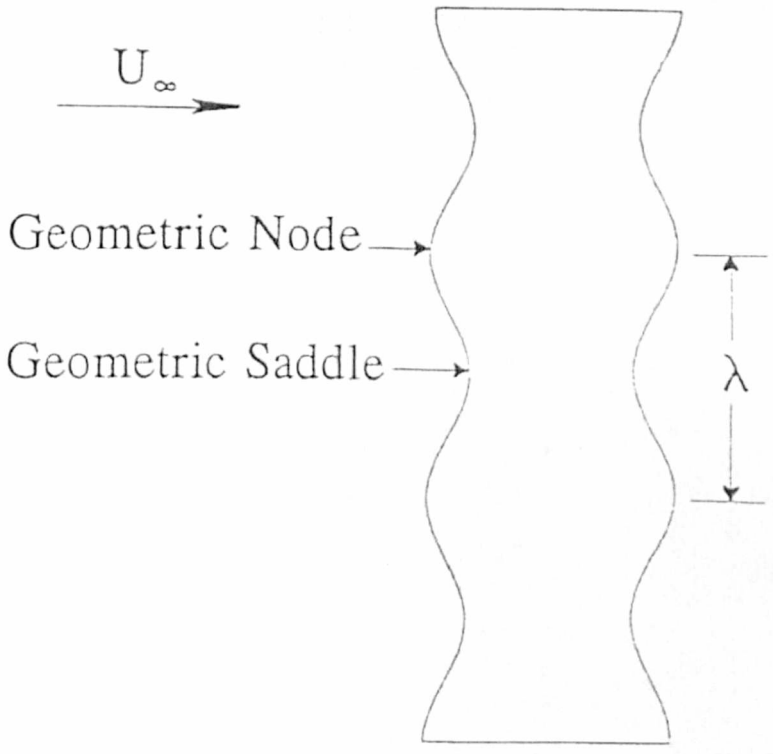


Figure 6.1 Schematic diagram of the wavy cylinder investigated by Ahmed *et al.* (1993).

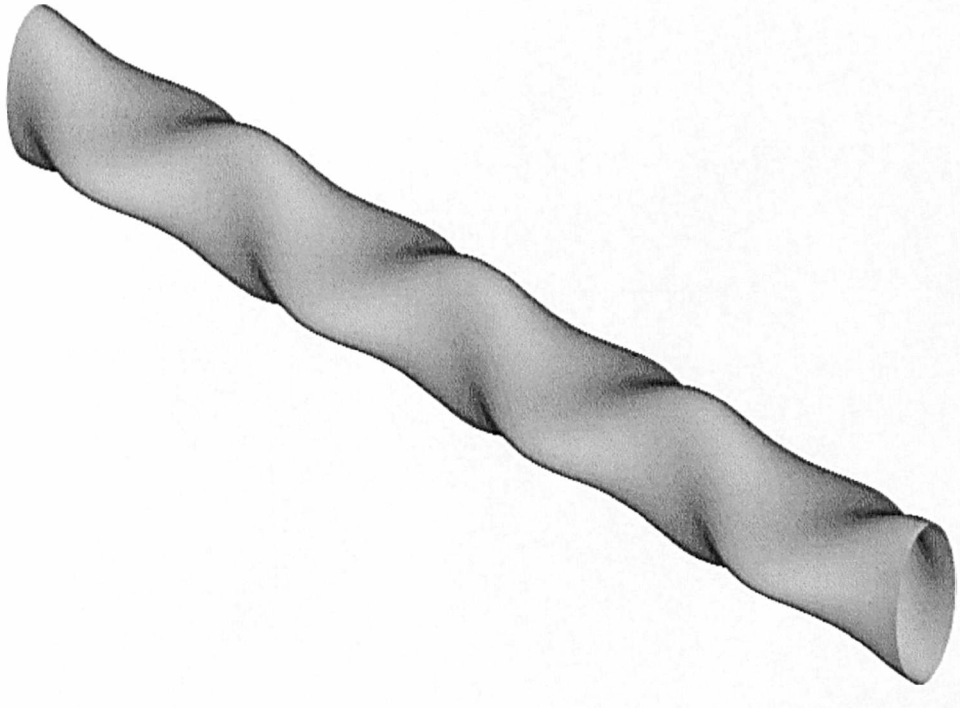


Figure 6.2 Schematic representation of a body where the waviness of the front and back is half a wavelength out of phase with the waviness of the sides.

were then defined as a geometric saddle (where the diameter is smallest) and a geometric node (where the diameter is largest), figure 6.1.

Initial investigations in the wake of this wavy cylinder using flow visualisation (Reynolds number 5×10^3 - 2×10^4) revealed Kármán type vortex shedding in the wake downstream of both a spanwise node and a spanwise saddle. However, flow visualisation also showed the wake to be narrower downstream of a node than the wake downstream of a saddle. Hence, the wake was widest where the diameter was smallest and narrowest where the diameter was largest. This result is surprising as it would be conventionally expected for a two-dimensional cylinder that the wake width would scale on the diameter and hence the wake would be widest were the body was widest. However, this phenomenon can be explained by re-examination of the three-dimensional flow around the sinuous cylinder from the previous chapter. By considering the leading edge geometry of both the Ahmed *et al.*'s wavy cylinder and, the sinuous cylinder it is found that a narrow wake is formed in both instances where the body extends furthest upstream. In addition, a wide wake is formed in both instances where the body extends furthest downstream. Hence, for the wavy cylinder, the variation in wake width caused by the effect of the leading edge geometry tends to work in opposition with the variation in cylinder diameter resulting in the formation of a wake of approximately constant width. Therefore, it is apparent that the introduction of spanwise three-dimensionality in this configuration is ineffective at suppressing Kármán type vortex shedding in the wake. Hence, this result demonstrates that the simple introduction of spanwise three-dimensionality to cylinder geometry is not sufficient condition to suppress or even disrupt vortex shedding in the wake.

6.1.2 The design of a vortex suppression device.

Investigation of the wavy cylinder of Ahmed *et al.* leads to the realisation that a more effective geometric configuration can be developed if the effects of the wavy leading edge and the variation in diameter can be made to be additive along the span. This

could be achieved if the waviness of the leading and trailing edges and the waviness of the sides (currently in phase along the span for the wavy cylinder) were shifted half a wavelength out of phase. Hence, in the spanwise regions where the body was the narrowest it would also extend furthest upstream. Therefore, as a result of the local leading edge geometry it is likely that a narrow wake would be formed at these spanwise locations where the body is narrowest. Similarly, it would also be expected that as a result of the local leading edge geometry, a wide wake would be formed where the body is widest. An initial sketch of how such a body might look is illustrated in figure 6.2. However, whilst the body should work in principle, in practice it would be extremely difficult to manufacture, making it impractical as a viable suppression device. Therefore, a simpler design is required that can combine ease of manufacture with the important geometric features needed for the suppression of vortex shedding in the wake.

In the search for a simpler geometric configuration many designs were considered although ultimately only one design was manufactured and tested. The final design involved fitting the cylinder with elliptically shaped surface protuberances as shown in figure 6.3. These surface protuberances are parts of ellipsoids that can be fitted to the cylinder in various arrangements as illustrated in the figure. The advantages of this design were twofold. Firstly, from an experimental perspective it allowed many different geometric configurations to be easily investigated, whilst from a practical perspective, such surface protuberance could be easily retrofitted to existing cylindrical structures in engineering environments. Ultimately these protuberances were designed to be fitted in the configuration illustrated in figure 6.3b although other configurations as illustrated in the figure were also investigated.

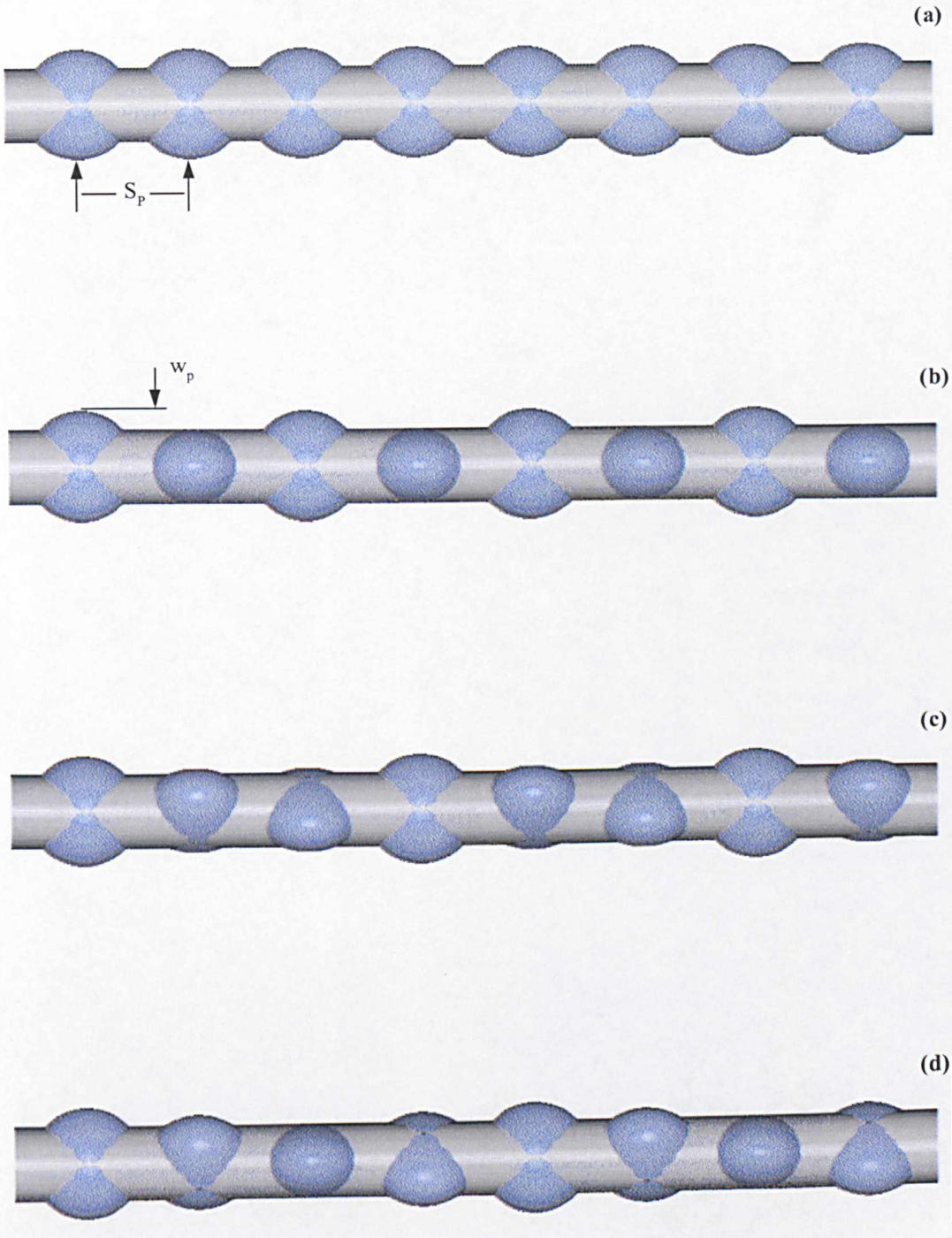


Figure 6.3 Various geometric configurations of elliptically shaped surface protuberances: (a), protuberances fitted to the front and back of the cylinder; (b), protuberances fitted to the front, back and sides of the cylinder; (c), protuberances fitted in a spiral pattern around cylinder – angular separation 60°; (d), spiral pattern – angular separation 45°.

6.2 Experimental models.

6.2.1 Model construction.

The elliptically shaped surface protuberances were moulded in two halves using a fast set epoxy resin system that was cast in a semi-ellipsoidal shaped mould. In order to position the protuberances precisely on the cylinder surface an accurate grid pattern was drawn on the cylinder using a three-axis milling machine and dividing head. Using this grid pattern the protuberances could then be simply taped or glued on to the cylinder in the desired configuration.

The base cylinder used for initial drag measurements and PIV had a diameter of $40mm$ and an aspect ratio of $l_{span}/D = 22$. In addition a second cylinder of larger diameter ($110mm$) was also manufactured for the purpose of surface pressure and drag measurements at higher Reynolds numbers. This second cylinder had a shorter aspect ratio of $l_{span}/D = 9$ and incorporated 36 circumferential surface pressure tappings located at 10° intervals around the centre span of the cylinder. The pressures sensed by these tappings were then measured using an ultra sensitive Honeywell pressure transducer and 48 way scanivalve installed within the cylinder model. The cylinder itself was manufacture from a piece of PVC tubing that was supported within the tunnel via an internal metal skeleton. In addition, as the model was to be tested within the critical transition regime, great care was taken during the manufacture of the cylinder to ensure that the surface was free from any scratches that may cause the premature turbulent transition of boundary layer.

The wind tunnel used during these experiments (4½'×4' wind tunnel, section 3.4) had a turbulence intensity of less than 0.5% and in all instances cylinder models were fitted with circular endplates of diameter 5D. Wind tunnel blockages for the small and large cylinders were 3% and 8% and were corrected in all instances by the method describe in Allen & Vincenti (1944).

6.2.2 Model configurations.

As a means of comparison with the sinuous cylinder and between various geometric configurations of surface protuberances the parameter of surface steepness is introduced. Similar to wave steepness it is defined for the present models as w_P/S_P where w_P is the height of the protuberance above the surface and S_P is the spanwise spacing between adjacent protuberances, figure 6.3. However, unlike the wavy square cylinders and sinuous circular cylinders where only the wave height was varied whilst the wavelength was held fixed, for these models the protuberance height (w_P) will be constant and only the spanwise spacing (S_P) varied. In addition to the spanwise spacing, for the omnidirectional configurations of surface protuberances the relative rotation between adjacent protuberances will also be investigated. These rotations will be 180°, 90°, 60° & 45° as illustrated in figure 6.3.

6.3 Initial results.

6.3.1 Introduction.

In this section the results of various arrangements of surface protuberances will be presented. The results that follow will be divided into two sections, unidirectional suppression devices and omnidirectional suppression devices. In each case attempts have been made to determine the optimum configuration of surface protuberances. However, it should be noted that it is not the intention of this investigation to develop a perfectly optimised commercial suppression device. Overall the aim of this work is to demonstrate the potential for the suppression of vortex shedding in the wakes of cylindrical structures by simple modifications to the body form. Hence, the configurations developed subsequently are only an introduction to what could be achieved with further research.

Determination of the optimum configuration of surface protuberances for the suppression of vortex shedding is in practice very difficult. Parameters such as size, shape, spanwise spacing and rotation of protuberances are all factors that could, in

theory, affect the vortex shedding in the wake. Therefore, for the purpose of this initial investigation a fixed size and shape of protuberance will be used and only the spanwise spacing and relative rotation varied.

In order to confirm the suppression of vortex shedding in the wake of the sinuous cylinder an extensive investigation was conducted, chapter 5. However, such a detailed investigation in the wake of each model would be impractical if many configurations of surface protuberances were to be tried. Therefore, a simpler way for quickly determining the relative success of a particular configuration was needed. One simple way that the intensity of vortex shedding in the wake could be estimated was by measuring the C_D of each configuration. From the previous results of chapters 4 & 5 it was shown that the attenuation or suppression of vortex shedding in the wake typically results in reductions in C_D of up to 35%. Therefore, by making the assumption that any reduction in C_D was primarily the result of weaker vortex shedding in the wake, then it was relatively simple to optimise the configurations for minimum drag and hence minimum vortex shedding. Hence all subsequent configurations are only optimised for minimum C_D and not minimum strength of vortex shedding.

6.3.2 Unidirectional suppression of vortex shedding.

A unidirectional suppression device would be highly practical in an engineering situation where the flow is from predominantly up or downstream. An example of such a situation could be the tidal flow in a river estuary past a pipeline or the cylindrical leg of a pier. In such a situation unidirectional suppression of vortex shedding could be achieved relatively easily by using the previously described sinuous cylinder (chapter 5). However, it is unlikely that a cylinder with such a distorted or wavy axis would ever be practical in any type of load bearing or structural applications. Therefore, a cylinder with a straight axis fitted with surface protuberances offers a far more practical solution for most engineering applications.

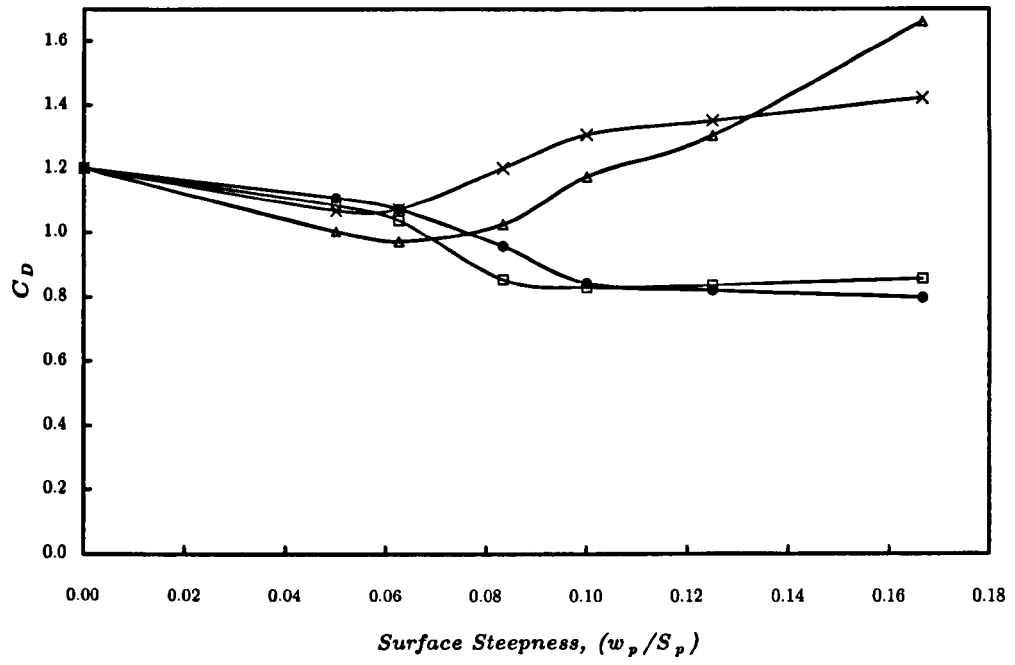


Figure 6.4 The effect of surface steepness on C_D at various incidences for a cylinder fitted with front and rear surface protuberances, Re = 8×10^4: •, 0° incidence; □30° incidence; ×, 60° incidence; Δ, 90° incidence.

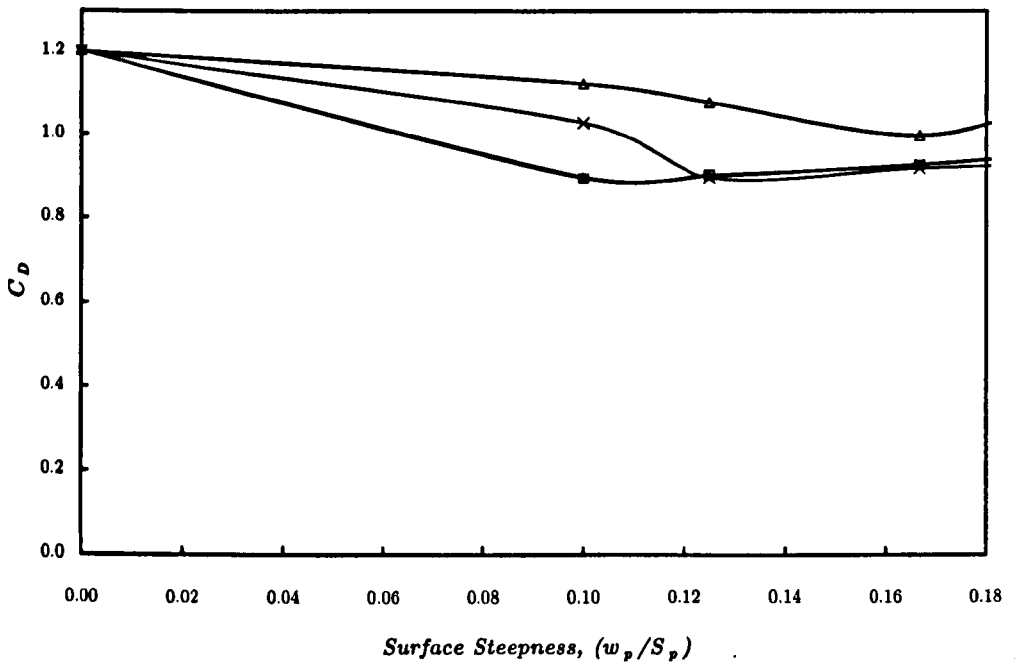


Figure 6.5 The effect of surface steepness on C_D at various incidences for a cylinder fitted with surface protuberances on the front, back and sides, Re = 8×10^4: •, 0° incidence; □15° incidence; ×, 30° incidence; Δ, 45° incidence.

Initial drag experiments with the surface protuberances fitted to the front and rear face of the cylinder showed a similar trend to the sinuous circular cylinder with an increase in surface steepness leading to a reduction in C_D, figure 6.4. From the figure it can be seen that the C_D is reduced from a value of 1.2 to approximately 0.8 for a surface steepness in excess of $w_P/S_P = 0.10$. For the current protuberance height (0.25D) this level of surface steepness can be achieved by a spanwise spacing of approximately 2.5D. A similar trend is also found for the cylinder at an incidence of 30° where the surface protuberances are found to be of similar effectiveness to an incidence of 0° for values of surface steepness in excess of $w_P/S_P = 0.10$. Therefore, a drag reduction of this magnitude is comparable with the drag reduction achieved using the sinuous cylinder (section 5.2.2) where vortex shedding in the wake was suppressed.

However, at higher incidences (60° & 90°) the surface protuberance are found to be less effective with the C_D rising sharply from a value of 1.2 to almost 1.65 for a value of surface steepness of approximately $w_P/S_P = 0.167$. At these higher angles of incidence the projected frontal area of the cylinder fitted with protuberances is found to be significantly increased resulting in an additional increase in drag. However, evaluation of the C_D based on the frontal area still results in a C_D of approximately 1.2 suggesting that the surface protuberances at this incidence cause minimal disruption to the vortex shedding in the wake.

In summary, initial drag results have shown a 33% reduction in C_D by the fitting of surface protuberances to the front and rear of a circular cylinder. A drag reduction of this magnitude is sufficient to suspect that vortex shedding in the wake of the cylinder has been suppressed. The range of spanwise spacings over which this suppression is achieved is found to be between 1.5 & 2.5D and over an incidence range of +30° to -30°. The next stage was to investigate the possibility for development of an omnidirectional suppression device.

6.3.3 Omnidirectional suppression of vortex shedding.

Whilst the development of a unidirectional suppression device is useful, the development of an omnidirectional suppression device is of far greater engineering importance where the flow direction is rarely fixed.

The first stage in the development of an omnidirectional configuration was to modify the unidirectional configuration by orientating alternate pair's of protuberances at 90° to the freestream flow, figure 6.3b. In this configuration the effects of spanwise spacing and cylinder incidence were again investigated, figure 6.5. At an incidence of 0° the C_D is initially reduced from a value of 1.2 to approximately 0.9 as the surface steepness is increased up to $w_P/S_P = 0.10$. However, further increases in surface steepness result in an increase in C_D as a reduction in the spanwise spacing of protuberances results in an increase in projected frontal area of the model and hence an increase in drag.

The effect of increasing incidence can also be seen from figure 6.5 where due to the regular pattern of surface protuberances it was only necessary to make measurements of incidence up to an angle of 45°. At an incidence of 15° an almost identical trend in C_D is observed to 0°. This trend is approximately continued as the incidence is increased to 30°, particularly for value of surface steepness in excess of $w_P/S_P = 0.125$. However, at an incidence of 45° the C_D rises sharply for all spacings of surface protuberances. This sharp rise in C_D is too large to be accounted for by an increase in projected frontal area, implying an increase in base suction and hence an increased intensity of vortex shedding in the wake. Therefore, in this configuration, the body is not completely omnidirectional in it's ability to suppress vortex shedding in the wake.

To overcome this problem, the next step was to distribute the protuberances in a spiral pattern around the cylinder at a reduced angular interval between adjacent protuberances of 60°, figure 6.3c. In this instance it is only necessary to plot the variation of C_D with surface steepness (figure 6.6) up to an incidence of 30° due to the regular spacing of surface protuberance around the cylinder. However, it can be seen

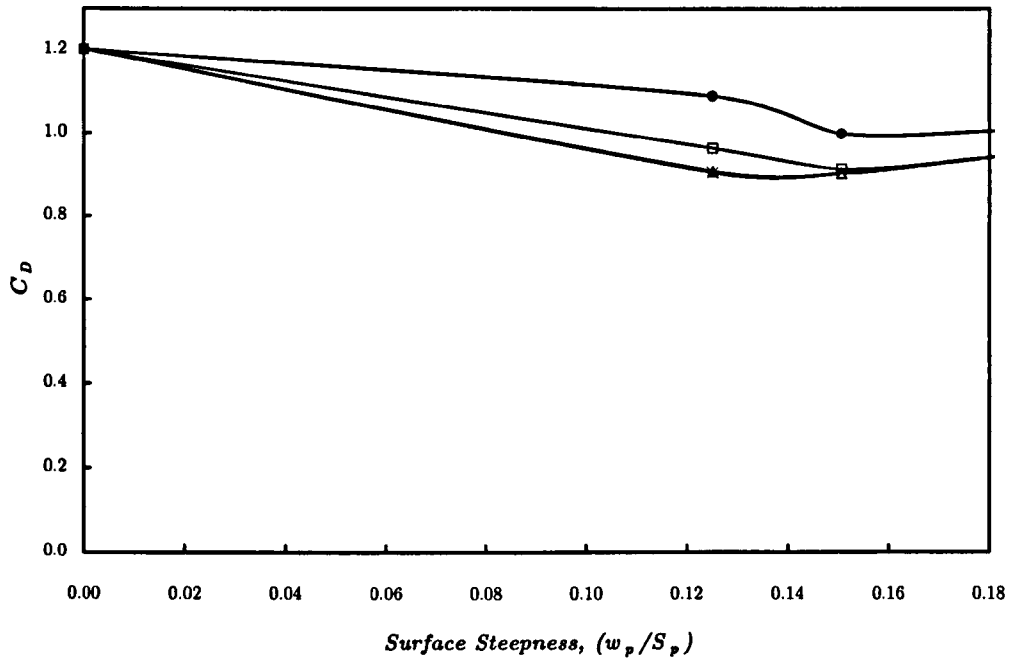


Figure 6.6 The effect of surface steepness on C_D at various incidences for a cylinder fitted with surface protuberances arranged in a spiral pattern – angular separation between adjacent protuberances = 60°, Re = 8×10^4: •, 0° incidence; □ 1 0° incidence; ×, 20° incidence; Δ, 30° incidence.

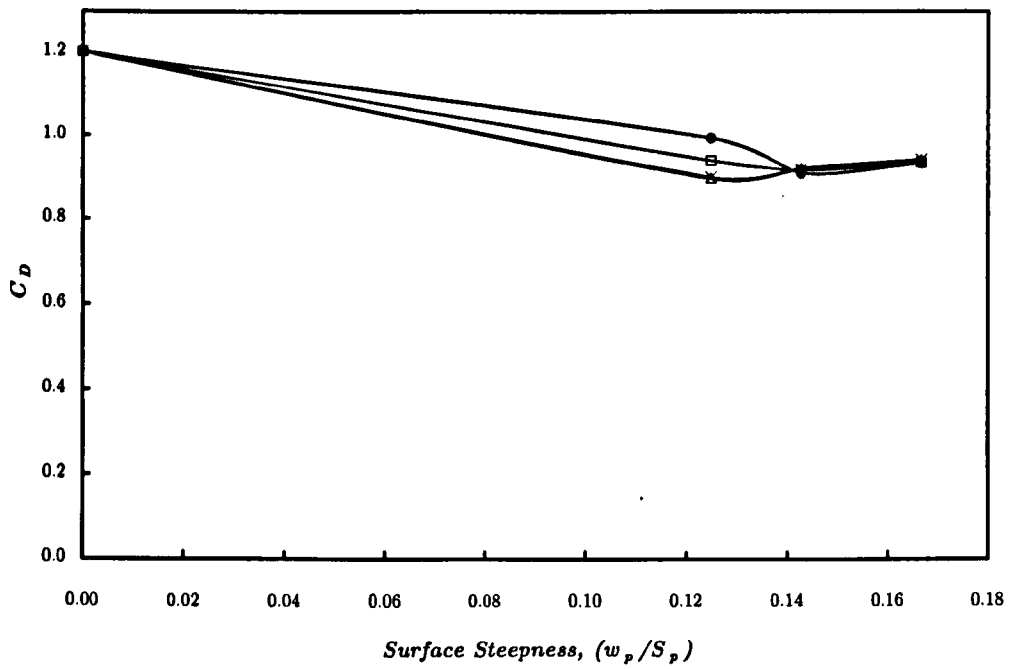


Figure 6.7 The effect of surface steepness on C_D at various incidences for a cylinder fitted with surface protuberances arranged in a spiral pattern – angular separation between adjacent protuberances = 45°, Re = 8×10^4: •, 0° incidence; □7 . 5° incidence; ×, 15° incidence; Δ, 22.5° incidence.

from the figure that this configuration of protuberances is again unsuccessful at producing a truly omnidirectional suppression device as the drag again rises sharply, this time at an incidence of 30°.

Therefore, the angular interval between adjacent protuberances was reduced still further from 60° to 45°, figure 6.7. In this configuration, and for a surface steepness in excess of $S_p/w_p = 0.14$ the cylinder was found to produce a constant reduction in C_D of 25% from all freestream directions suggesting a truly omnidirectional device. However, for lower values of surface steepness or a larger spanwise spacing between protuberances the C_D was again found to vary with increasing incidence. Therefore, a spanwise spacing of 1.5 -1.75D is required if the body is to be omnidirectional.

As a final example of the effectiveness of different configurations of surface protuberances for the omnidirectional reduction in drag, figure 6.8 is included. In the figure the spanwise spacing of the protuberance is held constant and only relative rotation between adjacent protuberances is varied. The figure clearly shows that the cylinder becomes far less directionally sensitive as the relative rotation between protuberances is reduced, although at this spanwise spacing (S_p = 2D) no configuration is found to be completely omnidirectional.

For further investigation it was decided that a unidirectional and omnidirectional configuration of surface protuberances should be selected. For the unidirectional configuration a spanwise spacing of S_p = 1.5D was chosen whilst for the omnidirectional configuration the spanwise spacing was S_p = 1.75D with a relative rotation between adjacent protuberances of 45°. This omnidirectional configuration can be essentially regarded as a spiral pattern with a geometric pitch of 7D.

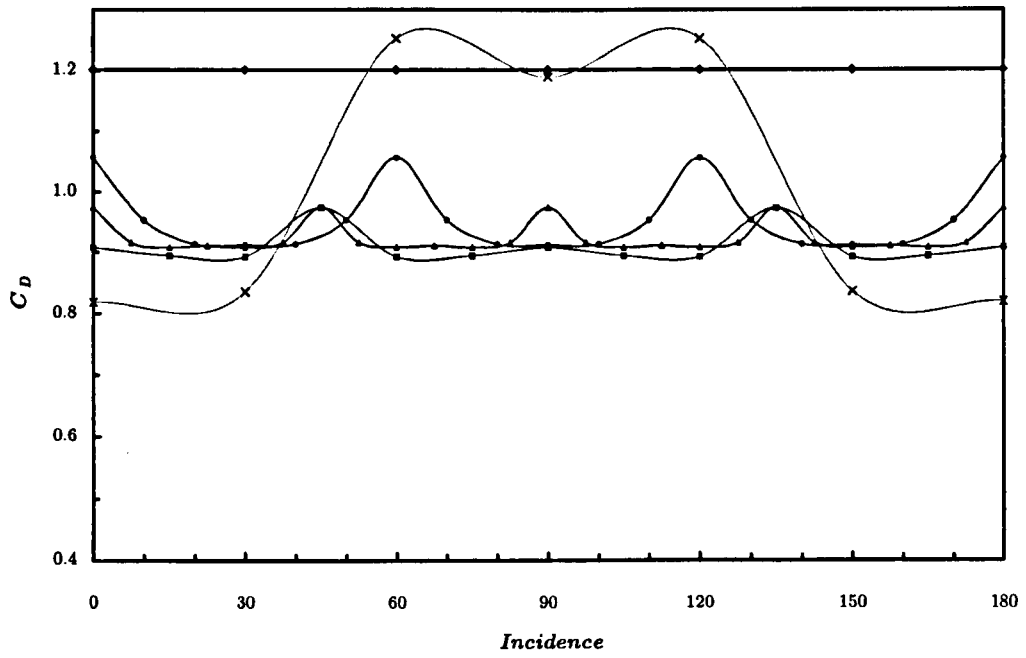


Figure 6.8 The effect of incidence on C_D for cylinders fitted with surface protuberances at a fixed spanwise spacing of S_P = 2D but of different relative rotations between adjacent protuberances: ×, 180° rotation between protuberances; □ 90° rotation between protuberances; •, 60° rotation between protuberances; Δ, 45° rotation between protuberances.

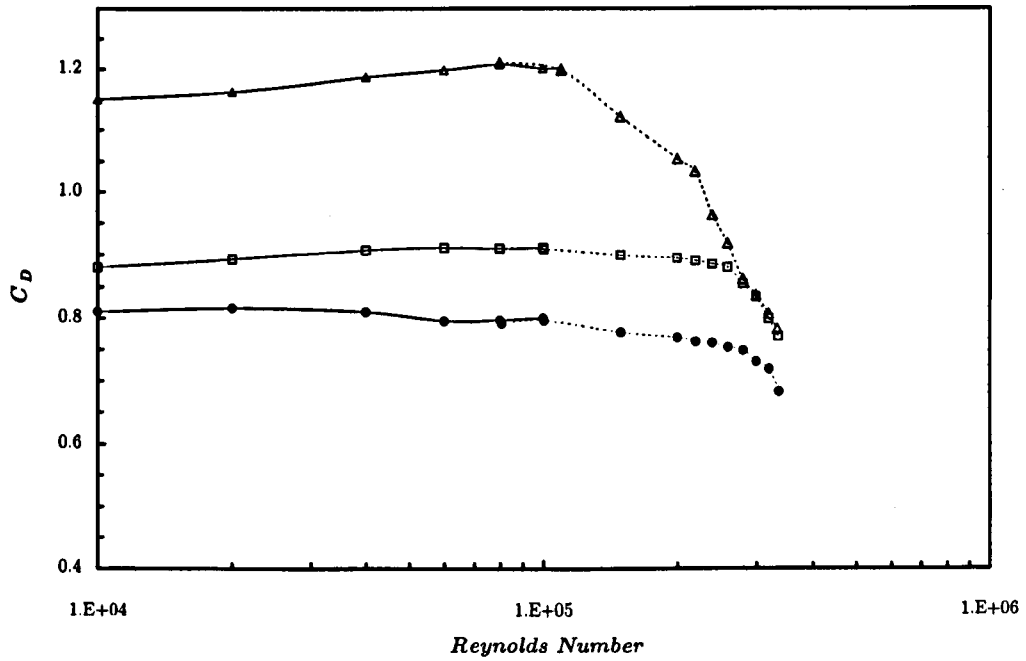


Figure 6.9 The effect of Reynolds number on C_D for cylinders fitted with surface protuberances: Δ, plain cylinder; •, unidirectional suppression device; □ omnidirectional suppression device.

6.4 Detailed results.

6.4.1 Variation of C_D with Reynolds number.

A common disadvantage of many suppression devices is that they increase the C_D of the cylinder. This increase is particularly evident in the critical transition regime (Re = 3×10^5 - 10^6) where the C_D of a plain circular cylinder falls from 1.2 to approximately 0.4 as a result of the separation and reattachment of the shear layers. However, for a cylinder fitted with helical strakes the C_D is found to be constant throughout this regime at a value of approximately 1.45 (section 1.5). Therefore, it was of interest to understand how the C_D of a cylinder fitted with surface protuberances would vary within this regime.

Initially the effect of Reynolds number was investigated on the plain cylinder although due to experimental restrictions the maximum Reynolds number that could be achieved was only 3.4×10^5. At this Reynolds number the cylinder was only just into the critical transition regime and as a result the C_D was only found to be reduced from a value of 1.2 to approximately 0.8, figure 6.9. However, unlike helical strakes, it can be seen from the figure that the C_D for the cylinders fitted with surface protuberances reduces in a similar fashion to the plain cylinder. For the unidirectional configuration the C_D has dropped to a value of approximately 0.7 at a Reynolds number of 3.4×10^5 whilst for the omnidirectional configuration this value is found to be approximately 0.8. From the figure it would appear that these values will continue to drop as the Reynolds number is increased further although it would be difficult to accurately predict the resulting C_D for the cylinders on the basis of these results. However, it can be expected that the omnidirectional configuration will ultimately have a higher C_D than the plain cylinder in the supercritical regime as unlike the unidirectional one not all the protuberances are inline with the flow resulting in an increase in frontal area.

It is unfortunate that these trends could not be investigated to a higher Reynolds numbers although on the basis of these results it can be expected that the boundary

layer transition process from laminar to turbulent will be largely unaffected by the addition of the surface protuberances.

6.4.2 Surface pressure distribution.

In this section the circumferential variation in surface pressure around the cylinder at centre span is presented for the various arrangements of surface protuberances. The layout of the surface pressure tappings used to measure these pressure distributions is described in section 6.2.1 and illustrated for the omnidirectional configuration in figure 6.10.

Initially the surface pressure distribution was investigated for all cylinder configurations at a Reynolds number of 10^5, figure 6.11. At this Reynolds number it can be seen from the figure that the pressure distribution for all cylinders is approximately symmetrical about the centre wake. For the plain cylinder the base pressure coefficient is found to be C_{Pb} = -1.5 with the flow separating from the cylinder surface at an angle of approximately 80° from the front stagnation point. However, on examination of the C_P distribution for the cylinders fitted with protuberances it is quickly apparent that the drag reductions achieved by these devices is as a result of a substantial increase in base pressure. For both the uni and omnidirectional configurations this value of base pressure coefficient is found to be reduced by approximately 50% to C_{Pb} = -0.75. To accommodate this increase in base pressure the flow separation point is also observed to move forward from 80° from the front stagnation point to 65°.

At a higher Reynolds number of 2×10^5 a similar trend is apparent with both the unidirectional and omnidirectional configurations showing an increase in base pressure over the plain cylinder, figure 6.12. However, at this Reynolds number the base pressure for the plain cylinder has increased slightly whilst the base pressure for the cylinders fitted with surface protuberances has reduced. Therefore, and as confirmed

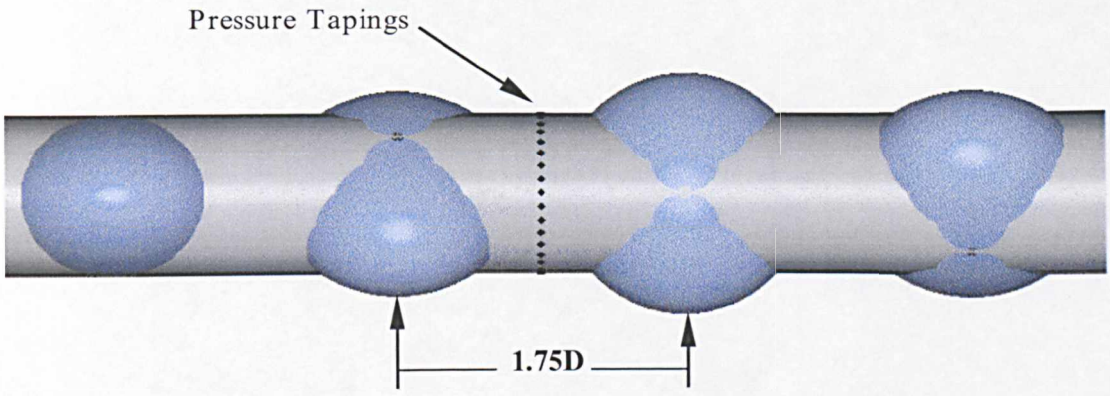


Figure 6.10 Schematic diagram of the layout of surface protuberances and surface pressure tapings for the omnidirectional suppression device.

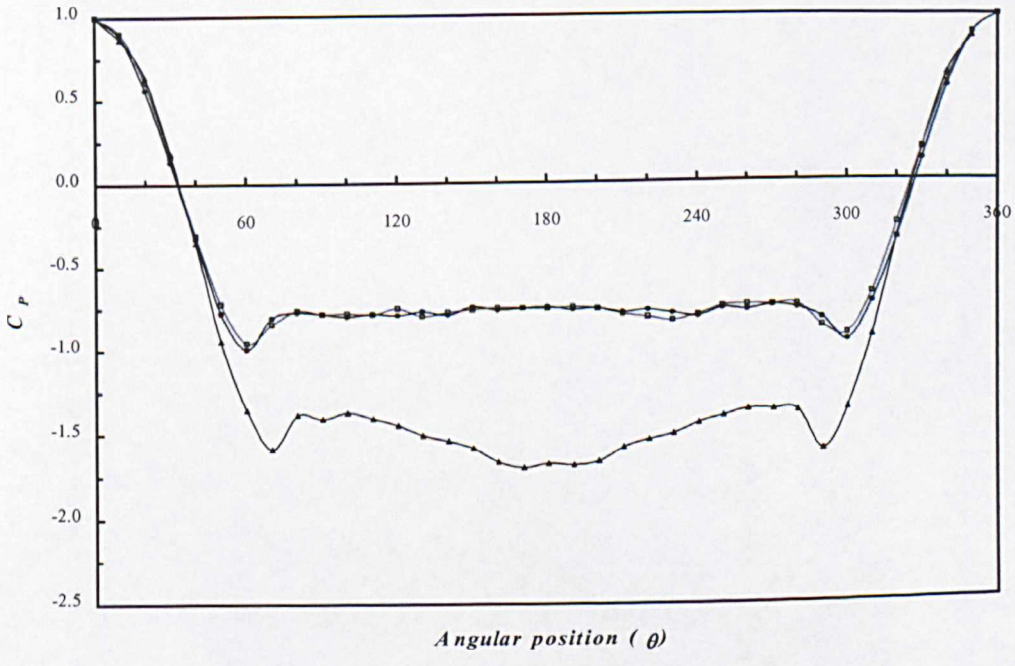


Figure 6.11 Circumferential variation in surface pressure coefficient around the cylinder at a Reynolds Number of 10^5: Δ, plain cylinder; •, unidirectional suppression device; □, omnidirectional suppression device.

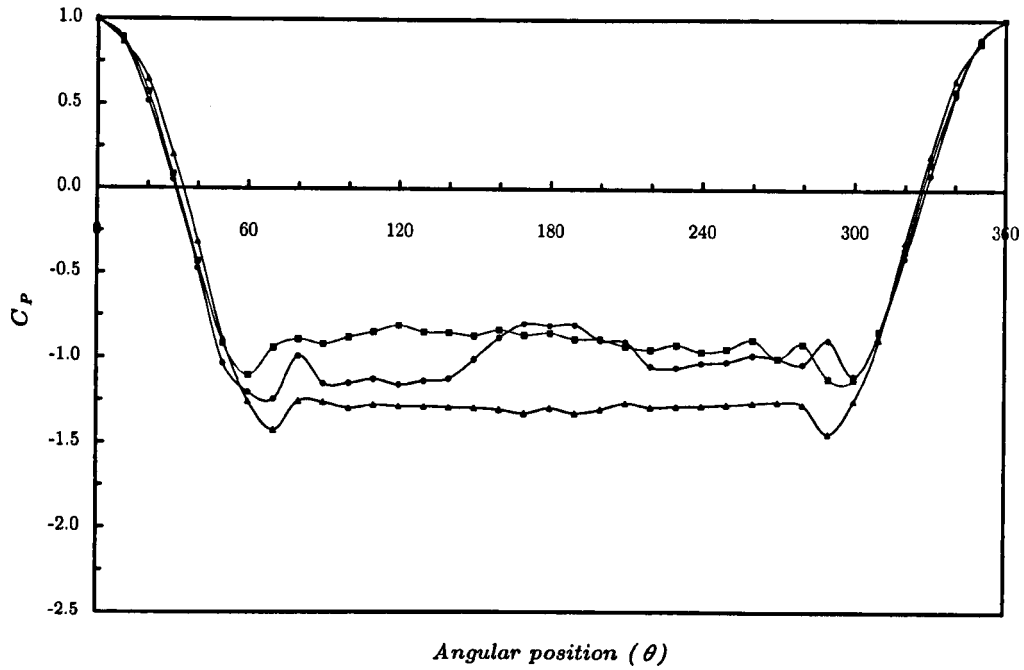


Figure 6.12 Circumferential variation in surface pressure coefficient around the cylinder at a Reynolds Number of 2×10^5: Δ, plain cylinder; •, unidirectional suppression device; □omn i directional suppression device.

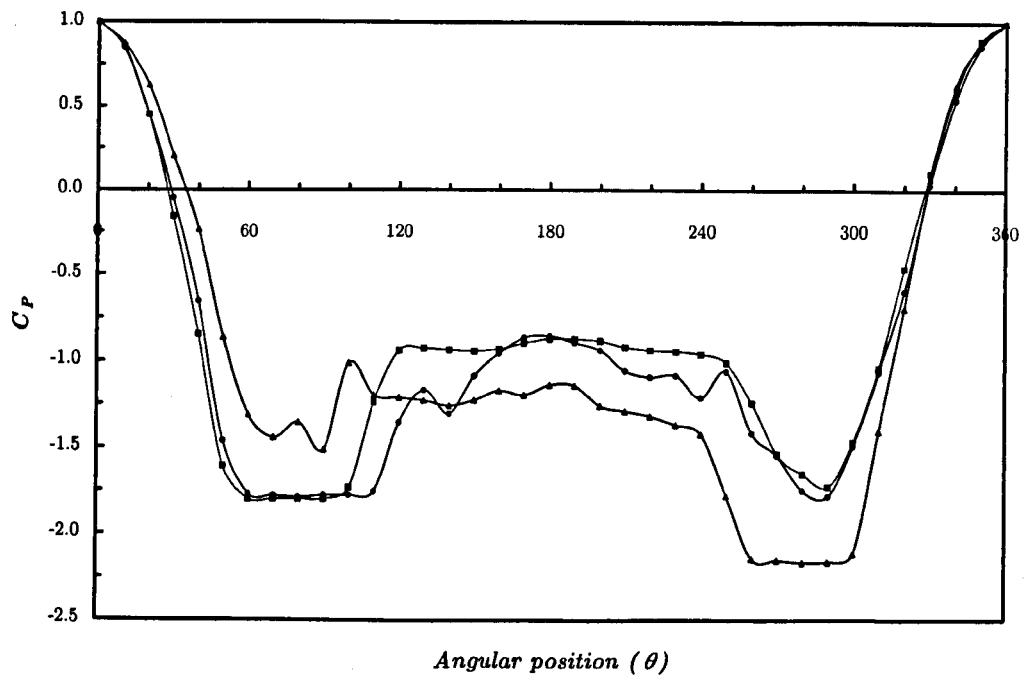


Figure 6.13 Circumferential variation in surface pressure coefficient around the cylinder at a Reynolds Number of 3×10^5: Δ, plain cylinder; •, unidirectional suppression device; □omn i directional suppression device.

by the drag measurements (figure 6.9) the reductions in C_D achieved by the surface protuberances are comparatively less at this Reynolds number.

In figure 6.13 the pressure distribution for the cylinders at a Reynolds number of 3×10^5 is observed to be substantially different. It is now apparent that for the plain cylinder the pressure distribution is asymmetric. On one side of the cylinder the flow separation point has moved forward to an angle of approximately 70° from the front stagnation point. Whilst on the other side the flow initially separates from the surface at an angle of 60° (from the front stagnation point) but then reattaches a short distance downstream at an angle of 100° forming a separation bubble, before finally separating at an angle of 120°. Bearman (1969) showed that at this Reynolds number the cylinder would only form a separation bubble on one side and found that despite no obvious asymmetry in the freestream flow or experimental set-up that it would always form on the same side of the cylinder. A similar observation was made in the present investigation where the separation bubble was always found to form on the lower side of the cylinder (between 260° & 300°). Again no obvious asymmetry could be identified in the flow or experimental set-up which could account for this observation.

This asymmetry in the pressure distribution is also observed for the cylinders fitted with surface protuberances. In this instance a separation bubble is again only formed on one side of the cylinder but for both the unidirectional and omnidirectional configurations of surface protuberances it is formed on the opposite side to the plain cylinder (between 60° & 100° - 110°), figure 6.13. Therefore, on the basis of these initial investigations it would appear that the formation of separation bubbles on a circular cylinder in the critical transition regime is also unaffected by the addition of surface protuberances.

6.4.3 Particle image velocimetry.

In order to gain an insight into the wake dynamics and also to confirm the suppression of vortex shedding, the wake was briefly investigated using PIV at a Reynolds number of 2.7×10^4. Due to the brief nature of this investigation, only the wake of the omnidirectional configuration was investigated as it was expected that the wake of the unidirectional configuration would probably be similar to the wake of the sinuous cylinder, section 5.3.4. For comparison purposes, the results for the plain cylinder obtained at the slightly lower Reynolds number of 1.7×10^4 in section 5.3.4 will be used.

Figure 6.14 shows three instantaneous vorticity plots obtained in the wake at various spanwise positions. Figure 6.14a represents a randomly chosen PIV image of the wake at a spanwise position where the surface protuberances are inline with the flow. As can be seen from the figure a narrow wake is formed (similar to the wake for the sinuous cylinder, figure 5.21) and at this time instant no Kármán type vortex shedding can be observed in the wake. This observation was also confirmed by subsequent analysis of the remaining 24 PIV images taken at this spanwise location. Therefore, investigation of the wake over 25 random time instants reveals no evidence of vortex shedding suggesting the possibility that vortex shedding at these spanwise locations has been suppressed.

Figure 6.14c shows a typical PIV image of the wide wake downstream of a spanwise location where the surface protuberances are at 90° to the freestream flow. Again subsequent analysis of a further 24 PIV images revealed no evidence of Kármán type vortex shedding in the wake. However, a different behaviour was observed in the wake downstream of where the protuberances are at 45° to the freestream flow. In these spanwise locations the wake is observed to be periodically unsteady, figure 6.14b. From the figure the presence of anti-symmetric vorticity contours can be observed indicating the occasional presence of Kármán type vortex shedding in the wake. However, investigation of the remaining 24 PIV images from this spanwise

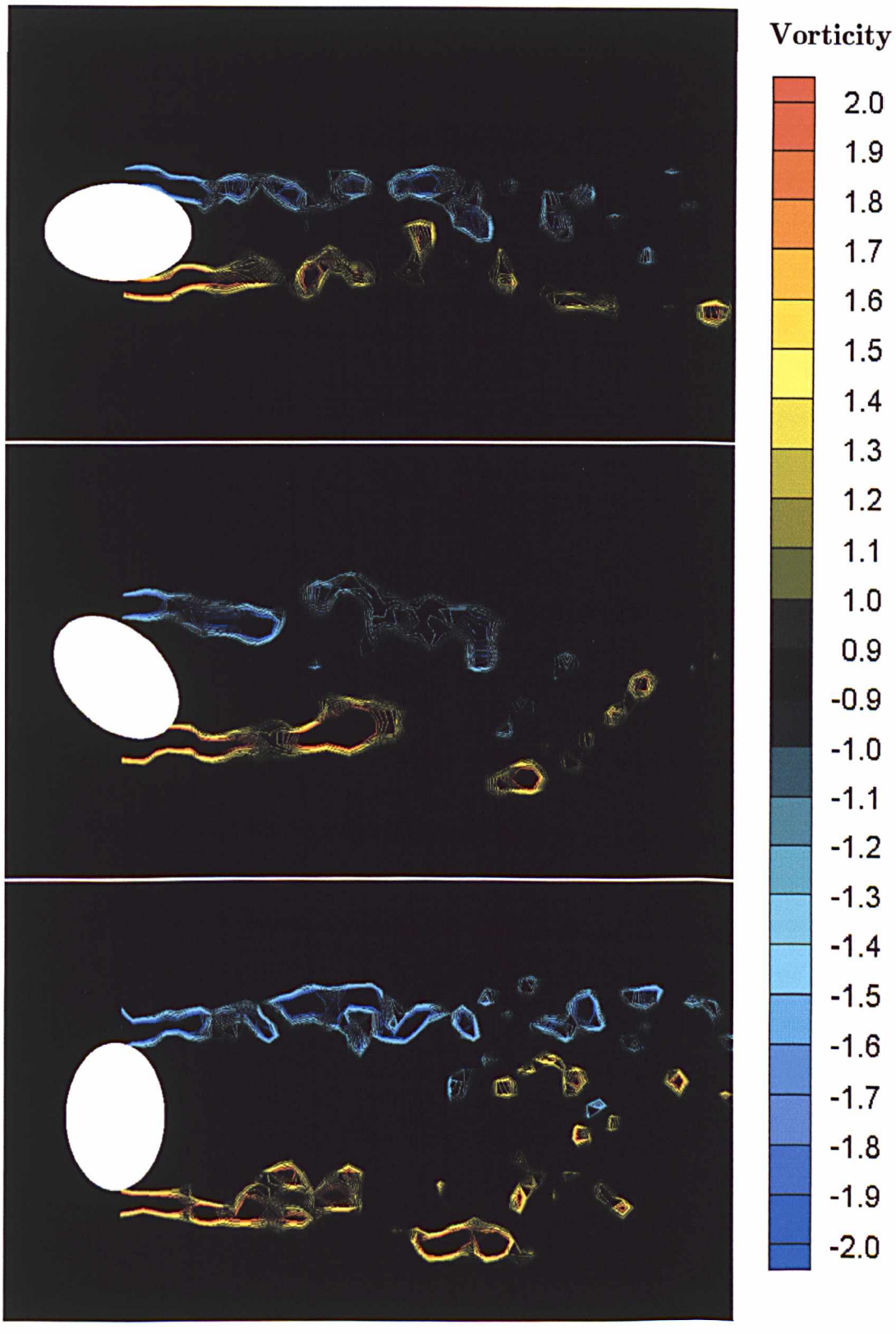


Figure 6.14 Non-dimensional vorticity contours in the wake of the omnidirectional suppression device at various spanwise positions, Re = 2.7×10^4: (a), protuberances inline with flow; (b), protuberances at 45° to flow; (c), protuberances at 90° to flow.

location revealed that the wake was predominately stable although weak vortex shedding was observed in 3 of these images.

Figure 6.15 shows a vector plot of the time-averaged flow (averaged from 15 time instantaneous images) in the centre plane of cylinder. For clarity, the vector colour is also used in the figure to indicate the magnitude of the velocity up or downstream (similar to plots in figures 5.24 &5.26). In comparison with the flow in the wake of the plain cylinder (figure 5.24b) the most striking feature is the large region of reversed flow downstream of the body. This region is observed to extend approximately 3D downstream of the inline and 45° protuberances and approximately 4D downstream of the 90° protuberances. Overall the wake shows general similarities to the wake of the sinuous cylinder (figure 5.24a) although it is not possible to confidently determine the critical points in the wake on the basis of such a brief wake investigation.

6.5 Discussion.

6.5.1 The effects of surface protuberances on vortex shedding.

The preceding results have demonstrated the development of both unidirectional and omnidirectional configurations of surface protuberances for the suppression of vortex shedding and the reduction of drag. However, whilst the drag reductions have been accurately measured, accurate determination of the nature of the flow in wake has not been possible during this brief investigation. Therefore, after such a brief investigation it is only possible speculate whether vortex shedding in the wake is actually suppressed or just simply reduced.

In the design of the surface protuberances it was intended that vortex shedding would be suppressed and that a wake similar to the wake of the sinuous cylinder would be produced. For the unidirectional configuration of surface protuberance it is not possible to confirm whether vortex shedding is fully suppressed as no wake investigations were conducted. However, as previously mentioned, a drag reduction of

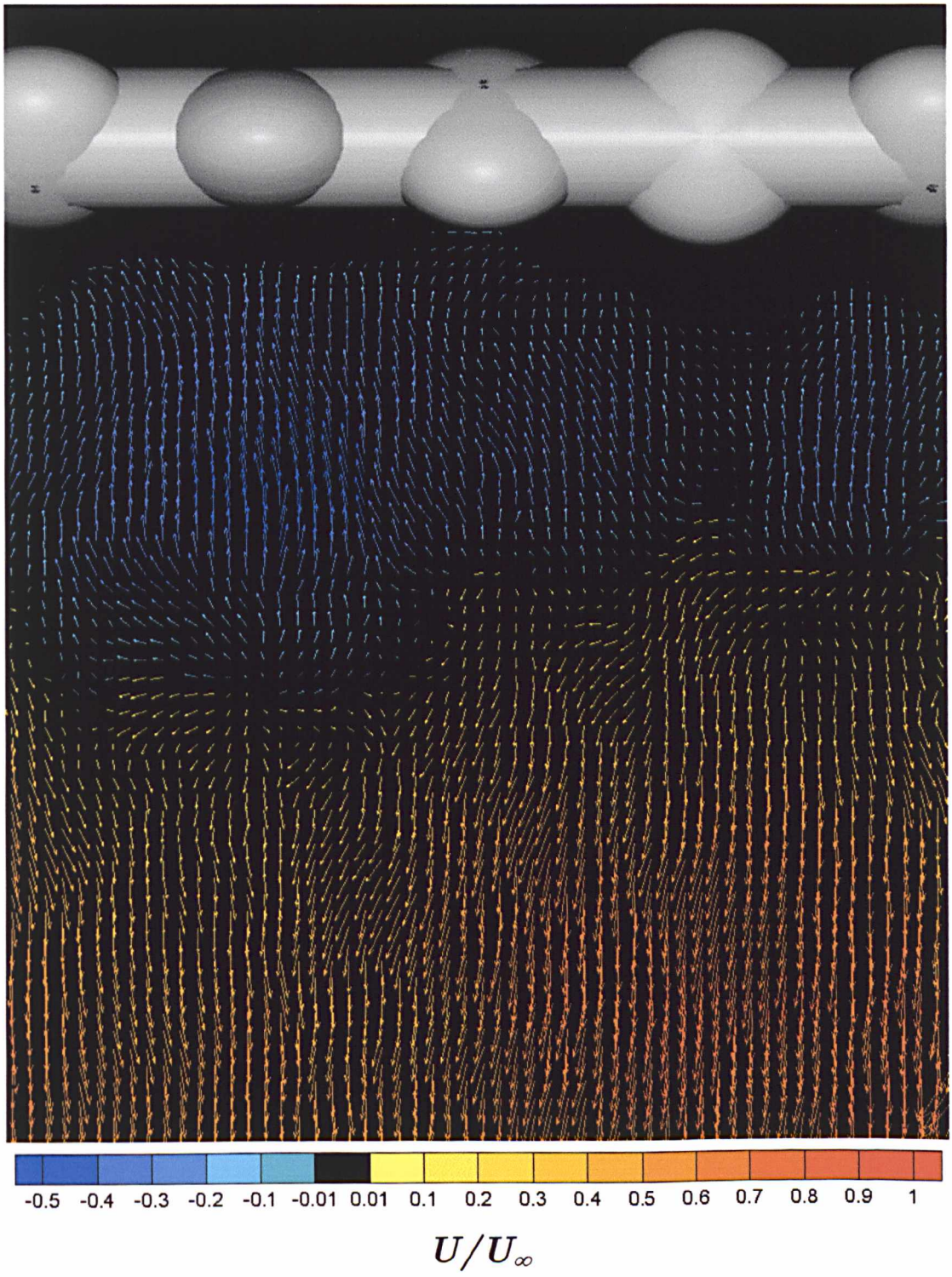


Figure 6.15 Plan view PIV image of the centre wake of the omnidirectional suppression device at a Reynolds number of 2.7×10^4. The vector magnitude is represented by both it's length and colour to help highlight regions of reversed flow.

the order of 33% as achieved by the unidirectional configuration of surface protuberances would be consistent with the suppression of vortex shedding in the wake. Therefore, it can be speculated, although not confirmed, that the unidirectional configuration is effective at the suppression of vortex shedding in the wake of a circular cylinder.

In the case of the omnidirectional configuration, the results from PIV have shown a wake which varies in both width and character along the span in a similar fashion to the sinuous cylinder. However, the results also reveal evidence of intermittent Kármán vortex shedding in the wake downstream of where the surface protuberances are orientated at 45° to the flow. Therefore, for the omnidirectional configuration of surface protuberances the level of spanwise three-dimensionality is not sufficient to fully suppress vortex shedding across the entire span. For the sinuous cylinders (chapter 5) and wavy rectangular section bodies (chapter 4) the vortex shedding in the wake was only found to be suppressed once a sufficient level of wave steepness had been exceeded. Therefore, for the cylinders fitted with surface protuberances it may be possible to fully suppress vortex shedding using a configuration of higher surface steepness or reduced spanwise spacing of protuberances.

Determination of the mechanism by which vortex shedding is disrupted or suppressed would be difficult without a detailed investigation into the wakes of both the unidirectional and omnidirectional configurations of surface protuberances. For the sinuous cylinder such a comprehensive investigation in the wake revealed that non-uniformity in the flow direction at separation was of fundamental importance, section 5.4.4. The result of this non-uniformity was the generation of streamwise vortices and three-dimensional shear layers that were unable to rollup into the coherent two-dimensional spanwise vortices necessary for vortex shedding. In the design of the elliptically shaped surface protuberances it was this disruption to the flow at separation and the generation of a regular field of streamwise vortices that was to be utilised as the mechanism for the suppression of vortex shedding. In the case of the unidirectional configuration it is likely that the flow in the wake is very similar to that

of the sinuous cylinder due to the geometric similarity of the leading edge. However, for the omnidirectional configuration it is expected that the wake will be more complex due to the asymmetric nature of a cylinder fitted with protuberances in this way. Despite this complexity, it is also likely that the non-uniform flow orientation at separation is again the key to the disruption of vortex shedding in the wake, although the orientation of this flow is likely to be far from optimum for the current configuration of surface protuberances.

As the Reynolds number is increased within the critical transition regime both the drag and pressure values are found to become more closely similar for all three cylinders, figures 6.9 & 6.13. This is particularly evident at the maximum Reynolds number where the pressure distributions of the three cylinder configurations are approximately similar. At this Reynolds number the surface protuberances appear to offer only a small benefit and it is likely that the wakes of the cylinders fitted with protuberances are similar to the wake of the plain cylinder. Therefore, it can be concluded that the surface protuberances are far less effective at altering the wake of the plain cylinder at this Reynolds number. However, this does not necessarily imply that the protuberances have become ineffective at suppressing vortex shedding in this regime. Bearman (1969) showed that for a plain cylinder in this critical transition regime that the vortex shedding in the wake becomes significantly weakened and increasingly chaotic. Therefore, the apparent similarity between the cylinders fitted with protuberances and the plain cylinder is not as a result of the protuberances becoming ineffective at disrupting shedding but instead due to the inherent disruption of shedding in the wake of a plain cylinder at this Reynolds number. Beyond this Reynolds number it would be difficult to predict how effective the surface protuberances would be at suppressing vortex shedding in the supercritical and postcritical regimes where the boundary layers at separation are turbulent.

6.5.2 Optimisation of surface protuberances.

For the optimisation of both configurations the drag of the body was used as a guide to the intensity of vortex shedding in the wake. In all cases the assumption was made that lower drag was as a result of weaker vortex shedding. This raises the question as to whether or not this was a good assumption to make? For example, in the case of the sinuous cylinder, for low values of wave steepness the majority of the drag reduction was due to the suppression of vortex shedding. However, at higher values of wave steepness the streamline effects of the swept leading edge of the cylinder became significant and were found to account for approximately 25% of the total drag reduction (figure 5.6). Therefore, it is also possible that the total drag reduction experienced by the cylinders fitted with surface protuberance is not entirely as a result of a reduction in the strength of vortex shedding. Hence it is likely that different configurations of surface protuberances used in this investigation may have proved more effective at the suppression of vortex shedding but at the expense of overall drag reduction.

In the design of a second generation of surface protuberances it is likely that many improvements could be made as the current design is far from perfect. For example, despite the attachment of surface protuberances, PIV results for the omnidirectional configuration still show the presence of vortex shedding in the wake downstream of the cylinder, although weak and intermittent, figure 6.14b. Also the current protuberances form a sharp corner when attached to the cylinder surface which could potentially act as a vortex generator for streamwise vortices. However, whether such a vortex would be of the right sign and hence beneficial for the stabilisation of the wake remains unclear at this stage. Therefore, there still remains much further investigation into the current set of protuberances and their effectiveness at disrupting vortex shedding before any new designs can be considered.

The intention of this work was to demonstrate the potential for the suppression of vortex shedding in the wake of a circular cylinder using simple surface protuberances. On the basis of the results presented it would appear that the initial attempts have

been a success. Substantial drag reductions have been achieved and PIV visualisations have revealed a predominantly steady wake. However, whilst the suppression of vortex shedding on engineering structures is highly beneficial in the prevention of fatigue failure, the suppression and reduction of vortex induced vibrations (VIV) on structures of low stiffness (typical marine structures) is of far greater importance. Therefore, the next stage in the investigation was to investigate the potential for the reduction of vortex induced vibrations on circular cylinders fitted with surface protuberances. The results of this investigation will be presented in Chapter 7.

6.5.3 Experimental errors.

Many of the techniques used in this part of the investigation and the errors or inaccuracies associated with them have already been discussed in the preceding chapters (3,4&5). Therefore, only errors associated directly with the work in this chapter will be considered.

As described in section 6.2.1, the grid structure produced on the surface of the cylinder was accurately marked out using a three-axis milling machine and dividing head. However, it was still possible to introduce a small positional error whilst fitting the protuberances to the cylinder surface as protuberances were only aligned by eye before being taped on. A conservative estimate of this error would be $\pm 2^{\circ}$ in angular position and $\pm 0.02D$ in spanwise position. Whilst these errors many initially appear quite large, in practice positional inaccuracies of this order were found to have no measurable effect on the resulting drag of the model. However, for any subsequent experiments it would be important to align the protuberances more accurately on the cylinder surface.

7 Vortex induced vibrations.

7.1 Introduction.

In the previous three chapters it has been demonstrated how vortex shedding in the wakes of nominally two-dimensional bluff bodies can be reduced or even suppressed by the introduction of spanwise three-dimensionality. However, whilst the suppression or the reduction of vortex shedding in the wake of a bluff body is of benefit, it is the suppression or reduction of vortex induced vibrations (VIV) that act on such bodies that is of far greater importance for typical engineering applications. Typically, vibrations may be reduced by using devices such as helical strakes although these have the disadvantage of increase drag, section 1.5.3. Therefore, it is important to know whether the introduction of spanwise three-dimensionality in the form of surface protuberances can provide an effective method for the disruption and suppression of VIV without increasing drag.

7.1.1 Vortex induced vibrations of circular cylinders.

The problem of vortex induced vibrations has been the subject of much research for over 100 years. In recent times, however, the results of this work have become of far more importance with the growth of the offshore and marine industries that typically use cylinders of very high aspect ratio but very low mass ratio. This makes such cylinders particular sensitive to VIV. The circular cylinder is again the body that has received the majority of research, as the structures used in these industries typically comprise of many elements of circular cross-section. In this section some of the important parameters determined from this previous research into circular cylinders will be presented. However, this section is not intended to provide a comprehensive review of vortex induced vibrations but only to serve as an introduction to the results that will be presented from this investigation. For a more detailed review of vortex induced vibrations the reader is directed towards one of the many excellent review

papers on the subject, such as Sarpkaya (1979), Bearman (1984) and Parkinson (1989).

The response of a flexibly mounted cylinder to a fluid flow is governed by many factors relating to both the fluid dynamics and the structural dynamics of the system. In this investigation attempts to limit the response of a cylinder are through the reduction of the fluid dynamic forcing due to vortex shedding. However, if only the structural dynamics are considered, then for a circular cylinder submerged in a uniform flow the response is primarily governed by two parameters, the mass ratio, and the damping ratio, which are defined as

$$m^* = \frac{m_{sys}}{m_d} \qquad \zeta = \frac{C_{sys}}{C_{crit}}$$

where m_{sys} is the mass of the oscillating system, m_d is the mass of the displaced fluid, c_{sys} is the system damping and c_{crit} is the critical damping. Although these quantities affect different terms in the equation of motion it is convenient to express them in the form of a combined mass-damping parameter $m^*\zeta$ (Bearman 1984) as increasing mass and increasing damping are observed to have similar effects on the amplitude of oscillations. At low mass ratios it is also important to take account of the added fluid mass which is accelerating with the cylinder during the oscillation cycle. This added mass can be calculated from potential flow theory and is equal to a value of $C_A = 1$ for an infinitely long circular cylinder undergoing small oscillations in still water although this value of C_A will change from 1 for cylinders in flowing water. Therefore, if the effects of added mass are to be included then combined mass damping parameter can be written as

$$(m^* + C_A)\zeta$$

The effects of mass damping parameter on the amplitude of rigid body oscillation of a flexibly mounted circular cylinder are plotted in figure 7.1. From the figure it can be

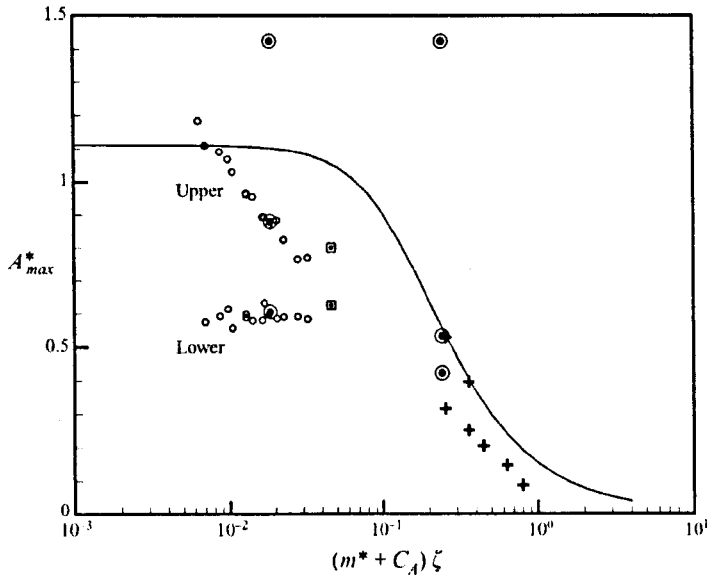


Figure 7.1 Compilation of various results by Govardhan & Williamson (2000) showing the effect of combined mass damping parameter on the maximum non-dimensional amplitude of cylinder oscillation, A^*_{max}.

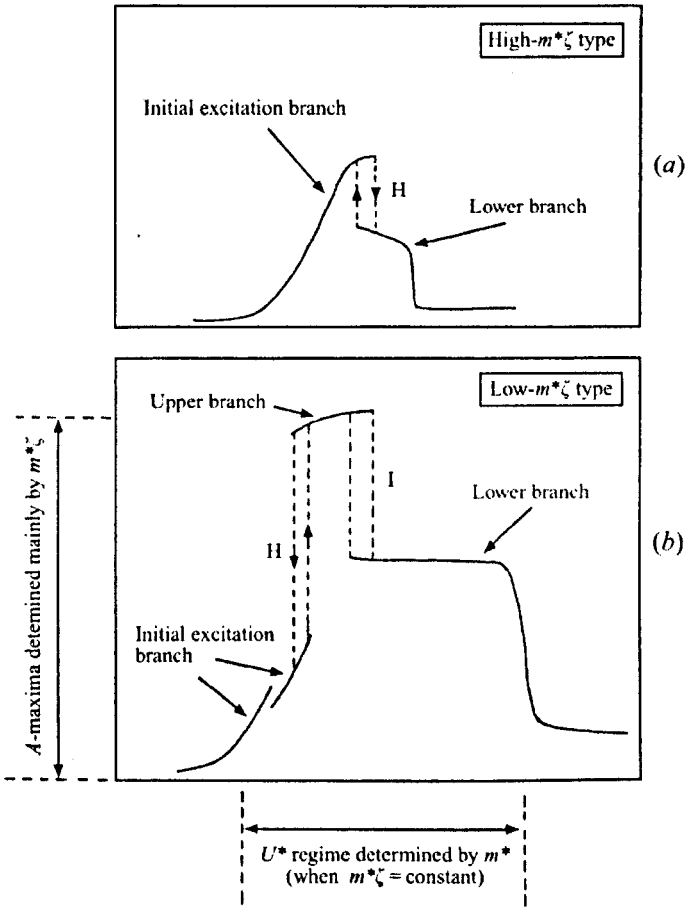


Figure 7.2 The maximum transverse response amplitude for a circular cylinder as a function of reduced velocity (U^*), Govardhan & Williamson (2000): (a), Typical two branch response for a cylinder of high mass ratio; (b), Three branch response for a cylinder of low mass ratio.

seen that increasing mass damping has the effect of reducing the amplitude of oscillation with oscillations completely suppressed for a value of mass damping parameter in the range of 1 to 5. The figure also indicates that oscillations of up to 1.5 cylinder diameters are possible for structures of low mass and damping.

In addition, the amplitude of oscillation of the cylinder is also affected by the reduced velocity U* of the fluid stream, where U* is defined as

$$U^* = \frac{nD}{U_\infty}$$

and n is the oscillation frequency of the body in still water, D is the diameter of the cylinder and U_∞ the velocity of the freestream flow. Figure 7.2 shows the effect of reduced velocity on the amplitude of oscillation for circular cylinders of both high and low mass damping parameters. It can be seen from the figure that the maximum amplitude of oscillation is only reached over a relatively small reduced velocity range. This effect is particularly apparent at high value mass ratios where the excitation range is significantly reduced. Govardhan and Williamson (2000) showed that the width of this reduced velocity range over which the cylinder was excited to oscillate was decreased by increasing mass ratio for a constant level of mass damping. The level of mass damping to be investigated in the present investigation is approximately half way between the two cases shown in figure 7.2.

In the results that follow, only cylinders of relatively low mass ratio are investigated. The range of mass damping parameters covered would typically range from those for marine cables and risers to lightweight steel chimneys, which are conventionally protected with helical strakes. In these applications the body can be excited into large amplitude oscillations (up to 1D) when the natural frequency of the body and the vortex shedding frequency are approximately similar.

7.2 Experimental Set-up.

7.2.1 Introduction.

All vortex induced vibration tests were conducted in a water channel in the hydrodynamics laboratory at the Department of Aeronautics at Imperial College (figure 3.6b). This facility has a steady flow of water that can be varied in speed up to a maximum of $0.3ms^{-1}$. The test section is 0.61m wide by 0.69m deep by 1.8m long and is fitted with large glass panel windows that allow the flow to be observed from all sides. To ensure good flow quality in the test section, the settling chamber is fitted with a honeycomb grid and several fine screens, followed by a smooth 4:1 contraction into the test section. The main advantages of using the water channel as opposed to a wind tunnel for vibration experiments are that the Reynolds number is higher for a given flow speed, frequencies of oscillation are lower and it is possible to achieve much lower mass ratios, m*. In the present investigation the mass-damping parameter was varied between $m^*\zeta = 2\times10^{-2}$ to 5 and over the range of Reynolds numbers 10^3-10^4.

7.2.2 Vortex induced vibrations.

For vibration experiments cylinders were elastically mounted in the water channel using a double pendulum suspension system that produced near perfect parallel motion, figure 7.3. This double pendulum system is essentially a large parallelogram that keeps the lower platform to which the cylinder is attached parallel to the horizontal plane by means of two sets of pendulum arms. By using a pendulum system such as this, the cylinder will also be subjected to small vertical oscillations during one motion cycle due to the small rotation of the pendulum arms. In order to minimise this undesirable vertical motion, it is important that the arms of the pendulum are made as long as possible and that the horizontal movement of the lower platform is kept to a minimum. In the present investigation the arms were approximately 30D long and the amplitude of oscillations not more than 1D (where D is the diameter of the test cylinder). This resulted in a vertical oscillation of the cylinder of less than 0.02D during one oscillation cycle with amplitude D and hence,

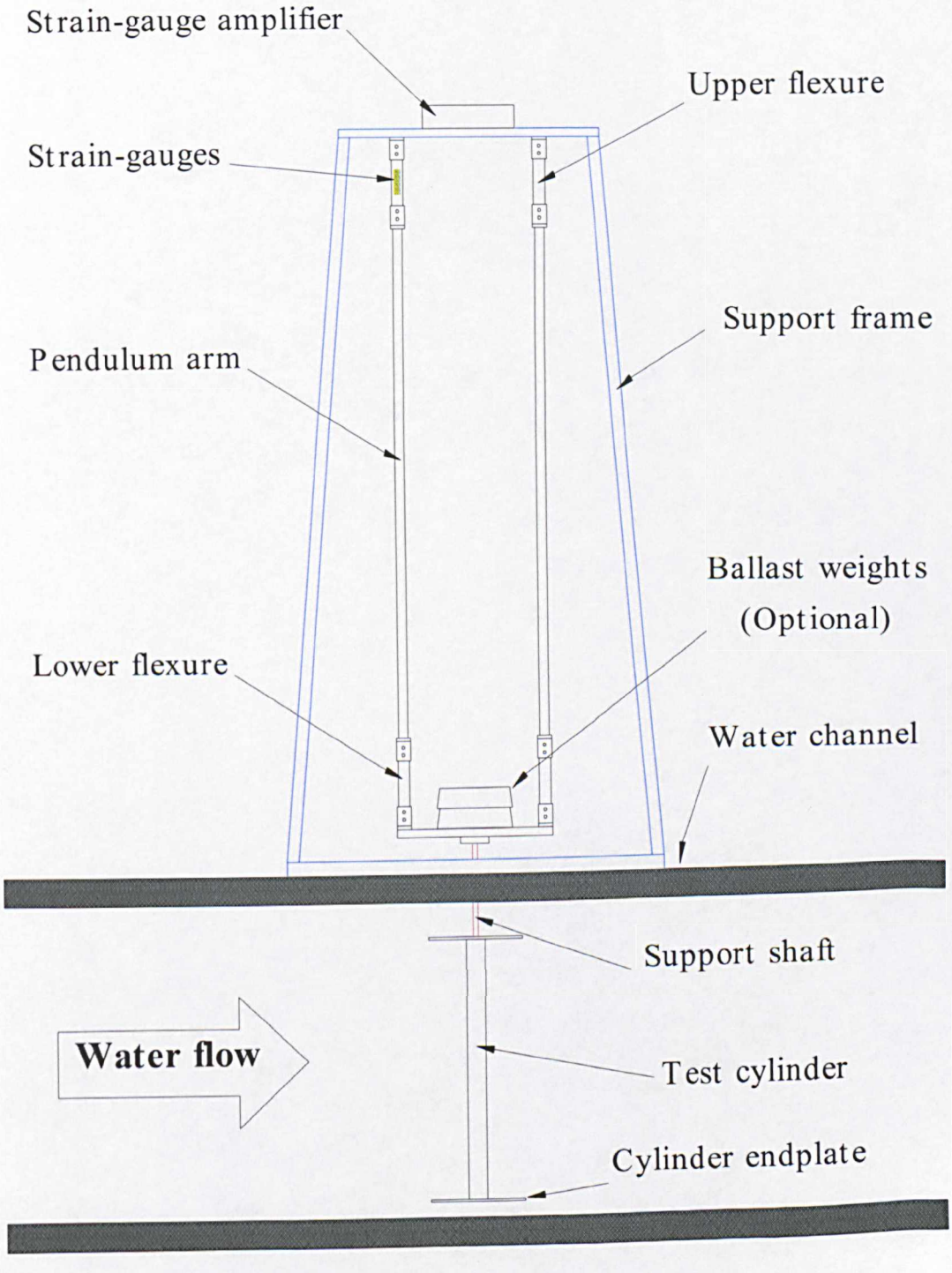


Figure 7.3 A schematic diagram showing the double pendulum suspension rig used to investigate vortex induced vibrations mounted above the water channel.

this small vertical oscillation was assumed to have a negligible effect on the fluid dynamics.

In order to keep the system damping to a minimum, the pendulum arms were attached at each end via metal flexures made from thin strips of spring steel that allowed displacement only in the transverse direction. This arrangement resulted in a very low normalised damping for the system of $\zeta = 8.5\times10^{-4}$. It was desirable during some of the later experiments to not restrict the cylinder to movement only in the transverse direction but to allow it to move in the streamwise direction as well. For these experiments the simple flexures were substituted for double flexures (two strips of spring steel fixed 90° opposed) that allowed the pendulum system complete freedom of movement in the horizontal plane.

For the purpose of measuring cylinder displacements two strain gauges were fitted to opposite sides of one of the upper flexures and connected to a precision bridge amplifier. To prevent any drift in the signal due to the effect of temperature changes, two gauges of the same type were attached to a non-stressed part of the support frame and connected to the bridge amplifier to be used as temperature compensation. The bridge amplifier incorporated a five component filter which produced a very clean electrical signal that once calibrated could be used to accurately determine the position of the cylinder (to within ± 0.01D). This signal from the bridge amplifier was then recorded via a DAS08-AOH PC capture card for a period of 300 seconds and at a frequency of 200Hz.

The speed of the water channel was evaluated by an industrial flow meter that was situated in the main feed pipe to the channel (see figure 3.6b). The speed of the channel could then be simply calculated using the volume flow rate through the flow meter and the cross-sectional area of the water in the channel. In this way it was possible to calculate the average flow speed in the channel to within 1%.

In order to vary the mass-damping parameter ($m^*\zeta$) over a large range of values, the system mass and system damping could both be varied independently. The system mass could be varied by adding ballast weights to the lower platform, while the system damping could be varied by means of a simple viscous damper. The damper consisted of a large metal plate that was attached to the pendulum and which moved inline with the pendulum motion in a large tank of viscous oil. The level of system damping could then be adjusted by simply varying the amount of the plate submerged in the oil. This arrangement of damping resulted in highly linear system dynamics with the pendulum behaving like a damped harmonic oscillator to within 0.5%.

Test cylinders were constructed from thin walled acrylic tube (for low mass) and in all instances were of $40mm$ diameter and of an aspect ratio of 12, figure 7.4. In addition, all cylinders were fitted with top and bottom circular endplates that contributed a small fraction to the total damping of the system. This additional damping was taken into account by measuring the structural damping with the cylinder removed but with the endplates attached and in the water.

For the static cylinder in the water channel the maximum solid blockage was 6.5%. Whilst there are many papers available that deal with blockage corrections for static bluff bodies (Maskell 1963 is an excellent example) there are as yet no corrections that can be applied to oscillating bluff bodies, in particular to correct for the effect of blockage on amplitude of oscillation. Therefore, the data presented was not subject to any correction as it was not possible to quantify the effect of blockage and hence the reader should always keep this in mind when making comparisons with other results.

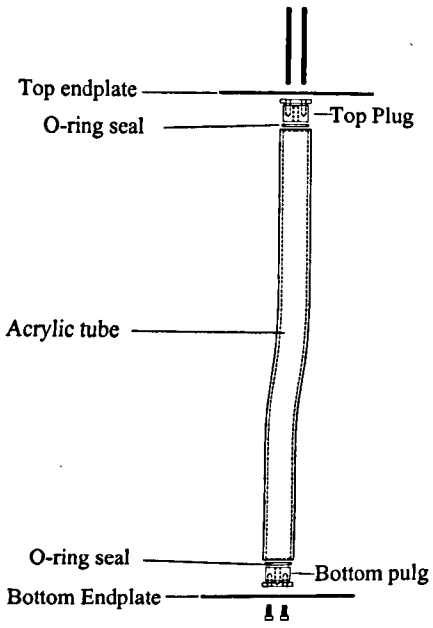


Figure 7.4 Construction details of the lightweight acrylic test cylinders used on the double pendulum suspension rig.

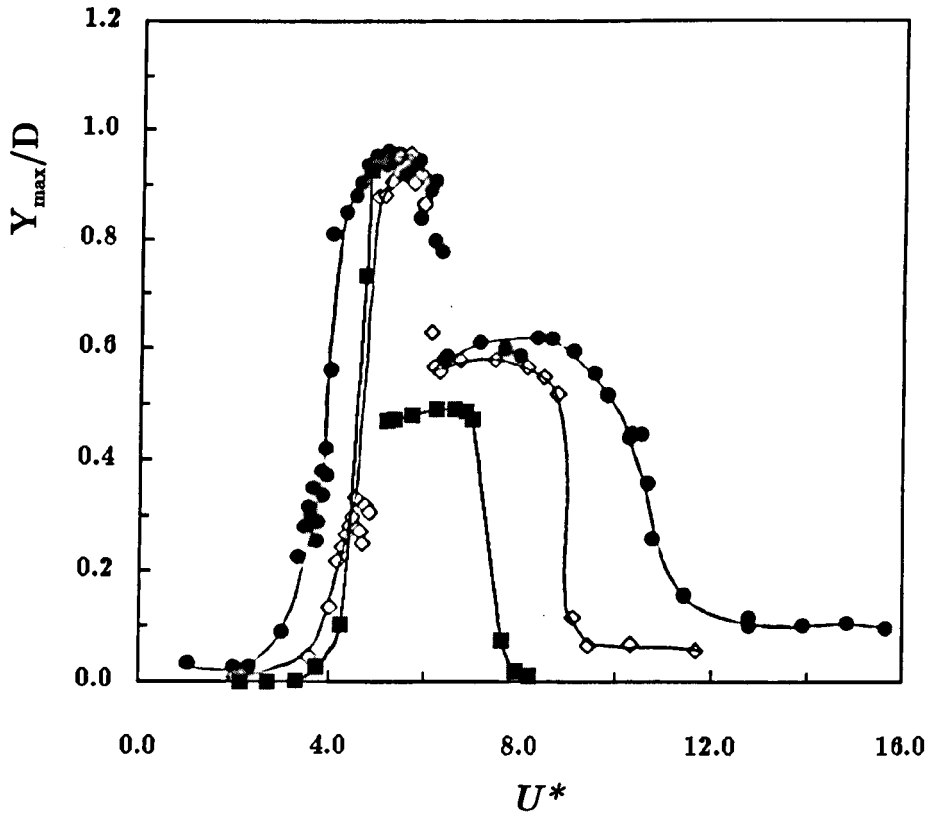


Figure 7.5 Maximum transverse response amplitude of an oscillating circular cylinder: •, Khalak & Williamson (1996), $m^* = 2.4$, $m^*\zeta = 1.3\times10^{-2}$; ◊, Khalak & Williamson (1996), $m^* = 10.0$, $m^*\zeta = 1.3\times10^{-2}$; , present results, $m^* = 14.3$, $m^*\zeta = 3.6\times10^{-2}$.

7.3 Results.

7.3.1 The response of a cylinder at low mass and damping.

For comparison purposes, the response of a circular cylinder was initially investigated over the Reynolds number range 1650 – 7500. The cylinder used for these experiments had a system mass m^* of 14.3 and a system damping ζ of 2.5×10^{-3} resulting in a value of combined mass and damping $m^*\zeta$ of 3.6×10^{-2}. Although, it would have been relatively simple to include the effects of added mass, its inclusion would have only resulted in a 6% increase in the value of combined mass and damping. Therefore, as a simplification for these initial experiments, the additional added fluid mass has not been included in the value of combined mass and damping.

The maximum transverse response amplitude Y_{max}, normalised by cylinder diameter (D) for this cylinder is plotted as a function of reduced velocity U^* in Figure 7.5. In addition, the results of Khalak & Williamson (1996) are also plotted for a cylinder of similar combined mass and damping. It can be seen that the current results are in good agreement with the previous results of Khalak & Williamson, showing a maximum transverse response amplitude of 0.95D at a reduced velocity of approximately 5. The results also demonstrate the effect of increasing system mass with response observed over a smaller reduced velocity range when the mass ratio is increased.

Having confirmed a good comparison for the circular cylinder with the work of previous researchers the next stage was to investigate the response of a circular cylinder fitted with surface protuberances in both the unidirectional and omnidirectional configurations as previously discussed in chapter 6. Figure 7.6 shows a comparison of the maximum transverse response amplitudes for the circular cylinders fitted with surface protuberances as a function of reduced velocity. From the figure the surface protuberances would appear relatively ineffective at suppressing oscillations with maximum transverse amplitudes of 0.65D and 0.70D for the unidirectional and omnidirectional cylinders respectively. These results indicate that

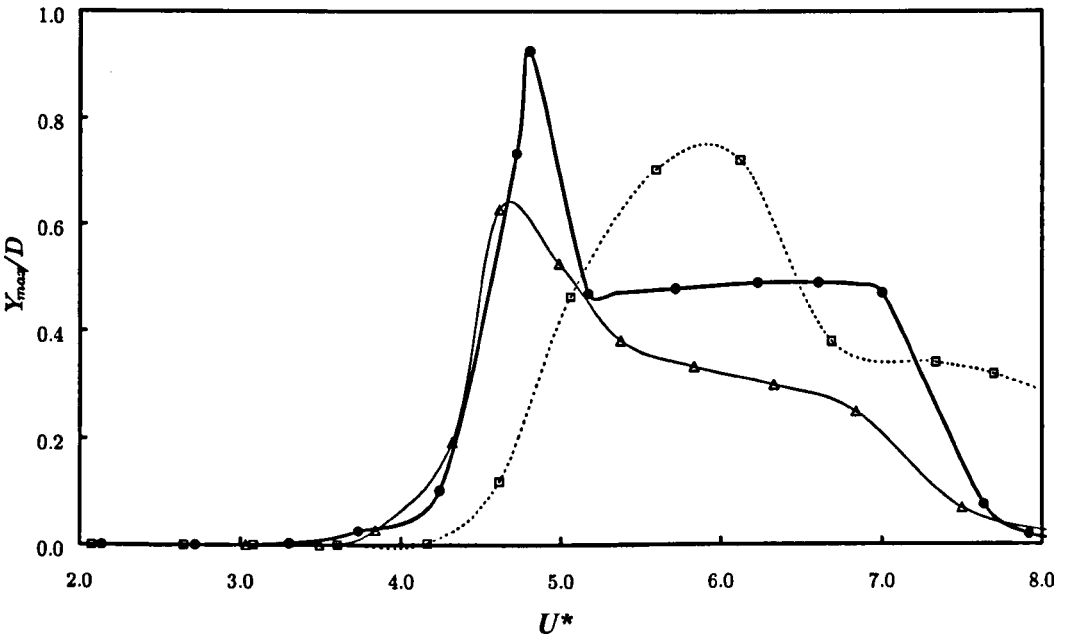


Figure 7.6 Maximum transverse response amplitude of an oscillating cylinder: •, circular cylinder; Δ, unidirectional configuration of surface protuberances; □, omnidirectional configuration of surface protuberances. $m^*\zeta = 3.6\times10^{-2}$, Reynolds number = 1650 – 7500.

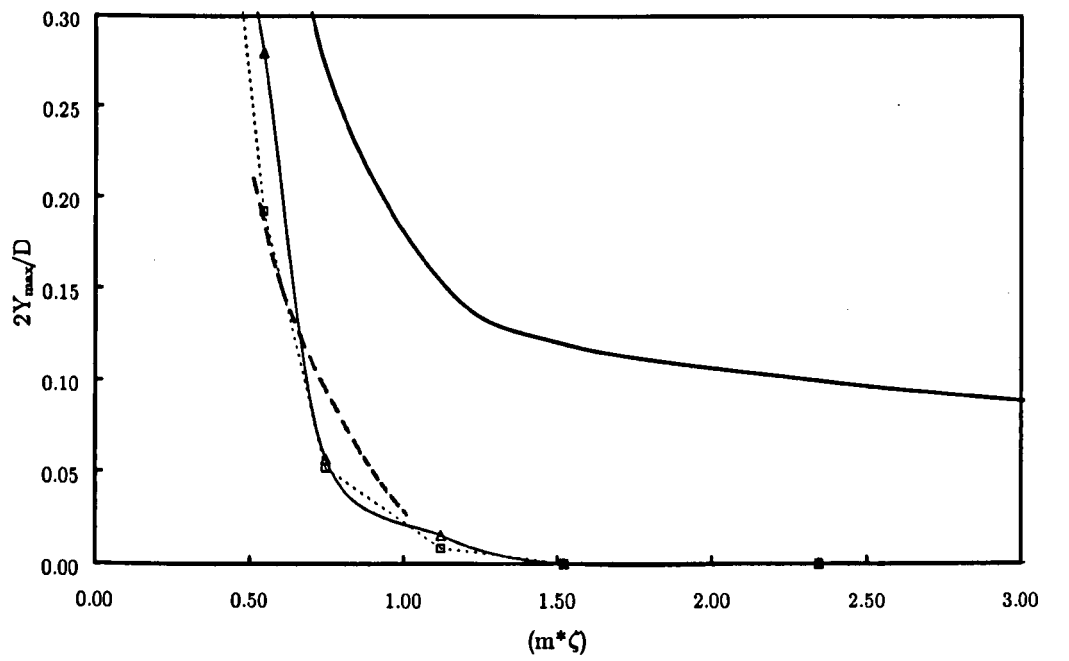


Figure 7.7 The effect of mass damping parameter ($m^*\zeta$) on the maximum transverse response amplitude of various bodies: •, circular cylinder; Δ, unidirectional configuration of surface protuberances; □, omnidirectional configuration of surface protuberances. --, three start helical strakes, $h_{st}/D = 0.08$, Wong & Cox (1978).

when the body is flexibly mounted it is still able to detect a very weak force fluctuation at a shedding frequency and consequently the amplitude of oscillation slowly builds up. Another notable feature of the figure is that the resonance peak for the omnidirectional cylinder is shifted to the right with a maximum transverse response amplitude observed at a reduced velocity of approximately 6. This results from the addition of surface protuberances all the way around the cylinder for the omnidirectional configuration that leads to an increase in the cylinders mean diameter and hence lower vortex shedding frequency. In turn this leads to the onset of oscillations at a higher value of reduced velocity.

However, the protuberances are potentially more effective than the figure might suggest. Unlike the circular cylinder, the transverse oscillations of the cylinder fitted with surface protuberances were observed to developed extremely slowly, typically five to ten times as long as for the circular cylinder. This behaviour is similar to that found for cylinders fitted with helical strakes which are also observed to develop oscillations at low mass damping parameters, Scruton & Walshe (1957). Typically helical strakes are only effective at suppressing oscillations of cylinders in air where values of mass damping parameter are substantially higher. Therefore, the next stage was to investigate the effectiveness of surface protuberances at higher values of mass damping parameter.

7.3.2 The effect of mass damping.

The effect of increasing mass damping parameter is illustrated in figure 7.7 where $2Y_{max}/D$ is plotted against $m^*\zeta$ for the circular cylinder and for the cylinder fitted with protuberances, where Y_{max} is the maximum amplitude of oscillation throughout the lock-in regime. However, it should be noted that although increasing the mass or damping may have similar effects on the amplitude of oscillation, they each effect different terms in the governing equation of motion. Therefore, only measurements where both the system mass and system damping are equal are directly comparable. In the present investigation, this problem was addressed by holding the system mass

(m^*) constant at a value of 14.3 and only varying the system damping by the use of a simple viscous damper.

From the figure it can be seen that both the unidirectional and omnidirectional configurations of surface protuberances completely suppresses oscillations at significantly lower values of mass damping parameter than the circular cylinder. However, it can be seen from the figure that oscillations built up rapidly if the mass damping parameter drops below a value of approximately 0.75. The experimental results of Wong & Cox (1978) for three start helical strakes are also included in the figure which indicate that overall, the surface protuberances are of similar effectiveness for the suppression of oscillations as strakes of height 0.08D. It should be noted that no detailed attempt has been made to optimise the shape of the protuberances, or their distribution, but the results demonstrate the potential for using this idea for suppressing VIV and reducing drag.

7.3.3 The effect of two degrees of freedom.

In addition to the transverse experiments, tests were also performed where the cylinder was not restricted to oscillations only in the transverse direction but where the cylinder could also move in the streamwise direction as well. However, whilst some interesting phenomena were observed, inherent problems in the suspension rigs double flexure design (section 7.2.2) prevented any detailed investigation. These problems resulted from minute differences in the natural frequencies of the suspension rig's two axes that caused a circular orbit of the pendulum to become elliptical. Therefore, whilst these experiments showed that the cylinder was susceptible to oscillations in both the streamwise and transverse directions, the problems with the experimental set-up meant that the results are too inaccurate to be included here.

7.4 Discussion.

The results show that the amplitude of oscillation of a circular cylinder can be reduced for low levels of mass and damping of the order found on marine structures and completely suppressed at the higher levels of mass and damping, similar to those for the majority of structures in air. However, these high mass damping parameters were achieved at a mass ratio of 14.3 and with heavy damping. Therefore, as the mass and damping operate on different terms in the equation of motion for the cylinder it is possible the value of combined mass and damping at which oscillations are suppressed may be slightly different when higher mass ratios are used.

In section 7.3.1, it was observed that cylinders fitted with surface protuberances would take a substantially longer time than a circular cylinder for oscillations to build up. This behaviour was particularly apparent in the case of the unidirectional cylinder which would typical take up to 500 cycles to build up to maximum amplitude. This slow build up of oscillations suggests that there is a significantly lower component of lift force in phase with the cylinder velocity for the cylinders fitted with surface protuberances. In addition, it was also observed that at small amplitude oscillations would sometimes decay, even when the reduced velocity was at a value where the maximum transverse response amplitude had been previously recorded. However, it was also observed that oscillations would always build up to maximum amplitude once an amplitude of approximately 0.1D had been exceeded. Therefore, these observations suggest the possibility that the unidirectional cylinder is in fact mildly stable for small oscillations and only unstable at larger amplitudes.

The above results suggest that it may be possible to develop a design and configuration of surface protuberances that are stable to small amplitudes of oscillation. However, at very low combined mass and damping ever highly three-dimensional bodies such as spheres are observed to oscillate. Jauvtis *et al.* (2000) showed how even a tethered sphere would oscillate periodically at amplitudes of up to almost 1D and over a large range of reduced velocities when tested at low mass and

damping. The exact level of the combined mass and damping was not reported although it can be expected to be at least an order of magnitude lower than the lowest value investigated in the present investigation. Hence, it would appear that the use of imposed spanwise three-dimensionality for the complete suppression of oscillations is unlikely on a cylindrical body of low mass and damping. Even if a body is able to shed vortices in a completely random or symmetric manner when fixed, a significant perturbation from the equilibrium position will introduce a periodic oscillation into the body as a result of the system dynamics. If this oscillation is sufficiently large then at certain reduced velocities oscillations may build up to large amplitudes. Therefore, it would appear unlikely that VIV will be effectively suppressed with imposed spanwise three-dimensionality on structures of very low mass and stiffness where small perturbations may result in relatively large transverse oscillations and hence the correlation of Kármán type vortex shedding. However, it is possible at moderate levels of mass damping that the further development of surface protuberances may offer the potential for significant reductions in the amplitudes of vortex induced vibrations on cylindrical bodies.

8 Conclusions and recommendations for further work.

8.1 Conclusions.

1. The main aim of this work was to gain an understanding of the physical mechanisms that prevent vortex shedding in the wakes of bluff bodies with imposed spanwise waviness. The effectiveness of this spanwise waviness at suppressing vortex shedding has been demonstrated during the present investigation for both square section and circular section bodies. In addition, the ability to prevent vortex shedding by other 'non-wavy' types of imposed three-dimensionality has also been demonstrated using elliptically shaped surface protuberances attached to a circular cylinder in various arrangements. A common feature of all of these bodies is that the ability to suppress vortex shedding is dependent on the geometric parameter of wave or surface steepness defined as the ratio of the wave or protuberance height to the wavelength or spanwise spacing of protuberance (wave height/wavelength). It is shown that in all instances a critical value of this parameter must be exceeded before vortex shedding can be suppressed completely.

2. It is shown that the use of imposed spanwise three-dimensionality results in substantial drag reduction as a result of the disruption or suppression of Kármán vortex shedding. For a wavy square section cylinder this drag reduction is shown to be in excess of 30% and equal to the drag reduction achieved by inserting a long splitter plate along the centre line of the wake. Similar drag reductions are also shown for a circular cylinder when vortex shedding is suppressed. By fitting elliptically shaped surface protuberances to the cylinder drag reductions of up to 33% are achieved. However, it is possible to achieve drag reductions of almost 50% if the axis of a circular cylinder is deformed inline with the flow in the form of a sinusoid.

3. The introduction of spanwise waviness is observed to result in a highly three-dimensional near wake that varies in width periodically along the span. This variation in wake width is shown to be as a result of an array of streamwise vortices that drive flow across the near wake from downstream of a geometric peak (where the wake is narrowest) to downstream of a geometric trough (where the wake is widest).

4. Previous researchers have highlighted the geometry of the flow separation line as an important parameter in the suppression of vortex shedding, concluding that vortex shedding could be weakened or even suppressed if the separation line was broken or wavy along the span. However, on the basis of the present results it is proposed that the geometry of the separation line is only of secondary importance and it is the orientation of the flow at separation that is the fundamental factor in determining whether vortex shedding in the wake will be suppressed.

5. Results show that the flow in the wake of a circular cylinder can be substantially altered by the introduction of imposed spanwise three-dimensionality in the form of surface protuberances. Optimum configurations of protuberances demonstrate almost total suppression of vortex shedding regardless of flow direction resulting in drag reductions of up to 25%. Therefore, for a circular cylinder in the subcritical Reynolds number regime, it can be concluded that the vortex shedding in the wake can be significantly weakened (regardless of flow direction) by the fitting of a series of surface protuberances.

6. Results from vortex induced vibration experiments show that a cylinder fitted with surface protuberances is still susceptible to vibration (at low values of combined mass and damping) despite there being no detectable evidence of vortex shedding from the body when fixed. Therefore, at low values of combined mass and damping, the protuberances are ineffective at completely suppressing vortex induced vibrations. However, despite this tendency to vibrate at low mass-damping, it is shown that in

order to suppress vortex induced vibrations completely, a significantly lower value of combined mass and damping ($m^*\xi$) is needed when the cylinder is fitted with surface protuberances.

7. During the course of this investigation experiments were performed over a large range of Reynolds number in both air and water with little or no difference in the ability of spanwise waviness to disrupt or suppress shedding over this range. Therefore, these results suggest that the ability of spanwise waviness and surface protuberances to suppress vortex shedding is largely independent of Reynolds number. However, for circular cylinders, this conclusion is only valid for Reynolds numbers up to the start of the supercritical regime ($Re = 4\times10^5$) where the shear layers become turbulent at separation. Beyond this Reynolds number it is also expected that the surfaces protuberances would be effective at disrupting shedding although this could not be confirmed with the present experimental apparatus.

8. At low Reynolds numbers, a square section cylinder is observed to undergo many of the now familiar wake transitions previously observed for circular cylinders. An initially steady wake becomes unsteady as the Reynolds number is increased above approximately 40 resulting in laminar vortex shedding up to a Reynolds number of about 165. Above this Reynolds number the primary vortices are observed to become three-dimensionally unstable and form streamwise vortex loops as the wake undergoes mode – A transition. Mode – B transition is also observed with the generation of fine scale streamwise vortices as the Reynolds number is increased above about 230.

9. From flow visualisation results it is possible to confirm the existence of three flow regimes for the square section cylinder at low Reynolds number (before the transition to three-dimensionality) originally observed by Robichaux *et al.* (1999). As the Reynolds number is increased these results show an initial regime where the flow remains attached around the upstream corners, a second regime where the flow

separates but reattaches to the sides and a final regime where the flow separates but does not reattach.

8.2 Recommendations for further work.

1. Further investigation into streamwise vortices.

Whilst the results of chapter 5 propose the presence of a regular arrangement of streamwise vortices as the mechanism for the disruption and suppression of vortex shedding, at this stage very little is known about them, particularly at high Reynolds numbers. Therefore, it is of interest to establish the exact nature of these streamwise vortices through the use of more advanced experimental facilities (for example Digital particle image velocimetry or DPIV) to determine their size, strength and distribution across the span. Of particular interest would be the effect of wave steepness or surface geometry on the strength of these streamwise vortices.

2. Further investigation of the near wake flow field.

In the suppression of vortex shedding in the wake of a body using spanwise three-dimensionality it is shown that a new three-dimensional near wake structure results, chapters 4,5 & 6. However, whilst an interconnecting structure of vortex loops is observed at low Reynolds numbers, at high Reynolds numbers only a small insight into this near wake structure has been gained. At these higher Reynolds numbers hot wire anemometry and PIV in the wake of the sinuous cylinder have revealed the presence of low frequency streamwise oscillations of the wake. Therefore, further investigation using PIV and flow visualisation would be of interest in determining the time dependency of near wake structures.

3. Investigation into the effect of geometric wavelength.

During the current research, the wavelength of the imposed waviness of the body has been kept approximately constant for each cross-section investigated with only the wave height varied to investigate the changing effect of wave steepness. However, the recent work of Darekar & Sherwin (2001) has demonstrated for wavy square section cylinders at low Reynolds numbers that an optimum wavelength exists where vortex shedding can be suppressed with a minimum amount of wave steepness. Therefore, these results suggest the benefit of an investigation into the effect of geometric wavelength to determine whether an optimum configuration for the suppression of vortex shedding can be found at higher Reynolds numbers.

4. Further investigation into surface protuberances.

The work presented in chapter 6 has shown that by the fitting of elliptically shaped surface protuberances to the cylinder surface that vortex shedding can be disrupted or suppressed and substantial drag reductions achieved. However, despite the relative such success of the original design, the fitting of protuberances was only found to be moderately successful at the reduction of vortex induced vibrations (VIV). Therefore, much further investigation is required in order to develop a more effective shape and arrangement of protuberances for the reduction of VIV.

5. Further flow visualisation of the cylinders fitted with surface protuberances.

The wake of the cylinder fitted the surface protuberances was only investigated with PIV and hence the time evolution of structures in the wake has not been observed. Also it would be of interest to visualise the wake whilst the body is oscillating in the water channel at various different reduced velocities to observe how the transverse motion of the cylinder affects its ability to disrupt vortex shedding. Therefore, further visualisations of the wake using an array of streamlines in the water channel would be of interest.

References

[1] AHMED, A., KHAN, M.J. & BAYS-MUCHMORE, B. 1993 Experimental investigation of a three-dimensional bluff-body wake. AIAA Journal, Vol. 31: 559 – 563.

[2] ALLEN, H.J. & VINCENTI, W.G. 1994 Wall interference in a two-dimensional-flow wind tunnel with consideration of the effects of compressibility. NACA Rep. 782.

[3] APELT, C.J., WEST, G.S. & SZEWCZYK, A.A. 1973 The effects of wake splitter plates on the flow past a circular cylinder in the range $10^4<R<5x10^4$. J. Fluid Mech. Vol. 61: 187 – 198.

[4] ARIE, M. & ROUSE, H. 1956 Experiments on two-dimensional flow over a normal wall. J. Fluid Mech. Vol. 1: 129 – 141.

[5] BARKELEY, D. & HENDERSON, R. 1996 Three-dimensional Floquet stability analysis of the wake of a circular cylinder. J. Fluid. Mech. Vol. 322: 215 - 241

[6] BEARMAN, P.W 1965 Investigation of the flow behind a two-dimensional model with a blunt trailing edge and fitted with splitter plates. J. Fluid Mech. Vol. 21: 241 - 255.

[7] BEARMAN, P.W. 1967 The effect of base bleed on the flow behind a two-dimensional model with a blunt trailing edge. Aero. Quart. Vol. 18: 207 - 224.

[8] BEARMAN, P.W 1969 On vortex shedding from a circular cylinder in the critical Reynolds number regime. J. Fluid Mech. Vol. 37: 577 - 585.

[9] BEARMAN, P.W 1984 Vortex shedding from oscillating bluff bodies. Ann. Rev. Fluid Mech. Vol. 16: 195 - 222.

[10] BEARMAN, P.W. 1997 Developments in the understanding of bluff body flows. JSME Inter. J. series B, Vol. 41, no. 1.

[11] BEARMAN, P.W. & OWEN, J.C. 1998 *a* Reduction of bluff-body drag and suppression of vortex shedding by the introduction of wavy separation lines. J. Fluids & Structures. Vol. 12: 123 – 130.

[12] BEARMAN, P.W. & OWEN, J.C. 1998 *b* Suppression of vortex shedding from bluff bodies by the introduction of wavy separation lines. ASME Fluids Engineering Division Summer Meeting, June 21-25, 1998, Washington, DC.

[13] BEARMAN, P.W. & TOMBAZIS, N. 1993 The effect of three-dimensional imposed disturbances on bluff body near wake flows. J. Wind Eng. & Ind. Aero. Vol. 49: 339 - 350.

[14] BEARMAN, P.W. & TRUEMAN, D.M. 1972 An investigation into the flow around rectangular cylinders. Aero. Q. Vol. 23: 229 – 237.

[15] BLOOR, M.S. 1964 Transition to turbulence in the wake of a circular cylinder. J. Fluid Mech. Vol. 19: 290 – 304.

[16] DALTON, C., XU, Y. & OWEN, J.C. 2001 The suppression of lift on a circular cylinder due to vortex shedding at moderate Reynolds numbers. *To appear* J. Fluids & Structures April 2001.

[17] BREDE, M., ECKELMANN, H. & ROCKWELL, D. 1996 On secondary vortices in the cylinder wake. Phys. Fluids. A. Vol 8: 2117 – 2124.

[18] DAREKAR, R 2001 Drag reduction on bluff bodies by the introduction of a wavy stagnation face. PhD thesis, University of London.

[19] DAREKAR, R. & SHERWIN, S. 2001 Flow past a square section cylinder with a wavy stagnation face. J. Fluid Mech. Vol. 426: 263 – 295.

[20] EISENLOHR, H. & ECKELMANN, H. 1989 Vortex splitting and its consequese in the vortex street wakes of cylinders at low Reynolds numbers. Phys. Fluids A. Vol 1: 189 – 192.

[21] ELLIOTT, M.S. 2000 An investigation into the wing-rock of an 80 degree delta wing. PhD thesis, University of London.

[22] GASTER, M. 1969 Vortex shedding from slender cones at low Reynolds numbers. J. Fluid Mech. Vol. 38: 565 – 576.

[23] GASTER, M. 1971 Vortex shedding from circular cylinders at low Reynolds numbers. J. Fluid Mech. Vol. 46: 749 – 756.

[24] GERICH, D. & ECKELMANN, H. 1982 Influence of end plates & free ends on the shedding frequency of circular cylinders. J. Fluid Mech. Vol. 122: 109 - 122.

[25] GERRARD, J.H. 1966 The mechanics of the formation region of vortices behind bluff bodies. J. Fluid Mech. Vol. 25, part 2: 401 - 413.

[26] GERRARD, J.H. 1978 The wakes of cylindrical bluff bodies at low Reynolds number. Phil. Trans. Royal Soc. A288, 351 - 382.

[27] GOVARDHAN, R. & WILLIAMSON, C.H.K. 2000 Modes of vortex formation and frequency response of a freely vibrating cylinder. J. Fluid Mech. Vol. 420: 85 - 130.

[28] HENDERSON, R.D. 1995 Details of the drag curve near the onset of vortex shedding. Phys. Fluids. Vol 7, No. 9: 2102 – 2104.

[29] HONJI, H. & ISHI-I, K. 1976 Wake shedding from a distorted cylinder. J. Phys. Soc. Japan. Vol. 41, No. 3:1089 – 1090.

[30] HOURIGAN, K. & TOMPSON, M.C. 2000 Flow around elongated bodies: Flow structure and resonance. Presentation at IUTAM Conf. On bluff body wakes and vortex induced vibrations. Marseille, France.

[31] JAROCH, M.P. & FERNHOLZ, H.-H. 1989 The three-dimensional character of a normally two-dimensional separated turbulent shear flow. J. Fluid Mech. Vol. 205: 523 – 552.

[32] JAUVTIS, N., GOVARDHAN, R. & WILLIAMSON, C.H.K. 2000 Vortex-induced vibrations of a sphere. Presentation at IUTAM Conf. On bluff body wakes and vortex induced vibrations. Marseille, France.

[33] KELLAR, K.M. & PATANKAR, S. 1992 Numerical prediction of vortex shedding behind a square cylinder. Int. J. Numer. Meth. Fluids. Vol 14: 327 – 348.

[34] KHALAK, A. & WILLIAMSON, CHK. 1996 Dynamics of a hydroelastic cylinder with very low mass damping. J. Fluids & Structures. Vol. 10: 455 – 472.

[35] LEWEKE, T. & PROVANSAL, M. 1999 Vortex dynamics in the wake of a sphere. Gallery of Fluid Motion, Phys. Fluids. Vol. 11, No. 9: 1 – 14.

[36] MANSY, H., YANG, P. & WILLIAMS, D.R. 1994 Quantitative measurements of spanwise-periodic three-dimensional structures in the wake of a circular cylinder. J. Fluid Mech. Vol 270: 277 – 296.

[37] MILLER, G.D. & WILLIAMSON, C.H.K. 1994 Control of three-dimensional phase dynamics in a cylinder wake. Exp. Fluids. Vol. 18: 26 – 35.

[38] NAUMANN, A., MORSBACH, M. & KRAMER, C. 1966 The conditions of separation and vortex formation past cylinders. AGARD Conference Proceedings No. 4: 539 – 574.

[39] NEWMAN, D.J & KARNIADAKIS, G.E. 1997 A direct numerical simulation study of flow past a freely vibrating cable. J. Fluid Mech. Vol. 344: 95 -136.

[40] NORBERG, C. 1994 An experimental investigation of the flow around a circular cylinder: influence of aspect ratio. J. Fluid Mech. Vol. 258: 287 –316.

[41] NORBERG, C. 1996 Unpublished data. Available in Sohankar, A., Norberg, C. & Davidson, L. (1999), Simulation of three-dimensional flow around a square cylinder at moderate Reynolds numbers. Phys. Fluids. Vol 11, No. 2: 288 – 306.

[42] MASKELL, E.C. 1963 A theory of the blockage effects on bluff bodies and stalled wings in a closed wind tunnel. ARC R&M 3400.

[43] OKAJIMA, A. 1982 Strouhal numbers of rectangular cylinders. J. Fluid Mech. Vol. 123: 379 – 398.

[44] OWEN, J.C. 1997 The effect of three-dimensional disturbances on bluff body base drag. *Final year MEng Project Report*, Department of Aeronautics, Imperial College, London.

[45] OWEN, J.C., SZEWCZYK, A.A. & BEARMAN, P.W. 2000 Suppression of Karman vortex shedding. Gallery of Fluid Motion, Phys. Fluids. Vol. 12: 1 – 13.

[46] OWEN, J.C., BEARMAN, P.W. & SZEWCZYK, A.A. ~~2000~~ 2001 Passive control of VIV with drag reduction. *In press*, J. Fluids & Structures.

[47] PARKINSON, G. 1989 Phenomena and modelling of flow-induced vibrations of bluff bodies. Prog. Aerospace Sci. Vol. 26: 169 – 224.

[48] PETRUSMA, M.S. & GAI, S.L. 1994 The effect of geometry on the base pressure recovery of segmented blunt trailing edges. Aeron. J. Vol. 98: 267 - 274.

[49] PETRUSMA, M.S. & GAI, S.L. 1996 Bluff body wakes with free, fixed, & discontinuous separation at low Reynolds numbers & low aspect ratio. E. Fluids vol. 20: 189 - 198.

[50] PICCIRILLO, P.S. & VAN ATTA, C.W. 1993 An experimental study of vortex shedding behind linearly tapered cylinders at low Reynolds number. J. Fluid Mech. Vol. 246: 163 – 195.

[51] PRASAD, A. & WILLIAMSON, C.H.K. 1997 Three-dimensional effects on turbulent bluff body wakes at moderate Reynolds numbers. J. Fluid Mech. Vol. 333: 375 – 402.

[52] PRICE, P. 1956 Suppresion of the fluid induced vibration of circular cylinders. Proc. Am. Soc. Civ. Eng., J. Mech. Div. Vol. 82: pap. 1030.

[53] RICHARDS, B.E. 1977 Measurement of Unsteady Fluid Dynamic Phenomena. McGRAW-HILL.

[54] ROBICHAUX, J., BALACHANDAR, S. & VANKA, S.P. 1999 Three-dimensional Floquet instability of the wake of square cylinder. Phys. Fluids. Vol 11, No. 3: 560 – 578.

[55] RODRIGUEZ, O. 1991 Base drag reduction by the control of three-dimensional unsteady vortical structures. E. Fluids vol. 11: 218 - 226.

[56] ROSHKO, A. 1954 On the drag and shedding frequency of two-dimensional bluff bodies. NACA tech. note 3169.

[57] ROSHKO, A 1993 Perspectives on bluff body aerodynamics. J. Wind Ind. Aerodynamics. Vol. 49: 79 – 100.

[58] SALLET, D.W. 1980 Transverse motion of a buoy by surface wave. In: Practical experiences with flow induced vibrations, Naudascher, E. & Rockwell, D. Springer, p. 587.

[59] SARPKAYA, T. 1979 Vortex-induced oscillations. Trans. ASME. J. Appl. Mech. Vol 46: 241- 258.

[60] SCHAEFER, J.W. & ESKINAZI, S. 1959 An analysis of the vortex street generated in a viscous fluid. J. Fluid Mech. Vol. 6: 241 – 260.

[61] SCHEWE, G. 1983 On the force fluctuations acting on a circular cylinder in crossflow from subcritical up to transcritical Reynolds numbers. J. Fluid Mech. Vol. 133: 265 – 285.

[62] SCRUTON, C. & WALSHE, D.E.J. 1957 A means of avoiding wind-excited oscillations of structures with circular or nearly circular section. Natl. Phys. Lab. (U.K), Aero. Rep. 335.

[63] SLAOUTI, A. & GERRARD, J.H. 1981 An experimental investigation of the end effects on the wake of a circular cylinder towed through water at low Reynolds numbers. J. Fluid Mech. Vol. 112: 297 – 314.

[64] SOHANKAR, A., NORBERG, C. & DAVIDSON, L. 1995 Numerical simulation of unsteady flow around a square two-dimensional cylinder. 12th Australian Fluid Mech. Conf., Sydney.

[65] SOHANKAR, A., NORBERG, C. & DAVIDSON, L. 1998 Low Reynolds number flow around a square cylinder at incidence: Study of blockage, onset of vortex shedding and outlet boundary condition. Int. J. Numer. Meth. Fluids. Vol 26: 39 – 56.

[66] SOHANKAR, A., NORBERG, C. & DAVIDSON, L. 1999 Simulation of three-dimensional flow around a square cylinder at moderate Reynolds numbers. Phys. Fluids. Vol 11, No. 2: 288 – 306.

[67] SZEPESSY, S. & BEARMAN, P.W. 1992 Aspect ratio and end plate effects on vortex shedding from a circular cylinder. J. Fluid Mech. Vol. 234: 191 - 217.

[68] SZEWCZYK, A.A. 1998 Experiments on Vortex-Excited Oscillations of Axially-Varying Cylindrical Structures in Non-Uniform Approach Flow. Ocean Engineering and Marine Systems, Report Number: ONR 32199-4.

[69] TANEDA, A.S., HONJI, H. & TATSUNO, M. 1979 The electrolytic precipitation method of flow visualisation. Flow Visualisation, Hemisphere: 209 – 214.

[70] TANNER, M. 1972 A method of reducing the base drag of wings with blunt trailing edges. Aero. Q. Vol. 23: 15 - 23.

[71] TOMBAZIS, N. 1993 Effects of three-dimensional disturbances on bluff body near wakes. PhD thesis, University of London.

[72] TOMBAZIS, N. & BEARMAN, P.W. 1997 A study of three-dimensional aspects of vortex shedding from a bluff body with a mild geometric disturbance. J. Fluid Mech. Vol. 330: 85 - 112.

[73] TRITTON, D.J. 1959 Experiments on the flow past a circular cylinder at low Reynolds numbers. J. Fluid Mech. Vol. 6: 547 – 567.

[74] WALSHE, D.E. & COWDREY, C.F. 1959 Drag measurements at high Reynolds numbers of a circular cylinder fitted with helical strakes. Natl. Phys. Lab. (U.K), Aero. Rep. 384.

[75] WILLIAMSON, C.H.K. 1989 Oblique and parallel modes of vortex shedding in the wake of a circular cylinder at low Reynolds numbers. J. Fluid Mech. Vol. 206: 579 - 627.

[76] WILLIAMSON, C.H.K. 1992 The natural and forced formation of spot-like "vortex dislocations" in the transition of a wake. J. Fluid Mech. Vol. 243: 393 - 441.

[77] WILLIAMSON, C.H.K. 1996 *a* Three-dimensional wake transition. J. Fluid Mech. Vol. 328: 345 – 407.

[78] WILLIAMSON, C.H.K. 1996 *b* Vortex dynamics in the cylinder wake. Annu. Rev. Fluid Mech. Vol. 28: 477 – 539.

[79] WILLIAMSON, C.H.K. & BROWN, G.L. 1998 A series in $1/\sqrt{\mathrm{Re}}$ to represent the Strouhal-Reynolds number relationship of the cylinder wake. J. Fluids & Structures. Vol. 12: 1073 – 1085.

[80] WILLIAMSON, C.H.K., WU, J. & SHERIDAN, J. 1995 Scaling of streamwise vortices in wakes. Phys. Fluids. Vol. 7: 2307 – 2309.

[81] WONG, H.Y. & COX, R.N. 1978 The suppression of vortex induced oscillations of circular cylinders by aerodynamic devices. 3rd Colloquium industrial aerodynamics, Fachhoch-schule Aachen, Germany, Vol. 2.

[82] WOOD, C.J. 1967 Visualisation of an incompressible wake with base bleed. J. Fluid Mech. Vol. 29: 259 – 272.

[83] WOODGATE, L. & MAYBREY, J.F.M. 1959 Further experiments on the use of helical strakes for avoiding wind-excited oscillations of structures with circular or nearly circular section. Natl. Phys. Lab. (U.K), Aero. Rep. 381.

[84] WU, J., SHERIDAN, J., SORIA, J. & WELSH, M.C. 1994 An experimental investigation of streamwise vortices in the wake of a bluff body. J. Fluids & Structures. Vol. 8: 621 – 635.

[85] ZDRAVKOVICH, M.M. 1971 Circular cylinder enclosed in various shrouds. ASME Vibration Conf. Pap. 71-VIBR-28, 1971, Toronto.

[86] ZDRAVKOVICH, M.M. 1981 Review and classification of various aerodynamic and hydrodynamic means for the suppressing of vortex shedding. J. Wind Eng. & Ind. Aero. Vol. 7: 145 - 189.